ELECTROMAGNETIC PROPERTIES AND MACROSCOPIC CHARACTERIZATION OF COMPOSITE MATERIALS

QIU CHENGWEI

NATIONAL UNIVERSITY OF SINGAPORE

AND

ÉCOLE SUPÉRIEURE D'ÉLECTRICITÉ

ELECTROMAGNETIC PROPERTIES AND MACROSCOPIC CHARACTERIZATION OF COMPOSITE MATERIALS

QIU CHENGWEI

B. ENG., UNIVERSITY OF SCIENCE AND TECHNOLOGY OF CHINA, 2003

A DISSERTATION SUBMITTED FOR
THE JOINT DEGREE OF DOCTOR OF PHILOSOPHY
DEPARTMENT OF ELECTRICAL AND COMPUTER ENGINEERING
NATIONAL UNIVERSITY OF SINGAPORE AND ÉCOLE SUPÉRIEURE
D'ÉLECTRICITÉ
2007

Acknowledgements

First and foremost, I would like to wholeheartedly thank Prof. Le-Wei Li and Prof. Saïd Zouhdi for their constant encouragement and patient guidance throughout the research carried out in this thesis. The author would also like to thank Prof. Li particularly for his invaluable help in selecting the proper and interesting research topic at the beginning, conveying the fundamentals of electromagnetics, and recommending me to the NUS-Supélec Joint PhD programme. I also want to take this opportunity to express my most sincere gratitude to the support from Prof. Zouhdi in France, who helps me broaden the research horizons, teaches me how to lead, negotiate and communicate with a variety of people, and provides me a lot of chances to interact with outstanding scientists across Europe.

I am also indebted to Prof. Tat-Soon Yeo and Prof. Mook-Seng Leong for their support throughout my graduate student career and their encouragement to study electromagnetics. I am grateful to their willingness of taking the time to provide me valuable advice and experience on both technical and non-technical topics alike.

I am aslo grateful for the precious suggestions and help from Dr. Yao Haiying at National University of Singapore, and Dr. Burokur and Dr. Ouchetto in Supélec.

I would like to thank Mr. Yuan Tao, Mr. She Haoyuan and Ms. Li Yanan for their helpful discussions in the past few years.

Importantly, I deeply appreciate the unwavering support from my family. Mom, Dad, without you, I certainly would not be where I am today. Even though for the last eight years, I've lived a couple of thousand miles away, it has always felt like you were right here next to me. Finally, I want to thank my beloved wife, Lisa. You spent much time accompanying me and waiting for me to complete my research work. You've always had such tremendous faith in me and never failed to remind me that I can do anything I set my mind to even when I most doubted myself. Without your love, patience, and encouragement, I would not finish this tough job so successfully. Thank you so much!

Abstract

Composite materials can be engineered to possess peculiar properties such as left-handed (LH) triad, scattering enhancement, and negative refraction. Since no such naturally existing materials were known, artificially engineered composites thus play an exciting role in the modern electromagnetic theory and applications. Recently, a composite material, also known as metamaterial, consisting of periodic split-rings and rods has been proposed and fabricated to obtain LH and negative-index properties. Due to the high impact of such new properties, the functionality of composites deserves further studies, especially the possibility of realizing negative-index materials (NIMs). In this thesis, the microscopic and macroscopic properties, the control of the geometry and functionality, and the potential applications of various composite materials, from simple to complex, are explored. In addition, various numerical and theoretical tools are presented for the purpose of characterizing structured composite designs.

Before studying the physical realization of NIMs, basic properties of propagation, scattering, resonance of LH materials and NIMs are studied. The properties obtained are found to be in contrast to those encountered in right-handed materials.

For instance, using the rigorous line-source analysis of propagation and transmission into an isotropic negative-index cylinder, it is presented that power refracts at a negative angle, together with the hybrid effects of cylindrical curvature. The focusing phenomena of cylindrical lens are studied. In what follows, particular bi-isotropic cylinders, which also favour the negative refraction, are discussed. When the composite cylinder is small, the resonance will occur at particular ratio of the inner over outer layer. The scattering is greatly enhanced even for an electrically small composite cylinder, since the surface plasmons come into play at the interface within the composite cylinder. It is seen that the proper cloaking is a key step to generate the surface plasmon, and the cloaking theory has been studied not only for a small composite cylinder but also for a large one. The rotating effects are considered to examine the resonance shift and different mechanisms of resonances are clarified. In terms of the scattering, modified potentials of anisotropic spheres are proposed. Since most of the metamaterials are anisotropic, these modified potentials provide a robust method for considering the anisotropy ratio and its effects on scattering by using fractional-order Bessel or Hankel functions. Furthermore, the scattering properties of gyrotropic spheres are investigated. Hence, the results have a wide range of applications due to the robustness and generality. It can be applied to study the LH spheres, negative-index spheres and anisotropic spheres with partial negative parameters, only if appropriate algebraic signs of wave numbers are taken.

Next, the possibility of realizing negative refraction from geometrically ordered composite materials is discussed by proper manipulation of the functionalities and frequency selection. Theory and application of magnetoelectric composites are explored, where different levels of the magnetoelectric couplings are considered to achieve negative refraction and other exotic properties. For example, dispersive bulk chiral materials are studied by using Condon model to take into account frequency dispersion. The properties related to negative refraction and the frequency dependence are studied. Furthermore, the Faraday effects are combined with the magnetoelectric composites in order to produce gyrotropy in material parameters. It is seen that the gyrotropic parameters induced by the external fields will greatly favor the realization of negative-index material. In addition, the wave properties such as impedance, backward-wave region, and polarization status are presented. So as to further explore the merits of magnetoelectric composites in the realm of NIMs, nihility routes are proposed where the isotropic, nonreciprocal and gyrotropic chiral nihility are discussed. Medium constraints and the control of realizing such nihility conditions are also presented.

Finally, the multilayer algorithm is further employed in the construction of dyadic Green's functions (DGFs) to model systematic response of the structured composite materials. However, dyadic Green's functions cannot be applied straightforwardly to some periodic structured composites such as periodic lattices. Thus, an improved homogenization based on limit process is developed for bianisotropic composites (the most general material) to describe first the systematic response in terms of effective parameters, followed by using DGFs. It can be seen that the homogenization and dyadic Green's functions are two powerful and complementary tools to macroscopically characterize the engineered composites, which possess wide applicability in treating various geometries and material constitutions.

Contents

List of Figures

List of Tables

Chapter 1

Introduction

In a broad sense, the term *composite* means *made of two or more different parts.* The different natures of constituents allow us to obtain a material whose set of performance characteristics is greater than that of the components taken separately. The properties of composite materials result from the properties of the constituent materials, the geometrical distribution and their interactions. Thus to describe a composite material, it is necessary to specify the nature and geometry of itsconstituents, the distribution of the inclusions and their microscopic response. In the field of electrical engineering, electromagnetics of composite materials are especially important, since the electromagnetic behavior of rather complicated structures has to be understood before the design and fabrication of new devices. Deep understanding of physical phenomena in materials and structures is a necessary prerequisite for engineering process. In the last few decades, there has been an increasing interest in the research community in the modeling and characterization of negative-index materials. Negative-index materials represent a class of composite materials artificially constructed to exhibit exotic electromagnetic properties not readily found in naturally existing materials. This type of composite materials refracts light in a way which is contrary to the normal *right handed* rules of electromagnetism. Researchers hope that those peculiar properties will lead to superior lenses, and might provide a chance to observe some kind of negative analog of other prominent optical phenomena, such as reversal of the Doppler shift and Cerenkov radiation. When the dielectric constant (ϵ) and magnetic permeability (μ) are both negative, waves can still propagate in such a medium. In this case, the refractive index in the Snell's law is negative, consequently an incident wave experiences a negative refraction at the interface, resulting in a backward wave for which the phase of the wave moves in the direction opposite to the direction of the energy flow.

The first study of general properties of wave propagation in such a negative-index medium (NIM) has been usually attributed to the work of Russian physicist Veselago [3]. In fact, related work can be traced up to 1904 when physicist Lamb [4] suggested the existence of backward waves in mechanical systems. In fact, the first person who discussed the backward waves in electromagnetics was Schuster [5]. In his book, he briefly noted Lamb's work and gave a speculative discussion of its implications for optical refraction. He cited the fact that, within the absorption band of, for example, sodium vapour, a backward wave will propagate. Because of the high absorption region in which the dispersion is reversed, he was however pessimistic about the applications of negative refraction. Around the same time, Pocklington [6] showed that in a specific backward-wave medium, a suddenly activated source produces a wave whose group velocity is directed away from the source, while its velocity moves toward the source. Several decades later, negative refraction and lens applications (not perfect yet) was revisited and further discussed [7–9]. However, it is the translation of Veselago's paper into english version that the negative-index materials is revived, which are also referred now to as left-handed materials (LHM) or metamaterials. Very influential were the papers by Pendry [1,10,11]. The interest is further renewed after negative refraction was experimentally confirmed by Smith and Shelby [12–15]. A further boost to the field of NIM came when the applicability of lensing is proposed to relax the diffraction limit [16] by focusing both periodic and evanescent electromagnetic waves. The field keeps expanding owing to the fact that the Maxwell equations are scalable, thus practically the same strategies can be employed in the microwave and optical regions.

1.1 Background

1.1.1 Fundamentals of NIM

In order to realize the negative refraction [17–19], the composite material must have effective permittivity and permeability that are negative over the same frequency band. When the real parts of permittivity and permeability possess the same sign, the electromagnetic waves can propagate. For lossless media, if those two signs are opposite, wave cannot propagate unless the incident wave is evanescent itself. Historically, the development of artificial dielectrics was one of the first electromagnetic

NIMs by the design of a composite material [20]. If both ϵ and μ are negative, the refractive index of the given composite is defined as

$$n = \sqrt{|\epsilon||\mu|}\sqrt{e^{2j\pi}} = -\sqrt{|\epsilon||\mu|}. \tag{1.1}$$

More detailed investigation on the causality of negative-index materials can be found in [21]. Usually, solution for $n < 0$ consists of waves propagating toward the source, rather than plane waves propagating away from the source. Since such a solution would normally be rejected by the principles of causality, the physical proof of the solution for $n < 0$ can be supplied by the concept *average work* [13]. The work done by the source on the fields is

$$P = \Omega W = \pi \frac{\mu}{cn} j_0^2 \tag{1.2}$$

where Ω and j_0 represent the oscillation frequency and magnitude of the source current, and W is the average work done by the source on the field. It can be found that the solution of $n < 0$ leads to the correct interpretation that the current performs positive work on the fields because $\mu < 0$ for negative-index materials. Since the work done by the source on the fields is positive, energy propagates outward from the source, in agreement with Veselago's work [3].

No known material has naturally negative permittivity and permeability in RF band, and hence NIM has to be a composite of at least two kinds of materials which individually possess $\epsilon < 0$ and $\mu < 0$ in an overlapped frequency band. In order to creat negative permittivity in microwave region, the approach of an array of metallic rods with the electric field along with the axis was used [11]. Such structures act as a plasma medium. If the frequency is below the plasma frequency, the permittivity is negative. The Drude-Lorentz model can be utilized to characterize the wire medium with periodic cuts

$$\epsilon(\omega) = 1 - \frac{\omega_p^2 - \omega_{0e}^2}{\omega(\omega + i\Gamma_e) - \omega_{0e}^2}, \tag{1.3}$$

where ω_p, ω_{0e} and Γ_e denote respectively plasma frequency, resonant frequency, and damping constant. If the wires are continuous, the resonant frequency $\omega_{0e} = 0$.

In what follows, Pendry proposed the resonant structures of loops of conductor with a gap inserted to realize the negative permeability as in Fig. 1.1.

Figure 1.1: Schematic drawing of split ring resonator in [1].

The gap in the structure introduces capacitance and gives rise to a resonant frequency determined only by the geometry of the element. It is also known as the split-ring resonator (SRR), which could be described by

$$\mu(\omega) = 1 - \frac{F\omega^2}{\omega(\omega + i\Gamma_m) - \omega_{0m}^2}, \tag{1.4}$$

where F, Γ_m and ω_{0m} are respectively the filling fraction, resonant damping and resonant frequency [1]. New designs of SRR medium have been explored numerically and experimentally to overcome the narrow-band property, such as broadside SRR, complementary SRR, omega SRR, deformed SRR and S-ring SRR [22–28]. Current designs can yield large bandwidth, low loss and small size, which make the applications of SRRs wider.

The combination of a wire medium and SRR medium would present negative refraction due to the combined electric and magnetic responses [17,29–31]. However, such designs are normally anisotropic or bianisotropic, in which case the role of bianisotropy and extraction of those bianisotropic parameters were thus discussed [22,32]. Efforts were made to create isotropic composite NIM by ordering SRRs in three dimension [33] and the design was further scaled to IR frequencies [34]. However, at the wavelength approaching optical region, the inertial inductance caused by the electron mass and the currents through SRRs determines the plasma frequency and becomes dominant for scaled-down dimensions, which further makes the negative effects of permittivity and permeability totally disappear [35]. To overcome this difficulty, it is proposed to add more capacitive gaps to the original SRR [36]. Among the most recent results on experimental NIM structures with near-infrared response are those on NIMs in the 1.5 nm range with double periodic array of pairs of parallel gold nanorods [37], with a negative refractive index of about -0.3.

It is true that conventional SRR resonant structures are lossy and narrow-banded, and alternative approaches apart from exploring new designs may be of particular interest. Thus the transmission line (TL) approaches are proposed by the group at the University of Toronto to support negative refraction and backward waves [38–43]. Their basic idea is to use two-dimensional TL network with lump elements to achieve a high-pass filter, in which the backward wave can propagate. Thus, effective negative permittivity and permeability can be realized by suitable changes of configuration. The group at UCLA has further explored the TL approaches to realize the composite right- and left- handed structures [44–47]. The TL approach may provide broader band for negative refraction than SRR and wire medium, but it is obviously more difficult to be implemented in practical applications than the latter.

Another approach for generating negative refraction was to use photonic or electromagnetic bandgap structures [48–50]. PBGs or EBGs, first initiated by Yablonovitch [51] in 1987, are constructed typically from periodic high dielectric materials, and possess frequency band gaps eliminating electromagnetic wave propagation. Under certain circumstances, the Bloch/Floquet modes will lead to negative refraction. However the negative refraction behavior is different from the negative-index materials, in which the group velocity and phase vector are exactly anti-parallel. Electrically tunable nonreciprocal bandgap materials in the axial propagation along the direction of magnetization were considered in [52] to study cubic lattices of small ferrimagnetic spheres. Electromagnetic crystals [53, 54] operating at higher frequencies exhibit dynamic interaction between inclusions. Electromagnetic crystals (EC) are artificial periodical structures operating at the wavelengths comparable with their period while artificial dielectrics [20] only operate at long wavelengths as compared to the lattice periods. In the optical frequency range they are called photonic crystals (PC) [55]. In some particularly designed PCs, negative refraction will be present [56–58] and the application of open resonators with PCs of negative refraction [59–61] is also proposed in [62].

1.1.2 Focusing and lensing properties

Negative-index material would be a good starting point to achieve a perfect lens as shown in Fig. 1.2. Existence of a negative refractive index implies an entirely new form of geometrical optics. The example in Fig. 1.2 shows that a slab of NIM focuses the point source while a rectangular lens made of positive index material will expectedly diverge the beam.

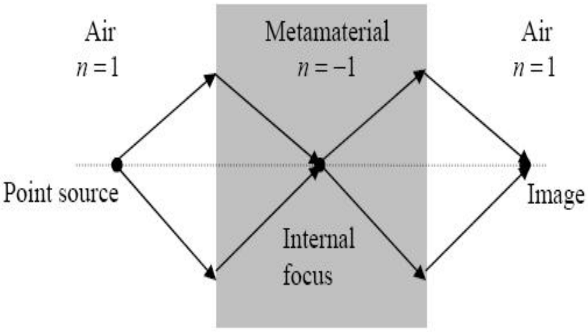

Figure 1.2: Schematic drawing of wave propagating in a split ring resonator (SRR) array in [2].

Making a conventional lens by positive-index materials with the best resolution requires a wide aperture, and the resolution limit is half a wavelength in free space.

The material with negative refractive index can make the lens more compact, and hence NIM is widely applicable in computer chips and storage devices. Pendry proposed the aniti-vacuum slab to perfectly focus a source [16]. Unfortunately, the perfect lens may be too difficult to realize as claimed by Gracia et al [63]. However, more practical lenses which consider the dispersion and absorption have been considered [64, 65] to avoid this debate. Another important aspect is that not all the information of the source can travel across the lens made of standard materials to the image. Negative refractive index materials restore not only the phase of propagating waves, but also the amplitude of evanescent states. By using the amplification of evanescent waves, higher resolution is anticipated. It is worth noting that on the interface of negative-index and positive-index media, the surface plasmon would be generated and makes decaying wave become growing wave. With the microwave TL lens, subwavelength focusing with the resolution of $\lambda_0/5$ has been realized [66]. The optical superlens made from a thin silver layer with a negative refractive index was fabricated with the resolution of $\lambda_0/6$ and it can image objects as small as 40 nm by the superlens [67]. It further confirms the Pendry's original conjecture that a NIM can focus near-fields and demonstrates clearly that evanescent mode enhancement leading to high resolution imaging [68].

1.2 Thesis work

There are two general viewpoints for the description of negative-index composite materials: macroscale and microscale. The macroscopic characterization of the electromagnetic wave property is the focus of this thesis, although the microscopic study is also touched. The macroscopic characterization is employed to gain a physical understanding of electromagnetics in special composite materials, particularly the composites of negative refraction, as well as to gauge the potentials of such NIM composites. Theoretical modeling and numerical simulation are typically developed for studying special composites as well as exploring the possibility of negative refraction based on the electromagnetics of those composites. The contributions of my dissertation are outlined briefly as follows.

Chapter 2 investigates fundamental electromagnetic behaviors of wave propagation, scattering and resonance in cylindrical composites with negative refractive index. The main contributions can be concluded that it provides a solid understanding of the hybrid effects on scattering properties of a multilayered composite NIM cylinder due to line sources and plane waves. Closed forms of electric and magnetic fields in each region are formulated using the eigenfunction expansion method as well as the proposed multilayer algorithm to systematically determine the scattering and transmission coefficients at each interface. Focusing properties and energy distribution associated with special scattering phenomena are presented. Based on the multilayer algorithm, the cloaking principles for cylindrical scatterers are given, and enhanced scattering can be observed even for very thin cylinders.

Chapter 3 provides a solid understanding of the scattering properties of anisotropic metamaterials. Since NIMs are anisotropic in general, it would be of great importance to investigate the electromagnetic wave interaction with anisotropic spheres.

In particular, the concept of the anisotropy ratio is proposed to characterize the anisotropic effects on the backscattered radar-cross section (RCS). The RCS reduction is discussed. RCS prediction rule and geometrical optics limit are found from an original potential formulation and numerical results are presented. Furthermore, the work is extend to gyrotropic spheres.

Chapter 4 is devoted to the isotropic and gyrotropic magentoelectric composites. Topics from theoretical formulation to potential applications are discussed. Due to the ability of magnetoelectric coupling of such composite materials, negative refraction and focusing properties can be realized under certain circumstances as shown in He's paper [69] for isotropic magnetoelectric materials. The gyrotropy in permittivity and permeability will further favor the realization of negative refraction. The contribution of the first two sections in this chapter is to provide an understanding of the wave propagation in isotropic/gyrotropic magnetoelectric composite materials and the advantage in achieving negative refraction over conventional chiral materials. For the isotropic case, the single-resonance model is used to study the materials' properties. For the gyrotropic case, I discuss the suitability of various constitutive descriptions, the backward waves and the impedance matching in subwavelength resonators. The last two sections are to discuss a special class of magnetoelectric composite materials: *chiral nihility*, as termed by Tretyakov [70]. Due to its potentials in achieving NIM, it deserves more research attention. The main contribution of this chapter is the in-depth study in the following topics : 1) the applicability of different medium formalisms is clarified for the first time for isotropic chiral nihility; 2) chirality effects of the wave propagation in chiral nihility are discussed where a wide Brewster angle range is found; 3) the mechanisms and conditions of realizing chiral nihility, nonreciprocal nihility and even gyrotropic nihility are investigated; and 4) image properties and related applications of chiral nihility are explored.

The last chapter is to present Maxwellian solutions to the periodically structured gyrotropic and bianisotropic composites. The contribution of the first half of this chapter is to establish the systematic response of the multilayered gyrotropic magnetoelectric composites by using Green's dyadics. Since dyadic Green's functions relate the source and field as a kernel, work in the first part still focuses on the gyrotropic magnetoelectric composite, which is the core medium discussed in Chapter 4. The contribution of the second half of this chapter is to provide an accurate approach to get the effective material parameters for a lattice periodically filled by bianisotropic inclusions. The bianisotropic material is the most general material and the artificial metal structures of NIMs may have bianisotropy. Hence the importance of this work is evident. Those two parts are complementary in Maxwellian solutions to electromagnetic problems. The first is based on the eigenfunction expansion while the latter is to discretize Maxwell's equations. The results obtained by the latter can be also used by the first to characterize the scattered and radiated fields.

Throughout the thesis, the time dependence of $e^{-i\omega t}$ is assumed, associated with the usage of first-kind Hankel functions.

Chapter 2

Electromagnetics of multilayered composite cylinders

2.1 Introduction

In this chapter, the fundamental electromagnetic properties of scattering, energy distribution, and multiple resonances of cylindrical scatterers will be considered. Throughout this chapter, the material in each region of the multi-layered cylinder is assumed to be homogeneous and isotropic, except for Section 2.4.3. However, in the macroscopic view, the whole layered structure in Fig. 2.1 is inhomogeneous.

The reflection and refraction of EM waves by a planarly stratified double negative medium, reflection and refraction of the waves were formulated by Kong [71]. The objective of the first part of this chapter is to extend the existing application from planar structures to cylindrical structures illuminated by a line source, so as to gain more insight into the hybrid effects of NIM and cylindrical curvature [72, 73]. Potential applications of the results in this work include the conformal antenna radome analysis and design, two-dimensional microwave and optical imaging, etc. First, a general formula of EM fields in all regions of a multilayered cylinder with negative-index and positive-index materials is derived. The eigenfunction expansion method is applied to express the EM fields in this structure. To verify proposed formulations and validate the analysis, the distant scattering cross sections for a two-layered composite cylinder with NIM are shown. Next, I consider some special cases of NIM in cylindrical geometry in the presence of a parallel line source, e.g., the energy distribution and focusing properties of isotropic and bi-isotropic subwavelength rods filled by NIMs.

The objective of the second part of this chapter is to study the multiple resonances and resonant scattering of composite cylinders filled by dispersive negative-index materials. Recently, the scattering of electromagnetic waves from a sphere fabricated from a negative-index material was studied in terms of the Mie coefficients that include magnetic effects [74], and it shows how the extinction spectra are affected by magnetic and plasmon polaritons. In this part, I investigate the multiple resonances in plasmonic cylinders as well as negative-index cylinders so as to yield a more complete vision of how plasmons and magnetic polaritons affect the resonant scattering of the composite cylinder.

In the last part, the cloaking effects and resonance shifts on the backscattering of both small and large cylinders are investigated for plane-wave illumination. The theoretical treatment starts from the formulation of electromagnetic fields in all three regions, i.e., the rotating core, the rotating cloaking and the background matrix. The angular velocities of the core and cloaking can be different and even anti-directional. The present results are thus useful due to the generality escpecially in studying specific cases such as rotating/stationary and left-handed/right-handed core-cloaking combinations. In particular, the optical resonances due to the plasmons and morphology-dependent resonances (MDRs) are examined. Due to the rotation, the resonances are found to shift and the effects of velocity on such phenomena are investigated. The results are also straightforward to be applied in studying metallic cloakings.

2.2 Multilayer algorithm

2.2.1 Eigenfunction expansion

Consider an N-layered infinitely-long cylinder situated in free space, as depicted in Fig. 2.1. Each layer is filled with arbitrary negative- or positive-refractive medium of different permittivities and permeabilities.

An incident wave with transverse electric (TE) or transverse magnetic (TM) polarization is assumed to illuminate the layered cylinder in free space at an arbitrary oblique angle. In the cylindrical coordinates system, the vector wave functions are

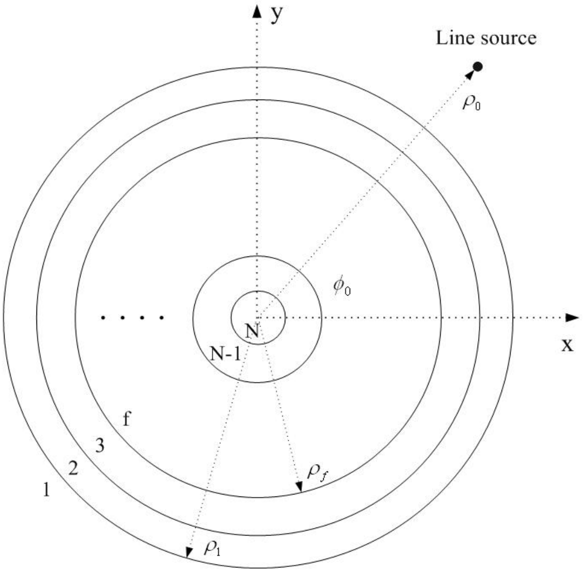

Figure 2.1: Cross-sectional view of a multilayered cylinder with the line source at $(\rho_0,\,\phi_0)$ in the outermost region.

given by Li *et al* in [75], and rewritten as follows:

$$\boldsymbol{M}_n^{(p)}(k_z) = \left[\widehat{\boldsymbol{\rho}}\frac{in}{\rho}B_n^{(p)}(k_\rho\rho) - \widehat{\boldsymbol{\phi}}\frac{dB_n^{(p)}(k_\rho\rho)}{d\rho}\right]e^{i(n\phi+k_z z)}, \tag{2.1a}$$

$$\boldsymbol{N}_n^{(p)}(k_z) = \frac{e^{i(n\phi+k_z z)}}{k}\left[\widehat{\boldsymbol{\rho}}ik_z\frac{dB_n^{(p)}(k_\rho\rho)}{d\rho} - \widehat{\boldsymbol{\phi}}\,\frac{nk_z}{\rho}B_n^{(p)}(k_\rho\rho) + \widehat{\boldsymbol{z}}k_\rho^2 B_n^{(p)}(k_\rho\rho)\right] \tag{2.1b}$$

where $B_n^{(p)}(k_\rho\rho)$ represents the cylindrical Bessel functions of order n, the superscript p equals 1 or 3 representing the Bessel function of the first kind or the cylindrical Hankel function of the first kind, and $k^2 = k_\rho^2 + k_z^2$. If the electromagnetic waves are normally incident on the surface, the vector wave functions expressed in Eq. (2.1) can be simplified as:

$$\boldsymbol{M}_n^{(p)}(k) = \left[\widehat{\boldsymbol{\rho}}\frac{in}{\rho}B_n^{(p)}(k\rho) - \widehat{\boldsymbol{\phi}}\frac{dB_n^{(p)}(k\rho)}{d\rho}\right]e^{in\phi}, \tag{2.2a}$$

$$\boldsymbol{N}_n^{(p)}(k) = \widehat{\boldsymbol{z}}kB_n^{(p)}(k\rho)\,e^{in\phi}. \tag{2.2b}$$

By using the eigenfunction expansion method, the electric and magnetic fields in the intermediate regions (e.g., the f^{th} region) are as follows:

$$\begin{aligned}
\boldsymbol{E}_f &= \sum_{n=0}^{\infty} \Big\{ a_{nf} \boldsymbol{N}_n^{(3)}(k_{zf}) + b_{nf} \boldsymbol{M}_n^{(3)}(k_{zf}) \\
&\quad + a'_{nf} \boldsymbol{N}_n^{(1)}(k_{zf}) + b'_{nf} \boldsymbol{M}_n^{(1)}(k_{zf}) \Big\}, \qquad (2.3a) \\
\boldsymbol{H}_f &= \frac{1}{i\eta_f} \sum_{n=0}^{\infty} \Big\{ a_{nf} \boldsymbol{M}_n^{(3)}(k_{zf}) + b_{nf} \boldsymbol{N}_n^{(3)}(k_{zf}) \\
&\quad + a'_{nf} \boldsymbol{M}_n^{(1)}(k_{zf}) + b'_{nf} \boldsymbol{N}_n^{(1)}(k_{zf}) \Big\} \qquad (2.3b)
\end{aligned}$$

where a_{nf}, b_{nf}, a'_{nf} and b'_{nf} are the unknown expansion coefficients and η_f denotes the wave impedance in the f^{th} layer.

For the outermost region (i.e., Region 1) and the inner-most region (i.e., Region N), the electromagnetic fields can be expanded as:

$$\begin{aligned}
\boldsymbol{E}_1 &= \boldsymbol{E}^i + \boldsymbol{E}^s = \boldsymbol{E}^i + \sum_{n=0}^{\infty} \Big[a_{n1} \boldsymbol{N}_n^{(3)}(k_{z1}) + b_{n1} \boldsymbol{M}_n^{(3)}(k_{z1}) \Big], \qquad (2.4a) \\
\boldsymbol{H}_1 &= \boldsymbol{H}^i + \boldsymbol{H}^s = \boldsymbol{H}^i + \frac{1}{i\eta_f} \sum_{n=0}^{\infty} \Big[a_{n1} \boldsymbol{M}_n^{(3)}(k_{z1}) + b_{n1} \boldsymbol{N}_n^{(3)}(k_{z1}) \Big], \qquad (2.4b)
\end{aligned}$$

and

$$\begin{aligned}
\boldsymbol{E}_N &= \sum_{n=0}^{\infty} \Big[a'_{nN} \boldsymbol{N}_n^{(1)}(k_{zN}) + b'_{nN} \boldsymbol{M}_n^{(1)}(k_{zN}) \Big], \qquad (2.5a) \\
\boldsymbol{H}_N &= \frac{1}{i\eta_N} \sum_{n=0}^{\infty} \Big[a'_{nN} \boldsymbol{M}_n^{(1)}(k_{zN}) + b'_{nN} \boldsymbol{N}_n^{(1)}(k_{zN}) \Big]. \qquad (2.5b)
\end{aligned}$$

For the electromagnetic fields in all the regions, one has the same longitudinal wave vector k_z due to phase matching condition, whereas the radial wave vector $k_{\rho f}$ is discontinuous.

In order to make use of the multilayer algorithm for layered structures, the incident waves are better to be expanded by those eigenfunctions. For TE and TM waves, the electromagnetic fields can be respectively expressed by

$$\begin{aligned} \boldsymbol{E}_{TE}^{i} &= \frac{E_0^{TE}}{ik\sin\theta_0}\sum_{n=0}^{\infty}\left(2-\delta_{n0}\right)i^n\boldsymbol{M}_n^{(1)}\left(k_z\right)e^{-in\phi_0}, && (2.6a)\\ \boldsymbol{H}_{TE}^{i} &= -\frac{E_0^{TE}}{\eta_0 k\sin\theta_0}\sum_{n=0}^{\infty}\left(2-\delta_{n0}\right)i^n\boldsymbol{N}_n^{(1)}\left(k_z\right)e^{-in\phi_0}; && (2.6b) \end{aligned}$$

and

$$\begin{aligned} \boldsymbol{E}_{TM}^{i} &= \frac{E_0^{TM}}{k\sin\theta_0}\sum_{n=0}^{\infty}\left(2-\delta_{n0}\right)i^n\boldsymbol{N}_n^{(1)}\left(k_z\right)e^{-in\phi_0}, && (2.7a)\\ \boldsymbol{H}_{TM}^{i} &= \frac{E_0^{TM}}{i\eta_0 k\sin\theta_0}\sum_{n=0}^{\infty}\left(2-\delta_{n0}\right)i^n\boldsymbol{M}_n^{(1)}\left(k_z\right)e^{-in\phi_0}. && (2.7b) \end{aligned}$$

For an infinitely long line source placed at (ρ_0, ϕ_0) and parallel to the cylinder, the incident electromagnetic wave can be expressed by

$$\begin{aligned} \boldsymbol{E}^{i} &= -\frac{k^2 I}{4\omega\varepsilon_0}\sum_{n=0}^{\infty}\left(2-\delta_{n0}\right)H_n^{(1)}\left(k\rho_0\right)\boldsymbol{N}_n^{(1)}\left(k\right)e^{-in\phi_0}, && (2.8a)\\ \boldsymbol{H}^{i} &= -\frac{kI}{4i}\sum_{n=0}^{\infty}\left(2-\delta_{n0}\right)H_n^{(1)}\left(k\rho_0\right)\boldsymbol{M}_n^{(1)}\left(k\right)e^{-in\phi_0}, && (2.8b) \end{aligned}$$

where I stands for the amplitude of the electric current, δ_{pq} denotes the Kroneker delta function, and the vector wave functions $\boldsymbol{M}$ and $\boldsymbol{N}$ are defined in Eq. (2.2).

Thus, one can have electromagnetic field expansions in all regions based on the field coupling together with the incoming/outgoing waves superposition. Those scattering coefficients can be solved in a multilayer algorithm associated with boundary conditions at each interface, which is to be shown.

2.2.2 Recursive algorithm of scattering coefficients

The electromagnetic fields satisfy the boundary conditions at each interface $\rho = \rho_f$

$$\widehat{\boldsymbol{\rho}} \times \begin{bmatrix} \boldsymbol{E}_f \\ \boldsymbol{H}_f \end{bmatrix} = \widehat{\boldsymbol{\rho}} \times \begin{bmatrix} \boldsymbol{E}_{(f+1)} \\ \boldsymbol{H}_{(f+1)} \end{bmatrix}. \tag{2.9}$$

Inserting Eqs. (2.3a) and (2.3b) into Eq. (2.9), one can obtain a linear equation of

$$[F_f]\,[C_f] = \left[F_{(f+1)}\right]\left[C_{(f+1)}\right] \tag{2.10}$$

where $[F_f]$ is a 4×4 matrix, and $[C_f]$ is a 4×1 vector consisting of the unknown scattering coefficients

$$[C_f] = \begin{bmatrix} a_{nf} & b_{nf} & a'_{nf} & b'_{nf} \end{bmatrix}^T. \tag{2.11}$$

For TE and TM incidences, a'_{n1} and b'_{n1} are represented respectively by

$$a'_{n1} = (2 - \delta_{n0})\, i^n \frac{E_1^{TM}}{k_1 \sin\theta_0} e^{-in\phi_0}, \tag{2.12a}$$

$$b'_{n1} = -(2 - \delta_{n0})\, i^{n+1} \frac{E_1^{TE}}{k_1 \sin\theta_0} e^{-in\phi_0}. \tag{2.12b}$$

The parameter matrix $[F_f]$, where $\rho = r_f$, can be obtained

$$[F_f] = \begin{bmatrix} \frac{-nk_z}{k_f\rho} H_n^{(1)}(k_{\rho f}\rho) & \frac{-dH_n^{(1)}\left(k_{\rho f}\rho\right)}{d\rho} & \frac{-nk_z}{k_f\rho} J_n(k_{\rho f}\rho) & \frac{-dJ_n\left(k_{\rho f}\rho\right)}{d\rho} \\ \frac{-k_{\rho f}^2}{k_f} H_n^{(1)}(k_{\rho f}\rho) & 0 & \frac{-k_{\rho f}^2}{k_f} J_n(k_{\rho f}\rho) & 0 \\ \frac{-1}{i\eta_f}\frac{dH_n^{(1)}\left(k_{\rho f}\rho\right)}{d\rho} & \frac{-nk_z}{i\omega\mu_f\rho} H_n^{(1)}(k_{\rho f}\rho) & \frac{-1}{i\eta_f}\frac{dJ_n\left(k_{\rho f}\rho\right)}{d\rho} & \frac{-nk_z}{i\omega\mu_f\rho} J_n(k_{\rho f}\rho) \\ 0 & \frac{-k_{\rho f}^2}{i\omega\mu_f} H_n^{(1)}(k_{\rho f}\rho) & 0 & \frac{-k_{\rho f}^2}{i\omega\mu_f} J_n(k_{\rho f}\rho) \end{bmatrix}. \tag{2.13}$$

For the line-source excitation which is parallel to cylinder's axis, a'_{n1} and b'_{n1} are represented by

$$a'_{n1} = -(2 - \delta_{n0}) \frac{k_1^2 I}{4\omega\epsilon_1} H_n^{(1)}(k_1\rho_0)\, e^{-in\phi_0}, \tag{2.14a}$$

$$b'_{n1} = 0. \tag{2.14b}$$

Similarly, $[F_f]$, where $\rho = r_f$, can be derived:

$$[F_f] = \begin{bmatrix} 0 & -H_n'^{(1)}(k_f\rho) & 0 & -J_n'^{(1)}(k_f\rho) \\ -H_n^{(1)}(k_f\rho) & 0 & -J_n(k_f\rho) & 0 \\ -\frac{H_n'^{(1)}(k_f\rho)}{j\eta_f} & 0 & -\frac{J_n'(k_f\rho)}{i\eta_f} & 0 \\ 0 & -\frac{H_n^{(1)}(k_f\rho)}{i\eta_f} & 0 & -\frac{J_n(k_f\rho)}{i\eta_f} \end{bmatrix}, \tag{2.15}$$

where the derivative is with respect to the argument.

By defining a new matrix

$$[T_f] = [F_{f+1}]^{-1}\,[F_f]\,, \tag{2.16}$$

one can rewrite

$$[C_N] = \left[T_N^{(1)}\right][C_1] \tag{2.17}$$

where

$$\left[T_N^{(f)}\right] = [T_{N-f}]\left[T_{N-(f+1)}\right]\ldots[T_2]\,[T_1]\,. \tag{2.18}$$

Therefore, the coefficient relationship between inner- and outer- most layer can be established

$$\begin{bmatrix} 0 \\ 0 \\ a'_{nN} \\ b'_{nN} \end{bmatrix} = \left[T_N^{(1)}\right] \begin{bmatrix} a_{n1} \\ b_{n1} \\ a'_{n1} \\ b'_{n1} \end{bmatrix}. \tag{2.19}$$

Since a'_{n1} and b'_{n1} are already known, a_{n1} and b_{n1} can be determined via the first two rows of $\left[T_N^{(1)}\right]$ in Eq. (2.19) , regardless of values of a'_{nN} and b'_{nN}. Provided $[C_1]$ is obtained, solution to $[C_f]$ is straightforward by using Eq. (2.17). As a result, electromagnetic fields in any region can be formulated.

2.3 Verification

To verify the correctness of the formulations derived above, I firstly calculate the far-field scattering pattern of a two-layer (three regions) cylinder filled with different materials, illuminated by the TE- and TM-waves, and radiated by the parallel line source, respectively. The geometry is shown in Fig. 2.2. The radii of two layers from inside to outside are $a = 0.25\lambda$ and $b = 0.3\lambda$, respectively. The corresponding relative permittivities are $\epsilon_{r1} = 4.0$, and $\epsilon_{r2} = 1.0$. The relative permeabilities of two layers are $\mu_{r1} = \mu_{r2} = 1.0$. Two different excitations are considered: (a) the plane waves are assumed to be at normal incidence; and (b) the line source is placed at a distance of $\rho_0 = 0.5\lambda$ from the center of the layered cylinder, and an observation angle $\phi_0 = 0°$. The far-field scattering pattern can be obtained by the asymptotic form of large-argument Hankel functions. The results are shown in Fig. 2.3 and Fig. 2.4, respectively.

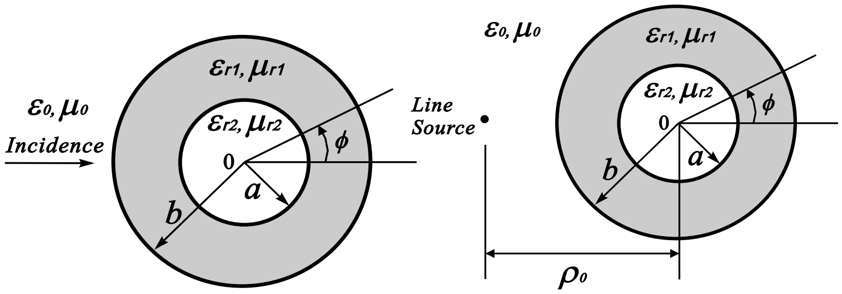

(a) A plane wave incidence. (b) Radiation of a parallel line source.

Figure 2.2: Geometry of a two-layered cylinder with DPS materials.

For the reference, the integral-equation solutions based on [76,77], are also given.

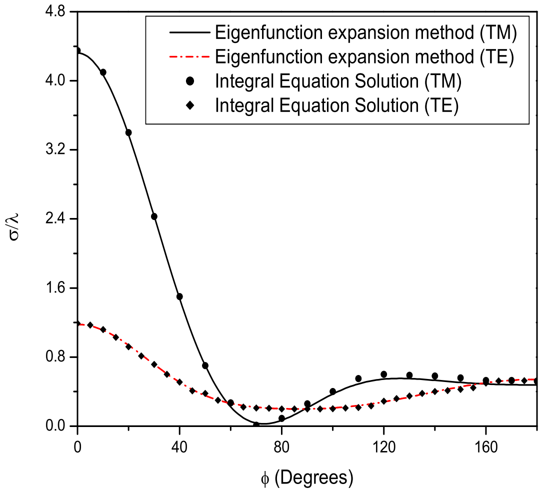

Figure 2.3: Far-field scattering patterns of TE- and TM-waves illuminating a two-layered cylinder with DPS materials.

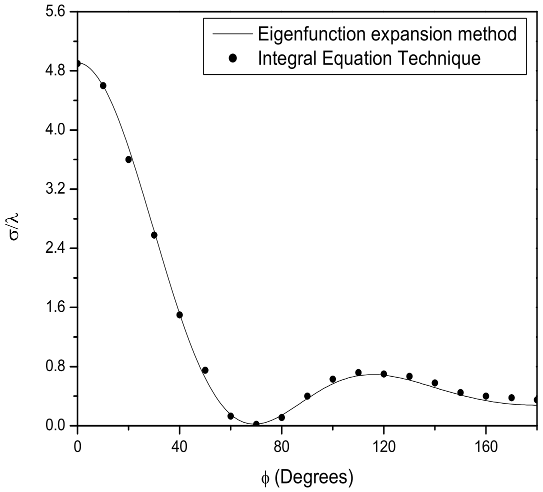

Figure 2.4: Radiated field pattern of a nearby parallel line source in the presence of a two-layered cylinder with DPS materials.

An excellent agreement is observed between the existing solution presented in [76,77] and those newly obtained. Those results partially verify the correctness of the derived theoretical formulas and developed codes in this thesis.

2.4 Numerical studies

In this section, only single-layer and two-layer cylinders are considered because they possess enough interesting scattering properties. The present work can be extended to study 3-layer or even 4-layer cylinders straightforwardly since the multilayer algorithm developed above is suitable for an arbitrary number of layers.

2.4.1 Discontinuity

First, the real parts of the field components, H_ρ, H_ϕ and E_z, scattered by a two-layered (three regions) cylinder filled alternately with negative-index and positive-index material are shown in Fig. 2.5. In such a case, a line source is placed at $\rho_0 = 9.5\lambda$ and $\phi_0 = 0^\circ$, the radii of two layers are $r_1 = 8\lambda$ and $r_2 = 5\lambda$, respectively. The region 1 is free space, regions 2 and 3 are filled with $(-\epsilon_0, -\mu_0)$ and (ϵ_0, μ_0), respectively. As expected, the tangential components H_ϕ and E_z are equal on the layered interfaces. The normal component H_ρ is not, and it satisfies by default the continuity of normal component of magnetic flux density $\boldsymbol{B}$ across the interfaces. The anti-symmetry in Fig. 2.5(a) is attributed to the sinusoidal function of $\sin\phi$ in the field expression of H_ρ, and the tangential components will be perturbed due to the images induced inside the cylinder.

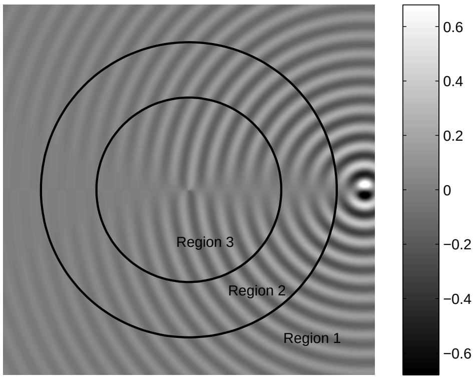

(a) The real part of H_ρ component

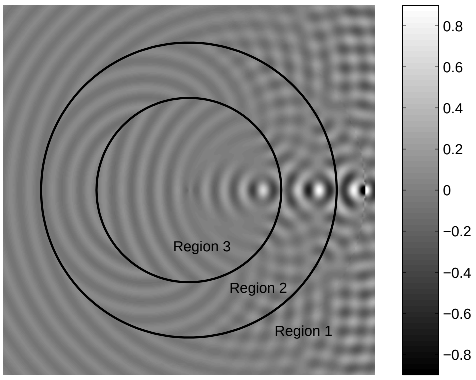

(b) The real part of H_ϕ component

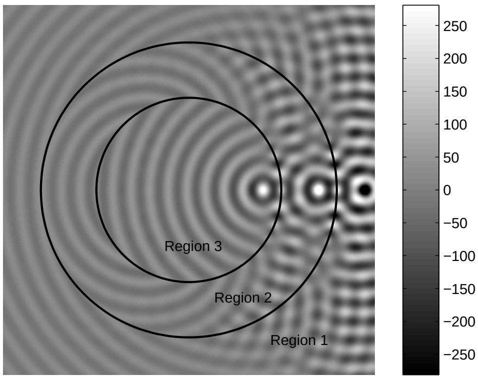

(c) The real part of E_z component

Figure 2.5: Electromagnetic wave propagating through a two-layered cylinder with DNG and DPS materials.

2.4.2 Single-layer isotropic cylinder

The normalized scattering cross section σ/λ of a single-layer (two regions) cylinder filled with DNG $(-\varepsilon_0, -\mu_0)$ material is calculated under the illumination by a TM wave with the incident angles of $\theta^i = \pi/2$ and $\phi^i = 0$ in free space. Curves for different radii a of the cylinder are plotted in Fig. 2.6.

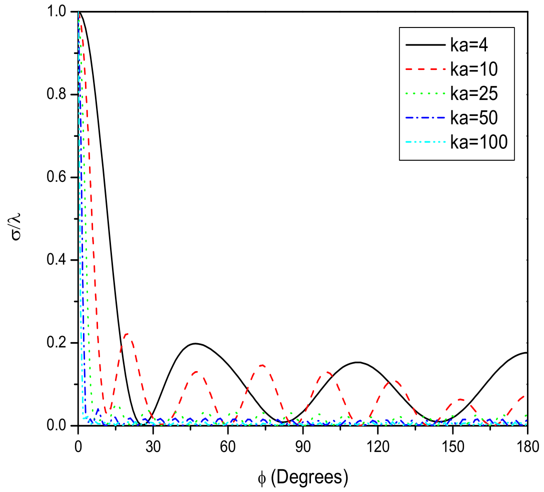

Figure 2.6: Normalized scattering cross section of a single-layer cylinder $(-\epsilon_0, -\mu_0)$ of different radii.

It is obvious that the reflection by the cylinder is quickly diminished with the increase of the radius. It can be also observed that the RCS data at and near $\phi = 0°$ are very large and it is of the impulse shape when the cylindrical radius is large. This phenomenon can be explained as follows.

- *Intensity*: First of all, in Fig. 2.6, the incident wave (a TM-polarized plane wave) is impinged at an angle of elevation $\theta^i = 90°$ and azimuth $\phi = 180°$. In this case, some portion of the wave energy is normally incident upon the cylinder, so the transmitted wave due to this portion propagates entirely through the dielectric cylinder when the impedance is matched ($\epsilon_r = \mu_r = -1$). This portion of waves contributes to part of bistatic RCS data of $\phi = 0°$. For a cylinder of large radius, the illumination area by normal or nearly normal incident waves is larger than that of a cylinder of smaller radius. In this case, the cylinder tends to be a perfectly matched layer and it is almost transparent to the incident wave. Therefore the percentage of the energy propagated through the cylinder will be relatively larger.

- *Beamwidth*: Secondly, the cylinder behaves as a dielectric lens. For RCS computations, I take the observation point at infinity. When the incident wave propagates through the cylinder filled with DNG, the focus point will approach to infinity due to the smoother dielectric curvature. For example, when $ka = 100$, the observation point (infinity) lies to the right of the focus point (which is already sufficiently far away from origin). Thus, it can be imagined that the angle of coverage is small at around $\phi = 0°$. When the radius becomes larger and larger, the observation point and the focus point will move closer and closer to each other. In an extreme case, when the cylinder tends to approach a flat slab, the angle of coverage is almost zero to form a delta pulse.

That is why the scattering cross sections around the angle of $\phi = 0°$ are thus much stronger, but confined within a very narrow beamwidth.

Then, the radiation by a line source in the presence of this cylinder is considered. The normalized amplitudes of the time-averaged Poynting vector, which is denoted by $\langle \boldsymbol{S} \rangle = \frac{1}{2}\mathrm{Re}\,(\boldsymbol{E} \times \boldsymbol{H}^*)$, are shown in Fig. 2.7-Fig. 2.9.

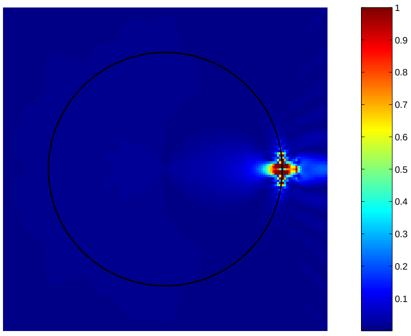

Figure 2.7: Normalized magnitude of Poynting vector of a cylinder of $a = 4\lambda$ filled with anti-vacuum and the line source at 4.5λ away from the origin.

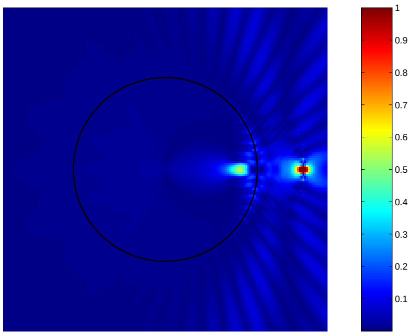

Figure 2.8: Normalized magnitude of Poynting vector of the same cylinder as in Fig. 2.7 except the line source at 6λ away from the origin.

The electrical size of the cylinder is fixed at $a = 4\lambda$. The material inside the cylinder in Fig. 2.7 is anti-vacuum (i.e, $\epsilon = -\epsilon_0$ and $\mu = -\mu_0$) with the negative

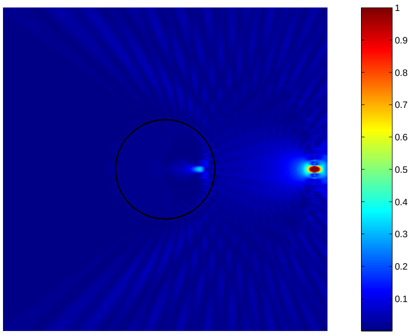

Figure 2.9: Normalized magnitude of Poynting vector of the same cylinder as in Fig. 2.7 except for the line source at 12λ away from the origin.

refraction index of -1. The line source is placed at a distance of 4.5λ from the origin, which is very close to the surface of cylinder. Partial focusing phenomenon can still be observed in Fig. 2.7. When the line source is located quite close to the cylinder, the partial focusing should be a sink because such situation is more like a impedance-matched flat interface. Therefore, most of the incident energy will be tunnelled and focused inside. If the line source is put further away as in Fig. 2.5(b) and (c), the focus inside the negative-index cylinder is obviously of source type. Also, some reflections can be observed at the positions behind the line source in Fig. 2.7 because of the cylindrical curvature. It can be seen that a ripple occurs at the cylinder's surface close to the line source, which is the incoming window of the incident wave. Certain points of this ripple carry comparably high energy as the line source. In Fig. 2.8 and Fig. 2.9, the line source is put further away from the cylinder's surface, while the radius of the cylinder keep unchanged. When the source is far away from the surface, the ripple effect in the incoming window on the cylinder will be reduced as expected. In Fig. 2.8 and Fig. 2.9, foculas are formed due to the imperfect focusing condition. By changing the position of line source, the energy distributions outside the cylinder are greatly modified as can be seen from Fig. 2.7 to Fig. 2.9. It is due to the fact that when the line source is very close to the cylinder's surface, the curvature is quite flat within the incoming window of incident wave, which is close to a slab configuration. If the line source is moved far away, the incoming window becomes larger and the cylindrical curvature takes effect.

From Fig. 2.7-Fig. 2.9, it is observed that a facula is formed inside the cylinder. The formation of the facula is due to the fact that the cylinder with $(-\epsilon_0, -\mu_0)$ is not a good focusing system. This observation can be verified by using the theory of arbitrary coordinate transformations [78]. According to the theory, if the wave scattering properties are kept unchanged after the geometrical dimension (e.g., the radius) is changed, μ and ϵ have to be adjusted accordingly. When the physical problem is changed from a perfect slab lens to a perfect cylindrical lens, the permittivity and permeability in the lens are required to be a function of position. Hence, the cylinder with $(-\epsilon_0, -\mu_0)$ cannot focus the light perfectly, and it will still reflect waves. However, a phenomenon of focus shown as in Fig. 2.10 and very small reflection shown as in Fig. 2.6 can be still be obtained. As a limiting example in Fig. 2.10, nearly perfect image is formed since the electrical size of the calculated problem is much larger than the wavelength of the incident wave.

In addition, of particular interest are scattering properties of subwavelength cylinders due to the line source radiation. The radii in Fig. 2.11 are both equal to 0.05λ, while the distances of the line source from the surface are 0.2λ and 1λ,

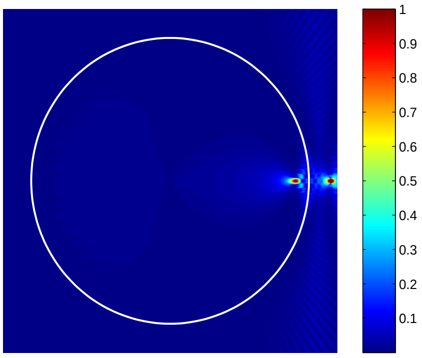

Figure 2.10: Normalized amplitudes of the time-averaged Poynting vector for a single-layer cylinder with $(-\epsilon_0, -\mu_0)$ and $a = 150\lambda$.

respectively. Note that the energy distribution around the line source is suppressed and only the distribution near the cylinder is plotted. Two foculas with giant energy distribution are found in Fig. 2.11(a) when the distance of line source from the surface is 4 times of the radius. Of particular interest is that the focula is not located inside the subwavelength cylinder any more. Instead, the foculas are formed in two particular areas around the cylindrical surface. If the distance of line source increases to 20 times of radius [see Fig. 2.11(b)], the magnitude of the two foculas decreases and the positions are more apart from each other. It should be noted that Rayleigh scattering is not held anymore when cylinder is weakly dissipative or without dissipation. In such cases, anomalous scattering occurs, and the peculiarities in re-entrance of field lines result in the localized energy at the interface of the cylinder. The near and far field patterns are much more complicated.

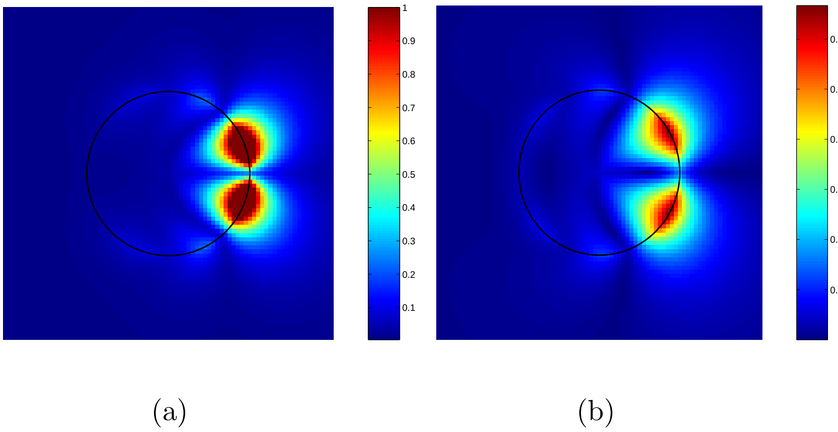

Figure 2.11: Normalized magnitude of Poynting vector in the presence of a cylinder of $a = 0.05\lambda$ filled with anti-vacuum due to the line source at: (a) 0.2λ away from the surface; and (b) 1λ away from the surface.

2.4.3 Single-layer bi-isotropic cylinder

Now bi-isotropic cylinders with magnetoelectric couplings are studied, whose physical properties will be discussed in detail in Chapter 4. The degree of magnetoelectric couplings is represented by the chirality parameter of κ. Different chiralities are chosen so as to study the effect of magnetoelectric coupling upon the scattering properties of the cylinder.

As a special case of bi-isotropic media, chiral nihility is considered first since it yields two special equivalent mediums: one is vacuum and the other is anti-vacuum. The judicious selection of parameters for chiral nihility is based on the findings in [79]. It is shown in Fig. 2.12 that there are several foculas inside the cylinder and both energy distributions inside and outside the cylinder are greatly modified by the existence of magnetoelectric couplings. Compared with Fig. 2.8, the energy in Fig. 2.12 behind the cylinder is enhanced and those enhanced distributions form some ribbon-shaped areas.

In what follows, normal bi-isotropic mediums with the same ϵ_r and μ_r, but different κ are considered. The reason for $\epsilon_r = \mu_r$ is that the wave impedance of bi-isotropic medium is independent of κ and identical to the impedance of free space. From the comparison between Fig. 2.12(b) and Fig. 2.12(c), it can be seen that the focusing is more obvious for bigger values of κ. More interestingly, in Fig. 2.12(c), the structure not only presents two focusing points, but also enhances the energy inside the cylinder and high energy distribution is confined along the diameter.

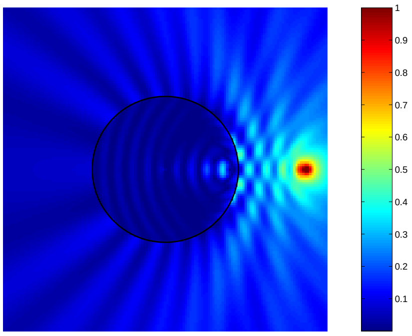

(a) $\epsilon_r = 1e-5$, $\mu_r = 1e-5$, and $\kappa = 1$

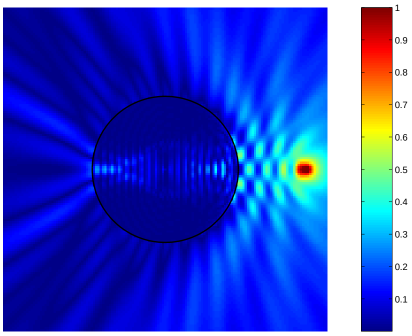

(b) $\epsilon_r = 1$, $\mu_r = 1$, and $\kappa = 2$

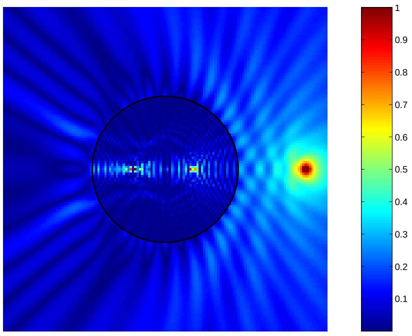

(c) $\epsilon_r = 1$, $\mu_r = 1$, and $\kappa = 4$

Figure 2.12: Normalized magnitude of Poynting vector in the presence of a bi-isotropic cylinder of $a = 2.5\lambda$ filled with chiral or chiral nihility medium due to the line source at 4.8λ away from the origin.

2.4.4 Coating

Here the coating by a thin cylinder and its parameters are studied. I consider two combinations of the core and coating layers: double positive against double negative pair (DPS-DNG) and ϵ-negative against μ-negative pair (ENG-MNG). Such combinations may give rise to the interface resonances, provided proper choice of radii ratios is made. In analogy with what has been noticed for thin planar resonators [80, 81], the condition of having a no-cut-off propagation mode in a thin coating cylinder filled with a pair of DPS-DNG or ENG-MNG layers, depends on the ratio of the radii of the core cylinder (i.e., ρ_2) and the coating layer (i.e., ρ_1) instead of the sum of radii or the outer radius. As shown in Fig. 2.13, a coating cylinder consists of 2 layers (i.e., 3 regions). The radius of the coating is ρ_1 and the radius of the core-cylinder is ρ_2. The line source is placed at ($\rho_0 = 0.8\lambda$, $\phi_0 = 0°$). The outer radius of the coating layer is fixed to be $\rho_1 = 0.01\lambda$. The scattering cross section (SCS) is plotted against the radii ratio in order to find resonances. SCS is defined

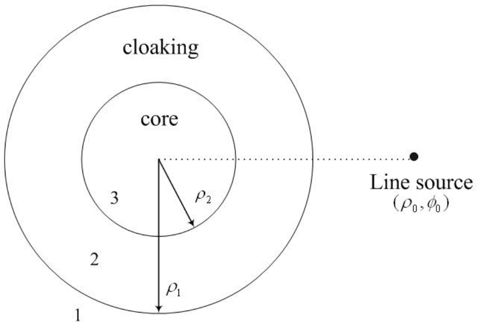

Figure 2.13: Scattering cross section versus ratio of core layer over coating layer in two pairs of combinations: DNG-DPS and DPS-DPS. The outer region is free space.

as the ratio of the power scattered by the scatterer to the incident power per unit area

$$SCS = \frac{\frac{1}{2}Re[E^{sca} \times H^{sca*}]}{\frac{1}{2}Re[E^{inc} \times H^{inc*}]}. \tag{2.20}$$

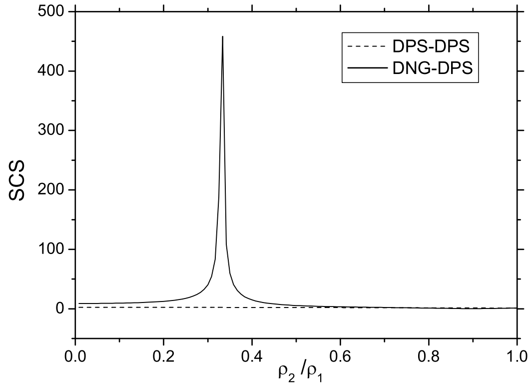

Figure 2.14: Scattering cross section versus ratio of the core layer over the coating layer in two pairs of combinations: DNG-DPS and DPS-DPS. In the case of DNG-DPS pairing, the coating layer is filled with DNG medium of (-3ϵ_0, -2μ_0), and in the case of DPS-DPS pairing, the coating layer is filled with DPS medium of (3ϵ_0, 2μ_0). The core layer remains the same DPS medium of (2ϵ_0, μ_0) for both pairs.

In Fig. 2.14, the dashed line refers to the case that both the core and coating layers are DPS mediums. Hence, one can see that the SCS is very small since the size of this scatter is in subwavelength regime. Note that the SCS of dashed line is very close to zero, but not exactly zero since the amplitude of dashed line for DNG-DPS is much higher than that of DPS-DPS. Interestingly, a resonant ratio can be observed for DNG-DPS pairing at $\rho_2/\rho_1 \approx 0.331$, where the SCS is significantly enhanced. It is attributed to the polaritons which are supported by this pairing. It

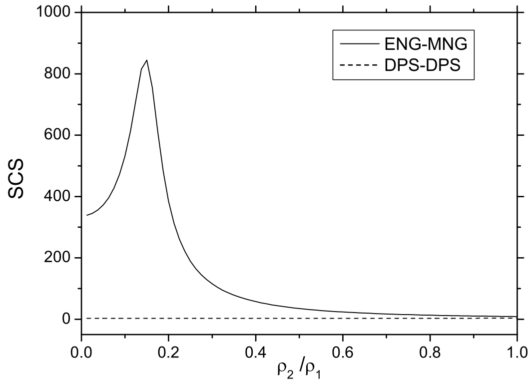

Figure 2.15: Scattering cross section versus ratio of the core layer over the coating layer in two pairs of combinations: ENG-MNG and DPS-DPS. In the case of ENG-MNG pairing, the coating layer is filled with ENG medium of (-3ϵ_0, μ_0), while the core layer is occupied by MNG medium of (4ϵ_0, -2μ_0). In the case of DPS-DPS pairing, the coating and core layers are filled with DPS media of (3ϵ_0, μ_0) and (4ϵ_0, 2μ_0), respectively.

also shows that a proper coating on a subwavelength conventional cylinder can yield a comparably large scattering beamwidth similar to that obtained from very thick cylinder. Therefore, the scattering properties of a geometrically small cylindrical scatterer can be amplified up to those of a big scatterer, if the coating material and the ratio of radii are properly chosen.

Analogous scattering properties are obtained for ENG-MNG s. In the solid line in Fig. 2.15, the core layer is a μ-negative cylinder while the coating is an ϵ-negative coating. Resonant ratio can be found at $\rho_2/\rho_1 \approx 0.152$. In contrast to DNG-DPS pairing, the resonant scattering in Fig. 2.15 is not as sensitive to ratio as in Fig. 2.14. By coating a MNG subwavelength cylinder by an ENG coating, the scattering is still much enhanced compared to DPS-DPS combination even if the radii ratio is smaller than the resonant ratio at about 0.152. However, when the inner radius ρ_2 of MNG core layer keeps increasing, the scattering cross section will reduce to that of DPS-DPS combination as the dashed line in Fig. 2.15.

2.5 Resonances of composite thin rods

2.5.1 Resonances of plasmonic cylinders

The scattering by conducting cylinders has been discussed by Kong [82] and surface-plasmonic scattering is investigate by Luk'yanchuk *et al* [83]. As is known, the plasmonic scattering of a cylinder made from noble metals will occur at $\epsilon_r = -1$ [83]:

$$Q_{sca} = \frac{\pi^2}{4}\left|\frac{\epsilon_r - 1}{\epsilon_r + 1}\right|^2 (k_0 a)^3, \tag{2.21}$$

where k_0 is the wavenumber of the light in free space and a represents the radius of the cylinder.

To avoid the divergence, finite dissipation (i.e., $\mathrm{Im}(\epsilon_r) \neq 0$) is necessary to make Eq. (2.21) finite, when $\mathrm{Re}(\epsilon_r) = -1$. However, the previous research is confined within the condition of $\epsilon_r = -1$ for first-order resonance of cylindrical plasmonic nanoparticles which is derived from the Rayleigh scattering approximation. It is also found possible for the plasmonic nanoparticles to have high-order multiple plasmonic resonances. Here, the TE mode incidence (H-polarization) with unit amplitude is considered. Therefore, one has

$$E^i_\rho = \sin\phi e^{-ik_0 r\cos\phi} \tag{2.22a}$$

$$E^i_\phi = \cos\phi e^{-ik_0 r\cos\phi} \tag{2.22b}$$

$$H^i_z = -e^{-ik_0 r\cos\phi} \tag{2.22c}$$

where k_0 is the wavenumber in free space. Thus the scattered (s) and transmitted (t) fields can be expressed by

$$\boldsymbol{E}^s = -\sum_{n=-\infty}^{+\infty}\Big[\frac{n}{k_0 r}H_n^{(1)}(k_0 r)\widehat{\boldsymbol{\rho}} + iH_n'^{(1)}(k_0 r)\widehat{\boldsymbol{\phi}}\Big](-i)^n a_n e^{in\phi} \tag{2.23a}$$

$$\boldsymbol{E}^t = \sum_{n=-\infty}^{+\infty}\Big[\frac{n}{kr}J_n(kr)\widehat{\boldsymbol{\rho}} + iJ_n'(kr)\widehat{\boldsymbol{\phi}}\Big](-i)^n b_n e^{in\phi} \tag{2.23b}$$

$$\boldsymbol{H}^s = \widehat{\boldsymbol{z}}\sum_{n=-\infty}^{+\infty}(-i)^n a_n H_n^{(1)}(k_0 r)e^{in\phi} \tag{2.23c}$$

$$\boldsymbol{H}^t = -\widehat{\boldsymbol{z}}n_{eff}\sum_{n=-\infty}^{+\infty}(-i)^n b_n J_n(kr)e^{in\phi} \tag{2.23d}$$

where $k = k_0 n_{eff} = k_0\sqrt{\epsilon_r\mu_r}$, the prime refers to the derivative with respect to the argument, and

$$a_n = \frac{n_{eff}J_n(ka)J_n'(k_0a) - J_n'(ka)J_n(k_0a)}{n_{eff}J_n(ka)H_n'^{(1)}(k_0a) - J_n'(ka)H_n^{(1)}(k_0a)} \tag{2.24a}$$

$$b_n = \frac{J_n(k_0a)H_n'^{(1)}(ka) - J_n'(k_0a)H_n^{(1)}(ka)}{n_{eff}J_n(ka)H_n'^{(1)}(k_0a) - J_n'(ka)H_n^{(1)}(k_0a)}. \tag{2.24b}$$

The energy intensity termed as $I = \boldsymbol{E}\cdot\boldsymbol{E}^*$ of light scattering by a plasmonic rod with the electric size of $k_0a = 0.1$ is shown for different cases in order to yield a comprehensive understanding.

It shows that the contribution of the dipole term ($n = 1$ in Eq. (2.24)) is very huge at the resonance. It is well known that the enhancement of the scattering is

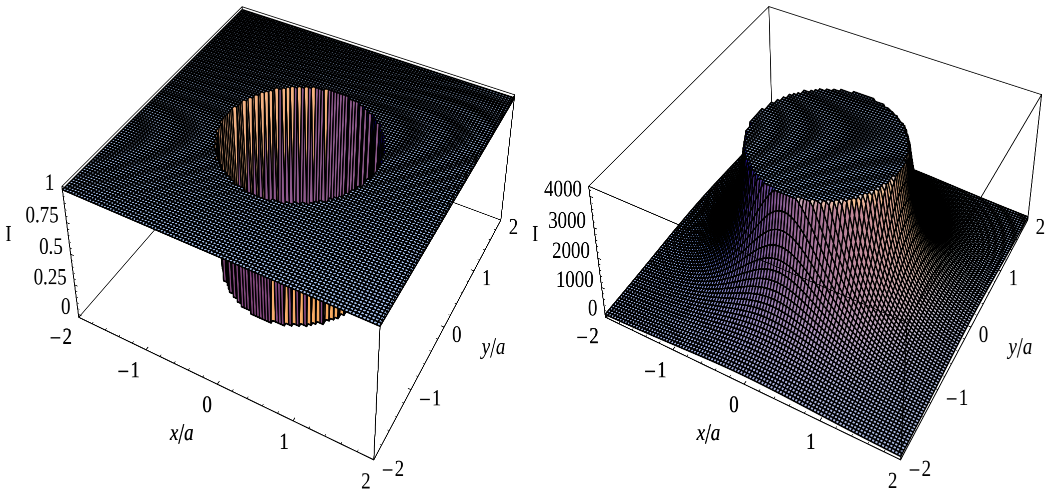

(a) Contribution of monopole term. (b) Contribution of dipole term.

Figure 2.16: The energy intensity of the plasmonic rod of $k_0a = 0.1$ and $\epsilon_r = -1$ in the cases of first two terms.

only for the near field and the field decays drastically away from the cylinder as observed in Fig. 2.16(b). Fig. 2.17 shows that when the order $n \geq 1$ the plasmonic resonances will be further enhanced (almost 1.5 times). Further simulation reveals that among those higher-order terms, the contribution due to the term of $n = 2$ in Eq. (2.24) is dominant and the other higher-order contributions are negligibly small in comparison. Therefore, one only needs to take into account two modes ($n = 1, 2$) for the nanowires at resonance.

When $\epsilon_r = -2$, the resonance of a rod at $k_0a = 0.1$ is also present but localized only on the rod's surface. Further simulation reveals that the dominant term for rod of $\epsilon_r = -2$ is the dipole term ($n = 1$), which is different from the case of the plasmonic rod of $\epsilon_r = -1$. In comparison with Fig. 2.17, the internal energy is almost

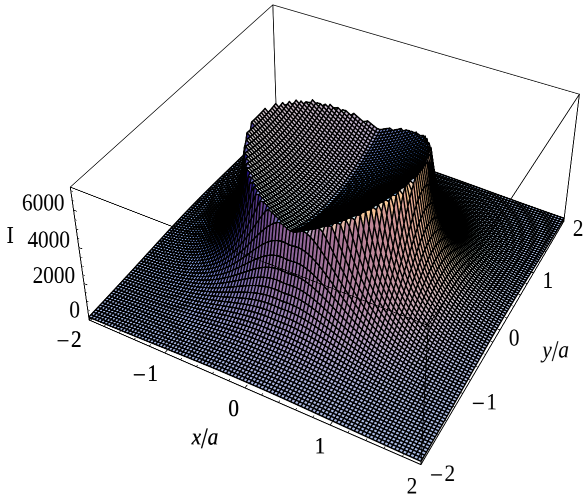

Figure 2.17: The energy intensity of the plasmonic rod of $k_0a = 0.1$ and $\epsilon_r = -1$ in the case of higher-order terms.

zero in the rod of Fig. 2.18. In addition, the resonance effects in Fig. 2.18 appear much smaller than in Fig. 2.16 (only at a ratio of 1/4000), which also confirms that the plasmonic resonance for very thin wires ($k_0a \rightarrow 0$) is due to $\epsilon_r = -1$ for all the modes.

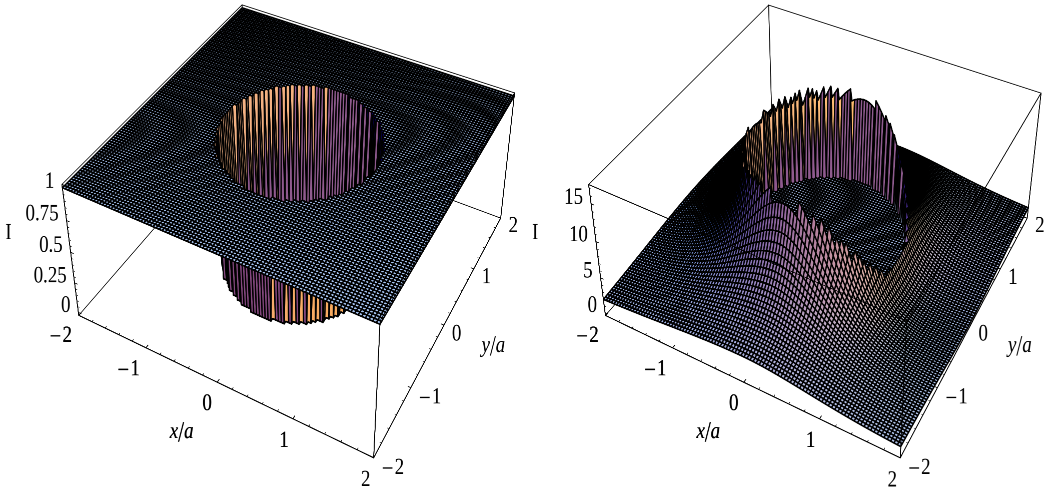

(a) Contribution of monopole term. (b) Contribution of dipole term.

Figure 2.18: The energy intensity of the same rod as in Fig. 2.16 except for $\epsilon_r = -2$ in the cases of first two terms.

2.5.2 Resonances of negative-index cylinders

In this section, the resonant scattering of electromagnetic waves by an infinitely long cylinder is investigated, which has the effective parameters $\epsilon_{eff} = 1 - \omega_p^2/\omega^2$ and μ_{eff} as shown in Eq. (1.4). The scattering properties of such a negative-index cylinder are evaluated by the total scattering cross section per unit length. When the electric field is polarized parallel to the axis, the scattering width for TM mode (E-polarization) is given as

$$C_s^e = \frac{4}{k_0} \sum_{-\infty}^{\infty} |b_n|^2 \tag{2.25}$$

where

$$b_n = \frac{n_{eff} J_n'(ka) J_n(k_0 a) - J_n(ka) J_n'(k_0 a)}{J_n(ka) H_n'^{(1)}(k_0 a) - n_{eff} J_n'(ka) H_n^{(1)}(k_0 a)}. \tag{2.26}$$

When the magnetic field is polarized parallel to the axis, the scattering width for TE mode (H-polarization) is given as

$$C_s^h = \frac{4}{k_0} \sum_{-\infty}^{\infty} |a_n|^2 \tag{2.27}$$

where a_n is identical to Eq. (2.24a).

Under the condition of low dissipation, the effective negative refractive indices of the combination of fine meshed wire and SRR medium depend on the magnetic fields [12] (i.e., $\perp/\|$ subscripts correspond to $\boldsymbol{H}$ fields perpendicular/parallel to the plane of SRRs)

$$n_{eff}^{\perp} = \frac{\sqrt{\omega^2 - \omega_p^2}}{\omega} \sqrt{\frac{\omega^2 - \omega_0^2/(1-F)}{\omega^2 - \omega_0^2}} \tag{2.28a}$$

$$n_{eff}^{\|} = \frac{\sqrt{\omega^2 - \omega_p^2}}{\omega} \sqrt{\frac{\omega^2 - \omega_f^2}{\omega^2 - \omega_0^2}} \tag{2.28b}$$

where

$$\omega_f^2 = \frac{\omega_0^2 \omega_p^2}{\omega_0^2 + \omega_p^2}. \tag{2.29}$$

The scattering properties in Fig. 2.19 and Fig. 2.20 are in the macroscopic view of the cylinder fabricated by geometrically ordered composites (i.e., SRR-wire mesh). The plasma frequency ω_p is 12 GHz and the resonant frequency ω_0 is 6 GHz, which gives the physical size of the radius $a = 1.25$ cm. There are two important factors which will affect the scattering properties significantly, namely, the incidence polarization and SRR plane. Comparing Fig. 2.20 with Fig. 2.19, one can see that whether the magnetic field penetrates the plane of SRR or not will change drastically the scattering width. In Fig. 2.19, $\boldsymbol{H}$ is assumed to be parallel to

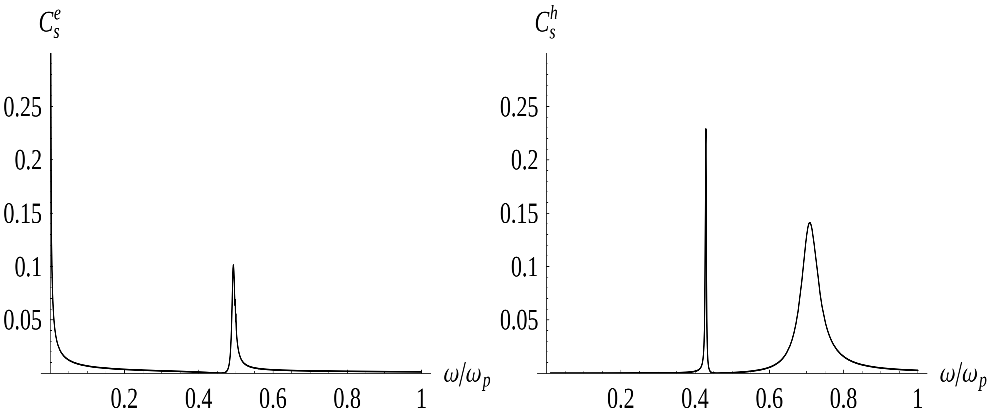

(a) E-polarization.

(b) H-polarization.

Figure 2.19: Scattering width for the case of $\boldsymbol{H}$ parallel to the plane of SRRs.

the SRR's plane for both TE and TM mode incidences. Interestingly, it is observed that TE mode incidence (*see* Fig. 2.19(b)) has two resonances instead of one as shown in Fig. 2.19(a). On the other hand, $\boldsymbol{H}$ is assumed to penetrate the SRR's plane for both TE and TM incident plane waves. It can be seen in Fig. 2.20(a) that the resonant peaks of the negative-index cylinder illuminated by TM waves will shift due to the filling fraction F (defined as the fractional area of the unit cell occupied by the interior of the split ring [12]). However, for the case of TE illumination as shown in Fig. 2.20(b), filling fraction plays an important role in scattering behavior instead of just shifting the resonant peaks. High filling fraction will suppress the resonance, making the scattering width at resonance very small.

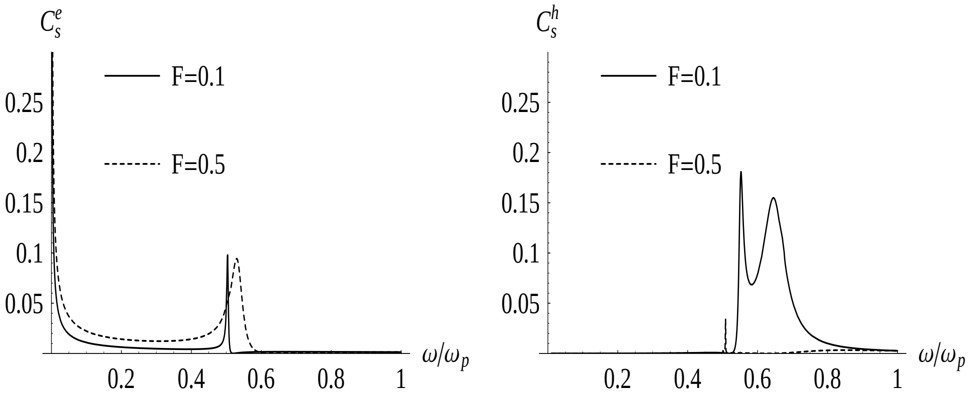

(a) E-polarization. (b) H-polarization.

Figure 2.20: Scattering width for the case of ***H*** perpendicular to the plane of SRRs.

2.6 Rotating coatings for large and small cylinders

Most of the existing reports on the scattering of cylindrical scatterers were based on the stationary case such as in [84–86]. The rotation effects on the scattering are taken into account, providing some new physical insights to the designs of plariton-resonant cylindrical devices [87]. Analytical solutions of field components in all regions have been explicitly derived, where the rotation factors are incorprated. Numerical results of particular core-shell pairings are presented, and we show how the resonant scattering for electrically small coated cylinders is modified by the velocity and size. We also extend the present theory to the rotating cloakings of electrically medium/large size, where morphology-dependent resonances (MDR) are presented and discussed. Hence, the theorem is more general and useful both in theory and applications.

2.6.1 Preliminaries

The geometry of the investigated coaxial cylinder immersed in a host medium is shown in Fig. 2.21. The case of E-polarization is considered as the illumination

$$\boldsymbol{E}^i = \hat{\boldsymbol{z}} e^{ik_i x} \tag{2.30}$$

and the material in each region of the concentric cylinder is homogeneous and rotating, and is characterized by its electric response (ϵ), magnetic response (μ), and angular velocity (Ω).

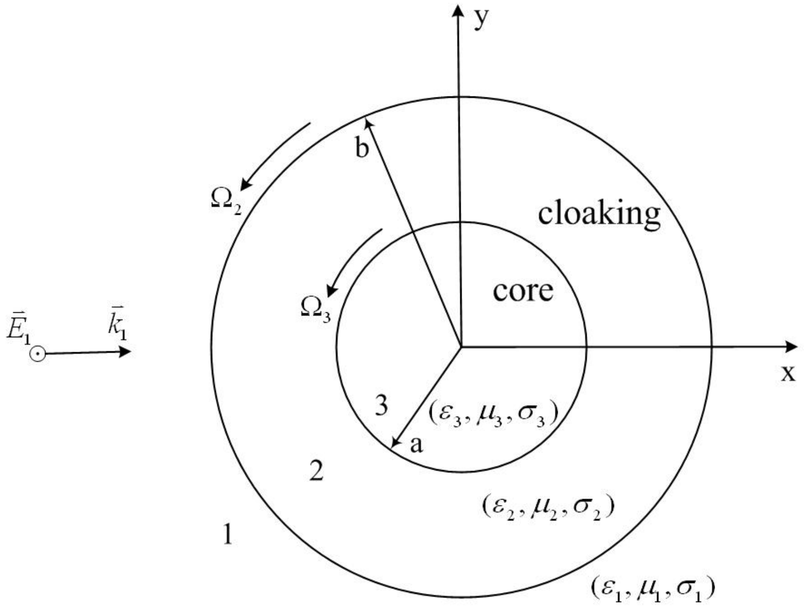

Figure 2.21: Plane wave scattered by a rotating coaxial cylinder.

The Maxwell's euqations for a general rotating materials can be formulated [88]

$$\boldsymbol{D} - n^2\beta^2\boldsymbol{D}_\perp = \epsilon(\boldsymbol{E} - \beta^2\boldsymbol{E}_\perp) + \frac{\mu_r\epsilon_r - 1}{c^2}\boldsymbol{v} \times \boldsymbol{H} \tag{2.31a}$$

$$\boldsymbol{B} - n^2\beta^2\boldsymbol{B}_\perp = \mu(\boldsymbol{H} - \beta^2\boldsymbol{H}_\perp) - \frac{\mu_r\epsilon_r - 1}{c^2}\boldsymbol{v} \times \boldsymbol{E} \tag{2.31b}$$

$$\boldsymbol{J} = \rho\boldsymbol{v} + \sigma\sqrt{1-\beta^2}\boldsymbol{E}_\parallel + \frac{\sigma}{\sqrt{1-\beta^2}}(\boldsymbol{E}_\perp + \boldsymbol{v} \times \boldsymbol{B}), \tag{2.31c}$$

where $\boldsymbol{v} = \Omega\rho\widehat{\boldsymbol{\phi}}$ represents the rotating velocity on the cylinder's surface, μ_r (ϵ_r) stands for the relative permeability (permittivity), $\beta = \Omega\rho/c$, and the $\perp$ and $\parallel$ denote perpendicular and parallel component with respect to the axial direction.

Throughout this paper, time dependence $e^{-i\omega t}$ and small angular velocity is assumed for the instantaneous rest-frame theory [89] so that the term of β^2 can be neglected. For the incident wave discussed here, the boundary conditions are

$$\widehat{\boldsymbol{\rho}} \cdot [\boldsymbol{D}^{sca} + \boldsymbol{D}^i - \boldsymbol{D}^t] \;=\; \rho_s \tag{2.32a}$$

$$\widehat{\boldsymbol{\rho}} \times [\boldsymbol{H}^{sca} + \boldsymbol{H}^i - \boldsymbol{H}^t] \;=\; J_s. \tag{2.32b}$$

Note that the surface current J_s and surface charge ρ_s are zero, implied from the E-polarization, the above boundary conditions, and Eq. (2.31). Hence, the Maxwell's equations (especially for the current) can be reformulated when small angular velocity is assumed so as to assure the instantaneous rest-frame theory

$$\boldsymbol{D} \;=\; \epsilon\boldsymbol{E} + \frac{\mu_r\epsilon_r - 1}{c^2}\boldsymbol{v} \times \boldsymbol{H} \tag{2.33a}$$

$$\boldsymbol{B} \;=\; \mu\boldsymbol{H} + \frac{\mu_r\epsilon_r - 1}{c^2}\boldsymbol{E} \times \boldsymbol{v} \tag{2.33b}$$

$$\boldsymbol{J} \;=\; \sigma\boldsymbol{E} + \sigma\mu\boldsymbol{v} \times \boldsymbol{H}. \tag{2.33c}$$

where μ_r (ϵ_r) stands for the relative permeability (permittivity) and $\boldsymbol{v} = \Omega\rho\widehat{\boldsymbol{\phi}}$ represents the rotating velocity on the cylinder's surface. Note that the surface current and surface charge are zero, implied from the E-polarization and the boundary condition.

The incident wave $\boldsymbol{E}^i = E_1^i \hat{\boldsymbol{z}}$ in Eq. (2.30) can be expressed in the form

$$E_1^i = \sum_{-\infty}^{\infty} i^n J_n(k_1\rho) e^{in\phi} \tag{2.34}$$

where

$$k_1^2 = \omega^2 \epsilon_1 \mu_1 + i\omega\sigma_1\mu_1. \tag{2.35}$$

The outer region can be filled with any dielectric or conducting material. For the simplicity of calculation, it is just put as $\epsilon_1 = \epsilon_0$, $\mu_1 = \mu_0$ and $\sigma_1 = 0$, and thus $k_1^2 = \omega^2\epsilon_1\mu_1 = \omega^2\epsilon_0\mu_0$. It follows that the scattered field in the 1^{st} region must carry the form

$$E_1^{sc} \;=\; \sum_{-\infty}^{\infty} i^n A_n H_n^{(1)}(k_1\rho) e^{in\phi}. \tag{2.36}$$

First, let us discuss the eigenwave number in a rotating wire. From Eq. (2.33), the following equations for transmitted waves can be arranged

$$\begin{aligned} \frac{1}{\rho}\frac{\partial E_z^t}{\partial \phi} &= i\omega\mu H_\rho^t - i\omega\Omega\rho\frac{\mu_r\epsilon_r - 1}{c^2}E_z^t & \text{(2.37a)} \\ -\frac{\partial E_z^t}{\partial \rho} &= i\omega\mu H_\phi^t & \text{(2.37b)} \\ \frac{1}{\rho}\frac{\partial}{\partial\rho}(\rho H_\phi^t) - \frac{1}{\rho}\frac{\partial H_\rho^t}{\partial\phi} &= (\sigma - i\omega\epsilon)E_z^t - \Omega\rho[\sigma\mu - i\omega\frac{\mu_r\epsilon_r - 1}{c^2}]H_\rho^t. & \text{(2.37c)} \end{aligned}$$

The transmitted electric field can be expressed by the Fourier expansion

$$E_z^t = \sum_{-\infty}^{\infty} U_n e^{in\phi} \tag{2.38}$$

where U_n is found to satisfy

$$\frac{1}{\partial\rho}\frac{\partial}{\partial\rho}\Big(\rho\frac{\partial U_n}{\partial\rho}\Big)+\Big(k_{nq}^2-\frac{n^2}{\rho^2}\Big)U_n=0. \qquad (2.39)$$

Eq. (2.39) is actually a definition of Bessel functions and thus Eq. (2.38) turns to be

$$E_z^t=\sum_{-\infty}^{\infty} i^n\Lambda_q J_n(k_{nq}\rho)e^{in\phi} \qquad (2.40)$$

where i^n is inherited from the incidence, Λ_q represents the unknown scattering coefficient, $q=2$ or 3 stands for the region number, and

$$k_{nq}^2=\omega^2\epsilon_q\mu_q+i\omega\mu_q\sigma_q+\frac{n\Omega_q\omega}{c^2}\Big(2\epsilon_{rq}\mu_{rq}-2+i\frac{\sigma_q\mu_{rq}}{\omega\epsilon_0}\Big). \qquad (2.41)$$

Now, one can obtain the following fields in regions 2 and 3 in Fig. 2.21

$$\begin{aligned} E_2 &= \sum_{-\infty}^{\infty} i^n[B_nH_n^{(2)}(k_{n2}\rho)+C_nH_n^{(1)}(k_{n2}\rho)]e^{in\phi} && (2.42\text{a}) \\ E_3 &= \sum_{-\infty}^{\infty} i^nD_nJ_n(k_{n3}\rho)e^{in\phi} && (2.42\text{b}) \end{aligned}$$

where the supscripts 1 and 2 denote Hankel functions of the first and second types, respectively.

Thus, the matching boundary conditions at $\rho=a$ and $\rho=b$ is performed for E_z and H_ϕ (see Eq. (2.37b)). One can obtain the following scattering coefficients after long algebraic calculations

$$\begin{aligned} A_n &= \frac{\frac{\mu_{r2}}{\mu_{r1}}\Delta_nJ_n'(k_1b)-\frac{k_{n2}}{k_1}\Pi_nJ_n(k_1b)}{\frac{k_{n2}}{k_1}\Pi_nH_n^{(1)}(k_1b)-\frac{\mu_{r2}}{\mu_{r1}}\Delta_nH_n'^{(1)}(k_1b)} && (2.43\text{a}) \\ B_n &= P_nC_n && (2.43\text{b}) \\ C_n &= \frac{-\frac{2i}{\pi(k_1b)}\frac{\mu_{r2}}{\mu_{r1}}}{\frac{k_{n2}}{k_1}\Pi_nH_n^{(1)}(k_1b)-\frac{\mu_{r2}}{\mu_{r1}}\Delta_nH_n'^{(1)}(k_1b)} && (2.43\text{c}) \\ D_n &= \frac{\frac{8}{\pi^2(k_1b)(k_{n2}a)}\frac{\mu_{r3}}{\mu_{r1}}}{\frac{k_{n3}}{k_{n2}}J_n'(k_{n3}a)H_n^{(2)}(k_{n2}a)-\frac{\mu_{r3}}{\mu_{r2}}J_n(k_{n3}a)H_n'^{(2)}(k_{n2}a)}\times \\ &\quad \frac{1}{\frac{k_{n2}}{k_1}\Pi_nH_n^{(1)}(k_1b)-\frac{\mu_{r2}}{\mu_{r1}}\Delta_nH_n'^{(1)}(k_1b)} && (2.43\text{d}) \end{aligned}$$

where the Wronskians have been used and

$$\Delta_n = H_n^{(2)}(k_{n2}b) \cdot P_n + H_n^{(1)}(k_{n2}b) \tag{2.44a}$$

$$\Pi_n = H_n'^{(2)}(k_{n2}b) \cdot P_n + H_n'^{(1)}(k_{n2}b) \tag{2.44b}$$

$$P_n = \frac{\frac{\mu_{r3}}{\mu_{r2}} J_n(k_{n3}a) H_n'^{(1)}(k_{n2}a) - \frac{k_{n3}}{k_{n2}} J_n'(k_{n3}a) H_n^{(1)}(k_{n2}a)}{\frac{k_{n3}}{k_{n2}} J_n'(k_{n3}a) H_n^{(2)}(k_{n2}a) - \frac{\mu_{r3}}{\mu_{r2}} J_n(k_{n3}a) H_n'^{(2)}(k_{n2}a)}. \tag{2.44c}$$

Note that the derivatives are all with respect to the argument.

The backscattering cross section is defined as the ratio of power scattered directly back toward the source to the incident power per unit area

$$\sigma_B = \frac{4}{k_1} \Big| \sum_{n=0}^{\infty} (2 - \delta_{n0})(-1)^n A_n \Big|^2. \tag{2.45}$$

In all calculations, the identity of backscattering cross section $C_B = \sigma_B / b$ is used, which is normalized by the physical size of the outer radius b.

2.6.2 Coating with dielectric materials

In this part, the geometry of a stationary core with a rotating coating is considered first. Assume that the core layer is made of conventional dielectrics ($\epsilon_{r3} = 2$; $\mu_{r3} = 1$) and the coating layer is a left-handed material (LHM) characterized by $\epsilon_{r2} = -2$ and $\mu_{r2} = -1$ with a velocity of $\beta_2 = \frac{\Omega_2 b}{c}$. In order to satisfy the first-order theory [89], it implies that $\beta_2 << 1$ so that β_2^2 can be neglected (see Equation (5) in [89]). Therefore, k_{n2} and N_2 can be rewritten as

$$k_{n2} \approx k_1 N_2 + \beta_2 \frac{N_2^2 - 1}{N_2} \frac{n}{b} \tag{2.46a}$$

$$N_2 = \sqrt{\epsilon_{r2}} \sqrt{\mu_{r2}}. \tag{2.46b}$$

Note that for the anti-vacuo coating, the rotation of the coating has no effect on the scattering properties since the second term in Eq. (2.46a) disappears. For the dielectric case, the calculations will be significantly simplified if the small-argument asymptotic forms of various Bessel and Hankel functions are employed.

Of particular interest is the pair of μ-negative (MNG) and ϵ-negative (ENG). It has been shown that the surface polaritons could be generated at the interface between the MNG layer and the ENG layer [81]. I studied two cases of such pairs in the sequence of core-coating, i.e, MNG-ENG and ENG-MNG. As shown in Fig. 2.22, one can see that only if the core and coating are respectively filled by conjugate materials, the resonance will arise at particular ratio of radii. I only plot a small range of ratio in the vicinity of resonance, because the resonance is quite sensitive to the ratio when the resonance of the coaxial wire is in the optical regime. In fact, one needs to plot the resonance in A_n in Eq. (2.43a) first over the whole range (0,1). Since the resonance in A_n is less sensitive and easier to observe, one can get the approximate resonant position, and then plots the backscattering cross section C_B using proper steps within the particular range. Otherwise, such resonant phenomena are much likely to be missed. In Fig. 2.22(a), two opposite rotating velocities of coatings (one is along $\widehat{\boldsymbol{\phi}}$ and the other is along -$\widehat{\boldsymbol{\phi}}$) are considered and compared with that of the stationary case. It shows that if the coating is stationary, the resonance happens at the ratio of $a/b \approx 0.7454$. Once the coating has a small rotating velocity ± 0.04, the original resonance will disappear and be shifted to $a/b \approx 0.7448$ instead. Apart from this region, the value of C_B is negligible. It is found that the direction of velocities is not important and once the absolute speeds are the same, they have equivalent effects on the backscattering cross section. In what follows, another type of conjugate pairs (i.e., core is filled by ENG and coating by MNG) is considered in Fig. 2.22(b) as a complementary case. Keep the absolute values of parameters unchanged as in Fig. 2.22(a) with only the change in plus and minus signs. The resonant characteristics are greatly modified in Fig. 2.22(b) compared with Fig. 2.22(a), and a stationary resonance occurs at $a/b \approx 0.447$ while the rotation resonances shift to $a/b \approx 0.4473$. One can find that the rotation resonances always arise below the stationary resonance for conjugate pairs of core and coating in optical region. In contrast, the situations will be very different for the left-handed material (LHM) and right-handed material (RHM) pairs of core and coating.

From Fig. 2.23, one can find that the rotation resonances are always above the stationary resonances. It also agrees with the results in Fig. 2.22 that the rotation of coating shifts the resonant position and opposite rotating directions yield identical results. More interestingly, let us examine Fig. 2.22(a) along with Fig. 2.23(b). It is evident that those two cases (i.e., conjugate pair and LHM-RHM pair) are quite similar. The stationary resonances appear at the same ratio, but the rotation of coating leads to different contributions at the resonance shift. Analogous phenomena can be found in Fig. 2.22(b) along with Fig. 2.23(a).

Next, the LHM coating for thick cylinders is presented in Fig. 2.24. Two cases of thick cylinders are presented and materials in each region are positive. When the physical thickness is comparable to the wavelength (i.e., $k_1 b = 4$), oscillations

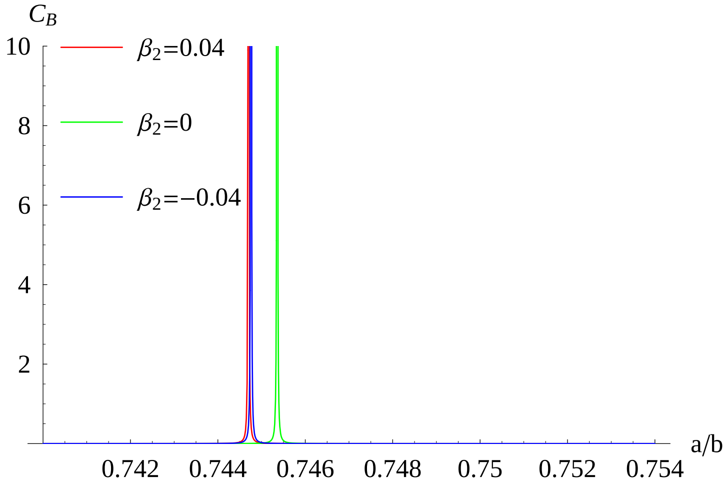

(a) MNG-ENG for the core-coating pair

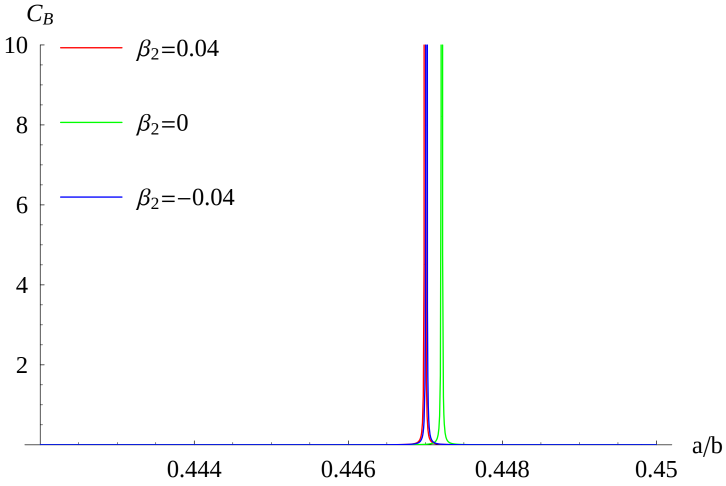

(b) ENG-MNG for the core-coating pair

Figure 2.22: The normalized backscattering and resonance of conjugate optical coating for $k_1 b = 0.001$ at different velocities with a stationary core. The 1^{st} region is free space. (a) ENG coating: $\epsilon_2 = -3\epsilon_0,\ \mu_2 = 4\mu_0$ and MNG core: $\epsilon_3 = \epsilon_0,\ \mu_3 = -2\mu_0$; and (b) MNG coating: $\epsilon_2 = 3\epsilon_0,\ \mu_2 = -4\mu_0$ and ENG core: $\epsilon_3 = -\epsilon_0,\ \mu_3 = 2\mu_0$

happen with several peak values as shown in Fig. 2.24(a). The effects of the rotating velocities and directions become remarkable, and the resonant peaks of clockwise rotation is always ahead of the stationary case while the anti-clockwise case comes after the stationary case. When the physical thickness is further increased (i.e., $k_1 b = 20$), multiple resonances can be observed when the ratio is bigger than 0.2. One can find that the resonant scattering amplitude of a thick cylinder coating reduces along with the increment of the thickness $k_1 b$. In addition, by comparing Fig. 2.24 with Fig. 2.23, one can find that the electric size plays an important role in the coating, dominated by different physics. Specifically, for an optical coating, the resonances occur mainly because of the existence of surface plasmons at the interface between the core and coating layers. In contrast, the morphology-dependent resonances (MDRs) occur for a large size as shown in Fig. 2.24. MDRs are not related to bulk excitations and do not require negative values of the dielectric response, but they are determined by the electric size of the scatterer.

Subsequently, the conventional coating in Fig. 2.24(b) is replaced by LHM coating as in Fig. 2.25. It shows that change of coating material from conventional to LHM will increase the zero-reflection ratio points but have no obvious influence on the amplitude at resonances. Therefore, it would be of great use in radar detection and stealth technology since the cross section can be significantly reduced via easy controls of appropriate LHM coating thickness.

2.6.3 Cloaking with metallic materials

In this section, the application is extended to the metallic cloakings. Given $\sigma_q/\omega\epsilon_0 = x_q$, Eq. (2.41) can be rewritten as

$$k_{n2}^2 = k_1^2 N_2^2 + 2n\beta_2 \frac{k_1}{b}(N_2^2 - 1) + i\Big[k_1^2 + 2n\beta_2 \frac{k_1}{b}\Big]\mu_{r2} x_2 \tag{2.47a}$$

$$k_{n3}^2 = k_1^2 N_3^2 + 2n\beta_3 \frac{k_1}{a}(N_3^2 - 1) + i\Big[k_1^2 + 2n\beta_3 \frac{k_1}{a}\Big]\mu_{r3} x_3. \tag{2.47b}$$

Hence, the role of conductivity of the cloaking in backscattering can be examined. No optical resonances can be found versus the ratio of a/b. Thus the application of metallic cloaking of small size is limited. Instead, only the thick cylinders are considered to investigate the morphology-dependent resonances. First, it is assumed that both layers are metals. A contrast between the two conductivities is defined as σ_3/σ_2. In Fig. 2.26, the ratio of inner over outer radius is set to be 0.8 and the conductivity in the cloaking is fixed so as to examine how the variance of the conductivities between core and cloaking affects the scattering properties. Interestingly, it is found that only when the contrast in conductivities is below 10, the backscattering will be greatly modified. The rotating velocity has little influence on scattering property for cloaking of thick conductive cylinders, which is very close to the stationary case. This is due to the case for thick cylinders is approaching to the planar case and the slow angular rotation thus has little effects on a flat face.

Regarding the conducting materials, there are two limiting cases: 1) the inner cylinder is PEC; and 2) the cloaking is PEC. As for the 2^{nd} case, it just reduces to a conventional problem, since wave cannot enter into the inner layer. Hence, this case can actually be treated as one PEC cylinder with the radius of b. The scattered wave is thus obtained by re-applying the boundary conditions only at $\rho = b$

$$E_1^{sca} = -\sum_{-\infty}^{\infty} i^n J_n(k_1 b) \frac{H_n^{(1)}(k_1\rho)}{H_n^{(1)}(k_1 b)} e^{in\phi}. \tag{2.48}$$

The solution in Eq. (2.48) is well-known. However, the 1^{st} case is of particular interest. If the material in $0 < \rho < a$ is a perfectly electric conductor, the coefficient D_n in Eqs. (2.42b) and (2.43d) is zero, and Eq. (2.43a) turns to be

$$A_n' = \frac{k_{n2} J_n(k_1 b)\Delta_n' - k_1 J_n'(k_1 b)\Pi_n'}{k_1 H_n'^{(1)}(k_1 b)\Pi_n' - k_{n2} H_n^{(1)}(k_1 b)\Delta_n'}, \tag{2.49}$$

where

$$\Delta_n' = H_n'^{(1)}(k_{n2} b) H_n^{(2)}(k_{n2} a) - H_n'^{(2)}(k_{n2} b) H_n^{(1)}(k_{n2} a) \tag{2.50a}$$

$$\Pi_n' = H_n^{(1)}(k_{n2} b) H_n^{(2)}(k_{n2} a) - H_n^{(2)}(k_{n2} b) H_n^{(1)}(k_{n2} a). \tag{2.50b}$$

In Fig. 2.27, the role of angular velocity has little contribution to the backscattering when $a < 0.15b$. Only when the radius of inner PEC is very small compared to the outer radius of cloaking, the impacts of rotation are noticeable. Given the same cloaking, high backscattering can be achieved by requiring the PEC radius to be small. It can be also observed that the oscillation appears quite regular especially after $a > 0.4b$, though negligible amplification is present. Since C_B has been normalized by the outer radius b, the electric size of the backscattering cross section can change within the range of (50,120) when a/b is sufficiently large. Further results yield that the difference due to the angular velocity at $a < 0.15b$ and the oscillation can be suppressed by increasing the dissipation in the cloaking. As a particular example, a high dissipative cloaking material with loss tangent of 6 is considered. As shown in Fig. 2.28, when the ratio is below 0.9, the backscattering is a constant value, which is independent from radii ratio and rotating velocity. Small variance occurs only when the inner PEC radius is getting very close to the outer radius.

2.7 Summary

In this chapter, the properties of scattering, energy, and resonances in composite cylinders are investigated extensively and intensively. First, the methodology is designed to treat multilayered cylinders, where the materials and the size of each layer can be arbitrary. Multiple scattering and transmission due to the interfaces are considered by a multilayer algorithm, and hence the total field in each layer can be obtained. This idea will be further employed to construct dyadic Green's functions for more complex composites as a macroscopic characterization tool in Chapter 5. Both the radiation of line sources and and the scattering of plane waves are considered. With the algorithm developed, the scattering properties of arbitrarily coated cylinders can be examined. Of special interest are thin rods with and without coatings/cloakings in the presence of line-source radiation, because it is straightforward to observe the focusing phenomena. For those single-layered thin rods, the wave propagation through those thin rods is examined. Focusing properties are found and the hybrid effects of cylindrical curvature and the material on the wave properties are studied. For thin rods with coating whose electric size is only 0.01λ, it is exciting to have scattering cross section enhanced over hundreds of times by proper pairing of the core layer and the coating layer. In fact, this enhancement can be attributed to the surface polaritons excited at the interface, and those polaritons compensate the decay of the scattered waves. Hence, the resonances of such thin composite rods deserve in-depth investigation. Further study reveals different contributions from monopole, dipole and higher-order multipoles, and it is found that plasmonic resonance of thin rods only occurs at $\epsilon_r = -1$. Also, all the modes except for the modes corresponding to $n = 1, 2$ can be neglected due to their negligible contributions at resonance. The roles of polarization of the incident wave and the geometry of the split rings on the scattering properties are studied. Although the coating/cloaking in the presence of a line source is briefly investigated, the theory and case studies of cloaking for both large and small cylinders are carried out, under the E-polarization incidence. The theory supports rotating and conductive composite coaxial cylinders. Resonant scattering and the shift of the resonances are discussed for rotating cloaking in optical region, and another type of resonances is also studied for a cloaking of large size. Conductive cloaking is aslo intensively investigated, and some interesting phenomena such as scattering enhancement for low conductivity contrast and constant backscattering are presented.

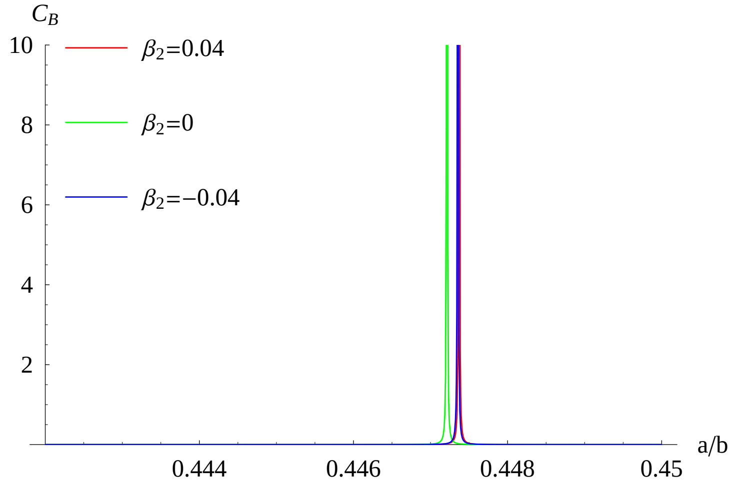

(a) RHM-LHM for the core-coating pair

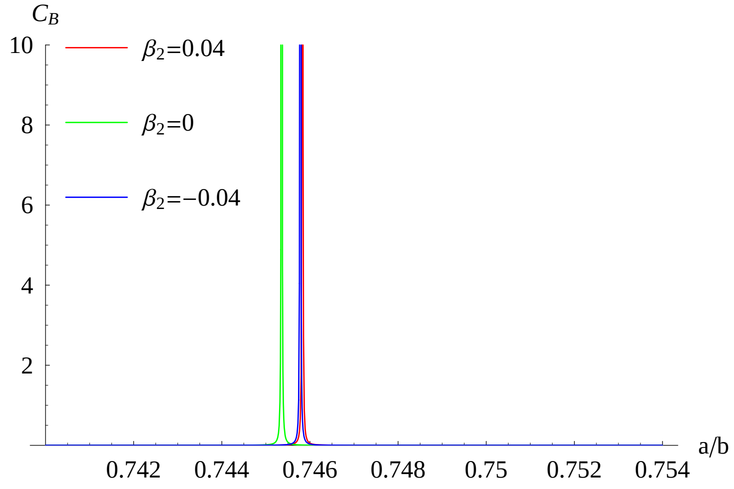

(b) LHM-RHM for the core-coating pair

Figure 2.23: The normalized backscattering and resonance of LHM (RHM) optical coating for $k_1 b = 0.001$ at different velocities with a stationary RHM (LHM) core. (a) LHM coating: $\epsilon_2 = -3\epsilon_0,\ \mu_2 = -4\mu_0$ and RHM core: $\epsilon_3 = \epsilon_0,\ \mu_3 = 2\mu_0$; and (b) RHM coating: $\epsilon_2 = 3\epsilon_0,\ \mu_2 = 4\mu_0$ and LHM core: $\epsilon_3 = -\epsilon_0,\ \mu_3 = -2\mu_0$.

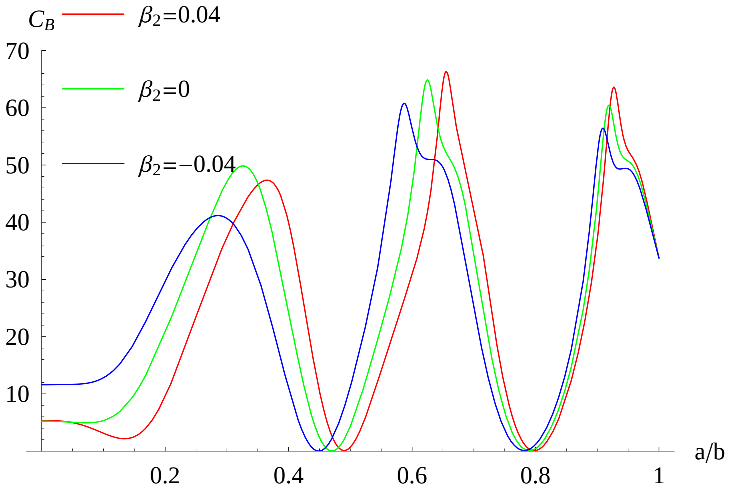

(a) $k_1 b = 4$

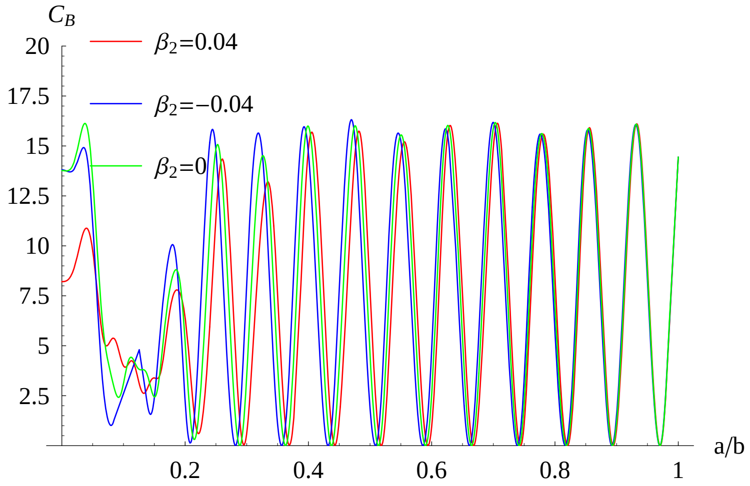

(b) $k_1 b = 20$

Figure 2.24: The normalized backscattering and resonance of conventional coating for thick cylinders at different velocities. The materials in core and coating are both conventional. Materials in each region are the same as in Fig. 2.23(a) except that the 2^{nd} region is positive: $\epsilon_2 = 3\epsilon_0,\ \mu_2 = 4\mu_0$.

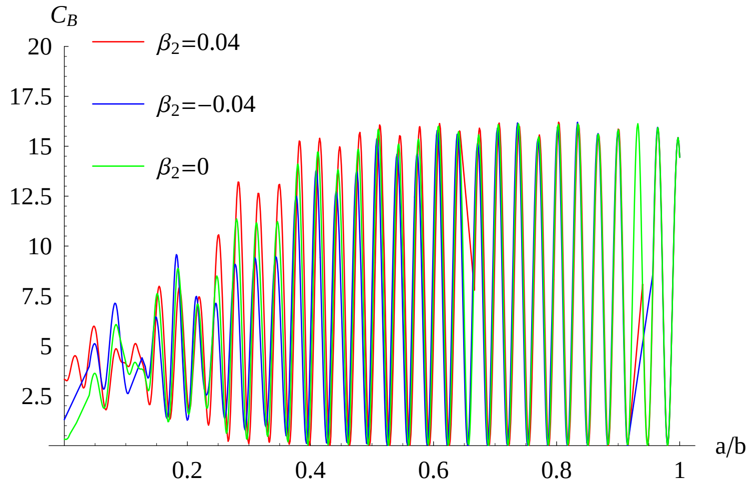

Figure 2.25: The normalized backscattering and resonance of LHM coating for thick cylinders of $k_1b = 20$. The materials in the core are the same as in Fig. 2.24, while the coating is changed to left-handed material: $\epsilon_2 = -3\epsilon_0$, $\mu_2 = -4\mu_0$.

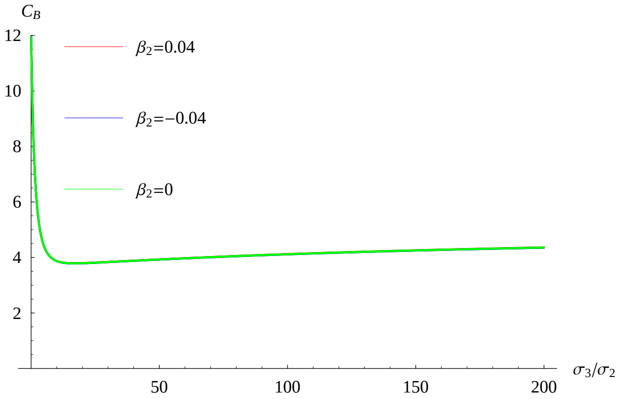

Figure 2.26: The normalized backscattering versus the conductivity contrast for cloaking of thick metallic cylinders of $k_1b = 20$. Cloaking layer: loss tangent=0.06 (i.e., $x_2 = 0.03$), and $\epsilon_2 = 4$. The core layer: $\epsilon_3 = 2$. The ratio of a/b is 0.8.

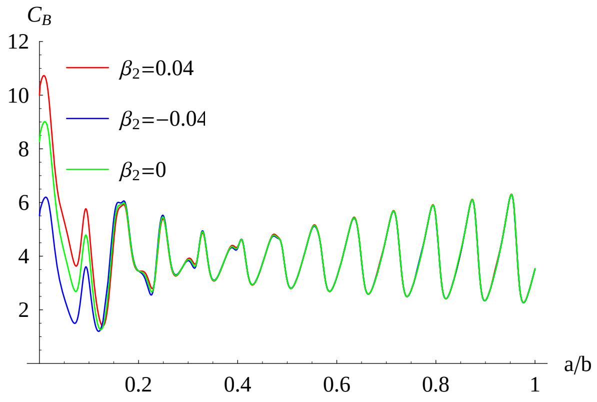

Figure 2.27: The normalized backscattering versus the ratio of inner over outer radius for thick metallic cylinders of $k_1 b = 20$. The same cloaking material as in Fig. 2.26 but the core is made of PEC.

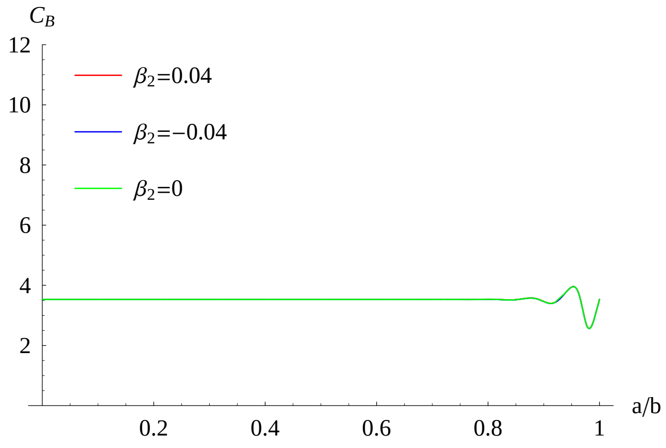

Figure 2.28: The normalized backscattering versus the ratio of inner over outer radius for thick metallic cylinders of $k_1 b = 20$. Cloaking layer: loss tangent=6 (i.e., $x_2 = 3$), and $\epsilon_2 = 4$. Core: PEC.

Chapter 3

Wave interactions with anisotropic composite materials

3.1 Introduction

In order to better understand the electromagnetic properties and potential applications of negative-index materials, the propagation and scattering in the presence of anisotropic composite materials will be studied. The isotropic negative-index composites can be regarded as just a subset of anisotropic composites. A medium composed of periodically placed scatterers generates polarization and magnetization densities. The densities are related to the distribution of the scatterers and their polarizabilities. As a result, a wave propagating through an array of these scatterers will see the material as an effective medium, if the wavelength is much greater than the periodicity. The theory of the effective medium has been studied by Maxwell and

Rayleigh [90, 91]. One notable work is that of Lewin [92], in which spheres are assumed to resonate either in the first or second resonance mode of the Mie theory. In earlier publications, electric polarizability of spheres in the magnetic resonant mode was not considered, but was later taken into account in the Maxwell-Garnett mixing rule [93]. The work in [94] also suggests the possibility of realizing negative-index materials that could be fabricated much more simply than those proposed up until now. An array of spherical particles can behave in a way similar to that of an array of geometrically more complicated conducting scatterers, and their effective electric and magnetic polarizabilities have the same characteristic of exhibiting a resonance. Hence, effective negative ϵ and μ are present in a certain frequency band. However, the problem is still quasistatic and it is a collective response of an infinite lattice of arrays of spherical particles, thus the application is limited although it has better isotropic properties compared to the existing metallic structures for NIMs.

Most of the known realizations of artificial negative-index materials are highly anisotropic composites or even exhibit bianisotropy. It is of great importance that the electromagnetic wave properties of anisotropic spherical composites are explicitly characterized. In the analysis of scattering problems associated with anisotropic materials, the 3-D Fourier transform technique was widely used [95] to relate the space and spectral domains and this is especially true for waves and fields in planar multilayered structures. The Lorenz-Mie analytical approach is an important theory and was usually employed [96,97] especially when the problem geometry is of spherical and radially layered configurations. The method of angular spectrum expansion is also often applied via a coordinate transformation [98]. For most of the published works, investigations on scattering behaviors of anisotropic materials are carried out by considering only the planar geometry [99,100] or cylindrical structures [101,102]. Due to the mathematical complexity of studying the spherical anisotropic objects, limited progress has been achieved in the analysis of 3-D anisotropic objects recently, which only focused on field expressions [103] using the method of moments [104], the second-harmonic generation approach [105] and the coupled-dipole methods [106].

This work is of great importance for both theory and applications, because it presents the exact field solutions in this particular configuration, characterizes the effects of anisotropy ratio [107], and provides ways to minimize the radar cross section especially when unintentional uniaxial anisotropy is introduced in the surface of the material due to the shear in manufacturing process. Furthermore, the interest is extended to a more generalized subject: gyrotropic spheres. Due to the coupling effects, the determination of the exact solutions to the scattering and propagation problems seems impossible. However, those coupled second-order differential equations are still solvable under certain circumstances [108]. This work is also important for scattering theory since the theoretical exploration often comes before the experimental study. Last but not least, the theory developed can not only treat anisotropic spheres with positive/negative anisotropy ratios but also be easily extended to study isotropic negative-index spheres.

3.2 Wave interaction with anisotropic spheres

Recently, some work on the scattering in the presence of negative-index spheres and infinite cylinders has been done [74,109–111]. However, those problems have already been solved and analyzed in the case of normal positive-index materials. It is more challenging and necessary to examine the wave interaction problems for the case of anisotropic spheres.

The field due to the interaction of an incident plane wave with anisotropic spheres is expressed by using the novel potential formulation. The scattered field and total field can be thus obtained by imposing boundary conditions at the spherical surface and using superposition technique, respectively. The parametric studies are of particular interest in this chapter, from which one can find how the RCS will be affected and what one could do to control its values. To gain physical insight, the RCS results are studied for a wide range of joint anisotropy ratios (AR_e and AR_m), and compared to the results of both the isotropic case and the single anisotropy (only AR_e or AR_m) case. It is shown that RCS exhibits some new characteristics in joint anisotropy cases and a general expression $\left|\frac{\sqrt{\mu_t}-\sqrt{\epsilon_t}}{\sqrt{\mu_t}+\sqrt{\epsilon_t}}\right|^2$ is constructed to predict RCS for anisotropic spheres, which will be of great use in radar detection and military purposes. It is of major interest to know how significantly anisotropy influences electromagnetic scattering, so that one can adjust the parameters of the 3-D objects to control the RCS values, either for enhancement or for reduction.

3.2.1 Novel potential formulation

Electromagnetic scattering of a plane wave by an anisotropic sphere (as shown in Fig. 3.1) is treated by a novel potential formulation, where the material parameters are characterized by constitutive tensors of permittivity and permeability specified as

$$\overline{\boldsymbol{\epsilon}} = \epsilon_0 \begin{bmatrix} \epsilon_r & 0 & 0 \\ 0 & \epsilon_t & 0 \\ 0 & 0 & \epsilon_t \end{bmatrix} \tag{3.1a}$$

$$\overline{\boldsymbol{\mu}} = \mu_0 \begin{bmatrix} \mu_r & 0 & 0 \\ 0 & \mu_t & 0 \\ 0 & 0 & \mu_t \end{bmatrix} \tag{3.1b}$$

where ϵ (or μ) is the permittivity (permeability), and ϵ_r (μ_r) and ϵ_t (μ_t) stand for the relative permittivities (permeabilities) perpendicular and parallel to the sphere surface, respectively.

For an anisotropic medium, the source-free Maxwell's equations can be rewritten as

$$\nabla \times (\overline{\boldsymbol{\epsilon}}^{-1} \cdot \boldsymbol{D}) = i\omega \boldsymbol{B} \tag{3.2a}$$

$$\nabla \times (\overline{\boldsymbol{\mu}}^{-1} \cdot \boldsymbol{B}) = -i\omega \boldsymbol{D}. \tag{3.2b}$$

Consider an anisotropic sphere of radius a located at the origin of a coordinate system as shown in Fig. 3.1. From Eq. (3.23), one can see that TE and TM waves are actually decoupled with each other. Thus $\boldsymbol{B}$ and $\boldsymbol{D}$ can be expressed in terms

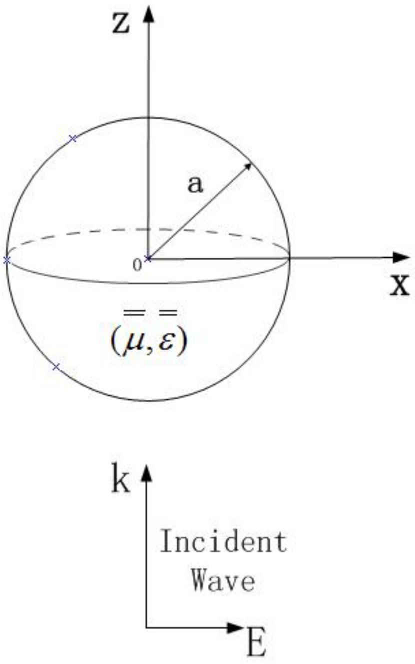

Figure 3.1: Scattering of a plane wave by an anisotropic sphere.

of the following two sets of scalar eigenfunctions

$$\boldsymbol{B}_{\text{TM}} = \nabla \times (\widehat{\boldsymbol{r}}\psi_{\text{TM}}) \tag{3.3a}$$

$$\boldsymbol{D}_{\text{TE}} = -\nabla \times (\widehat{\boldsymbol{r}}\psi_{\text{TE}})\,, \tag{3.3b}$$

where the ψ_{TE} and ψ_{TM} denote potentials for TM and TE modes, respectively with respect to $\widehat{\boldsymbol{r}}$ in the spherical coordinate system.

Substituting Eq. (3.3) into Eq. (3.2), one obtains

$$\boldsymbol{B}_{\text{TE}} = \frac{1}{i\omega}\left[\nabla \times \left(\overline{\boldsymbol{\epsilon}}^{-1} \cdot \nabla \times (\widehat{\boldsymbol{r}}\psi_{\text{TE}})\right)\right] \tag{3.4a}$$

$$\boldsymbol{D}_{\text{TM}} = \frac{1}{i\omega}\left[\nabla \times \left(\overline{\boldsymbol{\mu}}^{-1} \cdot \nabla \times (\widehat{\boldsymbol{r}}\psi_{\text{TM}})\right)\right]. \tag{3.4b}$$

After some manipulations of those equations, one obtains

$$\frac{\epsilon_r}{\epsilon_t}\frac{\partial^2\psi_{\mathrm{TM}}}{\partial r^2}+\frac{1}{r^2\sin\theta}\frac{\partial}{\partial\theta}(\sin\theta\frac{\partial\psi_{\mathrm{TM}}}{\partial\theta})+\frac{1}{r^2\sin^2\theta}\frac{\partial^2\psi_{\mathrm{TM}}}{\partial\phi^2}+\omega^2\mu_0\epsilon_0\mu_t\epsilon_r\psi_{\mathrm{TM}}=0, \tag{3.5a}$$

$$\frac{\mu_r}{\mu_t}\frac{\partial^2\psi_{\mathrm{TE}}}{\partial r^2}+\frac{1}{r^2\sin\theta}\frac{\partial}{\partial\theta}(\sin\theta\frac{\partial\psi_{\mathrm{TE}}}{\partial\theta})+\frac{1}{r^2\sin^2\theta}\frac{\partial^2\psi_{\mathrm{TE}}}{\partial\phi^2}+\omega^2\mu_0\epsilon_0\mu_r\epsilon_t\psi_{\mathrm{TE}}=0. \tag{3.5b}$$

It can be seen that in the case of $\epsilon_r = \epsilon_t$ and $\mu_r = \mu_t$, the above equations are reduced to the results of an isotropic material [112].

By using the method of the separation of variables, it is found that the solutions to the above equations are composed of a superposition of Ricatti-Bessel functions, associated Legendre polynomials, and trigonometric functions, *i.e.*,

$$\psi_{\mathrm{TM}} = \sum_{m,n} a_{m,n} j_{v_1}(k_t r) P_n^m(\cos\theta) \begin{matrix}\cos\\ \\ \sin\end{matrix} m\phi \tag{3.6a}$$

$$\psi_{\mathrm{TE}} = \sum_{m,n} b_{m,n} j_{v_2}(k_t r) P_n^m(\cos\theta) \begin{matrix}\cos\\ \\ \sin\end{matrix} m\phi \tag{3.6b}$$

$$v_1 = \Big[n(n+1)AR_e+\frac{1}{4}\Big]^{1/2}-\frac{1}{2} \tag{3.6c}$$

$$v_2 = \Big[n(n+1)AR_m+\frac{1}{4}\Big]^{1/2}-\frac{1}{2} \tag{3.6d}$$

$$k_t = \omega\sqrt{\epsilon_0\mu_0\epsilon_t\mu_t}, \tag{3.6e}$$

where $AR_e = \epsilon_t/\epsilon_r$ and $AR_m = \mu_t/\mu_r$ represent the electric and magnetic anisotropy ratios, respectively, $a_{m,n}$ and $b_{m,n}$ denote the expansion coefficients, and v_1 and v_2 stand for the orders of spherical Ricatti-Bessel functions which can be complex in value. Thus, the field expansions in spherical coordinates can be obtained using the TE/TM decompositions

$$E_r = \frac{\omega}{ik_t^2}\left(\frac{\partial^2}{\partial r^2}+k_t^2\right)\psi_{\mathrm{TM}} \tag{3.7a}$$

$$
\begin{aligned}
E_\theta &= \frac{-1}{\epsilon_0\epsilon_t r\sin\theta}\frac{\partial\psi_{\rm TE}}{\partial\phi} + \frac{\omega}{ik_t^2 r}\frac{\partial^2\psi_{\rm TM}}{\partial r\partial\theta} && (3.7\text{b})\\
E_\phi &= \frac{1}{\epsilon_0\epsilon_t r}\frac{\partial\psi_{\rm TE}}{\partial\theta} + \frac{\omega}{ik_t^2 r\sin\theta}\frac{\partial^2\psi_{\rm TM}}{\partial r\partial\phi} && (3.7\text{c})\\
H_r &= \frac{\omega}{ik_t^2}\left(\frac{\partial^2}{\partial r^2} + k_t^2\right)\psi_{\rm TE} && (3.7\text{d})\\
H_\theta &= \frac{\omega}{ik_t^2 r}\frac{\partial^2\psi_{\rm TE}}{\partial r\partial\theta} + \frac{1}{\mu_0\mu_t r\sin\theta}\frac{\partial\psi_{\rm TM}}{\partial\phi} && (3.7\text{e})\\
H_\phi &= \frac{\omega}{ik_t^2 r\sin\theta}\frac{\partial^2\psi_{\rm TE}}{\partial r\partial\phi} - \frac{1}{\mu_0\mu_t r}\frac{\partial\psi_{\rm TM}}{\partial\theta}. && (3.7\text{f})
\end{aligned}
$$

As one can see, the wave propagation is dependent on both AR_e and AR_m. In addition, it should be noted that the potentials used in Eqs. (3.3) and (3.4) are not unique. However, when the boundary conditions are applied, the field expressions become unique. Since only the fields involved in the numerical calculations, the uniqueness is still held.

3.2.2 Scattered field and RCS

Notice that if the off-diagonal components of the material tensors $\overline{\boldsymbol{\epsilon}}$ and $\overline{\boldsymbol{\mu}}$ are zero, then the rotations would be equivalent to letting $\hat{\boldsymbol{r}}\hat{\boldsymbol{r}}$ unchanged while rotating the transverse elements (to $\hat{\boldsymbol{r}}$) with respect to $\hat{\boldsymbol{r}}$ as axes. The material in the present study remains invariant under such a rotation, which is called the G-type [113] where the analysis is in 2-D with respect to $\hat{\boldsymbol{z}}$ as the axis of rotation. In that case, the G-type is referred to $\hat{\boldsymbol{z}}$. If one extends that to the present G-type with respect to $\hat{\boldsymbol{r}}$, one can have the characterization for anisotropic material tensors in spherical coordinates (r, θ, ϕ).

For absorbing spheres, the elements in $\overline{\boldsymbol{\epsilon}}$ and $\overline{\boldsymbol{\mu}}$, or at least one of these two tensors, are complex in value. An incident plane wave, as shown in Fig. 3.1, is characterized by

$$\boldsymbol{E}_i = \widehat{\boldsymbol{x}} e^{ik_0 r\cos\theta} \tag{3.8a}$$

$$\boldsymbol{H}_i = \widehat{\boldsymbol{y}} \sqrt{\frac{\epsilon_0}{\mu_0}} e^{ik_0 r\cos\theta} \tag{3.8b}$$

where the unity is assumed for the amplitude. To match the boundary conditions at the surface of the sphere, the exponential terms in the above equations can be expanded in terms of spherical harmonics by employing the following identity

$$e^{ik_0 r\cos\theta} = \sum_{n=0}^{\infty} \frac{i^{-n}(2n+1)}{k_0 r} j_n(k_0 r) P_n(\cos\theta). \tag{3.9}$$

By equating the radial components in Eqs. (3.8a)-(3.8b) to those in Eqs. (3.7a)-(3.7f), the scalar functions, ψ^i_{TE} and ψ^i_{TM}, for incident fields can be expressed

$$\psi^i_{\mathrm{TE}} = \frac{\sin\phi}{\omega\eta_0} \sum_{n=1}^{\infty} \frac{i^{-n}(2n+1)}{n(n+1)} j_n(k_0 r) P_n^1(\cos\theta), \tag{3.10a}$$

$$\psi^i_{\mathrm{TM}} = \frac{\cos\phi}{\omega} \sum_{n=1}^{\infty} \frac{i^{-n}(2n+1)}{n(n+1)} j_n(k_0 r) P_n^1(\cos\theta). \tag{3.10b}$$

Similarly for scattered fields, ψ^s_{TE} and ψ^s_{TM} can be thus derived

$$\psi^s_{\mathrm{TE}} = \frac{\sin\phi}{\omega\eta_0} \sum_{n=1}^{\infty} b_n h_n^{(1)}(k_0 r) P_n^1(\cos\theta) \tag{3.11a}$$

$$\psi^s_{\mathrm{TM}} = \frac{\cos\phi}{\omega} \sum_{n=1}^{\infty} a_n h_n^{(1)}(k_0 r) P_n^1(\cos\theta) \tag{3.11b}$$

where $j_n(\bullet)$ and $h_n^{(1)}(\bullet)$ denote the first kind spherical Bessel and the first kind Hankel functions, respectively. Then, ψ^t_{TE} and ψ^t_{TM} for the transmitted fields inside the sphere can be deduced

$$\psi^t_{\mathrm{TE}} = \frac{\sin\phi}{\omega\eta_0} \sum_{n=1}^{\infty} d_n j_{v_2}(k_t r) P_n^1(\cos\theta) \tag{3.12a}$$

$$\psi^t_{\mathrm{TM}} = \frac{\cos\phi}{\omega} \sum_{n=1}^{\infty} c_n j_{v_1}(k_t r) P_n^1(\cos\theta) \tag{3.12b}$$

where a_n, b_n, c_n and d_n are the unknown expansion coefficients to be determined by matching the boundary conditions which require the continuity of the tangential components of the electromagnetic fields on the surface at $r = a$. Normally, there are four sets of boundary equations

$$
\begin{aligned}
E_\theta^t(a) &= E_\theta^i(a) + E_\theta^s(a) && \text{(3.13a)}\\
E_\phi^t(a) &= E_\phi^i(a) + E_\phi^s(a) && \text{(3.13b)}\\
H_\theta^t(a) &= H_\theta^i(a) + H_\theta^s(a) && \text{(3.13c)}\\
H_\phi^t(a) &= H_\phi^i(a) + H_\phi^s(a). && \text{(3.13d)}
\end{aligned}
$$

Actually, after careful examination, it is found that only two sets of Eq. (3.13a) and Eq. (3.13c) or the other two sets of Eq. (3.13b) and Eq. (3.13d) are sufficient to determine the expansion coefficients. These coefficients are found to be

$$
\begin{aligned}
a_n &= \frac{\sqrt{\mu_t/\epsilon_t}\, j_n(k_0a) j'_{v_1}(k_ta) - j'_n(k_0a) j_{v_1}(k_ta)}{h_n^{(1)'}(k_0a) j_{v_1}(k_ta) - \sqrt{\mu_t/\epsilon_t}\, h_n^{(1)}(k_0a) j'_{v_1}(k_ta)} T_n && \text{(3.14a)}\\
b_n &= \frac{\sqrt{\mu_t/\epsilon_t}\, j'_n(k_0a) j_{v_2}(k_ta) - j_n(k_0a) j'_{v_2}(k_ta)}{h_n^{(1)}(k_0a) j'_{v_2}(k_ta) - \sqrt{\mu_t/\epsilon_t}\, h_n^{(1)'}(k_0a) j_{v_2}(k_ta)} T_n && \text{(3.14b)}\\
c_n &= \frac{i}{\sqrt{\mu_t/\epsilon_t}\, h_n^{(1)}(k_0a) j'_{v_1}(k_ta) - h_n^{(1)'}(k_0a) j_{v_1}(k_ta)} T_n && \text{(3.14c)}\\
d_n &= \frac{i\sqrt{\mu_t/\epsilon_t}}{h_n^{(1)}(k_0a) j'_{v_2}(k_ta) - \sqrt{\mu_t/\epsilon_t}\, h_n^{(1)'}(k_0a) j_{v_2}(k_ta)} T_n && \text{(3.14d)}\\
T_n &= \frac{i^{-n}(2n+1)}{n(n+1)} && \text{(3.14e)}
\end{aligned}
$$

where the Wronskians for spherical pairs of solutions are employed herewith. The derivative in the above equations is taken with respect to the argument (*i.e.*, $\partial[j_n(x)]/\partial x$). With these coefficients solved, the field components of the scattered, transmitted and total fields can be obtained by corresponding substitutions. Of particular interest is the backscattered field, from which one can calculate RCS

$$A_{xx} = \lim_{r\to\infty}\left(4\pi r^2 \frac{|E_x^s|^2}{|E_x^i|^2}\right). \tag{3.15a}$$

3.2.3 Numerical study

This section mainly focuses on the following two aspects, that is, the effects of (1) nondissipative spheres and (2) absorbing spheres. In each aspect, typical results for (a) single electric/magnetic anisotropy effects; (b) joint anisotropy effects; and (c) RCS prediction on the RCS values will be studied for a wide range of anisotropy. In all the following RCS calculations, the truncation of the summations is chosen to be 50, for which the convergence has been verified to be acceptable.

Nondissipative Spheres

For nondissipative spheres, all the elements in $\overline{\boldsymbol{\epsilon}}$ and $\overline{\boldsymbol{\mu}}$ are real values.

- *Electric/Magnetic Anisotropy Effects:*

For uniaxial Ferrite spheres, it is assumed that $\epsilon_r = \epsilon_t = 1$ applies to all the cases in Fig. 3.2. In Fig. 3.2(a), the RCS values due to a negative uniaxial sphere ($\mu_r < \mu_t$) with $AR_m = 1.2$, $AR_m = 1.4$ and $AR_m = 1.6$ are shown; while in Fig. 3.2(b), the RCS values due to a positive uniaxial sphere ($\mu_r > \mu_t$) with $AR_m = 0.9$, $AR_m = 0.7$ and $AR_m = 0.5$ are depicted. It is observed that the RCS values are quite sensitive to the anisotropy and the scattering characteristics of a nondissipative sphere are

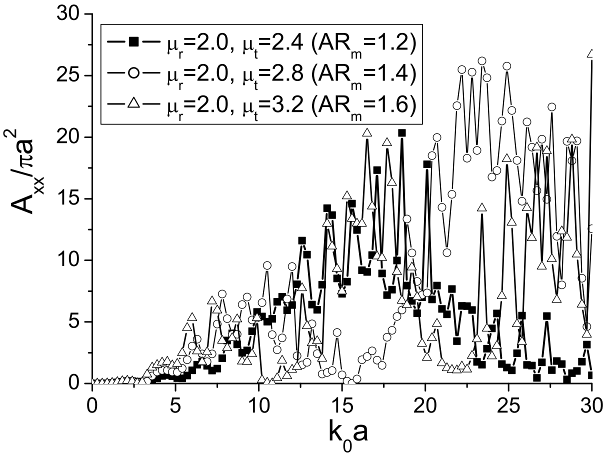

(a) Negative uniaxial Ferrite spheres

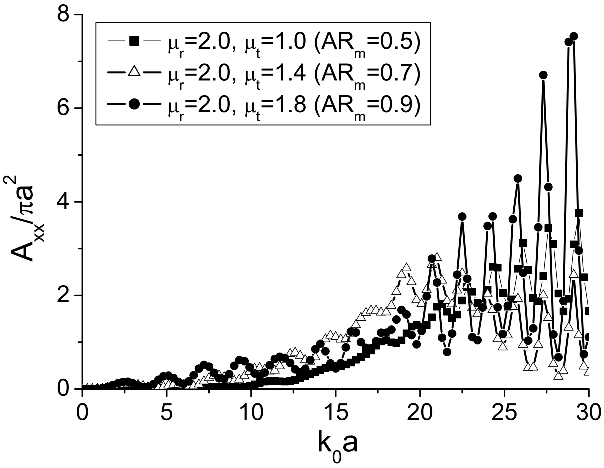

(b) Positive uniaxial Ferrite spheres

Figure 3.2: Normalized RCS values versus k_0a for uniaxial Ferrite spheres, under the condition of $\epsilon_r = \epsilon_t = 1$.

greatly affected by the presence of anisotropy. In addition, the oscillation of the RCS values due to negative uniaxial spheres is much sharper and more irregular than that due to positive uniaxial spheres, and the oscillation range of RCS values of negative uniaxial spheres are wider.

For electric anisotropic spheres, it is assumed that the condition of $\mu_r = \mu_t = 1$ applies to all the cases. After careful examination and simulation, it is found that the dependence of RCS exhibits the same scattering performance with ferrite spheres in both negative and positive uniaxial cases. Hence the figures of normalized RCS results for electric anisotropic spheres will not be given in detail due to the length restriction.

- *Hybrid Anisotropy Effect:*

In this case where $\epsilon_r \neq \epsilon_t$ and $\mu_r \neq \mu_t$, the hybrid effects due to AR_e and AR_m are of particular interest. In Fig. 3.3(a), keep the $\overline{\boldsymbol{\epsilon}}$ constant and change μ_r and μ_t so as to examine the anisotropy effect on the RCS values. By comparing Fig. 3.3 with Fig. 3.2, it is observed that under the same AR_m, the RCS values are affected significantly by the existence of AR_e, leading to hybrid anisotropy effects.

- *RCS Prediction:*

By comparing the results in Fig. 3.2 for uniaxial ferrite spheres with those in Fig. 3.3 for generalized anisotropic spheres, it can be concluded that (a) the scattering performance of a nondissipative sphere are significantly affected by the presence of anisotropy of the sphere, and (b) by studying many other different cases for a

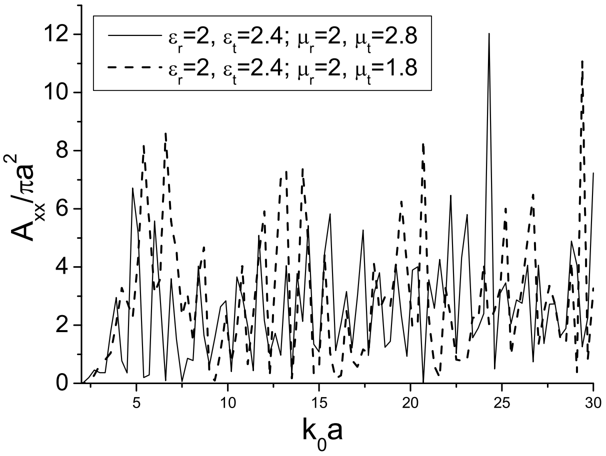

(a) Solid curve: $AR_e = 1.2$, $AR_m = 1.4$;

Dash curve: $AR_e = 1.2$, $AR_m = 0.9$.

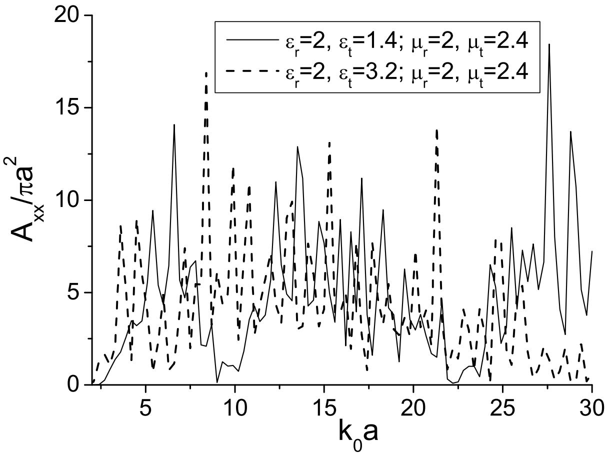

(b) Solid curve: AR_e=0.7, AR_m=1.2;

Dash curve: AR_e=1.6, AR_m=1.2.

Figure 3.3: Normalized RCS values versus k_0a for generalized anisotropic spheres.

wide range of anisotropy, it is obvious that the dependence of RCS on anisotropy is complex and no general rules to predict the scattering behavior due to the anisotropy have been found in the present work. Therefore, the control of the RCS values can be made by adjusting the factors or parameters in many different ways.

Absorbing Spheres

In the case of absorbing spheres, the elements of $\overline{\boldsymbol{\epsilon}}$ and $\overline{\boldsymbol{\mu}}$ in Eq. (3.1) have complex values. The imaginary parts represent absorptions. Subsequently, I will first examine the characteristics of isotropic absorbing spheres. In the cases given in Fig. 3.4, the orders of Bessel functions (*i.e.*, v_1 and v_2) in Eqs. (3.6a) and (3.6b) are still integers. Fig. 3.4 shows that for sufficiently large isotropic absorbing spheres ($k_0a > 17$), normalized RCS values steadily tend to 0.0529 and 0.0357 for solid and dashed curves, respectively. For small values of k_0a, high oscillation would be present, and

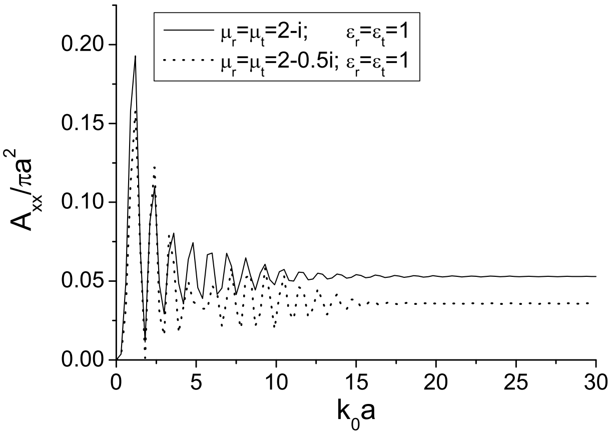

Figure 3.4: Normalized RCS values versus k_0a for isotropic absorbing spheres.

these results are comparable with the diagrams given in [114]. This fact confirms the validity of our theoretical formulation.

- *Electric/Magnetic Anisotropy Effects:*

In this part, it is assumed that $\epsilon_r = \epsilon_t = 1$ for all the single anisotropy cases. In Fig. 3.5(a), the RCS results for negative absorbing spheres ($\mu_r < \mu_t$) with $AR_m = 1.3 - 0.1i$, $AR_m = 1.4 - 0.3i$ and $AR_m = 1.5 - 0.5i$ are shown. It can be observed that when $k_0 a > 15$, all these three curves tend to their own limit values, 0.08665, 0.1088 and 0.1325, respectively. It is noted that the periods and limits of damped oscillations which occur for $k_0 a < 5$ exhibit an irregular form, and for bigger values of $k_0 a$, the oscillations start to show a regular decaying form, which agrees with the results for isotropic cases with perfectly conducting spheres [114]. In Fig. 3.5(b), RCS values for positive uniaxial absorbing spheres ($\mu_r > \mu_t$) in three cases are shown. It exhibits the characteristics of oscillation periods and limit values similar to those in Fig. 3.5(a). However, it can be seen that the higher the imaginary part of the complex permeability parallel to the spherical surface, the smaller the oscillation period for the region when $k_0 a > 5$. Higher absorption via the imaginary part in μ_t results in higher values of the limits of the damped oscillations. For the practical purposes of RCS reductions, the positive uniaxial absorbing spheres are preferred, since the backscattered field due to a positive absorbing sphere is only about one fifth of the field due to a negative uniaxial absorbing sphere.

- *Hybrid Anisotropy Effects:*

In this part, the AR_e and AR_m under consideration can be any complex num-

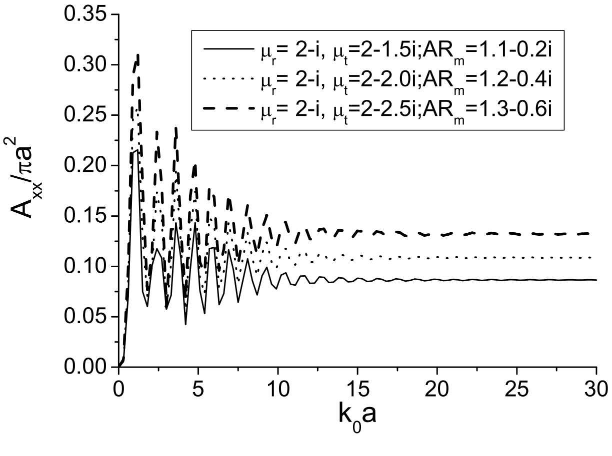

(a) Negative absorbing spheres.

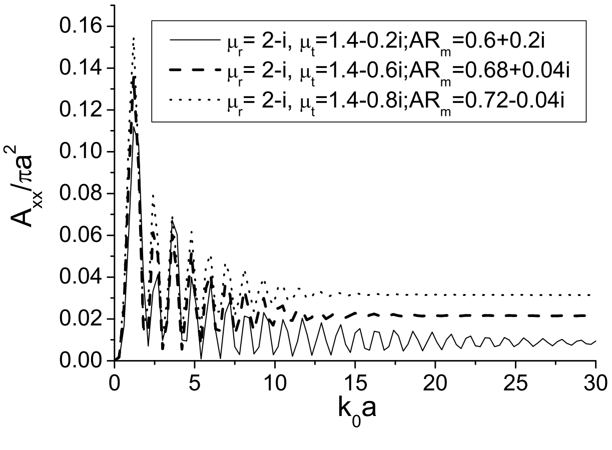

(b) Positive absorbing spheres.

Figure 3.5: Normalized RCS values versus k_0a for absorbing spheres when $\epsilon_r = \epsilon_t = 1$.

bers. It is worthwhile noting that some novel characteristics of RCS values will be presented. By comparing Fig. 3.6 with Fig. 3.3, it can be observed that the loss tangents or the imaginary parts of $\overline{\boldsymbol{\epsilon}}$ and $\overline{\boldsymbol{\mu}}$ significantly reduce the RCS values (almost hundreds of times) and also makes the oscillation more flattened and predictable. This observation might be very useful in practical applications, especially in identifying aircraft coating materials which may generate some invisibility effects.

Finally, RCS results are obtained for a special case where ϵ_r and μ_r can be arbitrary but $\epsilon_t = \mu_t$. As is shown in Fig. 3.7(a) and Fig. 3.7(b), for the absorbing spheres (regardless of single or joint anisotropy), once the parallel permittivity equals parallel permeability, RCS values will approach to zero in the region of $k_0 a > 3$ regardless of what ϵ_r and μ_r are. However, the nondissipative sphere still shows an irregular fluctuation in Fig. 3.7(c), and the oscillations do not end up with a stable limit.

- *RCS Prediction:*

From Fig. 3.4 to Fig. 3.7, it can be concluded that the transverse components of $\overline{\boldsymbol{\epsilon}}$ and $\overline{\boldsymbol{\mu}}$ dominate the scattering characteristics of the absorbing spheres, which makes it possible to control the backscattering effects of anisotropy. I propose a general RCS prediction scheme here to calculate the limit value of damped oscillations in all the figures in this section:

$$N_{\text{limit}} = \left| \frac{\sqrt{\frac{\mu_t}{\epsilon_t}} - 1}{\sqrt{\frac{\mu_t}{\epsilon_t}} + 1} \right|^2, \tag{3.16}$$

which is applicable to all the sufficiently large absorbing spheres and can be reduced to the geometrical optics limit given in [115].

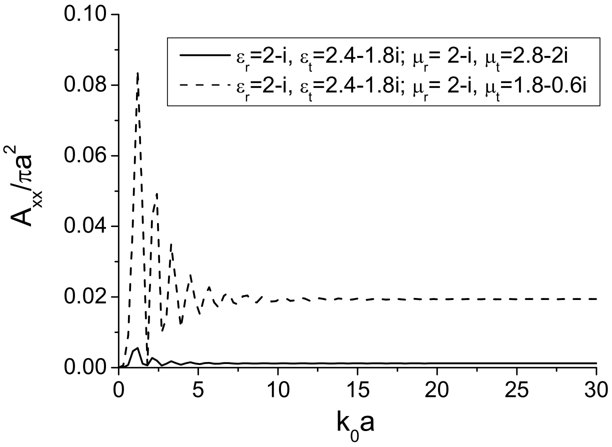

(a) Solid curve: $AR_e = 1.32 - 0.24i$ and $AR_m = 1.52 - 0.24i$;

Dash curve: $AR_e = 1.32 - 0.24i$ and $AR_m = 0.84 + 0.12i$.

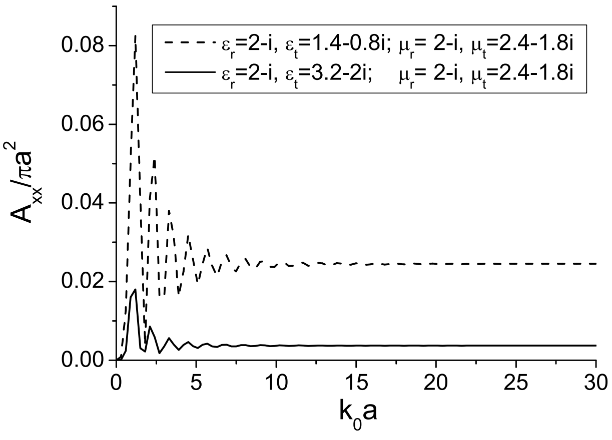

(b) Solid curve: $AR_e = 1.68 - 0.16i$ and $AR_m = 1.32 - 0.24i$;

Dash curve: $AR_e = 0.72 - 0.04i$ and $AR_m = 1.32 - 0.24i$.

Figure 3.6: Normalized RCS values versus k_0a for general absorbing spheres.

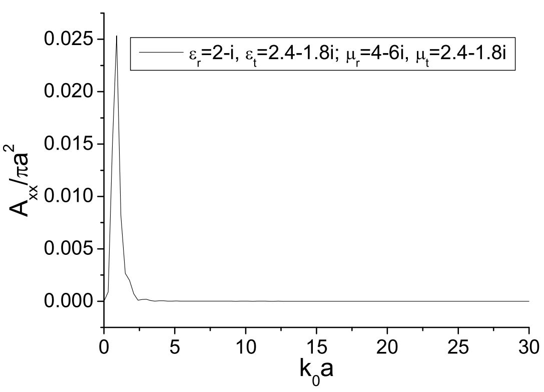

(a) Absorbing sphere with $\epsilon_t = \mu_t = 2.4 - 1.8i$.

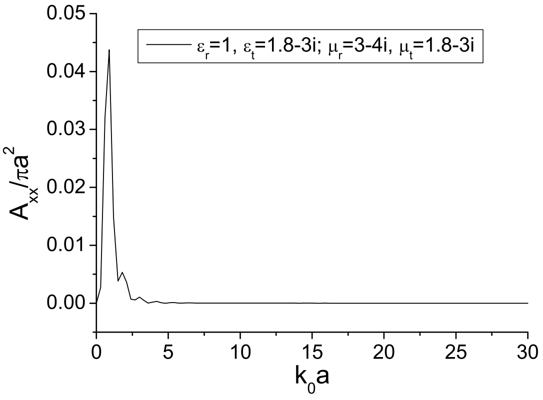

(b) Absorbing sphere with $\epsilon_t = \mu_t = 1.8 - 3i$.

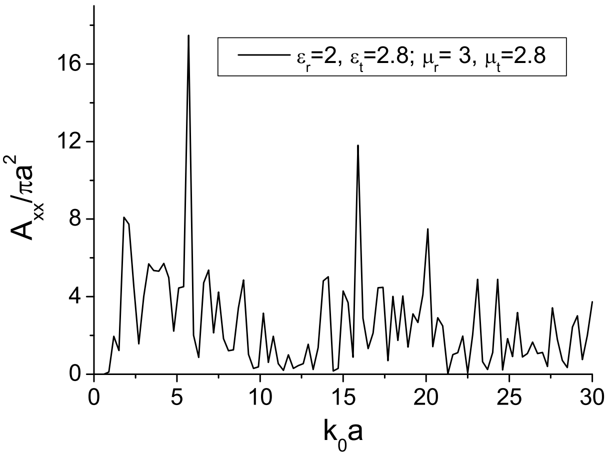

(c) Nondissipative sphere with $\epsilon_t = \mu_t = 2.8$.

Figure 3.7: Normalized RCS values versus k_0a for absorbing and nondissipative spheres when $\epsilon_t = \mu_t$.

The physical significance here is that for a sufficiently large sphere, the electric field vector of the incident plane wave is parallel to the boundary surface of the sphere. The effect of permittivity ϵ_r and permeability μ_r, which are perpendicular to the electromagnetic perturbations of the incident wave, does not affect the backscattering behavior. If one uses Eq. (3.16) to compute all the limit of the figures, it is found the theoretical results agree well with the numerical data.

3.3 Anisotropy ratio and the resonances of anisotropic spheres

Resonances occur if the denominators of the scattering coefficients in Eqs. (3.14a)-(3.14b) become sufficiently small. Then the corresponding mode will dominate the scattered field. These resonances are caused either by surface polaritons requiring negative values of the dielectric response of the bulk media, or the constructive interference of light waves, traveling inside a narrow domain in the vicinity of the spherical surface. The first case may be due, for example, to the presence of conduction electrons, excitons, or lattice vibrations. When the particle is small, surface polariton is the only possible source of resonances.

The TM-modes a_n are resonant if

$$h_n^{(1)\prime}(k_0a)j_{v_1}(k_ta) - \sqrt{\mu_t/\epsilon_t}h_n^{(1)}(k_0a)j'_{v_1}(k_ta) = 0, \qquad (3.17)$$

and the TE-modes b_n are resonant if

$$h_n^{(1)}(k_0a)j'_{v_2}(k_ta) - \sqrt{\mu_t/\epsilon_t}\,h_n^{(1)'}(k_0a)j_{v_2}(k_ta) = 0. \tag{3.18}$$

It is found that (3.17) and (3.18) can only be satisfied approximately. For sufficiently small particles ($x = k_0a << 1$), Ricatti-Bessel and Hankel functions can be expanded by their first term

$$\begin{aligned} j_l(x) &\approx \frac{x^{l+1}}{(2l+1)!!} && \text{(3.19a)} \\ h_l^{(1)}(x) &\approx \frac{x^{l+1}}{(2l+1)!!} - i\frac{(2l-1)!!}{x^l} && \text{(3.19b)} \end{aligned}$$

To yield more insight of the role of anisotropy in the resonant lightwave scattering, Eqs. (3.14a) and (3.14b) are thus rewritten

$$\begin{aligned} a_n &= \frac{[(v_1+1)-(n+1)\epsilon_t]T_n}{[(n+1)\epsilon_t-(v_1+1)] - i[n\epsilon_t+(v_1+1)]\cdot[(2n-1)!!]^2\cdot(2n+1)x^{-2n-1}} && \text{(3.20a)} \\ b_n &= \frac{[(n+1)\mu_t-(v_2+1)]T_n}{[(v_2+1)-(n+1)\mu_t] + i[n\mu_t+(v_2+1)]\cdot[(2n-1)!!]^2\cdot(2n+1)x^{-2n-1}} && \text{(3.20b)} \end{aligned}$$

In view of these scattering coefficients, of particular interest are the roles of anisotropy and the order of partial waves upon the lightwave scattering by spherical particles. Calculations are performed with $x = k_0a = 0.2$ and scattering coefficients normalized by their respective maxima. First, let us examine the effect of the anisotropy ratio. In contrast to the traditional resonant requirement for spherical particles (i.e., $\epsilon = -2$ [116, 117]), optical resonances are greatly modified by the presence of anisotropy ratio. Once we know the value of permittivity ϵ_r, which is perpendicular to the electric perturbations of the incident wave, the resonance only depends on the anisotropy ratio. In Fig. 3.8, two cases of permittivity ϵ_r are considered with particular interest. When ϵ_r is smaller than unity (i.e., the

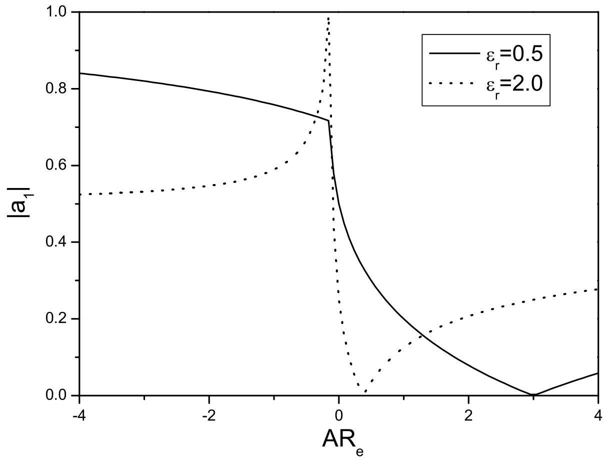

Figure 3.8: Normalized magnitude of TM-mode scattering coefficient a_1 versus anisotropy ratio in two cases.

relative permittivity of air), the amplitude of a_1 decreases with anisotropy ratio AR_e before arriving at $AR_e = 3$, where the amplitude is reduced to zero. No resonances are found in such cases. When ϵ_r is greater than unit, the resonance occurs at $AR_e = -0.125$, which is close to its transparency point at $AR_e = 0.375$.

Further simulations reveal that AR_e will stay in close vicinity of -0.125 to excite surface polaritons for anisotropic spherical particles at $x = 0.2$, whose permittivity is within the range $1 < \epsilon_r < 4$. Beyond this range, only one resonance can be found at a particular anisotropy ratio, which is illustrated later in Fig. 3.9. These peculiarities stems from the denominators of the scattering coefficients. In (3.20a), for example, the denominator can be separated into two portions: a real part and an imaginary part, and the real part is of the same value as the numerator but with an opposite sign. The resonance follows from the imaginary part being zero (i.e., $nAR_e\epsilon_r + (\sqrt{n(n+1)AR_e + 1/4} + 1/2) = 0$). If AR_e is positive, one can never meet the resonant requirement, and certain positive AR_e value will thus lead the numerator to be zero, which turns to be the transparency condition. However, if AR_e becomes negative, $nAR_e\epsilon_r + (\sqrt{n(n+1)AR_e + 1/4} + 1/2)$ will be a complex value, that in turn affects the separation of real and imaginary quantities and the resonant requirement. It is also clear that the scattering vanishes when $AR_e = 1$ for the case of $\epsilon_r = 1$ and $AR_e = 0.375$ for the case of $\epsilon_r = 2$, which means that the object becomes transparent to the incident wave. Hence, for TM-modes, one can choose an appropriate anisotropy ratio to minimize the corresponding scattering width or to enhance it.

Another interesting phenomenon follows from the case of higher values of permittivity ϵ_r. One can read from Fig. 3.9 that the optical resonances are quite sensitive to anisotropy ratio. For each case, the resonance only happens within a quite narrow band of AR_e, apart from which the magnitudes of a_n are almost zero. It can be seen that the permittivity only affects the resonant position. The resonant anisotropy ratio AR_e^{res} is -0.08 for resonances with $\epsilon_r = 10$, and $AR_e^{res} = -0.045$ with $\epsilon_r = 10$. It can be envisaged to have AR_e^{res} always negative and getting closer to zero with increasing permittivity.

The calculations have been carried out by considering the first partial wave since the electric size of the anisotropic spherical particle is very small. Compared to $|a_1|$, the amplitude of a_n is negligibly small for $n > 1$. If we take into account the second or even higher-order terms in the asymptotic expansion of Ricatti-Bessel functions,

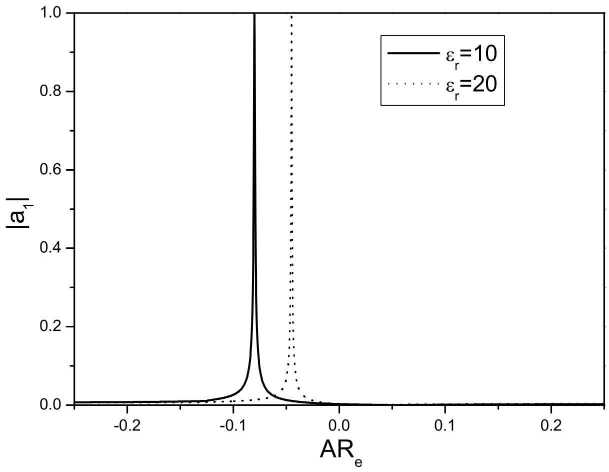

Figure 3.9: Normalized magnitude of TM-mode scattering coefficient a_1 versus anisotropy ratio for large permittivities.

the resonance feature suffers almost no change for the current size parameter 0.2. However, if the size is not extremely small, the higher-order asymptotic terms will have remarkable influence on resonances. The study can also be extended to resonant scattering problem dominated by TE-modes as well as the problem of dissipative anisotropic spheres whose resonant effects will decrease with the imaginary part of ϵ_r due to the damping.

3.4 Propagation and scattering in gyrotropic spheres

As a more general case, the gyrotropic spheres should be considered. The anisotropic spheres discussed before are just one subset of gyrotropic cases where the off-diagonal elements are zero. In this subject, some works developed certain methods such as scalar Hertz potentials [118] and scalar superpotentials [119]. Due to the complexity of the expression of the electromagnetic fields in the spherical coordinate systems, the formulations of EM fields are tedious, lengthy, and complicated. The relevant work [120] studied electromagnetic wave interactions with gyrotropic materials in spherical coordinates, and the materials had only electric gyrotropy though. Other works dealt with the fields and eigenvalues either in a uniaxial anisotropic material [121] or in the Cartesian and cylindrical coordinate systems [122], where the models are much simpler than what follows in the current work. It appears that no other work is available in literature to represent, in the present way, the EM fields for this kind of materials containing both electric and magnetic gyrotropies.

The general gyrotropic material are characterized by constitutive tensors of permittivity and permeability in the following forms:

$$\overline{\boldsymbol{\epsilon}} = \begin{bmatrix} \epsilon_r & 0 & 0 \\ 0 & \epsilon_\tau & \epsilon_\sigma \\ 0 & -\epsilon_\sigma & \epsilon_\tau \end{bmatrix}, \tag{3.21a}$$

$$\overline{\boldsymbol{\mu}} = \begin{bmatrix} \mu_r & 0 & 0 \\ 0 & \mu_\gamma & \mu_\zeta \\ 0 & -\mu_\zeta & \mu_\gamma \end{bmatrix} \tag{3.21b}$$

where the identity dyadic is in spherical coordinates.

Much effort is spent on solving the second-order differential equations and then obtaining all the electric and magnetic field components of TE and TM waves with respect to $\hat{\boldsymbol{r}}$. Different cases, both specific and general, are considered. In addition, this chapter makes some corrections to the field expressions in [120] when the solution is reduced to that of the simpler case discussed in [120].

3.4.1 Basic formulations

The source-free Maxwell's equations are written as

$$\nabla \times \boldsymbol{E} = i\omega\overline{\boldsymbol{\mu}} \cdot \boldsymbol{H}, \tag{3.22a}$$

$$\nabla \times \boldsymbol{H} = -i\omega\overline{\boldsymbol{\epsilon}} \cdot \boldsymbol{E}. \tag{3.22b}$$

To solve these equations, it is more convenient to pose the problem in terms of only the radial functions E_r and H_r. After a somewhat lengthy but careful algebra manipulation, one arrives at a coupled set of differential equations involving only radial components E_r and H_r:

$$\begin{aligned}\frac{1}{r^2}\frac{\partial^2(r^2E_r)}{\partial r^2} &+ \frac{\epsilon_\tau}{\epsilon_r}\frac{1}{r^2\sin\theta}\frac{\partial(\sin\theta\frac{\partial E_r}{\partial\theta})}{\partial\theta} \\ &+ \frac{\epsilon_\tau}{\epsilon_r}\frac{1}{r^2\sin^2\theta}\frac{\partial^2E_r}{\partial\phi^2} + \omega^2\frac{\epsilon_\tau}{\mu_\gamma}(\mu_\gamma^2+\mu_\zeta^2)E_r \\ &- i\omega\frac{\mu_r}{\mu_\gamma\epsilon_r}(\epsilon_\sigma\mu_\gamma+\epsilon_\tau\mu_\zeta)\frac{1}{r^2}\frac{\partial(r^2H_r)}{\partial r} = 0\end{aligned} \tag{3.23a}$$

$$\begin{aligned}\frac{1}{r^2}\frac{\partial^2(r^2H_r)}{\partial r^2} &+ \frac{\mu_\gamma}{\mu_r}\frac{1}{r^2\sin\theta}\frac{\partial(\sin\theta\frac{\partial H_r}{\partial\theta})}{\partial\theta} \\ &+ \frac{\mu_\gamma}{\mu_r}\frac{1}{r^2\sin^2\theta}\frac{\partial^2H_r}{\partial\phi^2} + \omega^2\frac{\mu_\gamma}{\epsilon_\tau}(\epsilon_\tau^2+\epsilon_\sigma^2)H_r \\ &- i\omega\frac{\epsilon_r}{\epsilon_\tau\mu_r}(\epsilon_\sigma\mu_\gamma+\epsilon_\tau\mu_\zeta)\frac{1}{r^2}\frac{\partial(r^2E_r)}{\partial r} = 0.\end{aligned} \tag{3.23b}$$

From the properties of the associated Legendre polynomials, one will have:

$$\frac{1}{r^2\sin\theta}\frac{\partial}{\partial\theta}(\sin\theta\frac{\partial}{\partial\theta}\bullet) + \frac{1}{r^2\sin^2\theta}\frac{\partial^2}{\partial\phi^2}\bullet = -n(n+1)\bullet \tag{3.24}$$

where the bullet • denotes the separated part of either E_r or H_r according to a specific case, but it should be, however, conformal through Eq. (3.24). And certainly, this will lead to the Legendre polynomial as its solution.

Using the method of separation of variables, it is found that the solutions are composed of superpositions of spherical Bessel functions, associated Legendre polynomials, and harmonic functions

$$\begin{bmatrix} E_r \\ \\ H_r \end{bmatrix} = \sum_{m,n} \begin{bmatrix} E_n \\ \\ H_n \end{bmatrix} P_n^m(\cos\theta) \begin{matrix} \cos \\ \\ \sin \end{matrix} m\phi \tag{3.25}$$

where the forms of E_n and H_n depend on the specific cases discussed later.

For the neat and simplicity of the further derivations, let me introduce some identities first:

$$z_v^{(q)}(\kappa r) = \begin{cases} j_v(\kappa r), & q = 1 \\ y_v(\kappa r), & q = 2 \\ h_v^{(1)}(\kappa r), & q = 3 \\ h_v^{(2)}(\kappa r), & q = 4 \end{cases} . \tag{3.26}$$

In Eq. (3.26), $j_v(\kappa r)$ and $y_v(\kappa r)$ denote spherical Bessel functions of the first kind and the second kind, respectively. The $h_v^{(1)}(\kappa r)$ and $h_v^{(2)}(\kappa r)$ represent spherical Hankel functions of the first kind and the second kind, respectively. The order v, when used to describe the waves and fields in isotropic media, is usually an integer; but it is not necessarily an integer in the case of gyrotropic media. Instead, it depends on the medium parameters and has two values:

$$v_1(v_1 + 1) = n(n+1)\frac{\epsilon_\tau}{\epsilon_r}, \tag{3.27a}$$

$$v_2(v_2+1)=n(n+1)\frac{\mu_\gamma}{\mu_r}. \tag{3.27b}$$

3.4.2 Field representations in different cases

In this section, much effort will be made on Eq. (3.23) dealing with the radial functions. Subsequently, Eq. (3.23) is solved for different cases.

Case 1: $\epsilon_\sigma\mu_\gamma+\epsilon_\tau\mu_\zeta=0$ **(**$\epsilon_\sigma\neq 0$ **and** $\mu_\zeta\neq 0$**)**

In this case, Eq. (3.23) is decoupled into

$$\begin{aligned}&\frac{1}{r^2}\frac{\partial^2(r^2E_r)}{\partial r^2}+\frac{\epsilon_\tau}{\epsilon_r}\frac{1}{r^2\sin\theta}\frac{\partial(\sin\theta\frac{\partial E_r}{\partial\theta})}{\partial\theta}\\&\quad+\frac{\epsilon_\tau}{\epsilon_r}\frac{1}{r^2\sin^2\theta}\frac{\partial^2E_r}{\partial\phi^2}+\omega^2\frac{\epsilon_\tau}{\mu_\gamma}(\mu_\gamma^2+\mu_\zeta^2)E_r=0 &(3.28a)\\&\frac{1}{r^2}\frac{\partial^2(r^2H_r)}{\partial r^2}+\frac{\mu_\gamma}{\mu_r}\frac{1}{r^2\sin\theta}\frac{\partial(\sin\theta\frac{\partial H_r}{\partial\theta})}{\partial\theta}\\&\quad+\frac{\mu_\gamma}{\mu_r}\frac{1}{r^2\sin^2\theta}\frac{\partial^2H_r}{\partial\phi^2}+\omega^2\frac{\mu_\gamma}{\epsilon_\tau}(\epsilon_\tau^2+\epsilon_\sigma^2)H_r=0. &(3.28b)\end{aligned}$$

Substituting Eq. (3.25) into Eq. (3.28) and after some lengthy manipulations, we obtain

$$E_n=\frac{\alpha_{t_1}}{r}z_{v_1}^{(q)}(k_{t_1}r) \tag{3.29a}$$

$$H_n=-i\eta_r^{-2}\eta_t\frac{\alpha_{t_2}}{r}z_{v_2}^{(q)}(k_{t_2}r) \tag{3.29b}$$

where

$$\alpha_{t_1}=k_r^{-\frac{3}{2}}\sqrt{\frac{2k_{t_1}}{\pi}}, \tag{3.30a}$$

$$\alpha_{t_2}=k_r^{-\frac{3}{2}}\sqrt{\frac{2k_{t_2}}{\pi}}. \tag{3.30b}$$

In Eq. (3.29) and Eq. (3.30), we have the following inter-parameters

$$k_{t_1}^2 = \omega^2 \frac{\epsilon_\tau}{\mu_\gamma}(\mu_\gamma^2 + \mu_\zeta^2), \tag{3.31a}$$

$$k_{t_2}^2 = \omega^2 \frac{\mu_\gamma}{\epsilon_\tau}(\epsilon_\tau^2 + \epsilon_\sigma^2), \tag{3.31b}$$

$$k_r^2 = \omega^2 \mu_r \epsilon_r; \tag{3.31c}$$

$$\eta_r = \sqrt{\mu_r/\epsilon_r}, \tag{3.31d}$$

$$\eta_t = \sqrt{\mu_\gamma/\epsilon_\tau}. \tag{3.31e}$$

In order to obtain the complete field representation, the tangential components of electromagnetic fields are needed and they are expressed as follows:

$$\frac{1}{r\sin\theta}\frac{\partial}{\partial\phi}E_r - \frac{1}{r}\frac{\partial}{\partial r}(rE_\phi) = i\omega\mu_\gamma H_\theta + i\omega\mu_\zeta H_\phi \tag{3.32a}$$

$$\frac{1}{r}\frac{\partial}{\partial\phi}(rE_\theta) - \frac{1}{r}\frac{\partial}{\partial\theta}E_r = -i\omega\mu_\zeta H_\theta + i\omega\mu_\gamma H_\phi \tag{3.32b}$$

and

$$\frac{1}{r\sin\theta}\frac{\partial}{\partial\phi}H_r - \frac{1}{r}\frac{\partial}{\partial r}(rH_\phi) = -i\omega\epsilon_\tau E_\theta - i\omega\epsilon_\sigma E_\phi, \tag{3.33a}$$

$$\frac{1}{r}\frac{\partial}{\partial\phi}(rE_\theta) - \frac{1}{r}\frac{\partial}{\partial\theta}E_r = i\omega\epsilon_\sigma E_\theta - i\omega\epsilon_\tau E_\phi. \tag{3.33b}$$

To make the solution more straightforward, we need to separate the field components into TE- and TM-field modes subsequently with respect to $\widehat{\boldsymbol{r}}$.

- *TE-field Modes to* $\hat{\boldsymbol{r}}$

For TE-field modes, Eq. (3.32) is reduced to

$$
\begin{aligned}
-\frac{1}{r}\frac{\partial}{\partial r}(rE_\phi^{TE}) &= i\omega\mu_\gamma H_\theta^{TE} + i\omega\mu_\zeta H_\phi^{TE} && \text{(3.34a)}\\
\frac{1}{r}\frac{\partial}{\partial r}(rE_\theta^{TE}) &= -\, i\omega\mu_\zeta H_\theta^{TE} + i\omega\mu_\gamma H_\phi^{TE}. && \text{(3.34b)}
\end{aligned}
$$

Substituting Eq. (3.34) into Eq. (3.33), we have

$$
\begin{aligned}
\frac{\partial^2}{\partial r^2}(rE_\theta^{TE}) + k_{t_2}^2(rE_\theta^{TE}) &= i\omega\mu_\gamma\frac{1}{\sin\theta}\frac{\partial}{\partial\phi}H_r - i\omega\mu_\zeta\frac{\partial}{\partial\theta}H_r, && \text{(3.35a)}\\
\frac{\partial^2}{\partial r^2}(rE_\phi^{TE}) + k_{t_2}^2(rE_\phi^{TE}) &= -i\omega\mu_\zeta\frac{1}{\sin\theta}\frac{\partial}{\partial\phi}H_r - i\omega\mu_\gamma\frac{\partial}{\partial\theta}H_r. && \text{(3.35b)}
\end{aligned}
$$

After careful manipulations, we finally obtain

$$
\begin{aligned}
E_\theta^{TE} =& \mp\,\omega\eta_r^{-2}\eta_t\alpha_{t_2}\sum_{m,n}\frac{a_{\substack{e\\o}mn}}{v_2(v_2+1)}z_{v_2}^{(q)}(k_{t_2}r)\Big[\mu_\gamma\frac{m}{\sin\theta}\\
&\times P_n^m(\cos\theta)\begin{matrix}\sin\\ \\ \cos\end{matrix}\, m\phi \pm \mu_\zeta\frac{dP_n^m(\cos\theta)}{d\theta}\begin{matrix}\cos\\ \\ \sin\end{matrix}\, m\phi\Big] && \text{(3.36a)}\\
E_\phi^{TE} =& \mp\,\omega\eta_r^{-2}\eta_t\alpha_{t_2}\sum_{m,n}\frac{a_{\substack{e\\o}mn}}{v_2(v_2+1)}z_{v_2}^{(q)}(k_{t_2}r)\Big[-\mu_\zeta\frac{m}{\sin\theta}\\
&\times P_n^m(\cos\theta)\begin{matrix}\sin\\ \\ \cos\end{matrix}\, m\phi \pm \mu_\gamma\frac{dP_n^m(\cos\theta)}{d\theta}\begin{matrix}\cos\\ \\ \sin\end{matrix}\, m\phi\Big] && \text{(3.36b)}
\end{aligned}
$$

$$
H_\theta^{TE} = -\, i\eta_r^{-2}\eta_t\alpha_{t_2}\sum_{m,n}\frac{a_{\substack{e\\o}mn}}{v_2(v_2+1)}\frac{\partial[rz_{v_2}^{(q)}(k_{t_2}r)]}{r\partial r}\frac{dP_n^m(\cos\theta)}{d\theta}\begin{matrix}\cos\\ \\ \sin\end{matrix}\, m\phi \qquad \text{(3.36c)}
$$

$$
H_\phi^{TE} = \pm\, i\eta_r^{-2}\eta_t\alpha_{t_2}\sum_{m,n}\frac{a_{\substack{e\\o}mn}}{v_2(v_2+1)}\frac{m}{\sin\theta}\frac{\partial[rz_{v_2}^{(q)}(k_{t_2}r)]}{r\partial r}P_n^m(\cos\theta)\begin{matrix}\sin\\ \\ \cos\end{matrix}\, m\phi. \qquad \text{(3.36d)}
$$

- *TM-field Modes to* $\hat{\boldsymbol{r}}$

For TM-field modes, Eq. (3.33) is similarly rewritten as

$$-\frac{1}{r}\frac{\partial}{\partial r}(rH_\phi^{TM}) = -\,i\omega\epsilon_\tau E_\theta^{TM} - i\omega\epsilon_\sigma E_\phi^{TM} \tag{3.37a}$$

$$\frac{1}{r}\frac{\partial}{\partial r}(rH_\theta^{TM}) = i\omega\epsilon_\sigma E_\theta^{TM} - i\omega\epsilon_\tau E_\phi^{TM}. \tag{3.37b}$$

Substituting Eq. (3.37) into Eq. (3.32), we have

$$\frac{\partial^2(rH_\theta^{TM})}{\partial r^2} + k_{t_1}^2(rH_\theta^{TM}) = -\,i\omega\epsilon_\tau\frac{1}{\sin\theta}\frac{\partial E_r}{\partial\phi} + i\omega\epsilon_\sigma\frac{\partial E_r}{\partial\theta} \tag{3.38a}$$

$$\frac{\partial^2(rH_\phi^{TM})}{\partial r^2} + k_{t_1}^2(rH_\phi^{TM}) = i\omega\epsilon_\sigma\frac{1}{\sin\theta}\frac{\partial E_r}{\partial\phi} + i\omega\epsilon_\tau\frac{\partial E_r}{\partial\theta}. \tag{3.38b}$$

Again after careful manipulations, we finally have:

$$\begin{aligned}H_\theta^{TM} = &\pm i\omega\alpha_{t_1}\sum_{m,n}\frac{b_{\substack{e\\o}mn}}{v_1(v_1+1)}z_{v_1}^{(q)}(k_{t_1}r)\Big[\epsilon_\tau\frac{m}{\sin\theta}\\ &\times P_n^m(\cos\theta)\begin{matrix}\sin\\ \\ \cos\end{matrix}\, m\phi \mp \epsilon_\sigma\frac{dP_n^m(\cos\theta)}{d\theta}\begin{matrix}\cos\\ \\ \sin\end{matrix}\, m\phi\Big]\end{aligned} \tag{3.39a}$$

$$\begin{aligned}H_\phi^{TM} = &\pm i\omega\alpha_{t_1}\sum_{m,n}\frac{b_{\substack{e\\o}mn}}{v_1(v_1+1)}z_{v_1}^{(q)}(k_{t_1}r)\Big[-\epsilon_\sigma\frac{m}{\sin\theta}\\ &\times P_n^m(\cos\theta)\begin{matrix}\sin\\ \\ \cos\end{matrix}\, m\phi \pm \epsilon_\tau\frac{dP_n^m(\cos\theta)}{d\theta}\begin{matrix}\cos\\ \\ \sin\end{matrix}\, m\phi\Big]\end{aligned} \tag{3.39b}$$

$$E_\theta^{TM} = \alpha_{t_1}\sum_{m,n}\frac{b_{\substack{e\\o}mn}}{v_1(v_1+1)}\frac{\partial[rz_{v_1}^{(q)}(k_{t_1}r)]}{r\partial r}\times\frac{dP_n^m(\cos\theta)}{d\theta}\begin{matrix}\cos\\ \\ \sin\end{matrix}\, m\phi \tag{3.39c}$$

$$E_\phi^{TM} = \mp\,\alpha_{t_1}\sum_{m,n}\frac{b_{\substack{e\\o}mn}}{v_1(v_1+1)}\frac{m}{\sin\theta}\frac{\partial[rz_{v_1}^{(q)}(k_{t_1}r)]}{r\partial r}\times P_n^m(\cos\theta)\begin{matrix}\sin\\ \\ \cos\end{matrix}\, m\phi. \tag{3.39d}$$

Case 2: $\epsilon_r/\mu_r = \epsilon_\tau/\mu_\gamma = \epsilon_\sigma/\mu_\zeta$

In this case, the coupled terms in Eq. (3.23) are not zero any more, which will increase the complexity of obtaining the solutions. If the condition of $\epsilon_r/\mu_r = \epsilon_\tau/\mu_\gamma = \epsilon_\sigma/\mu_\zeta$ is satisfied, one has $v_1 = v_2$ according to Eq. (3.27). Hence, to be neat, we let $v = v_1 = v_2$ in the following derivation. Similarly, much effort is made to get the expressions of E_r and H_r, which are the bases for obtaining the tangential components of the fields.

In this case, Eq. (3.25) should be revised into

$$\begin{bmatrix} E_r \\ \\ H_r \end{bmatrix} = \sum_{m,n} \begin{bmatrix} E_n \\ \\ H_n \end{bmatrix} P_n^m(\cos\theta) \begin{matrix} \cos \\ \\ \sin \end{matrix} m\phi. \tag{3.40}$$

In the given relationship between the parameters, with Eq. (3.24) obtained, Eq. (3.27) is reduced to

$$\begin{aligned} &\frac{1}{r^2}\frac{\partial^2(r^2E_r)}{\partial r^2} - v(v+1)r^2E_r + \omega^2\frac{\epsilon_\tau}{\mu_\gamma}(\mu_\gamma^2+\mu_\zeta^2)E_r \\ &\qquad - i\omega\frac{\mu_r}{\mu_\gamma\epsilon_r}(\epsilon_\sigma\mu_\gamma+\epsilon_\tau\mu_\zeta)\frac{1}{r^2}\frac{\partial(r^2H_r)}{\partial r} = 0, && \text{(3.41a)} \\ &\frac{1}{r^2}\frac{\partial^2(r^2H_r)}{\partial r^2} - v(v+1)r^2H_r + \omega^2\frac{\mu_\gamma}{\epsilon_\tau}(\epsilon_\tau^2+\epsilon_\sigma^2)H_r \\ &\qquad - i\omega\frac{\epsilon_r}{\epsilon_\tau\mu_r}(\epsilon_\sigma\mu_\gamma+\epsilon_\tau\mu_\zeta)\frac{1}{r^2}\frac{\partial(r^2E_r)}{\partial r} = 0. && \text{(3.41b)} \end{aligned}$$

I find it feasible to decouple Eq. (3.41) by taking (3.41a) ± (3.41b). After a very lengthy manipulation, we will arrive at two differential equations based on (3.41a) ± (3.41b) in the form of the Coulomb wave functions, and the solutions of these kinds of differential equations have been solved for in [123] and expressed in terms of cylindrical Bessel functions.

Substituting Eq. (3.40) into Eq. (3.41), we find actually that Eq. (3.41) is associated with E_n and H_n. Finally, with the solutions of the Coulomb wave differential equations in [123], we obtain:

$$E_n \pm i\eta_r^2\eta_t^{-1}H_n = \beta z_v^{(q)}(k_t r)e^{\pm k_s r} \tag{3.42}$$

where the inter-parameters k_s, k_t and β are defined as follows

$$k_s = \omega\sqrt{\mu_\zeta \epsilon_\sigma}, \tag{3.43a}$$

$$k_t = \omega\sqrt{\mu_\gamma \epsilon_\tau}, \tag{3.43b}$$

$$\beta = k_r^{-\frac{3}{2}}\sqrt{\frac{2k_t}{\pi}}. \tag{3.43c}$$

Hence, we obtain

$$E_n = \beta\frac{1}{r}z_v^{(q)}(k_t r)\cosh(k_s r), \tag{3.44a}$$

$$H_n = -i\eta_r^2\eta_t^{-1}\beta\frac{1}{r}z_v^{(q)}(k_t r)\sinh(k_s r). \tag{3.44b}$$

After obtaining the E_n and H_n, the tangential components of electromagnetic fields can be expressed by following the procedures similar to those in Section 3.4.2.

Case 3: $\epsilon_\sigma = \mu_\zeta = 0$

If $\overline{\boldsymbol{\epsilon}}$ and $\overline{\boldsymbol{\mu}}$ bear the uniaxial anisotropic form, namely $\epsilon_\sigma = \mu_\zeta = 0$, field representations were given in [120]. However, the representations of E_ϕ^{TM}, H_ϕ^{TE} and H_ϕ^{TM} are incorrect due to typos. Herein, we present the corrected forms for those terms with the notations used by Liu *et al* [120]

$$E_\phi^{TM} = \mp\alpha\sum_{m,n}\frac{b_{\substack{e\\o}mn}}{c}v_1(v_1+1)\frac{m}{\sin\theta}\frac{\partial[rz_{v_1}^{(q)}(k_t r)]}{r\partial r}\times P_n^m(\cos\theta)\begin{matrix}\sin\\ \\ \cos\end{matrix}m\phi, \tag{3.45a}$$

$$H_\phi^{TE} = \pm\, i\eta_r^{-2}\eta_t\alpha \sum_{m,n} \frac{a_{\substack{e\\o}mn}}{v_2(v_2+1)} \frac{m}{\sin\theta} \frac{\partial[r z_{v_2}^{(q)}(k_t r)]}{r\partial r} P_n^m(\cos\theta) \begin{matrix}\sin\\ \\ \cos\end{matrix}\, m\phi, \quad (3.45\text{b})$$

$$H_\phi^{TM} = i\omega\epsilon_t\alpha \sum_{m,n} \frac{b_{\substack{e\\o}mn}}{v_1(v_1+1)} z_{v_1}^{(q)}(k_t r) \frac{dP_n^m(\cos\theta)}{d\theta} \begin{matrix}\cos\\ \\ \sin\end{matrix}\, m\phi. \quad (3.45\text{c})$$

3.5 Summary

The scattering by anisotropic and gyrotropic spheres is studied extensively. Much effort has been spent not only in the formulation of potentials and TE/TM-wave (with respect to $\hat{\boldsymbol{r}}$) decomposition, but also in the parametric studies of RCS characteristics. Calculated RCS values for an incident plane wave reveal that the existence of anisotropy significantly influences the scattering behavior of spherical objects. Furthermore, the hybrid anisotropy greatly affects the characteristics and dependence of RCS results than a single anisotropy. If the material parameters are manipulated properly, the objects can be *transparent* to the detecting devices.

It is found that for the cases of nondissipative spheres, the scattering behavior depends on uniaxial anisotropy in a complex way. For the cases of absorbing spheres, however, the RCS values are affected primarily by the imaginary parts of the transverse component of $\overline{\boldsymbol{\epsilon}}$ and $\overline{\boldsymbol{\mu}}$. Therefore, the dependence of backscattering RCS on single/joint anisotropy is found to be predictable. It is also observed that the RCS values tend to a limit, which is determined by ϵ_t and μ_t, the permittivity and permeability elements parallel to the boundary surface. The determination of limit of damped oscillations has been proposed in Eq. (3.16). Hence, if unintentional anisotropy is introduced due to natural reasons or due to the shear in the surface plane during processing, an absorbing material would be a better choice than a lossless dielectric material as a coating on a scatterer, and if the single anisotropy exists, it will be much better to utilize the hybrid anisotropy to minimize or control the scattering behaviors further.

This chapter, therefore, not only derives an analytical series solution to the theoretical problem for field representations of anisotropic spheres (where both $\overline{\boldsymbol{\epsilon}}$ and $\overline{\boldsymbol{\mu}}$ are uniaxial tensors), but also carries out extensive parametric studies of single and joint anisotropic effects on scattering behaviors. Furthermore, the anisotropy ratio effects on the resonances are discussed to characterize the resonant scattering properties of anisotropic spheres. Finally, some special cases of scattering problems are solved for gyrotropic spheres.

Chapter 4

Theory and application of magnetoelectric composites

4.1 Introduction

In the previous chapters, the propagation of electromagnetic waves in isotropic and anisotropic composites are studied. However, those composite materials may suffer from bulkiness and difficulty in fabrication, which is a limiting factor in electromagnetic applications. Composites with magnetoelectric coupling properties may help alleviate some of those problems. The magnetoelectric composites are characterized by the cross coupling between electricity and magnetism inherent from the optical activity. These composites can be isotropic or anisotropic, and may depend on the existence of external biased fields. The phenomenon of optical activity was first discovered via experimentation by French scientists. In 1811, Arago found that quartz crystals rotate the plane of polarization of linearly polarized light which is transmitted in the direction of its optical axis [124]. Later, this property was further demonstrated by various experiments by Biot [125, 126], and it was found that optical activity is not restricted to solid crystals but may be exhibited by other materials such as the boiling turpentine. Formal discussion of the concept of polarization was proposed in 1822 by Fresnel [127] who constructed a prism of quartz to separate two circularly polarized components of a linearly polarized ray.

Based on the argument that the optical activity was due to molecules, recent studies have utilized the microwaves and wire spirals to achieve a macroscopic model for such phenomenon instead of using light and chiral molecules [128]. Bi-isotropic materials (which include chiral materials) are a subclass of magnetoelectric composites. Scientists have made extensive research effort on studying bi-isotropic materials such as the wave properties and interaction [129, 130, 82], light reflection and propagation through chiral interfaces [131], novel structures exhibiting cross coupling [132], mixing formulas to get effective parameters [133, 134], and chiral pattern for antennas [135]. However, it appears that the application of chiral materials may be limited to the case of polarization converters, which can be used as polarizator shields and absorbing coating in RCS reduction such as Salisbury screens. More recently, a renewed interest was given to bianisotropic media in the community of electromagnetic materials, especially in the research of negative-index materials. Pendry [136] proposed a chiral route to achieve negative refraction by wounding a metal plate into coils stacked by a log pile. As such, the inductance in the coiled helix and capacitance between inner and outer layers make this chiral structure resonant. Focusing properties of a slab made of chiral materials are reported in [69]. Similar focusing phenomena have been also discussed in Section 2.4.3 for chiral cylinders briefly. Based on the original work by the scientists in Helsinki, chiral materials have been proved to be a good alternative to realize negative-index materials since backward waves could be supported [134, 137]. The negative refraction can be easily obtained by properly mixing chiral particles [138, 139] and arranging dipoles to minimize electric/magnetic responses [70]. Due to the wide application potentials of magnetoelectric coupling in negative refractive, lensing, and focusing devices, magnetoelectric composites, including but not limited to chiral materials, deserve further investigation, not only in theory but also in application.

4.2 Isotropic magnetoelectric composites

Since artificial composite NIMs in microwave region were experimentally verified by Shelby [14], more studies have been carried out such as tensor-parameter retrieval using quasi-static Lorentz theory [140], S-parameter retrieval using the plane wave incidence [32, 141], and constitutive relation retrieval using transmission line method [44]. However, the artificial metamaterials depend on the creation of metal inclusions of strong magnetic response. It is a big challenge especially in the optical region if one wants to realize negative refraction and superlens for optical applications.

Such problems could be alleviated by using isotropic magnetoelectric materials. The key advantage is that backward-wave regime can be, in principle, realized even if the medium has very weak or no magnetic properties. Thus, it appears that one could realize negative refraction in the optical region without the need to create artificial magnetic materials operational in optical frequencies.

Chiral composites as shown in Fig. 4.1, in which the magnetoelectric coupling is present in terms of the chirality and/or Tellegen parameters, are of particular interest.

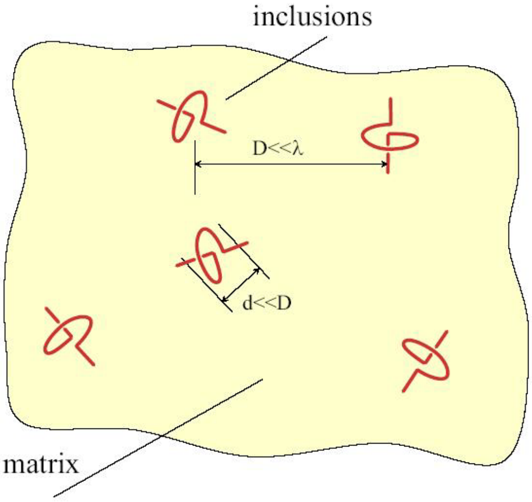

Figure 4.1: The typical configuration of a chiral medium composed of the same handed wire-loop inclusions distributed uniformly and randomly.

There are two definitions widely used to describe chiral media: i) the Post's relations given by

$$\boldsymbol{D} = \epsilon_P \boldsymbol{E} + i\xi_c \boldsymbol{B}, \tag{4.1a}$$

$$\boldsymbol{H} = i\xi_c \boldsymbol{E} + (1/\mu_P)\boldsymbol{B}; \tag{4.1b}$$

and the Tellegen's relations expressed as

$$\boldsymbol{D} = \epsilon_T \boldsymbol{E} + i\kappa\sqrt{\mu_0\epsilon_0}\boldsymbol{H}, \tag{4.2a}$$

$$\boldsymbol{B} = -i\kappa\sqrt{\mu_0\epsilon_0}\boldsymbol{E} + \mu_T \boldsymbol{H}, \tag{4.2b}$$

where ϵ_0/μ_0 is the permittivity/permeability in free space, the subscripts P/T denote permittivity and permeability under the Post/Tellegen constitutive relations, and κ/ξ_c is the chirality used in the Post/Tellegen constitutive relations,

These two constitutive relations were found to be applicable to chiral media composed of short wire helices as well as reciprocal chiral objects of arbitrary shape [142]. One can note that the chirality (i.e., κ or ξ_c) is the manifestation of the handedness of the chiral medium. The following summary can be made:

1. when chirality is positive, the polarization is right-handed and the medium is right-handed;
2. when chirality is negative, the right-handed system is reversed to the left-handed system;
3. when no chirality is present, neither magnetoelectric couplings nor optical activity exists.

Note that the source-free Maxwell equations have the following form:

$$\begin{aligned} \boldsymbol{\nabla} \times \boldsymbol{E} &= i\omega \boldsymbol{B}, \\ \boldsymbol{\nabla} \times \boldsymbol{H} &= -i\omega \boldsymbol{D}. \end{aligned} \tag{4.3}$$

Hence, from Eqs. (4.1)-(4.3), one can see that $\boldsymbol{D}/\boldsymbol{B}$ at a given point also depends on the value of derivatives of $\boldsymbol{E}/\boldsymbol{H}$ at that particular point, which can be characterized by non-locality. In order to force chiral materials to fall into the backward wave regime, one only needs to make either permittivity or permeability appropriate to produce resonances, which will form a very small value of the product of $\epsilon\mu$. On the other hand, the effect of the chirality should be another solution, where the big chirality also favors the realization of backward waves and negative refraction.

A chiral medium can be regarded, in a macroscopic view, as a continuous medium composed of chiral composites which are uniformly distributed and randomly placed. The optical activity and circular dichroism of chiral media have been studied, and the chirality of the medium's molecules can be seen as the cause of optical activity as deduced by Pasteur in 1848. Born [143] put forward the interpretation of optical activity for a particular molecular model, in which a coupled-oscillator model was used. In what follows, Condon [144] gave a single-oscillator model in a dissymmetric field for optically active material, based on the molecular theories of Drude, Lorentz and Livens. The following constitutive relations were suggested

$$\begin{aligned} \boldsymbol{D} &= \epsilon\boldsymbol{E} + \tfrac{i\omega\alpha}{c_0}\boldsymbol{H}, \\ \boldsymbol{B} &= -\tfrac{i\omega\alpha}{c_0}\boldsymbol{E} + \mu\boldsymbol{H} \end{aligned} \tag{4.4}$$

where c_0 is the light velocity in free space and α is the rotatory parameter. The parameter of α for rotatory power is frequency dependent [133]:

$$\alpha(\omega) \sim \sum_b \frac{R_{ba}}{\omega_{ba}^2 - \omega^2 + i\omega\Gamma_{ba}} \tag{4.5}$$

where a and b stand for quantum states, ω_{ba} is the frequency of the light absorbed in the jump $a \rightarrow b$, R_{ba} means the rotational strength of the absorbed line, and the damping term of Γ_{ba} has been included for the consideration of the absorption. Finally, by comparing the Tellegen's relations and the Condon's model, the dispersion of the dimensionless chirality κ can be expressed in such a way that

$$\kappa(\omega) = \frac{\omega\omega_c}{\omega_c^2 - \omega^2 + id_c\omega\omega_c} \tag{4.6}$$

where ω_c represents the characteristic frequency and d_c means the damping factor. Note that Eq. (4.6) is valid for the one-phase transition, in which only one rotatory term in Eq. (4.5) is considered due to the assumption that each transition between quantum states lies far off the others. Using the wavefield theory [134], a chiral medium can be characterized as two sets of equivalent dielectric parameters $\epsilon_{\pm}$ and $\mu_{\pm}$, given by

$$\begin{aligned} \epsilon_{\pm}(\omega) &= \epsilon(1 \pm \frac{\kappa(\omega)\sqrt{\mu_0\epsilon_0}}{\sqrt{\mu\epsilon}}), && (4.7a) \\ \mu_{\pm}(\omega) &= \mu(1 \pm \frac{\kappa(\omega)\sqrt{\mu_0\epsilon_0}}{\sqrt{\mu\epsilon}}). && (4.7b) \end{aligned}$$

The imaginary parts of $(\epsilon_{\pm},\ \mu_{\pm})$ are also studied but not included, which are almost zero over the whole region except in the vicinity of ω_c. From Fig. 4.2, one can find that the medium $(\epsilon_{+},\ \mu_{+})$ becomes a double negative (DNG) medium in the frequency band [10, 13.3] GHz. When the frequency drops below ω_c or exceeds it, it turns to a double positive (DPS) medium. In Fig. 4.3, such a DNG-DPS reversion also happens. In the frequency band of [7.52, 13.3]GHz, the negative refraction occurs to $+$ and $-$ effective mediums, alternatively.

Hence, the electromagnetic fields within the chiral medium can be obtained by

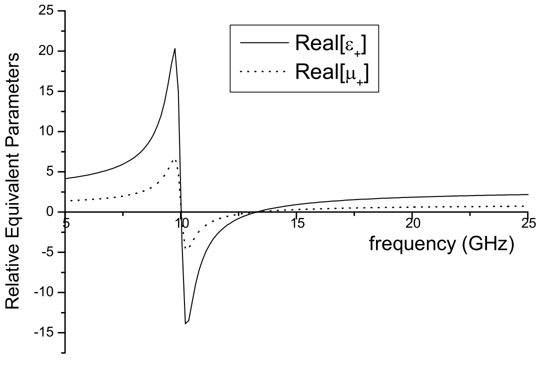

Figure 4.2: The frequency dependence of relative (ϵ_+, μ_+) in the range of [5, 25] GHz, the chirality's characteristic frequency $\omega_c = 2\pi \times 10^{10}$ (rad/s), $d_c = 0.05$, $\epsilon = 3\epsilon_0$, and $\mu = \mu_0$.

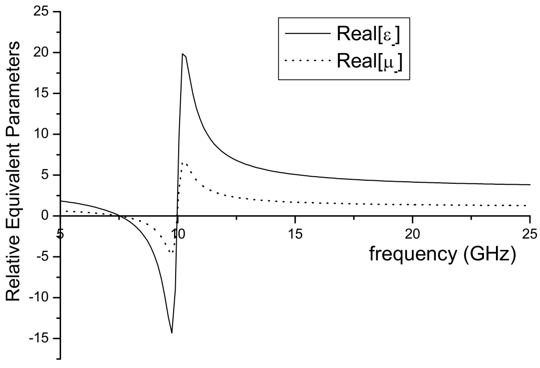

Figure 4.3: The same as Fig. 4.2, for the frequency dependence of relative (ϵ_-, μ_-).

the superposition of components as follows:

$$\begin{aligned} \boldsymbol{E} &= \boldsymbol{E}_+ + \boldsymbol{E}_-, \\ \boldsymbol{H} &= \boldsymbol{H}_+ + \boldsymbol{H}_-, \end{aligned} \tag{4.8}$$

where ± fields correspond to the results calculated from two separate sets of effective materials $(\epsilon_+,\ \mu_+)$ and $(\epsilon_-,\ \mu_-)$, respectively. Interestingly, if we consider the case of a plane wave impinged upon an air-chiral interface, two frequencies where no chirality is actually present are: i) if $f_l = 7.52$ GHz, the chiral medium is characterized only by the + equivalent medium composed of $(\epsilon_+,\ \mu_+)$, which results in that only half of the power can be transmitted from the air to the chiral medium; and ii) if $f_h = 13.3$ GHz, only the pair of $(\epsilon_-,\ \mu_-)$ remains. It can be observed that their geometrical mean is the characteristic frequency of chirality (i.e, $f_c = \omega_c/2\pi$), demonstrating the symmetric relation:

$$f_l f_h = f_c^2. \tag{4.9}$$

To summarize, the chirality dispersion in the Condon's model, based on the molecular theory of quantum mechanics, can lead to negative-index media (i.e, $n_\pm = Re[\sqrt{\epsilon_\pm}\sqrt{\mu_\pm}]$) at certain frequency bands. One, however, has to mind that $n_\pm$ cannot be simultaneously negative within the region of $(f_l,\ f_h)$. The plus and minus signs of refractive indices will be exchanged when the working frequency oversteps the resonant frequency f_c.

In view of Eqs. (4.1) and (4.2), both constitutive relations are applicable to reciprocal media only. When the nonreciprocity is present in the chiral magnetoelectric materials, the constitutive relations are expressed for the Post's relations

$$\begin{aligned} \boldsymbol{D} &= \epsilon_P \boldsymbol{E} + (i\xi - \nu)\boldsymbol{B}, \\ \boldsymbol{H} &= (i\xi + \nu)\boldsymbol{E} + (1/\mu_P)\boldsymbol{B}; \end{aligned} \tag{4.10}$$

and for the Tellegen's relations

$$\begin{aligned} \boldsymbol{D} &= \epsilon_T \boldsymbol{E} + (\chi + i\kappa)\sqrt{\mu_0\epsilon_0}\boldsymbol{H}, \\ \boldsymbol{B} &= (\chi - i\kappa)\sqrt{\mu_0\epsilon_0}\boldsymbol{E} + \mu_T \boldsymbol{H}, \end{aligned} \tag{4.11}$$

where χ and ν denote the nonreciprocity parameters used in these two commonly used constitutive relations. The conversion between these two relations for time harmonic fields is given by

$$\begin{aligned} \epsilon_T &= \epsilon_P + \mu_P(\xi^2 + \nu^2), \\ \chi &= \mu_P \nu c_0, \\ \kappa &= \mu_P \xi c_0, \\ \mu_T &= \mu_P. \end{aligned} \tag{4.12}$$

In particular, I only consider the Tellegen's relations for the nonreciprocal example, since such a condition can be transformed to the Post's relations in isotropic cases. The dispersion of nonreciprocity has not been clearly worked out independently so far. From general considerations, it can be envisioned that the dispersion relations of χ and κ in Eq. (4.11) would be in a similar alteration of the Condon model:

$$\chi(\omega) = \frac{d_c \omega^2 \omega_c^2}{\omega^4 + \omega_c^4 - (2 - d_c^2)\omega^2\omega_c^2}, \tag{4.13a}$$

$$\kappa(\omega) = \frac{(\omega_c^2 - \omega^2)\omega\omega_c}{\omega^4 + \omega_c^4 - (2 - d_c^2)\omega^2\omega_c^2}. \tag{4.13b}$$

The refractive indices can be expressed by reading from the corresponding eigenwave

$$n_\pm = \sqrt{\epsilon\mu/\epsilon_0\mu_0 - \chi^2} \pm \kappa. \tag{4.14}$$

The frequency dependence and the role of damping are shown in Fig. 4.4, noting that the indices for the '-' effective medium carry a similar fashion by mirroring the curves of the '+' medium along the vertical line at $f = 10$ GHz. When the

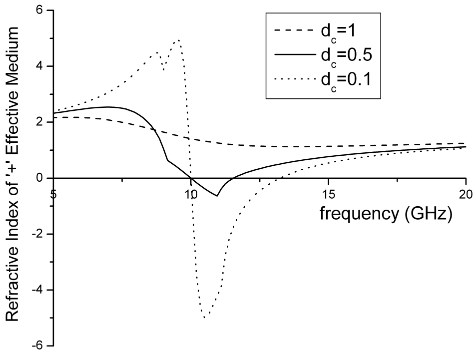

Figure 4.4: The frequency dependence of refractive indices for '+' effective medium in the range of [5, 20] GHz, with the same parameters as in Fig. 4.2 except for d_c.

damping factor $d_c = 1$, the refractive index varies limitedly against the frequency even at the characteristic frequency of ω_c, and it can be proved that high damping of the chiral material will hold back the rotatory power and the curve appears more flat (approaching to $\sqrt{3}$ over all frequencies), which means that the chirality does not resonate for chiral media of high damping. When the damping factor becomes smaller, more power is rotated and the resonant phenomenon becomes fairly clear. The resonance will further induce negative refraction of eigenmodes within certain frequency bands. Those negative-index bands are inversely proportional to the damping factor. However, such single-oscillator model for nonreciprocal chiral materials is only for lossless χ and κ. If one wants to study, an improved oscillator model should be proposed to characterize the nonreciprocity parameter so that both χ and κ are complex-valued.

4.3 Gyrotropic magnetoelectric composites

Generally, bianisotropic media can be considered as the most general linear magnetoelectric media. However, in a practical case, parameters in those four dyadics characterizing bianisotropic effects can be retrieved only for particularly structured composites. In this section, instead of conceptual bianisotropic materials whose parameters are manually set, those gyrotropic magnetoelectric composites which can be practically manufactured are of greater interest. Moreover, the gyrotropic magnetoelectric composites are found to be a better candidate than normal bi-isotropic composites for the following merits: 1) negative index of refraction in a gyrotropic magnetoelectric medium can be realized with less restrictions, while chiral material requires small permittivity at a working frequency so as to obtain negative refractive index; 2) two backward eigenwaves are found due to the effects of the gyro-electric and gyro-magnetic parameters; and 3) all parameters in permittivity and permeability tensors as well as chirality admittance can be positive when negative refraction occurs.

4.3.1 Backward waves in different medium formalisms

The optical rotation exhibited by chiral composites in Section 4.2 is called natural optical activity, and there is another similar phenomenon of rotation with a different mechanism which is called Faraday rotation induced by external biased fields. The former is independent of the propagation direction and invariant under time reversal, while the latter is dependent of propagation and invariant under spatial inversion. A biased magnetic field leads to the gyrotropy in permeability and crossed external electric and magnetic fields perpendicular to the direction of propagation create gyrotropy in both permittivity and permeability [145].

Different approaches are developed in studying the eigenmodes in different medium formalisms, and those two relations are compared. It is found that backward-wave propagation and negative refractive indices arise in gyrotropic magnetoelectric material far from the resonance because the gyrotropic parameters can decrease the refractive index of the eigenmodes.

In this part, I first discuss the difference between the Post's formalism given by

$$\boldsymbol{D} = \overline{\boldsymbol{\epsilon}}_P \cdot \boldsymbol{E} + i\xi_c \boldsymbol{B} \tag{4.15a}$$

$$\boldsymbol{H} = i\xi_c \boldsymbol{E} + \overline{\boldsymbol{\mu}}_P^{-1} \cdot \boldsymbol{B}; \tag{4.15b}$$

and the Tellegen's formalism given by

$$\boldsymbol{D} = \overline{\boldsymbol{\epsilon}}_T \cdot \boldsymbol{E} + (\chi - i\kappa) \boldsymbol{H} \tag{4.16a}$$

$$\boldsymbol{B} = (\chi + i\kappa) \boldsymbol{E} + \overline{\boldsymbol{\mu}}_T \cdot \boldsymbol{H}. \tag{4.16b}$$

In these two formalisms, $\overline{\boldsymbol{\epsilon}}$ and $\overline{\boldsymbol{\mu}}$ are tensorial permittivity and permeability, respectively; κ and ξ_c denote chirality in corresponding relations; χ is defined as nonreciprocity parameter. The permittivity and permeability tensors are

$$\overline{\boldsymbol{\epsilon}} = \begin{bmatrix} \epsilon & -ig & 0 \\ ig & \epsilon & 0 \\ 0 & 0 & \epsilon_z \end{bmatrix} \tag{4.17a}$$

$$\overline{\boldsymbol{\mu}} = \begin{bmatrix} \mu & -il & 0 \\ il & \mu & 0 \\ 0 & 0 & \mu_z \end{bmatrix} \tag{4.17b}$$

where g and l are the electric and magnetic gyrotropic parameters, respectively. This kind of material includes chiroplasma consisting of chiral objects embedded in a magnetically biased plasma, or chiroferrites made of chiral objects immersed into a magnetically biased ferrite. Note that the elements in Eq. (4.17) may not be necessarily identical in the Post's and Tellegen's formalisms. In what follows, the material parameters refer to the value under respective formalisms. The subscripts of P are T are suppressed for simplicity.

Post formalism

Substituting Eq. (4.15) into Maxwell equations, one finally has

$$\boldsymbol{\nabla} \times \Big[\overline{\boldsymbol{\alpha}}_P \cdot \boldsymbol{\nabla} \times \boldsymbol{E}\Big] - 2\omega\xi_c \boldsymbol{\nabla} \times \boldsymbol{E} - \omega^2 \overline{\boldsymbol{\epsilon}}_P \cdot \boldsymbol{E} = i\omega \boldsymbol{J} \tag{4.18}$$

where $\boldsymbol{J}$ is the current excitation,

$$\overline{\boldsymbol{\alpha}}_P = \overline{\boldsymbol{\mu}}_P^{-1} = \begin{bmatrix} \alpha_t & i\sigma & 0 \\ -i\sigma & \alpha_t & 0 \\ 0 & 0 & \alpha_z \end{bmatrix} \tag{4.19}$$

and

$$\alpha_t = \frac{\mu}{\mu^2 - l^2} \tag{4.20a}$$

$$\sigma = \frac{l}{\mu^2 - l^2} \tag{4.20b}$$

$$\alpha_z = \frac{1}{\mu_z}. \tag{4.20c}$$

Assuming waves of the form $\boldsymbol{E}_0 e^{i\boldsymbol{k}\cdot\boldsymbol{r}}$ (where $\boldsymbol{k}$ is the wave vector), plane wave propagation in gyrotropic magnetoelectric composites can be examined by setting $\boldsymbol{J}$ zero. Under these conditions, the electric field satisfies

$$\overline{\boldsymbol{\Phi}} \cdot \boldsymbol{E} = 0 \tag{4.21}$$

with $[\Phi]$ defined as

$$[\Phi] = \begin{bmatrix} \Phi_1 & \Phi_2 & \Phi_3 \end{bmatrix} \tag{4.22}$$

where

$$[\Phi_1] = \begin{bmatrix} \omega^2\epsilon - \alpha_z k_y^2 - \alpha_t k_z^2 \\ i\omega^2 g + \alpha_z k_x k_y + i\sigma k_z^2 + 2i\xi_c\omega k_z \\ \alpha_t k_x k_z - 2i\xi_c\omega k_y + i\alpha_z k_y k_z \end{bmatrix} \tag{4.23a}$$

$$[\Phi_2] = \begin{bmatrix} -i\omega^2 g + \alpha_z k_x k_y - i\sigma k_z^2 - 2i\xi_c\omega k_z \\ \omega^2\epsilon - \alpha_z k_x^2 - \alpha_t k_z^2 \\ \alpha_t k_y k_z + 2i\xi_c\omega k_x - i\alpha_z k_x k_z \end{bmatrix} \tag{4.23b}$$

$$[\Phi_3] = \begin{bmatrix} \alpha_t k_x k_z + i\sigma k_y k_z + 2i\xi_c \omega k_y \\ \alpha_t k_y k_z - i\sigma k_x k_z - 2i\xi_c \omega k_x \\ \omega^2 \epsilon_z - \alpha_t k_x^2 - \alpha_t k_y^2 \end{bmatrix}. \tag{4.23c}$$

Eq. (4.21) only has nontrivial solutions if the determinant of $[\Phi]$ is zero. Note that the obtained polynomial expression for k is tedious to solve. However, a certain case can still be considered, which gives much insight into the physical properties of the magnetoelectric composites. Considering that the waves are propagating along z-direction, one can solve $\det\overline{\boldsymbol{\Phi}} = 0$ and obtain the wavenumbers supported by the medium. By reducing Eq. (4.22), one finally obtains:

$$k_{p\pm} = \omega \frac{\pm\xi_c + \sqrt{\xi_c^2 + (\alpha_t \mp \sigma)(\epsilon \pm g)}}{\alpha_t \mp \sigma} \tag{4.24a}$$

$$k_{a\pm} = \omega \frac{\mp\xi_c - \sqrt{\xi_c^2 + (\alpha_t \pm \sigma)(\epsilon \mp g)}}{\alpha_t \pm \sigma} \tag{4.24b}$$

where p and a represent the parallel and anti-parallel directions of energy flow (i.e., real part of the Poynting's vector) and the ± signs refer to as the right-circular polarization (RCP) and left-circular polarization (LCP), respectively. Note that the k_{p-} and k_{a-} could represent the wavenumbers for backward eigenwaves under some situations as shown in Table 4.1, which will be discussed later. The helicity and polarized state of each wavenumber can be obtained by inserting Eq. (4.24) into Eq. (4.21). It can be found that the helicity of k_{p+} and k_{a-} is positive while the helicity of k_{p-} and k_{a+} is negative, provided that negative helicity is defined as left-handedness to positive z-direction and right-handedness to negative z-direction. The refraction indices of k_{p-} and k_{a-} are obtained:

$$n_{R1} = \frac{c_0}{(\alpha_t + \sigma)} [\sqrt{\xi^2 + (\alpha_t + \sigma)(\epsilon - g)} - \xi_c] \tag{4.25a}$$

$$n_{R2} = \frac{c_0}{(\alpha_t - \sigma)}[\sqrt{\xi^2 + (\alpha_t - \sigma)(\epsilon + g)} - \xi_c] \tag{4.25b}$$

where c_0 is the light's velocity in vacuum; subscript of R denotes RCP; and the subscripts of 1 and 2 correspond to k_{p-} and k_{a-}, respectively. The chirality under the Post's relations will appear twice in the final expressions of refractive indices. By amplifying the gyrotropic parameter or increasing the chirality, negative refraction can be achieved.

Tellegen formalism

In this part, Tellegen formalism for gyrotropic magnetoelectric composites will be discussed so as to realize NIM. The relations can be referred to Eq. (4.16). The same assumption as in Post's relations is made, that is, the wave is propagating along z-direction. Hence D_z and B_z vanish due to the fact that $\boldsymbol{E}$ and $\boldsymbol{H}$ only have transverse component and the form of the tensorial $\overline{\boldsymbol{\epsilon}}_T$ and $\overline{\boldsymbol{\mu}}_T$ is gyrotropic. Thus one can have the following relations:

$$\begin{bmatrix} D_x \\ \\ D_y \end{bmatrix} = \begin{bmatrix} \epsilon E_x - igE_y + (\chi - i\kappa)H_x \\ \\ \epsilon E_y + igE_x + (\chi - i\kappa)H_y \end{bmatrix} \tag{4.26a}$$

$$\begin{bmatrix} B_x \\ \\ B_y \end{bmatrix} = \begin{bmatrix} \mu H_x - ilH_y + (\chi + i\kappa)E_x \\ \\ \mu H_y + ilH_x + (\chi + i\kappa)E_y \end{bmatrix}. \tag{4.26b}$$

Considering $\boldsymbol{\nabla}$ operator can be replaced by $i\boldsymbol{k}$ for plane waves, the Maxwell equations can be rewritten

$$\boldsymbol{k} \times \boldsymbol{E} = \omega \boldsymbol{B} \tag{4.27a}$$

$$\boldsymbol{k} \times \boldsymbol{H} = -\omega \boldsymbol{D} \tag{4.27b}$$

where $\boldsymbol{k} = \{0, 0, k\}$ is assumed as aforementioned.

By substituting Eq. (4.26) into (4.27), one can express the electric fields in terms of magnetic fields:

$$\begin{bmatrix} E_x \\ E_y \end{bmatrix} = \begin{bmatrix} A & -B \\ B & A \end{bmatrix} \begin{bmatrix} H_x \\ H_y \end{bmatrix} \tag{4.28}$$

where

$$A = \frac{1}{k^2 + \omega^2(\chi + i\kappa)^2}[i\omega l k - \omega^2 \mu(\chi + i\kappa)] \tag{4.29a}$$

$$B = \frac{-1}{k^2 + \omega^2(\chi + i\kappa)^2}[\omega \mu k + i\omega^2 l(\chi + i\kappa)]. \tag{4.29b}$$

After careful algebraic formulations in Eqs. (4.26)-(4.28), one finally obtains

$$\Big(\frac{k}{\omega} + \epsilon B + igA\Big)^2 + \Big[(\epsilon A - igB) + (\chi - i\kappa)\Big]^2 = 0. \tag{4.30}$$

Thus two sets of expressions can be obtained as follows

$$\frac{k}{\omega} + (\epsilon \pm g)(B \pm iA) = \mp i(\chi - i\kappa). \tag{4.31}$$

From Eq. (4.29), the following relations used in Eq. (4.31) can be yielded as

$$B \pm iA = -\frac{\omega(\mu \pm l)}{k \mp i\omega(\chi + i\kappa)}. \tag{4.32}$$

Substituting Eq. (4.32) in turn into Eq. (4.31), four roots of k are obtained:

$$k_{p\pm} = \omega[\mp\sqrt{(\epsilon + g)(\mu + l) - \chi^2} - \kappa] \tag{4.33a}$$

$$k_{a\pm} = \omega[\pm\sqrt{(\epsilon - g)(\mu - l) - \chi^2} + \kappa]. \tag{4.33b}$$

By taking Eq. (4.33) and their polarization states into account, the refractive indices of the backward waves (i.e., RCP k_{p-} and RCP k_{a-}) inside the gyrotropic chiral medium can be determined

$$n_{R1} = c_0\left[\sqrt{(\epsilon + g)(\mu + l) - \chi^2} - \kappa\right] \tag{4.34a}$$

$$n_{R2} = c_0\left[\sqrt{(\epsilon - g)(\mu - l) - \chi^2} - \kappa\right] \tag{4.34b}$$

where subscripts are similarly defined as in Eq. (4.25). Since the chirality is generally small in natural and composite chiral media, one can reduce the product of $\epsilon\mu$ in order to achieve NIM. But the difficulty of doing so also increases. Thus the theorem proposed here will be a good alternative way to achieve NIM by increasing the gyrotropic parameters. By the optical parameter amplification technique [146] and the arrangement of angular momentum of the light beams and electronic spins, the gyrotropic parameters can be lifted to the same order as those diagonal elements in tensors. Hence the conditions of $\epsilon - g \approx 0$ and $\epsilon - g < 0$ are believed to be realizable.

Comparison

- *Gyrotropic versus isotropic cases:*

In gyrotropic magnetoelectric materials, negative refraction and backward-wave propagation can arise without forcing the permittivity and permeability to be extremely small at working frequencies, which means that NIM properties can be achieved off the resonances. Second, those gyrotropic parameters play an important role in making refraction index negative and achieving backward waves. Instead of controlling chirality in normal chiral media, gyrotropic parameters show more flexibilities to be controlled by amplification techniques [146]. Third, I have found that, if $\epsilon_T = \mu_T = 0$ in the Tellegen's relation, two parameters (ϵ_B and μ_B) in the Born's relations [79] must be zero by transformation, which will further lead to the chirality $\kappa_T = 0$ in Tellegen's relation. Hence, in the Tellegen's relation, $\epsilon_T = \mu_T = 0$ actually indicates $\epsilon_T = \mu_T = \kappa_T = 0$ unless $\beta \to \infty$, which has no nontrivial solutions to the Maxwell's equations. This problem can be removed by introducing gyrotropic effects since the gyrotropy parameters can make refractive index negative without requiring chiral nihility. Hence gyrotropic magnetoelectric materials provide an exciting opportunity to realize NIM.

- *Post versus Tellgen formalisms:*

Two different constitutive relations of the gyrotropic cases have been considered (i.e., the Post's and Tellegen's relations). As one can see in Eq. (4.25), under the Post's relations, $\alpha_t \pm \sigma < 0$ will not make the wave propagate backwardly. The only possible way of obtaining NIM is to amplify gyrotropic parameters g and l simultaneously to achieve $(\alpha_t \mp \sigma)(\epsilon \pm g) > 0$ while $\alpha_t \mp \sigma < 0$. However, for the Tellegen's relations, the representations of the refractive indices are explicit. By amplifying any of the parameters g, l, χ and κ, refractive indices can be negative. Mathematically, it can be seen that in the description of the Tellegen's relations for gyrotropic cases, it is not necessary to require gyrotropic parameters to be big in order to get negative refractive indices. Even if $\epsilon - g$ and $\mu - l$ are positive, the amplification of g and l can still lead to negative refraction indices. However, most of the known ferrite or plasma devices adopts Post's formalism [147, 148], hence the Post formalism will be more suitable to describe the gyrotropic magnetoelectric composites in practical applications, though the physical properties do not depend on the description formalism.

4.3.2 Waves in gyrotropic chiral materials

To make it easier to compare with normal chiral materials, the gyrotropic magnetoelectric composites are termed as gyrotropic chiral materials. In this part, the Post formalism is adopted.

Chiroplasma

The constitutive relations of chiroplasma are shown:

$$\begin{aligned}\boldsymbol{D} &= \epsilon_0\epsilon_r\begin{bmatrix}\epsilon & -ig & 0\\ ig & \epsilon & 0\\ 0 & 0 & \epsilon_z\end{bmatrix}\cdot\boldsymbol{E}+i\xi_c\boldsymbol{B},\\ \boldsymbol{H} &= i\xi_c\boldsymbol{E}+\frac{1}{\mu_0\mu_r}\boldsymbol{B}\end{aligned}\tag{4.35}$$

where

$$\epsilon = \Big(1-\frac{\omega_p^2(\omega+i\omega_{eff})}{\omega[(\omega+i\omega_{eff})^2-\omega_g^2]}\Big)\tag{4.36a}$$

$$g = \frac{\omega_p^2\omega_g}{\omega[(\omega+i\omega_{eff})^2-\omega_g^2]},\tag{4.36b}$$

$$\epsilon_z = 1-\frac{\omega_p^2}{\omega^2},\tag{4.36c}$$

where ω_{eff}, ω_g, and ω_p represent collision frequency, electron gyrofrequency and plasma frequency [148], respectively. Such gyroelectric chiral media can be managed by distributing chiral objects into a controllable biasing magnetic field, which is applied externally. If the plane wave $\boldsymbol{E}e^{-i(\omega t-\boldsymbol{k}\cdot\boldsymbol{r})}$ is propagating inside gyroelectric chiral media, the wave equations can be expressed as:

$$\boldsymbol{k}\times(\boldsymbol{k}\times\boldsymbol{E})+2i\omega\mu_r\mu_0\xi_c\boldsymbol{k}\times\boldsymbol{E}+k_0^2\mu_r\epsilon_r\begin{bmatrix}\epsilon & -ig & 0\\ ig & \epsilon & 0\\ 0 & 0 & \epsilon_z\end{bmatrix}\cdot\boldsymbol{E}=0, \tag{4.37}$$

where k_0 represents the wavenumber in free space. Algebraically, wave numbers corresponding to parallel and antiparallel eigenmodes for two mutually perpendicular polarizations can be obtained from nontrivial solutions in terms of a quartic polynomial, which would be cumbersome to solve. Thereafter, to yield some physical insight, longitudinal waves with respect to the external biasing field are considered with the interest in backward waves and negative phase velocity. For the longitudinally propagating eigenwaves along the biasing plasma, one can yield the following four wave numbers corresponding to the eigenmodes

$$k_{\frac{1}{2}} = \omega[\mp\mu_0\mu_r\xi_c \pm \sqrt{\mu_0^2\mu_r^2\xi_c^2+\mu_0\mu_r\epsilon_0\epsilon_r(\epsilon\mp g)}], \tag{4.38}$$

$$k_{\frac{3}{4}} = \omega[\pm\mu_0\mu_r\xi_c \pm \sqrt{\mu_0^2\mu_r^2\xi_c^2+\mu_0\mu_r\epsilon_0\epsilon_r(\epsilon\pm g)}]. \tag{4.39}$$

With the reference to the energy transportation direction, eigenwaves corresponding to eigen wavenumbers k_1 and k_2 may become backward waves because the handedness of these two eigenwaves will change within certain frequency bands. Note that the propagation direction of k_1 eigenwave is parallel to the energy transportation direction while k_2 eigenwave is opposite, and in backward-wave frequency bands both eigenwaves are right-handed circularly polarized [149]. In particular, the phase velocity against frequency is studied in order to observe characteristics of LHM. In

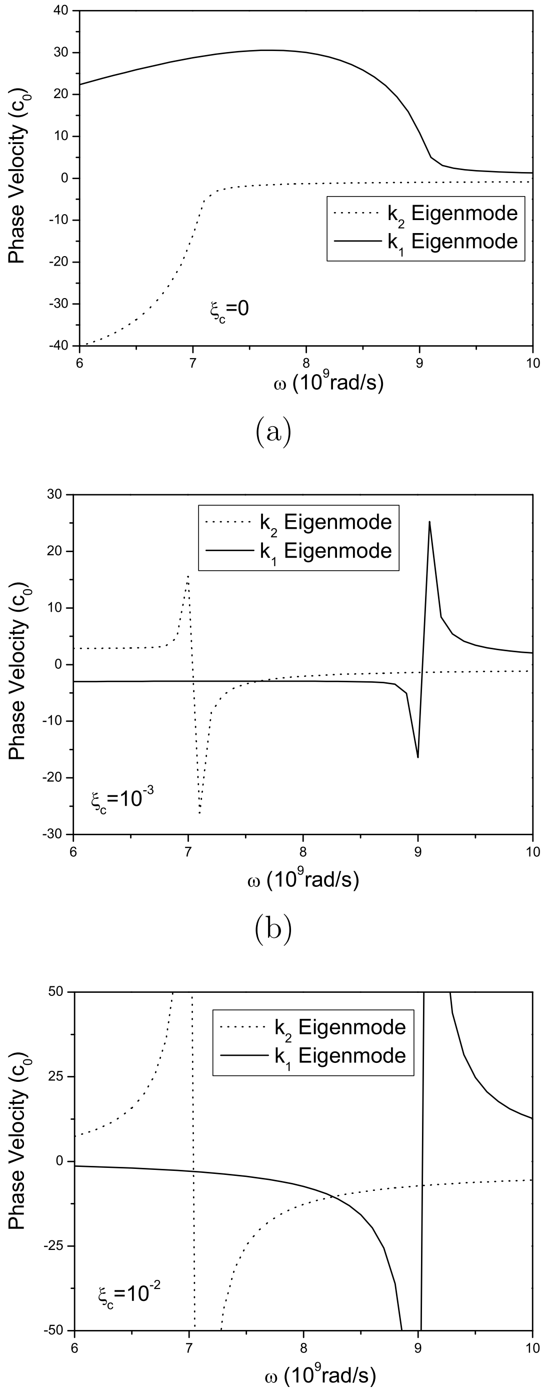

(a)

(b)

(c)

Figure 4.5: Phase velocities for backward-wave eigenmodes as a function of frequency near the plasma frequency, with parameters $\omega_p = 8 \times 10^9$ rad/s, $\omega_{eff} = 0.1 \times 10^9$ rad/s, and $\omega_g = 2 \times 10^9$ rad/s under different degrees of magnetoelectric couplings: (a) decoupling plasma $\xi_c = 0$; (b) ξ_c=0.001; and (c) $\xi_c = 0.01$.

Fig. 4.5(a), it can be observed that when no magnetoelectric coupling is present, the phase velocity of k_2 eigenmode is always negative and that of k_1 eigenmode is positive. Substituting these two eigenmodes into Eq. (4.37), one can note that negative phase velocity in Fig. 4.5(a) does not mean a backward-wave phenomenon. Instead, when $\xi_c = 0$, negative phase velocity means that k_2 eigenmode is left-handed with reference to the opposite direction of external magnetic field, and positive velocity shows that k_1 eigenmode is left-handed along with the direction of the external field. When slight magnetoelectric coupling exists (e.g., $\xi_c = 10^{-3}$ in Fig. 4.5(b)), backward-wave phenomena arise for both k_1 and k_2 eigenmodes, in which resonances can be observed. In what follows, a gyroelectric chiral medium is considered with bigger magnetoelectric coupling effect, as shown in Fig. 4.5(c). Compared with the case shown in Fig. 4.5(b), one can note that the shift of resonant frequencies is neglectable, while resonant amplitudes in Fig. 4.5(c) are drastically enhanced. In both weak-coupling and strong-coupling cases, it can be found that backward-wave regions arise before respective resonances. After passing the resonant frequency, the handedness and polarization status of those eigenmodes become an analogy to the non-magnetoelectric case.

Generalized Gyrotropy

It can be either regarded as a generalization of the gyrotropic (chiral) media without the assumption of $\boldsymbol{H} : \boldsymbol{H} = \boldsymbol{B}$ [150], or an advanced mixture of chiroplasma and chiroferrite due to the crossed biased fields. In the textbook [151], the assumption of $\boldsymbol{H} : \boldsymbol{H} = \boldsymbol{B}$ is addressed as "the effects due to the difference of μ from unity are in general indistinguishable from those of the spatial dispersion of the permittivity". However, it is not necessary to impose such assumption and the spatial dispersion in permeability is also meaningful especially in realization of negative-index materials.

- *Wave impedance:*

One parallel LCP (*i.e.*, k_{p-}) and one anti-parallel LCP (*i.e.*, k_{a-}) can be backward propagating with opposite directions of phase and energy velocities. The directions of the energy velocities are identical with those of the Poynting's vectors which can be verified from the Maxwell equations:

$$\boldsymbol{S}_{p+} = \hat{\boldsymbol{z}}\frac{|\boldsymbol{E}_0|^2}{2\eta_1} \tag{4.40a}$$

$$\boldsymbol{S}_{a-} = -\hat{\boldsymbol{z}}\frac{|\boldsymbol{E}_0|^2}{2\eta_1} \tag{4.40b}$$

$$\boldsymbol{S}_{p-} = \hat{\boldsymbol{z}}\frac{|\boldsymbol{E}_0|^2}{2\eta_2} \tag{4.40c}$$

$$\boldsymbol{S}_{a+} = -\hat{\boldsymbol{z}}\frac{|\boldsymbol{E}_0|^2}{2\eta_2} \tag{4.40d}$$

where η_1 and η_2 denote the wave impedances of the positive and negative helicities, respectively.

In view of the above equations, the z-axis component of the Poynting vector can be shown as

$$S_z = \frac{1}{2}\Big[E_x H_y^* - E_y H_x^*\Big] \tag{4.41}$$

where the transverse magnetic fields can be obtained from Eq. (4.28)

$$\begin{bmatrix} H_x \\ \\ H_y \end{bmatrix} = \begin{bmatrix} i\Big(\xi_c + \frac{k_z}{\omega}\sigma\Big)E_x - \frac{k_z}{\omega}\alpha_t E_y \\ \\ i\Big(\xi_c + \frac{k_z}{\omega}\sigma\Big)E_y + \frac{k_z}{\omega}\alpha_t E_x \end{bmatrix}. \tag{4.42}$$

Before solving η_1 and η_2, one condition should be noted

$$\left(2\xi_c + \frac{\omega}{k_z}g + \frac{k_z}{\omega}\sigma\right)^2 = \left(\frac{\omega}{k_z}\epsilon - \frac{k_z}{\omega}\alpha_t\right)^2 . \tag{4.43}$$

Substituting Eq. (4.42) into Eq. (4.41) with the aid of solution in Eq. (4.43), it is finally obtained

$$\eta_1 = \frac{1}{\sqrt{\xi_c^2 + (\alpha_t - \sigma)(\epsilon + g)}} = \frac{1}{\sqrt{\xi_c^2 + \dfrac{\epsilon + g}{\mu + l}}} \tag{4.44a}$$

$$\eta_2 = \frac{1}{\sqrt{\xi_c^2 + (\alpha_t + \sigma)(\epsilon - g)}} = \frac{1}{\sqrt{\xi_c^2 + \dfrac{\epsilon - g}{\mu - l}}}. \tag{4.44b}$$

Alternatively, by applying the Beltrami fields [152], $\epsilon_\pm$ and $\mu_\pm$ of the eigenmodes can be also obtained as belows

$$\epsilon_\pm = \sqrt{\xi_c^2 + \frac{\epsilon \pm g}{\mu \pm l}}\left[\pm\xi_c(\mu \pm l) + \sqrt{[\xi_c(\mu \pm l)]^2 + (\epsilon \pm g)(\mu \pm l)}\right] \tag{4.45a}$$

$$\mu_\pm = \sqrt{\frac{\mu \pm l}{\xi_c^2(\mu \pm l) + \epsilon \pm g}}\left[\pm\xi_c(\mu \pm l) + \sqrt{[\xi_c(\mu \pm l)]^2 + (\epsilon \pm g)(\mu \pm l)}\right]. \tag{4.45b}$$

Thus, the wave impedances of those eigenmodes can be verified by using $\eta_\pm = \sqrt{\mu_\pm/\epsilon_\pm}$, which agree with η_1 and η_2 respectively.

These findings are of importance for phase compensation and compact resonators [80], since a good impedance matching can be achieved at the interface between a gyrotropic chiral slab and the adjacent spaces. Note that the elements in permittivity and permeability tensors involve frequency, plasma frequency, electron gyrofrequency, gyromagnetic response frequency and saturation magnetization frequency [147, 148] and the realization of backward wave depends on the frequency selection. Within certain frequency ranges, k_{p-} and k_{a-} could be wavenumbers of backward wave simultaneously or only one of them could. Configurations of conventional and subwavelength cavity resonators are proposed using gyrotropic chiral slabs, when the working frequency is properly chosen to arrive at negative refractive index.

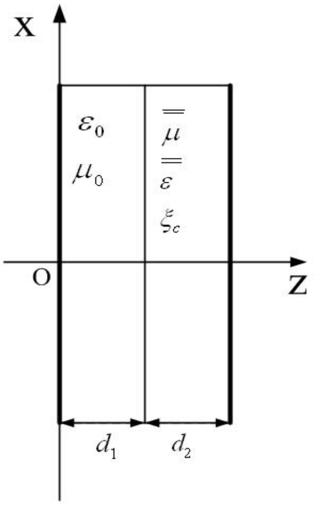

Figure 4.6: Compact resonator formed by a 2-layer structure consisting of air and gyrotropic chiral media backed by two ideally conducting planes.

In Fig. 4.6, it can be seen that, if a plane wave propagates in the direction penpendicular to the interfaces at a certain frequency range, its phase, which is increased in a conventional medium can be decreased in the gyrotropic chiral medium, which falls into the backward-wave region. It is noted that, the backward eigenmodes possess two impedances. Hence, by properly controlling the parameters and the external biased fields, $\eta_+ = \eta_0$ or $\eta_- = \eta_0$ could be chosen to match the wave impedance η_0 of free space, which means that two kinds of cavity resonators can be created as shown in Fig. 4.7.

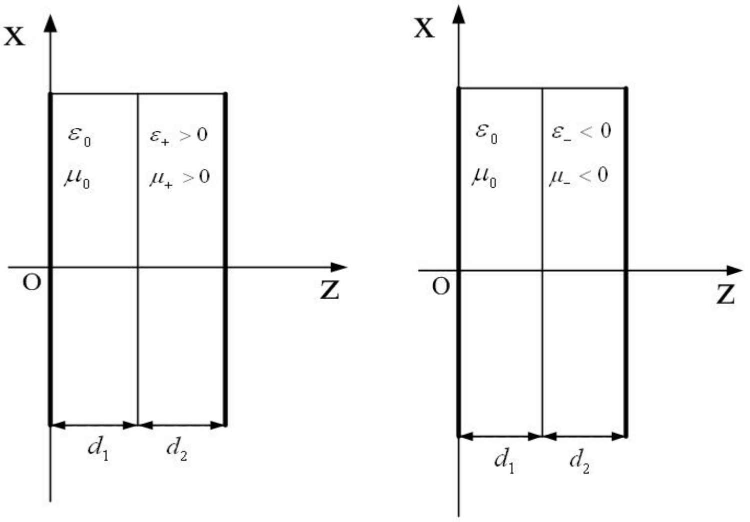

(a) Conventional (b) Subwavelength

Figure 4.7: Equivalent configuration of 1-D cavity resonator made of gyrotropic chiral materials.

The resonance condition for a cavity takes the following form [80]

$$\frac{n_2}{\mu_2}\tan(n_1 k_0 d_1) + \frac{n_1}{\mu_1}\tan(n_2 k_0 d_2) = 0, \tag{4.46}$$

where the subscripts, 1 and 2, correspond to the layers on the left-hand and right-hand sides, respectively. In the case shown in Fig. 4.7(a) when η_+ is matched, it turns to be the conventional cavity resonator, and thus Eq. (4.46) becomes

$$n_+ d_2 + d_1 = \frac{m}{2}\lambda_0, \quad \text{m=0, 1, 2...} \tag{4.47}$$

where λ_0 is the wavelength in free space.

Of particular and practical interest is the case of subwavelength cavity resonators, in which the arguments in the tangential functions can be assumed small. If η_- is matched as shown in Fig. 4.7(b), the resonant condition in Eq. (4.46) is

Table 4.1: Helicity and polarization states of k_{p-} and k_{a-} in three cases, under the conditions of $|l| < \mu$ and $\xi_c > 0$.

	$g < -\epsilon$		$-\epsilon < g < \epsilon$		$g > \epsilon$	
	HEL	POL	HEL	POL	HEL	POL
k_{p-}	$\ominus$	LCP	$\ominus$	LCP	$^*\ominus$	*RCP
k_{a-}	$^*\oplus$	*RCP	$\oplus$	LCP	$\oplus$	LCP
ω	$(0,\, \omega_{c1})$		—		$(\omega_g,\, \omega_{c2})$	

$*$Backward wave regions.

reduced to

$$\frac{d_1}{d_2} \cong \frac{\mid \mu_- \mid}{\mid \mu_0 \mid}. \tag{4.48}$$

It can be observed that to have simultaneously negative permittivity and permeability is not necessary to satisfy above condition, since only the first term in the Taylor expansion of a tangent function is kept for the thin layer on metal surfaces. The definition of $n_\pm$ will be given in the following part.

- *Negative refraction:*

The k_{p-} and k_{a-} are also of particular interest since they will represent the properties of the backward waves under specific cases as shown in Table 4.1. The quantities ϵ and g are given in [148] as follows

$$\epsilon = \epsilon_0\Big(1 - \frac{\omega_p^2(\omega + i\omega_{eff})}{\omega[(\omega + i\omega_{eff})^2 - \omega_g^2]}\Big) \tag{4.49a}$$

$$g = \epsilon_0 \frac{\omega_p^2 \omega_g}{\omega[(\omega + i\omega_{eff})^2 - \omega_g^2]}, \tag{4.49b}$$

where ω_p, ω_g and ω_{eff} are plasma frequency, electron's gyrofrequency and the collision frequency of the electrons, respectively.

It should be also noted that the positive/negative helicity is defined as right-/left- handedness to positive/negative z-axis. The helicity and polarized states can be found by inserting Eq. (4.24) into Eq. (4.18). When k_{p-} or k_{a-} becomes backward waves, the handedness changes.

A collisionless case is considered here (i.e., $\omega_{eff} = 0$). Two quantities are introduced first

$$\begin{aligned} \omega_{c1} &= \frac{1}{2}\Big[-\omega_g + \sqrt{\omega_g^2 + 4\omega_p^2} \Big] && (4.50a) \\ \omega_{c2} &= \frac{1}{2}\Big[\omega_g + \sqrt{\omega_g^2 + 4\omega_p^2} \Big]. && (4.50b) \end{aligned}$$

As shown in Table 4.1, in order to realize the backward eigenmode k_{a-}, one can see that $\epsilon + g < 0$ should be satisfied (i.e., $0 < \omega < \omega_{c1}$ should be held). To form the backward eigenmode k_{p-}, it shows $g > \epsilon$, which means $\omega_g < \omega < \omega_{c2}$. Note that if

$$\omega_p < \sqrt{2}\omega_g$$

is satisfied, there is no overlapping of the two intervals regarding the frequency condition in Table 4.1. If one chooses

$$\omega_p > \sqrt{2}\omega_g,$$

then both k_{p-} and k_{a-} are backward wavenumbers, and two impedances will be present in each of the layers of the slab in Fig. 4.6. In that case, it would be impossible to match those two impedances simultaneously at the material-air interface.

However, we can choose one impedance equal to that of air, and correspondingly the backward wave associated with that impedance can propagate through the slabs as shown in Fig. 4.7.

One can further split the external *dc* magnetic field into two parts as

$$B_{dc} = \mu_0(H_{dc} + M_{dc}) \tag{4.51}$$

where M denotes the magnetic moment in the whole volume occupied by gyrotropic chiral material and the H field has included account the demagnetizing field. Then the permeability tensor in Eq. (4.17b) can be characterized

$$\begin{aligned} \mu &= \mu_0\Big(1 - \frac{\omega_0\omega_M}{\omega^2 - \omega_0^2}\Big) && \text{(4.52a)} \\ l &= \mu_0\frac{\omega\omega_M}{\omega^2 - \omega_0^2}, && \text{(4.52b)} \end{aligned}$$

where

$$\begin{aligned} \omega_0 &= \frac{e}{m_e}\mu_0 H_{dc} && \text{(4.53a)} \\ \omega_M &= \frac{e}{m_e}\mu_0 M_{dc}. && \text{(4.53b)} \end{aligned}$$

Therefore, it can be shown that the restriction $|l| < \mu$ (as stated in Table 4.1) can be maintained by choosing proper external dc magnetic field and the number of electrons. Further study reveals that $l + \mu$ is always positive. Thus the restriction $l < \mu$ becomes

$$\frac{\omega_M}{\omega - \omega_0} < 1. \tag{4.54}$$

With these conditions clearly stated, the negative refractive indices of the generalized gyrotropic chiral medium can be obtained. Taking into account of Eq. (4.24), for respective polarization states and helicities, one can finally obtain two refraction indices for these backward eigenwaves:

$$n_{\pm} \quad = \quad \frac{c_0}{(\alpha_t \mp \sigma)}[\sqrt{\xi_c^2 + (\alpha_t \mp \sigma)(\epsilon \pm g)} - \xi_c] \tag{4.55}$$

where plus and minus signs are referred to as k_{a-} and k_{p-}, respectively.

It can be seen that n_+ will be negative when $g < -\epsilon$ and n_- will possess a minus sign when $g > \epsilon$ (which means that a backward wave propagates in such a medium). It also shows that a negative refraction index may be easily achieved even if the chirality admittance ξ_c is very small. Note that one can use all positive parameters (i.e., ϵ, g, μ, w and ξ_c) to achieve a negative index of refraction (i.e., n_-). In addition, $g > \epsilon$ can be realized with some advanced technology in the future based on the theory of off-diagonal parameter amplification in artificially gyrotropic media.

In what follows, Eq. (4.55) is analyzed in detail to discuss the possibility of backward waves:

We can further rewrite Eq. (4.55) as

$$n_{\pm} = c_0\Big[\sqrt{(\mu \pm w)^2\xi_c^2 + (\mu \pm w)(\epsilon \pm g)} - (\mu \pm w)\xi_c\Big]. \tag{4.56}$$

It is found that the negative refractive indices may be easily achieved if $\epsilon \pm g < 0$, and it has been pointed out how the frequency shall be selected so as to give rise to negative refraction indices in Fig. 4.6.

Then what is of particular interest turns out to be the case of $n_{\pm} = 0$ (i.e., $\epsilon \pm g = 0$). It follows that this case can be realized at two specific frequencies as given below

$$\omega_1 = -\frac{\omega_g}{2} + \sqrt{\left(\frac{\omega_g}{2}\right)^2 + \omega_p^2} \tag{4.57a}$$

$$\omega_2 = \frac{\omega_g}{2} + \sqrt{\left(\frac{\omega_g}{2}\right)^2 + \omega_p^2} \tag{4.57b}$$

where $\omega = \omega_1$ and $\omega = \omega_2$ lead to $\epsilon + g = 0$ and $\epsilon - g = 0$, respectively.

Therefore one can come up with an equivalent cover for patch antennas (see Fig. 4.8(a)) with zero refractive index and a positive wave impedance $1/\xi_c$ which is comprised of a gyrotropic chiral medium. Only normal incident waves are transmitted into the slab and the phases in any planes between $z = 0$ and $z = d$ will keep unchanged. Hence, potential application includes a radome of antennas, which will greatly enhance the directivity of the antennas. No reflected waves interfere with antennas if impedance matching at material-air interface has been achieved. In addition, the existence of a slab has no influence on the phase of the propagating waves.

Alternatively, in Fig. 4.8(b), if some sources are placed in such a substrate made from gyrotropic chiral slab which has $n = 0$ and finite impedance, all the transmitted waves will be perpendicular with the upper surface no matter what the form of the source would be. This property is attributed to the Snell's law when one of the material has zero refractive index. Due to the property of zero or nearly zero refractive index, gyrotropic chiral materials at two particular frequencies provide potentials in quantum devices because the discrete quantized field will be greatly enhanced. For instance, the critical field is assumed to be E_c. If the field strength has the same order of magnitude of E_c or less than E_c, the field can be viewed as a quantized one or a fluctuation of quantum vacuum. It is obvious that the critical field strength becomes very large when the refractive index is almost zero. Hence, the quantum vacuum fluctuation field becomes strong.

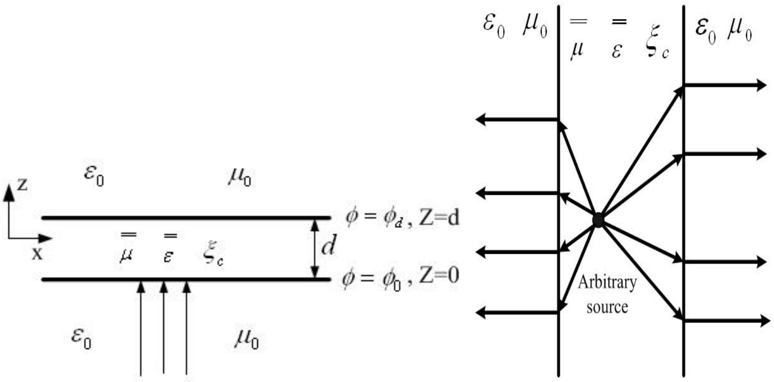

(a) Phase compensating cover. (b) A special substrate.

Figure 4.8: Application of a gyrotropic chiral slab with zero index but finite impedance.

4.4 Nihility routes for magnetoelectric composites to NIM

As is known, the NIMs in the microwave region have been measured and confirmed. However, realizing negative permeability from metallic structures as well as achieving low loss negative-index media at much higher frequencies is a very difficult task. Negative values can be even obtained simultaneously for the real parts of the permeability and the permittivity without achieving a negative index of refraction due to high values of the imaginary part of the permeability in the visible region [153]. Hence, the impact of NIM would be more far-reaching if negative refraction is realized at optical frequencies. In this connection, chiral composites have been proposed as a potential candidate to acheive negative refraction [136] in optical region since it is not necessary to create artificial magnetic materials anymore. In chiral materials with long helices, a backward wave can be excited along the helix which acts as a delay line. An electric or magnetic excitation will produce simultaneously both the electric and magnetic polarizations.

However, the chirality can not be very large in nature so as to satisfy the backward-wave condition $\sqrt{\epsilon_r \mu_r} - \kappa < 0$. Thus, a speical type of chiral materials with extremely small permittivity and permeability (termed as *chiral nihility* firstly by Tretyakov *et al*) helps a lot to enlarge the impact of chiral materials in the realm of negative-index materials. As a complementary counterpart of gyrotropic chiral materials which make use of gyrotropic parameters to reduce refractive indices, chiral nihility is based on the suppression of permittivity and permeability by appropriate wire-loop models [70].

Initially, the concept of nihility was conjectured by Lakhtakia [154] for the mixtures of DPS and DNG dielectric materials, which gives null parameters to the permittivity and permeability of the mixture. It can be found that this nihility is not physical since the Maxwell equations have no nontrivial solutions. However, this concept is still of use, based on which chiral nihility is generalized. Chiral nihility refers to the definition of the real parts of permittivity and permeability almost zero, nonzero chirality, and the imaginary parts of all the parameters much smaller than the chirality. In such exotic materials, electromagnetic wave propagates while negative refraction occurs. By the model in Fig. 4.1 ordered in arrays, it has been validated that chiral nihility is realizable if the radius of the loop and the length of the dipole are advisably chosen. More recently, it is reported that negative reflection will occur and any entry of electromagnetic wave will disappear in chiral nihility, when the chiral nihility slab is backed by a PEC [155].

In contrast to previous studies on chiral nihility, the original work in this section focuses on the macroscopic characterization of electromagnetic wave interaction with chiral nihility. First, the chirality effects in the slab of chiral nihility is examined when the slab is illuminated by an incident plane wave. The wave, scattered by and transmission through this slab, are characterized, which yields a lot of exciting phenomena such as a wide range of Brewster angle and power transport control. Next, I will explore different mechanisms of chiral nihility and how to realize it. Initially, the chiral nihility was for isotropic reciprocal chiral materials. In the following parts, different medium formalisms for such a chiral nihility are discussed. Furthermore, nonreciprocal chiral nihility and gyrotropic chiral nihility are proposed based on the related findings in Section 4.2, and chirality control is studied in order to meet the conditions of respective nihilities.

4.4.1 Energy transport in chiral nihility

This part studies eigenwaves propagating in a chiral nihility medium. The problem of reflection from a dielectric-chiral interface and wave propagation in an infinite chiral slab placed in free space is discussed. The E-field is analyzed and the results established from numerical calculations at different angles of incidence and for different sets of values of the constitutive parameters are presented.

Brewster angles and chirality effects in a semi-infinite chiral nihility medium

A plane wave incidence upon the interface between a dielectric and a chiral medium is considered as shown in Fig. 4.9.

The reflection and refraction in the configuration of Fig. 4.9 can be formulated as

$$\begin{bmatrix} E_{r\perp} \\ E_{r\parallel} \end{bmatrix} = \begin{bmatrix} R_{11} & R_{12} \\ R_{21} & R_{22} \end{bmatrix} \begin{bmatrix} E_{i\perp} \\ E_{i\parallel} \end{bmatrix} \tag{4.58a}$$

$$\begin{bmatrix} E_{1} \\ E_{2} \end{bmatrix} = \begin{bmatrix} T_{11} & T_{12} \\ T_{21} & T_{22} \end{bmatrix} \begin{bmatrix} E_{i\perp} \\ E_{i\parallel} \end{bmatrix} \tag{4.58b}$$

where

$$R_{11} = \frac{\cos\theta_{inc}(1-g^2)(\cos\theta_1+\cos\theta_2)+2g(\cos^2\theta_{inc}-\cos\theta_1\cos\theta_2)}{\cos\theta_{inc}(1+g^2)(\cos\theta_1+\cos\theta_2)+2g(\cos^2\theta_{inc}+\cos\theta_1\cos\theta_2)} \tag{4.59a}$$

$$R_{12} = \frac{-2ig\cos\theta_{inc}(\cos\theta_1-\cos\theta_2)}{\cos\theta_{inc}(1+g^2)(\cos\theta_1+\cos\theta_2)+2g(\cos^2\theta_{inc}+\cos\theta_1\cos\theta_2)} \tag{4.59b}$$

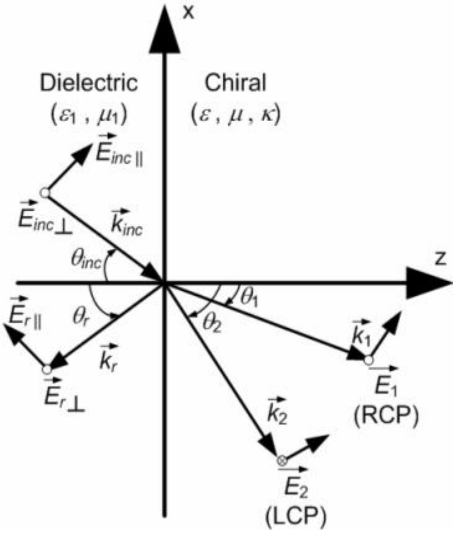

Figure 4.9: Orientation of the wave vectors at an oblique incidence on a dielectric-chiral interface. The subscripts $\|$ and $\perp$ respectively stand for parallel and perpendicular polarizations with respect to the plane of incidence.

$$R_{21} = \frac{-2ig\cos\theta_{inc}(\cos\theta_1 - \cos\theta_2)}{\cos\theta_{inc}(1+g^2)(\cos\theta_1+\cos\theta_2) + 2g(\cos^2\theta_{inc} + \cos\theta_1\cos\theta_2)} \tag{4.59c}$$

$$R_{22} = \frac{\cos\theta_{inc}(1-g^2)(\cos\theta_1+\cos\theta_2) - 2g(\cos^2\theta_{inc} - \cos\theta_1\cos\theta_2)}{\cos\theta_{inc}(1+g^2)(\cos\theta_1+\cos\theta_2) + 2g(\cos^2\theta_{inc} + \cos\theta_1\cos\theta_2)}, \tag{4.59d}$$

$$T_{11} = \frac{-2i\cos\theta_{inc}(g\cos\theta_{inc} + \cos\theta_2)}{\cos\theta_{inc}(1+g^2)(\cos\theta_1+\cos\theta_2) + 2g(\cos^2\theta_{inc} + \cos\theta_1\cos\theta_2)} \tag{4.60a}$$

$$T_{12} = \frac{2\cos\theta_{inc}(\cos\theta_{inc} + g\cos\theta_2)}{\cos\theta_{inc}(1+g^2)(\cos\theta_1+\cos\theta_2) + 2g(\cos^2\theta_{inc} + \cos\theta_1\cos\theta_2)} \tag{4.60b}$$

$$T_{21} = \frac{2i\cos\theta_{inc}(g\cos\theta_{inc} + \cos\theta_1)}{\cos\theta_{inc}(1+g^2)(\cos\theta_1+\cos\theta_2) + 2g(\cos^2\theta_{inc} + \cos\theta_1\cos\theta_2)} \tag{4.60c}$$

$$T_{22} = \frac{2\cos\theta_{inc}(\cos\theta_{inc} + g\cos\theta_1)}{\cos\theta_{inc}(1+g^2)(\cos\theta_1+\cos\theta_2) + 2g(\cos^2\theta_{inc} + \cos\theta_1\cos\theta_2)}, \tag{4.60d}$$

and $g = [(\mu_1/\epsilon_1)(\epsilon/\mu)]^{1/2}$.

The homogeneous reciprocal chiral material has been defined in Eq. (4.2), with only slight changes in notations here (i.e., $\epsilon_T \rightarrow \epsilon_r\epsilon_0$ and $\mu_T \rightarrow \mu_r\mu_0$). The wavenumbers of the two eigenwaves in the chiral medium then read

$$k_{1,2} = k_0(\sqrt{\mu_r \epsilon_r} \pm \kappa) \tag{4.61}$$

which corresponds to two eigenmodes respectively

$$\begin{aligned} \boldsymbol{E}_1 &= \boldsymbol{E}_{01}(\boldsymbol{e}_x + i\boldsymbol{e}_y)e^{ik_1 z} && \text{(4.62a)} \\ \boldsymbol{E}_2 &= \boldsymbol{E}_{02}(\boldsymbol{e}_x - i\boldsymbol{e}_y)e^{ik_2 z}. && \text{(4.62b)} \end{aligned}$$

The refractive indices are thus given by

$$n_{1,2} = \sqrt{\mu_r \epsilon_r} \pm \kappa. \tag{4.63}$$

Potential applications in phase compensator and quantum devices can also be envisaged similarly as the gyrotropic cases in Section 4.3.2, which is not the focus of the current part.

In order to study the reflected power at the interface between the dielectric and the chiral medium, the boundary condition has to be satisfied

$$\begin{aligned} \hat{\boldsymbol{z}} \times [\boldsymbol{E}_{inc} + \boldsymbol{E}_r] &= \hat{\boldsymbol{z}} \times [\boldsymbol{E}_1 + \boldsymbol{E}_2] && \text{(4.64a)} \\ \hat{\boldsymbol{z}} \times [\boldsymbol{H}_{inc} + \boldsymbol{H}_r] &= \hat{\boldsymbol{z}} \times [\boldsymbol{H}_1 + \boldsymbol{H}_2] && \text{(4.64b)} \end{aligned}$$

from which the method for retrieving Fresnel reflection and transmission coefficients [156] is adopted and further transformed into the Tellegen formalism. In Fig. 4.10, the reflected power is drawn versus the angle of incidence for two different configurations. The first case deals with a chiral medium where the permittivity is greater than that of the dielectric. It then exists a Brewster angle for an incidence at about 65° for the parallel polarization as shown in Fig. 4.10(a). For the second

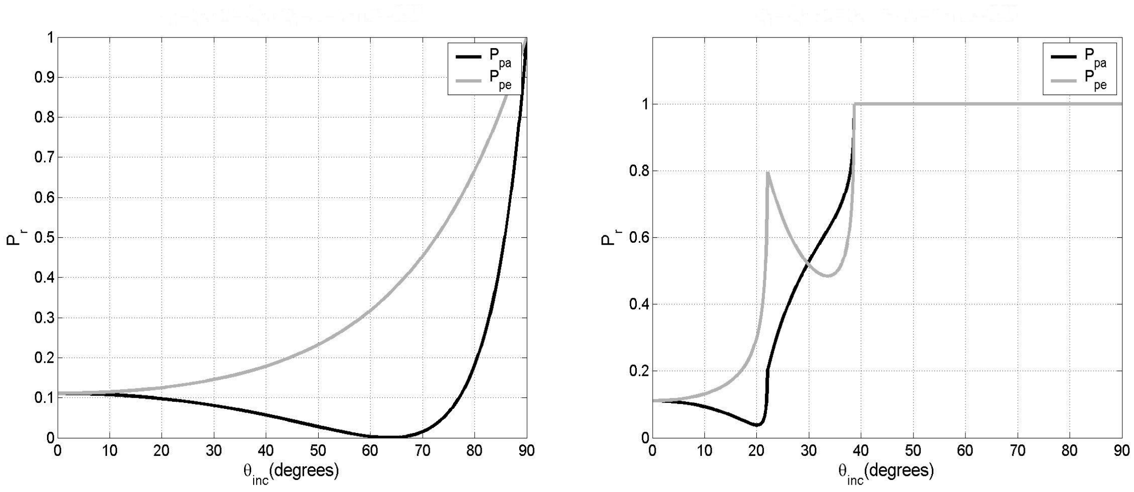

(a) $\epsilon_1 = 1$, $\epsilon = 4$, $\mu_1 = \mu = 1$, $\kappa = 0.25$

(b) $\epsilon_1 = 4$, $\epsilon = 1$, $\mu_1 = \mu = 1$, $\kappa = 0.25$

Figure 4.10: Reflected power as a function of the incidence with unit permeability, the same chirality but different permittivity.

case (Fig. 4.10(b)), the chiral medium has a lower permittivity compared to the surrounding dielectric. For the value of $\kappa = 0.25$, no Brewster angle can be observed for either polarization of the incident field. However, when $\theta = 22^\circ$, the reflected power of P_{pa} has a minimum, which is close to zero. Total reflection starts from the incidence at 40° for both P_{pa} ($\|$) and P_{pe} ($\perp$) polarizations. Further investigation yields that the permittivity ratio (i.e., permittivity of dielectics over permittivity of chiral medium) plays an important role in the zero and total reflection characteristics. As for the zero reflection, it only occurs to parallel polarization, which is consistent with the results of the conventional dielectric-dielectric interface. It is interesting to observe that the total reflection happens over a wide range of incidence angles and a secondary total-reflection angle at $\theta = 22^\circ$ appears for perpendicular polarization.

Next, the energy transport from the dielectric to the chiral nihility is investigated, where some interesting phenomena arise. Two cases of chiral nihilities are considered (i.e., impedance matching and mismatching to the air).

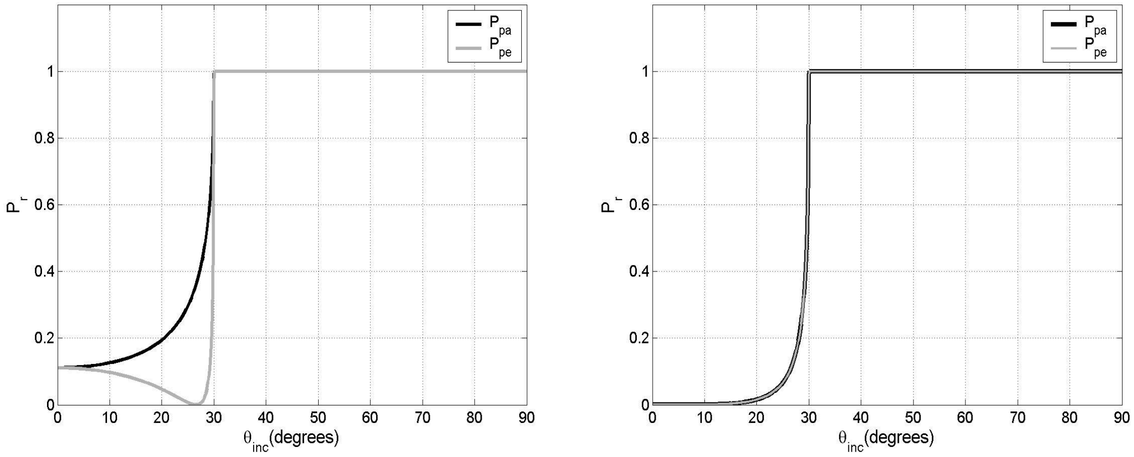

(a) $\epsilon_1 = \mu_1 = 1$, $\epsilon = 4 \times 10^{-5}$, $\mu = 10^{-5}$, $\kappa = 0.5$; (b) $\epsilon_1 = \mu_1 = 1$, $\epsilon = \mu = 10^{-5}$, $\kappa = 0.5$

Figure 4.11: Reflected power as a function of the incidence with different cases of chiral nihility.

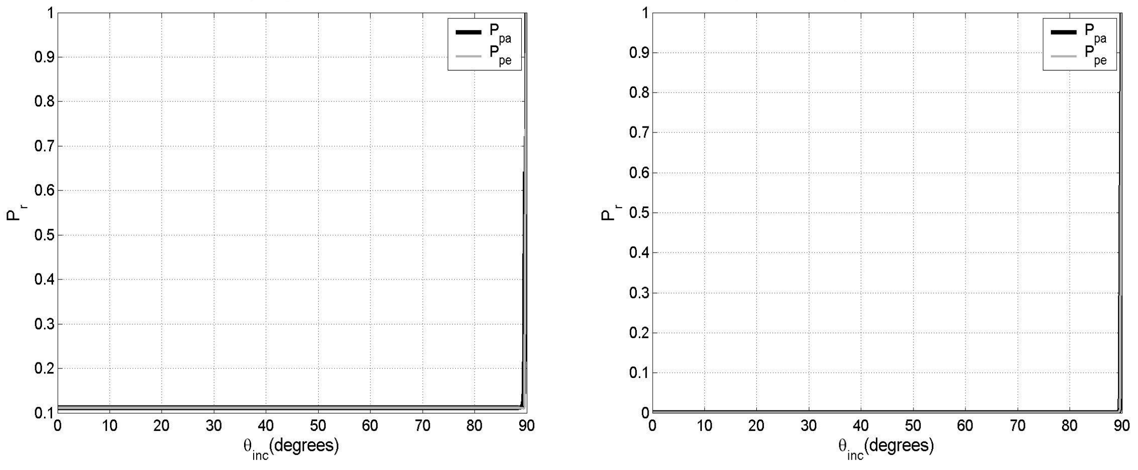

(a) (b)

Figure 4.12: Reflected power as a function of the incidence with the same permittivity and permeability as in Fig. 4.11 but with a higher chirality: (a) $\epsilon_1 = \mu_1 = 1$, $\epsilon = 4 \times 10^{-5}$, $\mu = 10^{-5}$, and $\kappa = 1$; and (b) $\epsilon_1 = \mu_1 = 1$, $\epsilon = \mu = 10^{-5}$, and $\kappa = 1$.

Comparing Fig. 4.11(a) with Fig. 4.10(a), it is seen that zero-reflection angle occurs to perpendicular polarization rather than parallel parallel polarization, which is in contrast to the situation for normal chiral or achiral materials. It is shown that the reflected power dependence on incident angle varies drastically within certain range. The zero-reflection angle at 27° is quite close to the lowest total reflection angle at 30°, which means that this range is quite angle sensitive. More surprisingly, the dependence of the reflected power on the incidence becomes identical for both polarizations when the impedance of chiral nihilty is matched to free space. In this special case shown in Fig. 4.11(b), the Breswter angle has a range rather than a single angle, and total reflection happens when incidence angle is greater than 30° though the impedance matching is achieved. It is due to the mismatch of the refractive indices.

As one can see, the chirality of each case in Fig. 4.11 is doubled in Fig. 4.12, if other parameters are unchanged. As such, the chirality effects in chiral nihility can be presented. In Fig. 4.12, the reflected powers of both polarizations carry a similar dependence on incidence, while the magnitude of the reflected power significantly differs with that in Fig. 4.11. In Fig. 4.12, the value is quite stable over the whole region except at 90°. If the impedance of chiral nihility is matched, the value will be further reduced to zero (see Fig. 4.12(b)), which means that the Brewster angle almost covers the whole range of incidence angles. Therefore, under such circumstances, all the energy will be transmitted to the chiral nihility if the incident angle is smaller than 90°. It may be of great importance to realize imaging characteristics without much loss of information of a point source or a line source, since one of the refractive indices of chiral nihility is very close to -1.

Fig. 4.13 shows the reflected power versus the chirality for the same two configurations as above at an oblique incidence of 45°. When the chiral medium is denser than the dielectric (Fig. 4.13(a)) and at a perpendicular polarization of the incident field, the reflected power shows a maximum of 0.8 for $\kappa = 2$ and tends to a stable value of 0.22 for $\kappa > 4$. Concerning the parallel polarization, two maxima are obtained ($P_r = 0.8$) at $\kappa = 1.29$ and $\kappa = 2.71$, respectively. In order to have a good transmission through the interface, the chirality must be either lower than 1.29 or greater than 2.71. On the contrary, when the dielectric is denser than the chiral medium (Fig. 4.13(b)), total reflection is observed for both polarizations for

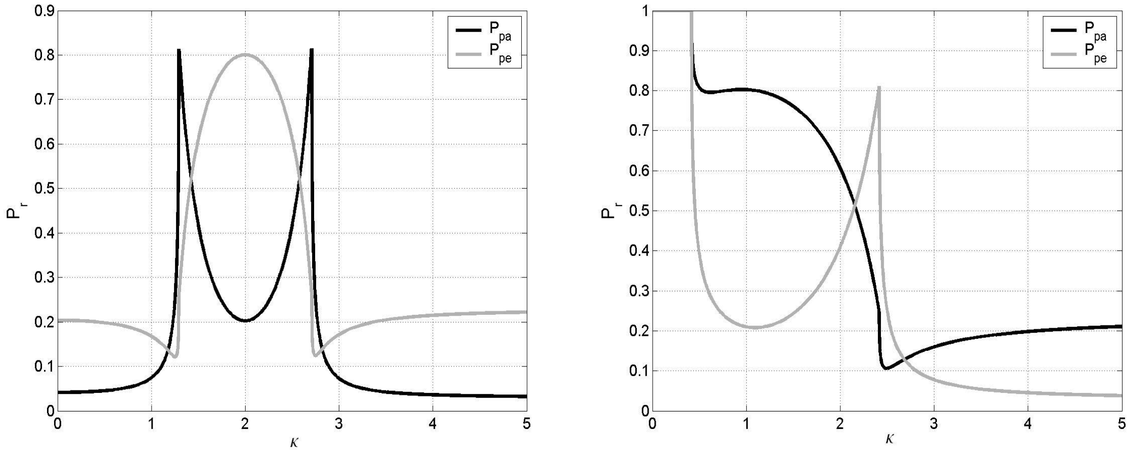

(a) $\epsilon_1 = \mu_1 = 1$, $\epsilon = 4$, $\mu = 1$

(b) $\epsilon_1 = 4$, $\mu_1 = 1$, $\epsilon = \mu = 1$

Figure 4.13: Reflected power as a function of the chirality at an oblique incidence of $\theta_{inc} = 45°$.

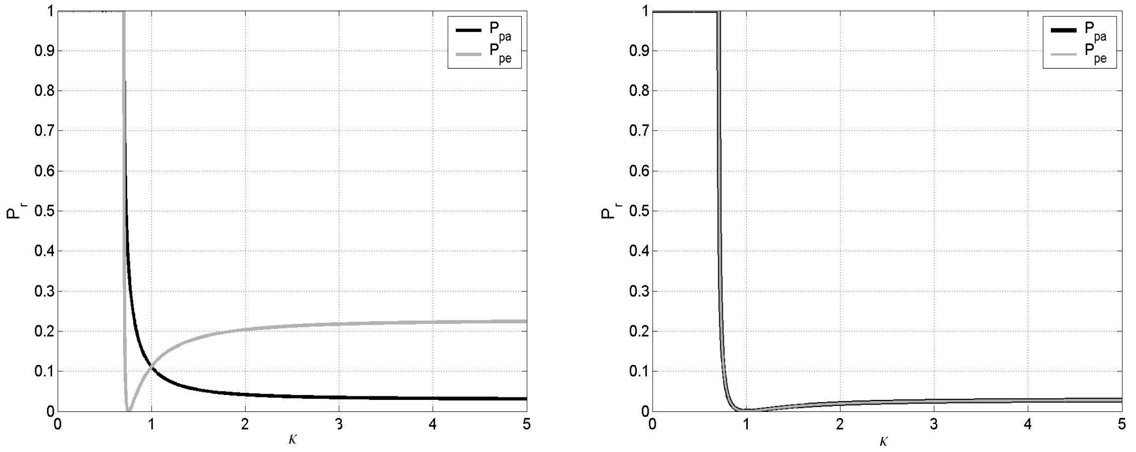

(a) $\epsilon_1 = \mu_1 = 1$, $\epsilon = 4 \times 10^{-5}$, $\mu = 10^{-5}$

(b) $\epsilon_1 = \mu_1 = 1$, $\epsilon = \mu = 10^{-5}$

Figure 4.14: Reflected power as a function of the chirality at an oblique incidence of $\theta_{inc} = 45°$ in different cases of chiral nihility.

chirality smaller than 0.42. Concerning the case of parallel polarization, the reflected power decreases to a stable value of 0.22 as chirality increases. For the perpendicular polarization of the incident field, a minimum is first observed for $\kappa = 1$ and then a maximum for $\kappa = 2.41$. For $\kappa > 3$, the reflected power tends to 0.04. If one further increases the mismatch of the permittivity between the dielectric and the chiral medium, the plots observed in Fig. 4.13 shift to the right (higher values of chirality) and the amplitude of the reflected power increases.

In addition to the normal chiral slabs, chiral nihility slabs at an oblique incidence are also studied in Fig. 4.14. Similarly, particular values of chirality will lead to zero reflection, which is so-called critical chirality κ_c. In Fig. 4.14(a), $\kappa_c \approx 0.75$ which only exists for perpendicular polarization. If the chirality is lower than κ_c, total reflection happens and no power can be transmitted to the chiral nihility slab. When the chirality is sufficiently large, the reflected powers are approaching their respective stable values, and it is found that the stable reflected power of P_{pa} is about 7 times larger than that of P_{pe}. If the chirality nihility slab has its impedance matched to the free space, both P_{pa} and P_{pe} have identical perfomance versus chirality, and κ_c can be observed for both cases. It suggests that a bigger chirality would be a better choice if energy transport is desired.

Power transmission in infinite chiral nihility slab

In this section, the propagation of a plane wave through an infinite chiral nihility slab of thickness d is considered (Fig. 4.15(a)). If one selects a frequency region where

$\Re[\kappa] > \Re[\mu_r \epsilon_r]$, then one of the two waves is backward according to Eq. (4.61). Hence for one of the two polarizations, the chiral medium will support a negative index of refraction and in such a case, subwavelength focusing will take place for waves of this polarization as shown in Fig. 4.15(b).

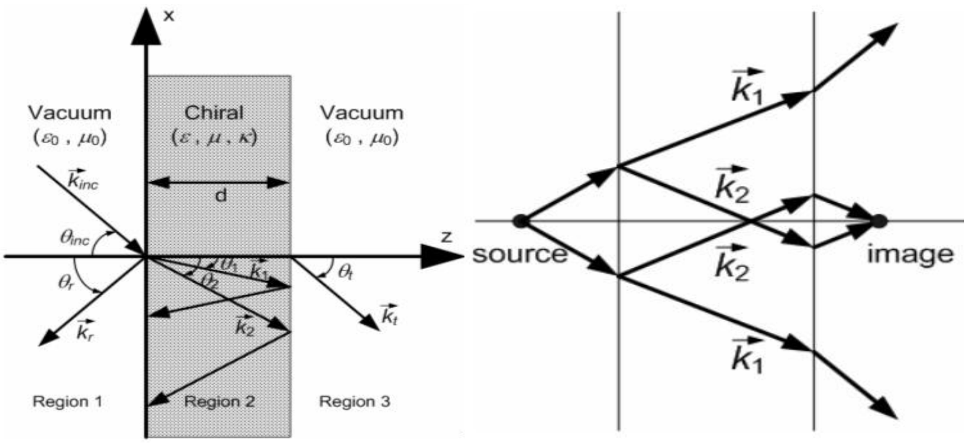

(a) (b)

Figure 4.15: (a) A chiral slab of thickness d placed in free space. The two interfaces of the chiral slab are situated at $z = 0$ and $z = d$. Regions 1 and 3 are considered to be vacuum and region 2 is the chiral medium; and (b) Illustration of negative refraction and subwavelength focusing by a chiral slab ($k_1 > 0$ and $k_2 < 0$).

The configuration for the chiral slab in a dielectric host medium is given in Fig. 4.13(a). Suppose that a plane wave propagating in a homogeneous isotropic dielectric medium is incident on the surface of a chiral slab. In this case, air is taken for the dielectric medium and the two interfaces with the chiral slab are situated at $z = 0$ and $z = d$. The angles θ_1 and θ_2 corresponding to the transmitted waves in the chiral slab are given by:

$$\theta_{1,2} = \sin^{-1}\left\{\frac{k_{inc}\sin\theta_{inc}}{k_{1,2}}\right\} \tag{4.65}$$

where $k_{inc} = k_0$, k_r and k_t denote the incident, reflected and transmitted wavenumber, respectively. The boundary conditions of the tangential electric and magnetic fields are applied at the two interfaces situated at $z = 0$ and $z = d$ and a matrix form is then used to solve the system in order to obtain the different E and H-field components.

First, let us consider a chiral slab with both the relative permittivity and permeability having values of 10^{-5} (very close to 0) and the chirality parameter taking values which vary from 0 to 2. Assume that the thickness of the slab along the z axis is $d = 5$ mm ($0 < z < 5$ mm) and a plane wave parallel to the plane of incidence (plane yoz in Fig. 4.15(a)) coming from vacuum is incident on the chiral slab. The electric and magnetic field vectors are taken to be oriented along the x and y directions, respectively. The working frequency here is set to 10 GHz. The wave vector k and index of refraction n of each circularly polarized plane wave in a chiral nihility slab are plotted versus the chirality parameter in Fig. 4.16. It can be noted that when $\Re[\kappa] > \Re[\mu_r\epsilon_r]$, one of the two waves has a negative index of refraction which corresponds to a backward wave in the chiral slab. For the whole set of values of κ, a matching of Z is achieved. But a matching of n with that of free space is achieved only for $\kappa = 1$ in this particular case.

Next, in Fig. 4.16, it presents a chiral slab with both the relative permittivity and permeability having values of 10^{-5} (very close to 0) and the chirality parameter

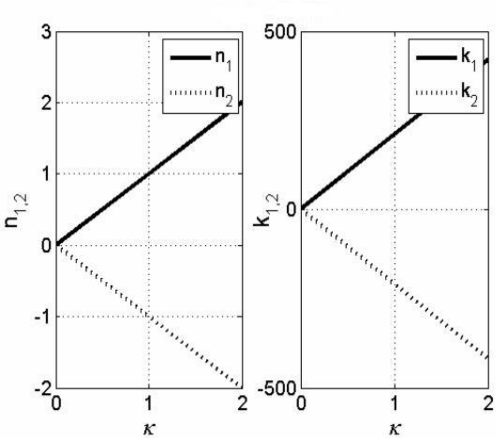

Figure 4.16: Indices of refraction and wave vectors in the chiral nihility slab versus the chirality.

taking values which vary from 0 to 2. A value close to zero but not exactly zero will be illustrated in the next section regarding the nihility conditions. The negative refraction and backward-wave properties are shown.

The transmitted power in vacuum on the right-hand side of a chiral nihility slab (i.e., region 3 of Fig. 4.15(a)) is plotted versus the angle of incidence θ_{inc} for the different values of permittivity/permeablity, and the results are shown in Fig. 4.17. Two types of transmission are considered for the incident parallel plane wave: the nominal transmission which is calculated from the ratio of the parallel transmitted E-field over the parallel incident E-field and the cross transmission which is calculated from the ratio of the perpendicular transmitted E-field over the parallel incident E-field.

It can be noted from Fig. 4.17 that the total transmitted power depends strongly on the value of κ. For $\kappa = 0$ (an achiral dielectric medium), the transmitted power

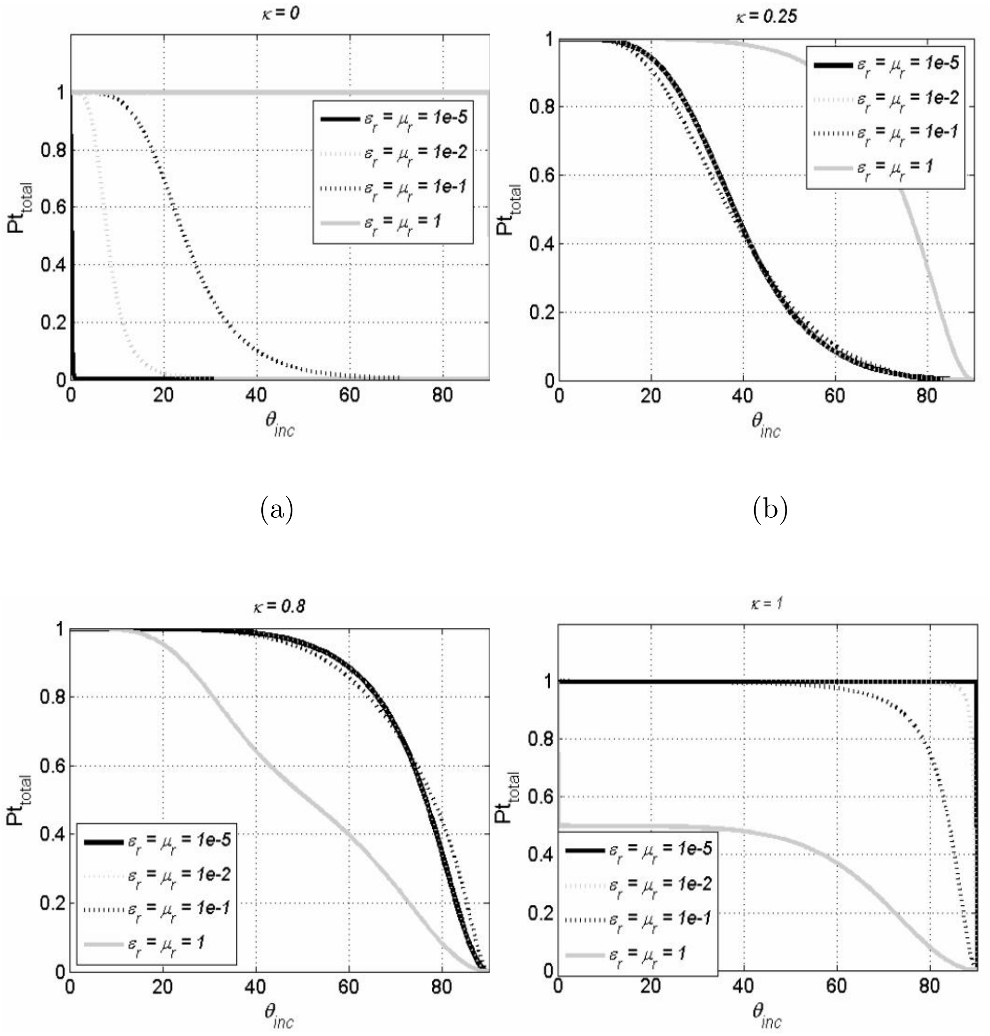

(a) (b)

(c) (d)

Figure 4.17: Total transmitted power in vacuum on the right side of the chiral nihility slab (region 3) for different values of ϵ_r and μ_r versus the angle of incidence θ_i.

drops from 1 to 0 when the incident angle of the plane wave is slightly bigger than zero in the case where $\epsilon_r = \mu_r = 10^{-5}$ (Fig. 4.17(a)). For any oblique incidence, the power transmitted is null. When the values of ϵ_r and μ_r increase simultaneously, a low pass characteristic is observed; and when $\epsilon_r = \mu_r = 1$ is reached, total transmission is obtained for the whole range of incidence varying from 0° to 90° where a drop to zero is noted. If chirality is introduced ($\kappa = 0.25$), a low pass characteristic is observed for each set of values for ϵ_r and μ_r (Fig. 4.15(b)). Increasing the values of ϵ_r and μ_r leads to a widening of the range of incidence where total transmission occurs. If $\kappa = 0.8$ (Fig. 4.17(c)), one can still observe the low pass characteristics, and the transmissions for $\epsilon_r = \mu_r = 10^{-5}$ and $\epsilon_r = \mu_r = 10^{-2}$ are the same. In the case of $\kappa = 1$ and $\epsilon_r = \mu_r = 10^{-5}$ (Fig. 4.17(d)), the total transmitted power is unity for any angle of incidence varying from 0° to 90° where it drops to zero then. It should be noted that in this case, one of the two eigenwaves in the chiral slab has a refractive index equal to -1. For $\epsilon_r = \mu_r = 10^{-2}$, the drop to zero transmission is smoother and occurs at a slightly lower incidence. A surprising phenomenon occurs when $\epsilon_r = \mu_r = 1$ together with $\kappa = 1$. In fact, the total transmitted power drops sharply from 1 to 0.5 when the angle of incidence of the plane wave is zero. This is because only one eigenwave with $n = 2$ propagates through the chiral medium. At an oblique incidence from 0° to approximately 30°, only half of the total power is transmitted. Above 30°, there is a smooth drop till 90° where the power transmitted is null. One possible and interesting application which needs to be mentioned in this particular case is a half-power divider for a selective range of incident angles.

Here, let us consider and compare the nihility slab with chiral nihility slab. For nihility slab, κ is assumed to be equal to zero when $\epsilon_r = \mu_r = 10^{-5}$ by considering $\gamma = 0$ in the Born formalism, since in the exact nihility there is no transportation of energy. To gain some insights into the behavior of the fields in different regions, the plots of the real and imaginary parts of the E-field (E_x and E_z components) in these three regions are presented for the selected value of parameters. In Fig. 4.18, only E_x component inside and outside the slab is shown when a plane wave is normally incident (the E_z component is null at 0° incidence). Here, one can notice that the imaginary and real parts of E_x are respectively null and unity inside the slab and we have also conservation of energy inside the slab. It can be observed that there exists no phase delay between the front face and the back face of the slab. This slab can then act as a phase compensator/conjugator. The slab is completely transparent to the electric field.

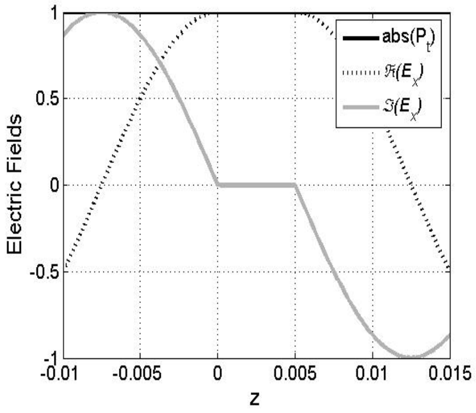

Figure 4.18: Electric field and transmitted power as a function of z coordinate when a normally incident wave illuminates a nihility slab with $\epsilon_r = \mu_r = 10^{-5}$ and $\kappa = 0$.

For the chiral nihility slab whose chirality is assumbed to be 0.25, E_y component

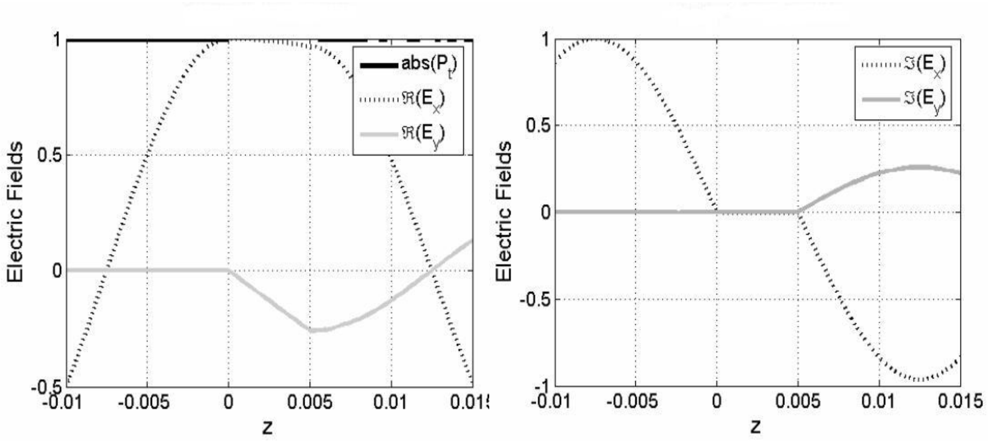

(a) (b)

Figure 4.19: Electric field and transmitted power as a function of z coordinate when a normally incident wave illuminates a chiral nihility slab of medium with $\epsilon_r = \mu_r = 10^{-5}$ and $\kappa = 0.25$: (a) Magnitude of real parts and transmitted power; and (b) Magnitude of imaginary parts.

is present as shown in Fig. 4.19. Note that here, the two eigenwaves propagating inside the slab have indices of refraction equal to -0.25 and 0.25, respectively. When $\kappa = 0.25$, the real part of E_x decreases very slightly in the slab (region 2) with a normally incident plane wave. The E_y component which is null in region 1 increases linearly to 0.22 in the chiral slab. Concerning the imaginary parts presented in Fig. 4.19(b), they are both equal to zero inside the slab and there is no phase delay between the front and back faces of the slab. The cases studied in Fig. 4.18 and Fig. 4.19 are examples where there is a matching of the wave impedance Z since $\epsilon_r = \mu_r$, but not for the refractive index n. In this section, a matched refractive index case is presented. Let us consider the case where there also exists a matching of the index of refraction by considering $\kappa = 1$. One of the two eigenwaves propagating in the slab will have $n = 1$ and the other backward wave will have $n = -1$. The electric field distribution for a normally incident plane wave is presented in Fig. 4.20. Fig. 4.20(a) shows that the real part of the E_y component takes quite high values in the slab due to the cross transmission and the power transmitted in region 3 is equal to 1. In Fig. 4.20(b), it is shown that the imaginary part of E_y arises after the wave propagates through the slab, while it does not exist in regions 1 and 2.

4.4.2 Constraints and conditions of isotropic/gyrotropic chiral nihility

The *physical* definition of chiral nihility is that the two eigenwaves have the opposite propagation constants and that the wave impedance is a finite number. Since the

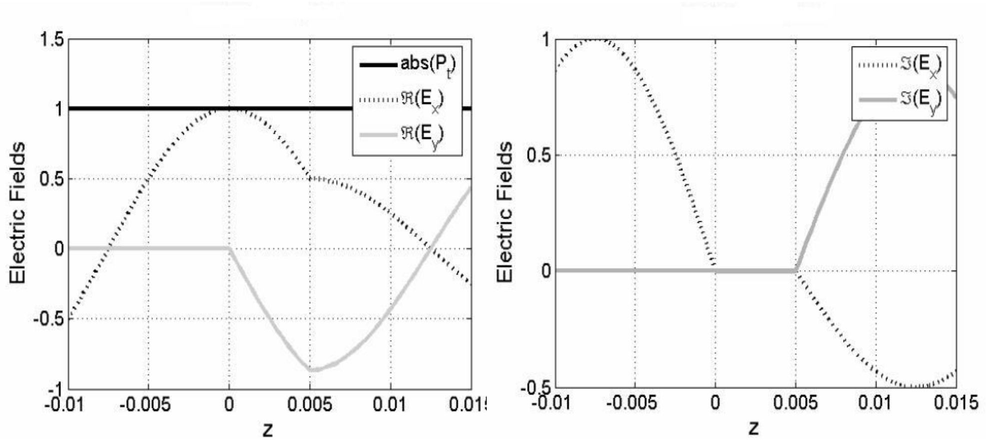

(a) (b)

Figure 4.20: Electric field as a function of z coordinate when a normally incident wave illuminates a slab of medium with $\epsilon_r = \mu_r = 10^{-5}$ and $\kappa = 1$: (a) Magnitude of real parts and transmitted power; and (b) Magnitude of imaginary parts.

chiral nihility is so promising in realizing negative refraction, it is of particular interest to explore the physics of chiral nihility and the conditions to satisfy not only isotropic chiral nihility, but also the nonreciprocal and gyrotropic chiral nihility.

Isotropic chiral nihility

As discussed in Section 4.2 and Section 4.3, different formalisms of isotropic magnetoelectric composites are equivalent, while each formalism of gyrotropic magnetoelectric composites has its own advantage, either in negative-index description or in practical application. However, for chiral nihility, the formalism dependence will be very critical and as we will see, some formalisms are not suitable at all.

- *Constraints of medium formalisms:*

1. **Tellegen:**

The Tellegen's formalism has been given in Eq. (4.2). When $\epsilon_T\mu_T \rightarrow 0$, the nihility condition of isotropic chiral media can be represented by

$$k_{\pm} = \omega(\sqrt{\epsilon_T\mu_T} \pm \kappa\sqrt{\epsilon_0\mu_0}) \rightarrow \pm k_0\kappa \tag{4.66}$$

where k_0 is the wave number in free space. Hence, one of the waves becomes backward wave and has a negative refractive index of $n = -\kappa$.

In the meantime, the wave impedance of the chiral medium $\eta = \sqrt{\mu_T/\epsilon_T}$ should remain finite which means

$$\lim\{\mu_T/\epsilon_T\} \rightarrow \text{const} \neq 0, \infty. \tag{4.67}$$

The combination of this relation with the nihility condition implies that $\epsilon_T \rightarrow 0$ and $\mu_T \rightarrow 0$.

2. **Post:**

In the Post's notation, the constitutive relations are shown in Eq. (4.1). The mapping relations between the Tellegen and Post formalisms are given below

$$\begin{aligned}
\mu_P &= \mu_T && \text{(4.68a)}\\
\epsilon_P &= \epsilon_T - \frac{\epsilon_0\mu_0}{\mu_T}\kappa^2 && \text{(4.68b)}\\
\xi_c &= \frac{\sqrt{\epsilon_0\mu_0}}{\mu_T}\kappa. && \text{(4.68c)}
\end{aligned}$$

The eigenwave numbers in the Post's formalism are found to be

$$k_{\pm} = \omega \left(\sqrt{\mu_P \epsilon_P + \mu_P^2 \xi_c^2} \pm \mu_P \xi_c \right). \tag{4.69}$$

Thus, the nihility condition is

$$\mu_P \epsilon_P + \mu_P^2 \xi_c^2 \to 0. \tag{4.70}$$

The condition in Eq. (4.70) is satisfied if $\epsilon_T \mu_T \to 0$ because the terms containing the chirality parameter κ cancel out.

The impedance

$$\eta = \frac{\sqrt{\mu_P \epsilon_P + \mu_P^2 \xi_c^2}}{\epsilon_P + \mu_P \xi_c^2} \tag{4.71}$$

remains finite if

$$\epsilon_P + \mu_P \xi_c^2 \to 0. \tag{4.72}$$

Substituting the Post parameters expressed via the Tellegen parameters, one sees that if the nihility condition in the Post formalism in Eq. (4.70) is satisfied, then the Tellegen permittivity

$$\epsilon_T = \epsilon_P + \mu_P \xi_c^2 \to 0, \tag{4.73}$$

which is consistent with the chiral nihility requirements in terms of the Tellegen parameters.

3. **Drude-Born-Fedorov:**

The Drude-Born-Fedorov (DBF) constitutive relations are

$$\boldsymbol{D} = \epsilon_{DBF}(\boldsymbol{E} + \beta\boldsymbol{\nabla} \times \boldsymbol{E}) \tag{4.74a}$$

$$\boldsymbol{B} = \mu_{DBF}(\boldsymbol{H} + \beta\boldsymbol{\nabla} \times \boldsymbol{H}), \tag{4.74b}$$

where β denotes the chirality in DBF formalism. The wave numbers obtained for the two eigenmodes are given by

$$k_{\pm} = \frac{\omega\sqrt{\epsilon_{DBF}\mu_{DBF}} \pm \omega^2\epsilon_{DBF}\mu_{DBF}\beta}{1 - \omega^2\epsilon_{DBF}\mu_{DBF}\beta^2} \tag{4.75}$$

and the wave impedance is

$$\eta = \sqrt{\mu_{DBF}/\epsilon_{DBF}}. \tag{4.76}$$

In this case, the conditions of chiral nihility look the same as in the Tellegen notation:

$$\epsilon_{DBF} \to 0, \qquad \mu_{DBF} \to 0. \tag{4.77}$$

But, if conditions in Eq. (4.77) are satisfied, then $k_{\pm} = 0$ unless the DBF chirality parameter $\beta \to \infty$. This is, however, consistent with the known relations between the chirality parameters in the Tellegen notation and the DBF formalism:

$$\epsilon_T = \frac{\epsilon_{DBF}}{1 - k_{DBF}^2\beta^2} \tag{4.78a}$$

$$\mu_T = \frac{\mu_{DBF}}{1 - k_{DBF}^2\beta^2} \tag{4.78b}$$

$$\kappa = \frac{\omega\mu_{DBF}\epsilon_{DBF}\beta}{\sqrt{\epsilon_0\mu_0}(1 - k_{DBF}^2\beta^2)}, \tag{4.78c}$$

where $k_{DBF}^2 = k_0^2\epsilon_{DBF}\mu_{DBF}$. Apparently, if $\mu_{DBF}\epsilon_{DBF} \to 0$, κ can remain finite only if $\beta \to \infty$. Inversely, if Tellegen's nihility is fulfilled ($\epsilon_T \to 0,\ \ \mu_T \to 0$), we will have zero values of μ_{DBF} and ϵ_{DBF}. Thus, the Tellegen chirality κ will be forced to zero in Eq. (4.78c), which is also why such values of $\epsilon = \mu = 10^{-5}$ are set instead of zero in the numerical part in Section 4.4.1.

Therefore, Tellegen and Post notations are equivalent and equally convenient to describe isotropic chiral nihility, while the Drude-Born-Fedorov formalism is less suitable due to the requirement of $\beta \to \infty$, which lacks physical meanings.

- *Nonreciprocal condition:*

The constitutive relations for general biisotropic nonreciprocal chiral media in the Tellegen's notation can be written in the following form [134]

$$\boldsymbol{D} = \epsilon_T \boldsymbol{E} + (\chi + i\kappa)\sqrt{\epsilon_0\mu_0}\boldsymbol{H} \tag{4.79a}$$

$$\boldsymbol{B} = \mu_T \boldsymbol{H} + (\chi - i\kappa)\sqrt{\epsilon_0\mu_0}\boldsymbol{E}, \tag{4.79b}$$

where χ is the nonreciprocity parameter. Let us see how the inclusion of the nonreciprocity parameter would modify the nihility condition. The expression of the propagation constants of the two eigenwaves is found to be [134]

$$k_\pm = \omega\Big(\sqrt{\epsilon_T\mu_T - \chi^2\epsilon_0\mu_0} \pm \kappa\sqrt{\epsilon_0\mu_0}\Big). \tag{4.80}$$

Thus, the nihility condition is

$$\sqrt{\epsilon_T\mu_T - \chi^2\epsilon_0\mu_0} \to 0. \tag{4.81}$$

When this condition is satisfied, one has

$$k_\pm = \omega\Big(\sqrt{\epsilon_T\mu_T - \chi^2\epsilon_0\mu_0} \pm \kappa\sqrt{\epsilon_0\mu_0}\Big) \to \pm k_0\kappa. \tag{4.82}$$

Apparently, the nonreciprocal nihility is easier to achieve than the chiral nihility $\epsilon_T\mu_T \rightarrow 0$ due to the role of the nonreciprocity parameter, which further reduces the value of the product of permittivity and permeability.

The wave impedances for a bi-isotropic nonreciprocal medium are found to be

$$\eta_{\pm} = \frac{\mu_T}{\sqrt{\epsilon_T\mu_T - \chi^2\epsilon_0\mu_0} \mp i\chi\sqrt{\epsilon_0\mu_0}} \tag{4.83}$$

which are independent on the the chirality parameter κ. If the chiral nihility condition in Eq. (4.81) is satisfied, the expressions of the impedances then reduce to

$$\eta_{\pm} = \pm i\frac{\mu_T}{\chi\sqrt{\epsilon_0\mu_0}} = \pm i\frac{\mu_T}{\epsilon_T} \tag{4.84}$$

which is a purely imaginary number for lossless media.

It is also found that if Eq. (4.81) is exactly zero, the effective permittivity and permeability seen by the LCP and RCP waves become also purely imaginary numbers (for lossless media)

$$\mu_T^{\pm} = i\mu_T\frac{\kappa}{\chi} \tag{4.85a}$$

$$\epsilon_T^{\pm} = -\frac{\mu_0}{\mu_T}i\kappa\chi\epsilon_0. \tag{4.85b}$$

Let us now consider the case of dispersive biisotropic media with single-resonance dispersion. The expressions of the permittivity and permeability in Eq. (4.79) read

$$\epsilon_T(\omega) = \epsilon_0\Big[1 - \frac{\omega_{pe}^2}{\omega(\omega + i\Gamma_e\omega_{pe})}\Big] \tag{4.86a}$$

$$\mu_T(\omega) = \mu_0\Big[1 - \frac{\omega_{pm}^2}{\omega(\omega + i\Gamma_m\omega_{pm})}\Big] \tag{4.86b}$$

where plasma frequency and damping term are assumed to be equal for both polarization and magnetization: $\omega_{pe} = \omega_{pm} = \omega_p$ and $\Gamma_e = \Gamma_m = \Gamma$. The nonreciprocity parameter and the chirality can be described in terms of a quantum mechanical model analogue to the classical lossy Drude model

$$\chi(\omega) = \frac{\Gamma_c \omega^2 \omega_c^2}{\omega^4 - (2 - \Gamma_c^2)\omega^2\omega_c^2 + \omega_c^4} \tag{4.87a}$$

$$\kappa(\omega) = \frac{(\omega_c^2 - \omega^2)\omega\omega_c}{\omega^4 - (2 - \Gamma_c^2)\omega^2\omega_c^2 + \omega_c^4} \tag{4.87b}$$

where ω_c is the characteristic frequency for the single-resonance model and the damping term Γ_c is consistent with the one for polarization/magnetization (i.e., $\Gamma_c = \Gamma$). Let us call the real part of $\sqrt{\epsilon_T(\omega)\mu_T(\omega)/\epsilon_0\mu_0 - \chi^2(\omega)}$ the nonreciprocal nihility parameter (NNP).

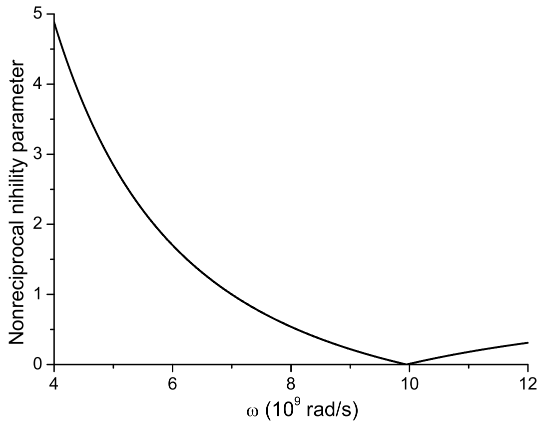

Figure 4.21: Nonreciprocal nihility parameter versus frequency for nonreciprocal chiral material: $\omega_p = 10 \times 10^9$ rad/s, $\omega_c = 1 \times 10^9$ rad/s, and $\Gamma = 0.1$.

In Fig. 4.21, it appears that for $\omega = 9.95 \times 10^9$ rad/s, NNP is of the order of 10^{-6} only, the nonreciprocal chiral nihility would then be realized. On the other hand, the imaginariy part for NNP is of the order of 0.1 at this frequency. As a consequence, the forward and backward waves propagating in the medium would be decaying waves. Thus, the nonreciprocity parameter χ might be used as an additional parameter to achieve chiral nihility. It is also worth noting that if the bi-isotropic medium has no dispersion and lossless, the limiting case of $\chi = \sqrt{\epsilon_T \mu_T}/\sqrt{\epsilon_0 \mu_0}$ implies that this medium carries zero power [134]. However, due to the dispersion, the lossy chiral medium can still convey some power even if the NNP is very close to zero. Thus, it can be concluded that dispersive nonreciprocal chiral nihility material has properties which are quite different from those of the reciprocal chiral nihility media. These properties are quite unique and interesting, but a detailed study is currently outside the scope of this thesis.

Correction to a problem in magnetoelectric composites

According to the *wavefield* theory in [134], the electric and magnetic fields in bi-isotropic materials (as shown in Eq. (4.2)) can be split into two portions corresponding to their respective polarizations

$$\boldsymbol{E} = \boldsymbol{E}_+ + \boldsymbol{E}_- \tag{4.88a}$$

$$\boldsymbol{H} = \boldsymbol{H}_+ + \boldsymbol{H}_-. \tag{4.88b}$$

Hence, the concept of effective medium can be introduced so that

$$\boldsymbol{D}^{\pm} = \epsilon_T^{\pm} \boldsymbol{E}^{\pm} \tag{4.89a}$$

$$\boldsymbol{B}^{\pm} = \mu_T^{\pm} \boldsymbol{H}^{\pm}, \tag{4.89b}$$

where the $\epsilon_T^{\pm}$ and $\mu_T^{\pm}$ are the effective isotropic mediums in equivalence. It can be found that the following relation between Eq. (4.2) and Eq. (4.89) reads

$$(\epsilon_T - \epsilon_T^{\pm})(\mu_T - \mu_T^{\pm}) = (\chi^2 + \kappa^2)\epsilon_0\mu_0. \tag{4.90}$$

From Eqs. (4.80) and (4.83), the equivalent mediums can be represented by

$$\begin{aligned}
\epsilon_T^{\pm} &= \frac{1}{\mu_T}\Big(\sqrt{\epsilon_T\mu_T - \chi^2\epsilon_0\mu_0} \pm \kappa\sqrt{\epsilon_0\mu_0}\Big)\Big(\sqrt{\epsilon_T\mu_T - \chi^2\epsilon_0\mu_0} \mp i\chi\sqrt{\epsilon_0\mu_0}\Big) && \text{(4.91a)}\\
\mu_T^{\pm} &= \mu_T\frac{\sqrt{\epsilon_T\mu_T - \chi^2\epsilon_0\mu_0} \pm \kappa\sqrt{\epsilon_0\mu_0}}{\sqrt{\epsilon_T\mu_T - \chi^2\epsilon_0\mu_0} \mp i\chi\sqrt{\epsilon_0\mu_0}}. && \text{(4.91b)}
\end{aligned}$$

A recent paper [157] also discussed the magnetoelectric composites in gyrotropic form. However, J. Q. Shen ended up with incorrect results due to the misuse of *wavefield* theory [134]. Similar notations as used in [157] (the Tellegen formalism) are employed for the convenience of comparison. The constitutive relations of the general nonreciprocal bi-isotropic media introduced by Sihvola *et al* [158] were used in [157]

$$\begin{aligned}
\boldsymbol{D} &= \epsilon\epsilon_0\boldsymbol{E} + (\chi + i\kappa)\boldsymbol{H} && \text{(4.92a)}\\
\boldsymbol{B} &= \mu\mu_0\boldsymbol{H} + (\chi - i\kappa)\boldsymbol{E}. && \text{(4.92b)}
\end{aligned}$$

It is certainly a special case of the gyrotropic chiral media, in which the permittivity and permeability are characterized by gyrotropic tensors

$$\overline{\boldsymbol{\epsilon}} = \begin{bmatrix} \epsilon_1 & -i\epsilon_2 & 0 \\ i\epsilon_2 & \epsilon_1 & 0 \\ 0 & 0 & \epsilon_3 \end{bmatrix} \tag{4.93a}$$

$$\overline{\boldsymbol{\mu}} = \begin{bmatrix} \mu_1 & -i\mu_2 & 0 \\ i\mu_2 & \mu_1 & 0 \\ 0 & 0 & \mu_3 \end{bmatrix}. \tag{4.93b}$$

Apparently, if the gyroelectric and gyromagnetic parameters are zero (i.e., $\epsilon_2 = \mu_2 = 0$), the material becomes bi-isotropic. According to the results obtained by the equivalent medium theory [134], the equivalent parameters for bi-isotropic materials can be deduced from [Eq. (6) in [157]] by assuming $\epsilon_2 = \mu_2 = 0$

$$\epsilon_{\pm} = \sqrt{\frac{\epsilon_1}{\mu_1}}\left[\sqrt{\epsilon_1\mu_1 - \frac{\chi^2}{\epsilon_0\mu_0}} \pm \frac{\kappa}{\sqrt{\epsilon_0\mu_0}}\right] \tag{4.94a}$$

$$\mu_{\pm} = \sqrt{\frac{\mu_1}{\epsilon_1}}\left[\sqrt{\epsilon_1\mu_1 - \frac{\chi^2}{\epsilon_0\mu_0}} \pm \frac{\kappa}{\sqrt{\epsilon_0\mu_0}}\right], \tag{4.94b}$$

and the wave impedance is then

$$\eta_{\pm} = \sqrt{\mu_{\pm}/\epsilon_{\pm}} = \sqrt{\mu_1/\epsilon_1}. \tag{4.95}$$

Thus, only one impedance is obtained for the two eigenwaves and it is independent of the nonreciprocity parameter χ and chirality κ. This is quite problematic for a nonreciprocal medium. Also, Eq. (4.94) is contradictory with my result in Eq. (4.91). My further derivation shows that the results in [157] are incorrect.

Let us consider the simplest situation (i.e., $\epsilon_2 = \mu_2 = 0$, $\epsilon_3 = \epsilon_1$, and $\mu_3 = \mu_1$) as a proof. Hence, the bi-isotropic medium can be expressed using J. Q. Shen's notation (e.g., $i \to j$)

$$\boldsymbol{D} = \epsilon_1\epsilon_0\boldsymbol{E} + (\chi + j\kappa)\boldsymbol{H} \tag{4.96a}$$

$$\boldsymbol{B} = \mu_1\mu_0\boldsymbol{H} + (\chi - j\kappa)\boldsymbol{E}. \tag{4.96b}$$

Substituting the above equations into Maxwell equations, we have

$$\boldsymbol{\nabla} \times \boldsymbol{\nabla} \times \boldsymbol{E} - 2\omega\kappa\boldsymbol{\nabla} \times \boldsymbol{E} - \omega^2[\epsilon_1\mu_1\epsilon_0\mu_0 - (\chi^2 + \kappa^2)] = 0. \tag{4.97}$$

By using the Bohren's method on decomposition [159], electromagnetic waves can be expressed linearly in terms of two right- and left-handed circularly polarized waves (RCP and LCP). In accordance with Shen's notation, the subscripts + and − denote RCP and LCP, respectively. Therefore, the fields $\boldsymbol{E}$ and $\boldsymbol{H}$ are defined as

$$\begin{bmatrix} \boldsymbol{E} \\ \boldsymbol{H} \end{bmatrix} = \overline{\boldsymbol{A}} \begin{bmatrix} \boldsymbol{Q}_- \\ \boldsymbol{Q}_+ \end{bmatrix} \tag{4.98}$$

where $Q_\pm$ satisfy the following Helmholtz equations

$$\boldsymbol{\nabla}^2\boldsymbol{Q}_- + k_-^2\boldsymbol{Q}_- = 0 \tag{4.99a}$$

$$\boldsymbol{\nabla}^2\boldsymbol{Q}_+ + k_+^2\boldsymbol{Q}_+ = 0. \tag{4.99b}$$

By modifying the results of diagonalization, one can end up with

$$\overline{\boldsymbol{A}} = \begin{bmatrix} 1 & -j\eta_+ \\ -j/\eta_- & 1 \end{bmatrix} \tag{4.100}$$

from which the electromagnetic fields can be presented finally

$$\boldsymbol{E} = \boldsymbol{Q}_- - j\eta_+\boldsymbol{Q}_+ \tag{4.101a}$$

$$\boldsymbol{H} = \frac{-j}{\eta_-}\boldsymbol{Q}_- + \boldsymbol{Q}_+. \tag{4.101b}$$

During the process, the wave numbers and wave impedances are found

$$k_\pm = \omega\Big(\sqrt{\epsilon_1\mu_1\epsilon_0\mu_0 - \chi^2} \pm \kappa\Big) \tag{4.102a}$$

$$\eta_\pm = \frac{\mu_1\mu_0}{\sqrt{\epsilon_1\mu_1\epsilon_0\mu_0 - \chi^2} \mp i\chi}, \tag{4.102b}$$

which agree with the previous result in Eq. (4.83).

Comparing my results in Eq. (4.102) with Shen's results in Eq. (4.94), it is obvious that if the medium is lossless, the equivalent parameters will still possess imaginary parts, contrary to Shen's results. On the other hand, I have obtained two independent wave impedances which are dependent on the nonreciprocity parameter χ (see Eq. (4.102b)) though the wave number is identical to the results obtained in [157].

Furthermore, Shen [157] discussed the negative refraction in a magnetoelectrically anisotropic material. Actually, it is just a case of uniaxial Ω-material, which has been well developed by Tretyakov *et al* [137]. If it is assumed as $\chi_{12} = -\chi_{21} = -iK$ (which is certainly one of the kinds of Shen's "magnetoelectrically anisotropic material"), the wave numbers of two mutually perpendicular polarized eigenmodes in [157] would be

$$k_{a,b}^{\pm} \quad = \quad \omega(\pm\sqrt{\epsilon\mu} - iK) \tag{4.103}$$

where K represents the magnetoelectric coupling effect of Ω-shaped particles.

Following all the assumptions made in [157] (i.e., propagation parallel to z-direction, $\overline{\boldsymbol{\epsilon}} = \epsilon\overline{\boldsymbol{I}}$, and $\overline{\boldsymbol{\mu}} = \mu\overline{\boldsymbol{I}}$), one can finally find that the wave numbers of eigenmodes can be expressed by taking Fourier transform of Maxwell equations

$$k = \omega\sqrt{\epsilon\mu - K^2} \tag{4.104}$$

which agrees with the results in [137, 160].

Therefore, it is proved that Shen's results in [157] are incorrect because the assumption forced by Shen at the Section IV will simplify the analysis of uniaxial Ω materials inappropriately, which will lose much information. Instead, if one still wants to study this case, one has to start from the wave splitting first by imposing

$$\boldsymbol{E} = E_z\hat{\boldsymbol{z}} + \boldsymbol{E}_t \tag{4.105a}$$

$$\boldsymbol{H} = H_z\hat{\boldsymbol{z}} + \boldsymbol{H}_t \tag{4.105b}$$

and use Fourier transform in Maxwell equations in the transverse plane and eliminate the normal fields. After obtaining the transverse components, the normal fields can thus be expressed by these transverse fields. Finally, the propagation constants for polarized eigenmodes will be found. Only after this stage, one can assume that the wave is traveling along z-direction (i.e., transverse wave number $k_t = 0$), and the proper solutions for the normal propagation can be yielded as in Eq. (4.104).

In summary, when the Beltrami [152] or wavefield theory [134] is involved, one has to be cautious. For instance, if we consider the most generalized form of materials

$$\boldsymbol{D} = \overline{\boldsymbol{\epsilon}}\boldsymbol{E} + \overline{\boldsymbol{\xi}}\boldsymbol{H} \tag{4.106a}$$

$$\boldsymbol{B} = \overline{\boldsymbol{\zeta}}\boldsymbol{E} + \overline{\boldsymbol{\mu}}\boldsymbol{H}. \tag{4.106b}$$

If all of the parameters in above equations are scalars, the Beltrami/wavefield theory can be employed without restriction. However, if any of the parameters is a gyrotropy tensor, the wavefield theory cannot be implemented directly. All the formulation has to be started from solving Maxwell's equations at the very beginning.

Gyrotropic chiral nihility

Since purely isotropic chiral material are hard to fabricate [161], I also studied the nihility effects in more general and practical chiral materials, the wave properties of which have been discussed in Section 4.3.

Although the nonreciprocity parameter in general bi-isotropic media offers an additional degree of freedom to achieve chiral nihility, the nihility condition is still a challenge to satisfy in practice due to the difficulty of realizing artificial nonreciprocal bi-isotropic media. In this section, another possibility of creating chiral nihility is investigated, it concerns gyrotropic chiral media with gyrotropy [149, 150, 162], either in permittivity/permeability or in magnetoelectric parameters. Introduction of certain anisotropy or gyrotropy may provide methods to control chirality. This category of chiral media has three subsets: 1) Ω–medium; 2) chiroplasma medium; and 3) chiroferrite medium. Although Ω–medium can exhibit negative refraction and most probably nihility, the investigation is mainly restricted to chiroplasma and chiroferrite [163]. Chiroplasma can be realized by embedding chiral inclusions in a magnetically biased plasma, which result in the gyrotropic tensor in permittivity, while chiroferrites can be made from chiral inclusions immersed into ferrites with biased magnetic fields, which leads to a gyrotropic tensor in permeability. An example of such media is the generalized form of Faraday chiral media.

Based on the viewpoint of practical application, Post notations are employed to describe such media as in Eq. (4.15) and the parameters are defined as in Eqs. (4.36) and (4.52). Looking back into the result of refractive indices shown in Eq. (4.55), one can further rewrite

$$n_{\pm} = c_0\Big[\sqrt{\xi_c^2(\mu \pm l)^2 + (\epsilon \pm g)(\mu \pm l)} - \xi_c(\mu \pm l)\Big]. \tag{4.107}$$

Therefore, the condition for achieving gyrotropic nihility is:

$$\xi_c^2 = -(\epsilon \pm g)/(\mu \pm l). \tag{4.108}$$

The off-diagonal elements (i.e., g and l) can be both modified to achieve the nihility condition. By a proper choice of the off-diagonal elements (i.e., g and l), the gyrotropic chiral nihility condition of Eq. (4.108) can be achieved even for media with low degree of chirality ξ_c. The frequency under the solid lines in Fig. 4.22 indicates the valid range to have the gyrotropic chiral nihility.

It can be shown from Fig. 4.22 that the electron collision frequency ω_{eff} plays an important role in achieving gyrotropic nihility. Only the values on the solid line where ξ_c^2 is positive is valid to realize the gyrotropic nihility, provided that the chirality is real. For high values of ω_{eff}, for instance for $\omega_{eff} = 0.02 \times 10^9$ rad/s, a much higher chirality is needed to match the requirement of gyrotropic nihility compared to the case when $\omega_{eff} = 0.5 \times 10^9$ rad/s. The smaller the collision frequency, the higher the chirality needed to satisfy the nihility condition. Therefore, the electron collision in the plasma is found to facilitate the chirality control of gyrotropic nihility. It is due to the fact that self-spin and the collision of electrons may strengthen the degree of magnetoelectric coupling in gyrotropic chiral media, which compensates the nihility requirement for chirality.

Therefore, in order to satisfy the condition of gyrotropic nihility, the frequency

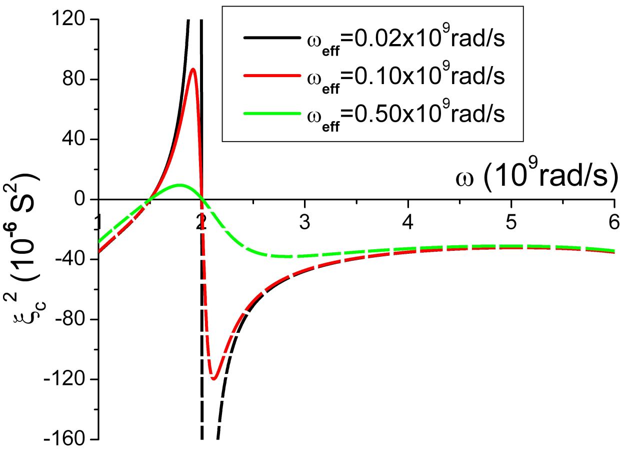

Figure 4.22: Chirality control at the scale of ξ_c^2 ($10^{-6} Siemens^2$) to satisfy the n_- condition of a gyrotropic nihility for gyrotropic chiral material at different electron collision frequencies: $\omega_p = 8 \times 10^9$ rad/s, $\omega_g = 2 \times 10^9$ rad/s, $\omega_0 = 1.5 \times 10^9$ rad/s, and $\omega_M = 6 \times 10^9$ rad/s.

should be chosen within a specific range, apart from which gyrotropic chiral nihility can never be realized no matter what the value of the chirality is. Once the gyrotropic nihility is satisfied, the refractive indices become

$$n_{+}^{nih} = -c_0(\mu + l)\xi_c \tag{4.109}$$

$$n_{-}^{nih} = c_0(l - \mu)\xi_c. \tag{4.110}$$

It can be found that n_{+}^{nih} will be negative because of $\mu + l > 0$ (see Eq. (4.52)). Of particular interest is the negative refraction for n_{-}^{nih}, which has resonance in the vicinity of ferromagnetic frequency ω_0. At the frequency range $0 < \omega < \omega_0^{-} \cup \omega_0 + \omega_M < \omega$, negative refraction will occur to n_{-}^{nih}.

Image of the chiral nihility

Another interesting case is that of a chiral nihility slab backed by a PEC plate. Negative reflection associated with partial focusing in strong chiral materials backed by PEC has been reported in [155]. In this part of the thesis, the image of the chiral nihility is particularly studied so as to replace the PEC with a “mirror” counterpart. In this way, the material-PEC interface will be changed into material-material interface, and thus multilayer algorithm as discussed in Section 2.2 can be employed to describe the multiple wave interaction in the layered structures.

Assuming that the half space $z > d$ is occupied by a perfectly conducting materials in Fig. 4.15, a linearly polarized wave is normally impinged upon the interface at $z = 0$

$$\boldsymbol{E}_{inc} = \widehat{\boldsymbol{y}} E_{inc}^{y} e^{ik_{inc}z} \tag{4.111a}$$

$$\boldsymbol{H}_{inc} \;=\; -\widehat{\boldsymbol{x}}\frac{E^y_{inc}}{\eta_{inc}}e^{ik_{inc}z}. \tag{4.111b}$$

Taking into account the boundary conditions at material-material interface ($z = 0$) and material-PEC interface ($z = d$) for x and y components of the electromagnetic fields, one can rewrite the incident and reflected waves in the region $z < 0$ and transmitted waves in the slab ($0 < z < d$) by setting θ_i to zero in [129]

$$\begin{bmatrix} E^y_r \\ 0 \\ E^+_{01} \\ E^+_{02} \\ E^-_{01} \\ E^-_{02} \\ 0 \\ 0 \end{bmatrix} = \overline{\boldsymbol{Q}}^{-1} \begin{bmatrix} 0 \\ E^y_{inc} \\ E^y_{inc} \\ 0 \\ 0 \\ 0 \\ 0 \\ 0 \end{bmatrix} \tag{4.112}$$

where E^+_{01}/E^+_{02} is the forward RCP/LCP waves inside the slab ($0 < z < d$) and E^-_{01}/E^-_{02} is the backward RCP/LCP waves inside the slab. Therefore the reflected wave is found to be copolarized with the incident wave, and the S-parameter for normal incidence on such a PEC-backed chiral nihility slab can be described in the Tellegen's formalism as

$$S_{11} = \frac{\frac{\sqrt{\frac{\mu}{\epsilon}}-\sqrt{\frac{\mu_0}{\epsilon_0}}}{\sqrt{\frac{\mu}{\epsilon}}+\sqrt{\frac{\mu_0}{\epsilon_0}}} - e^{2i\omega\sqrt{\mu\epsilon}d}}{1 - \frac{\sqrt{\frac{\mu}{\epsilon}}-\sqrt{\frac{\mu_0}{\epsilon_0}}}{\sqrt{\frac{\mu}{\epsilon}}+\sqrt{\frac{\mu_0}{\epsilon_0}}}e^{2i\omega\sqrt{\mu\epsilon}d}}, \tag{4.113}$$

where the condition of chiral nihility ($\sqrt{\mu/\epsilon} \rightarrow finite$ and $\sqrt{\mu\epsilon} \rightarrow 0$) further leads to

$$S_{11}^{nih} = -1. \tag{4.114}$$

Hence it is interesting to find that a chiral nihility slab ($0 < z < d$) backed by a PEC will behave like a perfect conductor to the normal incident waves. The wave will be totally reflected at $z = 0$ with a 180° phase change.

Apparently, the above finding is only applicable for chiral nihility slab backed by PEC. To consider similar problems for gyrotropic chiral nihility, it is better to introduce a *mirror* material for the space occupied by PEC. In such problems, the image properties of gyrotropic chiral nihility have to be first formulated, which can be certainly reduced to the isotropic chiral nihility. Consider a gyrotropic chiral nihility filling the half space $z > 0$ and a perfectly conducting plane is put at $z = 0$. Keep in mind that the gyrotropic chiral nihility is a special type of gyrotropic chiral material defined in Eq. (4.15), which takes the form of Eq. (4.108). In the space of $z > 0$ and $z < 0$, the source-incorporated Maxwell's equations can be established, respectively

$$\begin{aligned} \boldsymbol{\nabla} \times \boldsymbol{E} &= -\frac{\partial \boldsymbol{B}}{\partial t} && (4.115\text{a}) \\ \boldsymbol{\nabla} \times \boldsymbol{H} &= \frac{\partial \boldsymbol{D}}{\partial t} + \boldsymbol{J} && (4.115\text{b}) \end{aligned}$$

and

$$\begin{aligned} \check{\boldsymbol{\nabla}} \times \check{\boldsymbol{E}} &= -\frac{\partial \check{\boldsymbol{B}}}{\partial t} && (4.116\text{a}) \\ \check{\boldsymbol{\nabla}} \times \check{\boldsymbol{H}} &= \frac{\partial \check{\boldsymbol{D}}}{\partial t} + \check{\boldsymbol{J}} && (4.116\text{b}) \end{aligned}$$

where the ˇ denote the image materials in $z < 0$ with the removal of PEC. The conventional boundary conditions still hold so that the tangential electric fields are continuous and normal B_z vanishes at $z = 0$. Thus, the relation of EM fields and source between the original and mirror materials reads

$$\begin{aligned} \boldsymbol{J} &= \check{\overline{\boldsymbol{I}}}\check{\boldsymbol{J}} \qquad (4.117a) \\ \boldsymbol{E} &= \check{\overline{\boldsymbol{I}}}\check{\boldsymbol{E}} \qquad (4.117b) \\ \boldsymbol{B} &= -\check{\overline{\boldsymbol{I}}}\check{\boldsymbol{B}} \qquad (4.117c) \end{aligned}$$

where

$$\check{\overline{\boldsymbol{I}}} = -\overline{\boldsymbol{I}}_t + \hat{\boldsymbol{z}}\hat{\boldsymbol{z}}. \qquad (4.118)$$

$\overline{\boldsymbol{I}}_t$ is the 2-D unit dyad.

Using the algebraic relationship in [164], i.e.,

$$\check{\boldsymbol{\nabla}} \times \boldsymbol{A} = (\check{\overline{\boldsymbol{I}}}\boldsymbol{\nabla}) \times \boldsymbol{A} = -\check{\overline{\boldsymbol{I}}}[\boldsymbol{\nabla} \times (\check{\overline{\boldsymbol{I}}}\boldsymbol{A})], \qquad (4.119)$$

one can obtain the following relations of the material parameters between original and mirror gyrotropic chiral materials in Eq. (4.15) by manipulating Eqs. (4.115)-(4.117)

$$\begin{aligned} \overline{\boldsymbol{\epsilon}}_P &= \check{\overline{\boldsymbol{\epsilon}}}_P \qquad (4.120a) \\ \overline{\boldsymbol{\mu}}_P &= \check{\overline{\boldsymbol{\mu}}}_P \qquad (4.120b) \\ \xi_c &= -\check{\xi}_c. \qquad (4.120c) \end{aligned}$$

Thus, it is straightforward that, if the gyrotropic chiral nihility is present at the original material in the space $z > 0$, the mirror counterpart also possesses gyrotropic chiral nihility but with reversed handedness. In doing so, a PEC bounded problem is transformed into a layered problem. The multilayered gyrotropic chiral materials will be further investigated in Chapter 5 in detail.

If the current problem is reduced to an isotropic case (a chiral nihility slab backed by a PEC), it can be seen that the image of isotropic chiral nihility can be depicted by $-\xi_c$. According to the definition of handedness, if the condition of chiral nihility [70] is realized by the wire-loop configuration in Fig. 4.1, one can use the same structure simply by replacing the clockwise spirals with anti-clockwise spirals to achieve negative chiral nihility. Paring those two structures together will lead to an interesting bilayer device. Due to the insulation of this bilayer, the wave can never be transmitted to the other side of such device, because each layer in such bilayer can, in turn, behave as a effective PEC depending on the propagation direction.

4.5 Summary

In this chapter, the electromagnetic theory of magnetoelectric composites are intensively investigated, with the particular interest in realization of backward-wave and negative-index regimes. Wide applications in resonator, phase compensator, directive antennas and quantum devices are also reported. Different medium formalisms of isotropic and gyrotropic magnetoelectric composites are discussed, and it is found that for isotropic magnetoelectric cases the formalisms are all equivalent, while for gyrotropic magnetoelectric cases each formalisms have pros and cons in the viewpoints of NIM realization and practical application. The Post's formalism is therefore found to be more suitable to describe the gyrotropic magnetoelectric composites. The gyrotropy parameters also favor the realization of negative refraction because they will make the wave propagate backward. The eigenmodes at backward-wave regime and their frequency ranges are discussed for dispersive gyrotropic magnetoelectric composites. Based on that, the negative refraction can be achieved by a selection of working frequency. As more interesting cases, the chiral nihility, isotropic and gyrotropic, are examined. The energy transport in chiral nihility is extensively examined. The effects of magnetoelectric coupling in the energy transport are characterized through numerical studies. A wide range of Brewster angles is discovered and electromagnetic wave through a chiral nihility slab is studied. In the following, general nihility routes for magnetoelectric composites to NIMs are proposed for isotropic, nonreciprocal and gyrotropic chiral composites, where the requirements to meet respective nihility condition such as frequency control and chirality control are also presented. For the isotropic chiral nihility, the Drude-Born-Fedorov formalism is proven to be inappropriate due to the lack of physics. A nonreciprocal chiral nihility is thus shown, which makes the nihility condition easier to fulfill. Furthermore, the gyrotropic chiral nihility, based on the previous study on gyrotropic chiral composites Section 4.3, is investigated and one can find that it provides more degrees of freedom to meet the nihility condition due to the contributions of gyrotropic parameters. Chirality control is presented and it reveals that more of electron collision in plasma could alleviate the chirality requirement for gyrotropic chiral nihility. Finally, the total reflection by a slab of chiral nihility backed by PEC is founded by studying the S-parameters, and the image of chiral nihility is formulated in the presence of PEC. Based on the theoretical findings, some interesting applications are discussed.

Chapter 5

Macroscopic solutions to Maxwell's equations for inhomogeneous composites

In view of the inhomogeneity of various types and arrangments in composites, it invloves many intricacies in their rigorous modeling and characterization, theoretically as well as experimentally. Their eligibility as benchmarks or certified reference materials justifies their investigation for the purpose of material and instrumentation calibration, beyond the existing wide interest in them for other purposes and applications. Such composite specimens can be devised to yield a set of tailored and calculable material systems.

In analytical electromagnetic modeling, the macroscopic solutions to Maxwell's equations become meaningful. Such solutions provide the electromagnetic properties of periodically structured composites in a macroscopic view. In this respect, two issues are of great importance in the macroscopic studies of inhomogeneous composites: the Green's functions [165] and the homogenization process [166]. However, the conventional senses of these issues have respective drawbacks. For instance, conventional Green's functions can not provide an analytical series of results in a compact form, and homogenization process cannot consider the strong internal interaction or shape effects. Hence, the macroscopic modeling techniques presented in this chapter are developed at advanced levels, providing more direct and accurate descriptions of systematic responses of inhomogeneous composites.

In the first half of this chapter, I will discuss the dyadic Green's functions characterization for a particular type of magnetoelectric composites: gyrotropic chiral composites. This type of composites has been intensively investigated in Chapter 4, especially on addressing its possibility of realizing negative refraction, electromagnetic wave properties, and advantages over normal chiral materials. Due to its generality in constitution and potentials in application, dyadic Green's functions (DGFs) are constructed for unbounded and layered structured gyrotropic chiral composites. DGFs can be regarded as a dielectric response or a mathematical kernel, relating electromagnetic scattering/radiation with the structure's geometry/parameter and the illumination.

In contrast to the DGF interpretation, the effective medium theory based on improved homogenization will be proposed as a complementary interest in the second half of this chapter. The improved homogenization is based on the rigorous limit process instead of conventional averaging operations (e.g. Maxwell-Garnett and Bruggeman mixing rules). Also, the theorem will be extended to the most general case: bianisotropic composites. This mathematical tool, which employs the partial differential equations to describe the physical problem, is used to define the problems on the elementary period that identifies the fine periodic structure. From the solution, the macroscopic properties of the mixtures can be easily deduced, so that complex composites can be studied, avoiding unacceptable computational burden required by the solution to the electromagnetic field problem in the original inhomogenous domain. Therefore, it can be straightforwardly applied to study any composites of complex shape, either natural or artificial. Although the dyadic Green's functions have not been formulated for layered bianisotropic composites, the two theorems (i.e., DGFs and improved homogenization) can be still incorprated in many sub-cases in engineering. Once the effective medium paramters are determined, the electromagnetic waves in the composite and in near-/far- region outside the composite can be analytically determined.

5.1 Dyadic Green's functions for gyrotropic chiral composites

5.1.1 Introduction

Since gyrotropic chiral composites play an important role in the realm of the negative-index materials, further interests are extended to the macroscopic characterization of the structured gyrotropic chiral composites where Green's dyadics are constructed for various layered structures. The interaction between materials and electromagnetic waves is an important aspect in material characterization, Green dyadics are of particular interest for gyrotropic chiral media, which can describe the wave interaction in a macroscopic view. Dyadic Green's functions [165], which relate directly the radiated electromagnetic fields and the source distribution, provide a good way to characterize the macroscopic performance of artificial complex media including metamaterials. DGFs are powerful and can solve both source-free and source-incorporated boundary value problems for electromagnetic scattering, radiation, and propagation [167]. However DGFs in complex media like gyrotropic or metamaterials have not been well studied especially in multilayered structures, though the DGFs for some isotropic [168], chiral [169], anisotropic [170], chiroplasma [171] and bianisotropic [172] media have been formulated over the last three decades. The technique of eigenfunctional expansion provides a systematic approach in electromagnetic theory for interpreting various electromagnetic representations [95]. Most importantly, it is applicable in almost all the fundamental coordinates. Even in the cylindrical structure considered in detail in this section, the eigenfunctional expansion technique can provide an explicit form of the dyadic Green's functions, so that it becomes easy and convenient when the source distribution is independent from the azimuth directions or when the far-zone fields are computed. In the formulation of the dyadic Green's functions and their scattering coefficients, three cases are considered, *i.e.*, the current source is immersed in (1) the intermediate, (2) the first, and (3) the last regions, respectively. As compared to the existing results, the present work mainly contributes to: (1) the exact representation of the dyadic Green's functions, with irrotational part extracted out, for the gyrotropic chiral medium in multi-layered geometry, (2) scattering Green's dyadics in each layer are determined by a compact form of recurrence matrices, (3) due to the generality of the obtained DGFs, the present results can be reduced to either layered chiroferrite, chiroplasma or other simpler cases. After DGFs are obtained, the electromagnetic fields can be formulated analytically, provided that the source is known.

5.1.2 Preliminaries for DGFs in unbounded space

The gyrotropic chiral medium's constitution relations are described by the Post's relations:

$$\boldsymbol{D} = \overline{\boldsymbol{\epsilon}} \cdot \boldsymbol{E} + i\xi_c \boldsymbol{B} \tag{5.1a}$$

$$\boldsymbol{H} = i\xi_c \boldsymbol{E} + \overline{\boldsymbol{\mu}}^{-1} \cdot \boldsymbol{B}, \tag{5.1b}$$

where the gyrotropy in $\overline{\boldsymbol{\epsilon}}$ and $\overline{\boldsymbol{\mu}}$ has been given in Eqs. (4.17), (4.19) and (4.20).

Substituting Eq. (5.1) into the source incorporated Maxwell's equations, it is shown

$$\boldsymbol{\nabla} \times \Big[\overline{\boldsymbol{\alpha}} \cdot \boldsymbol{\nabla} \times \boldsymbol{E}\Big] - 2\omega\xi_c \boldsymbol{\nabla} \times \boldsymbol{E} - \omega^2 \overline{\boldsymbol{\epsilon}} \cdot \boldsymbol{E} = i\omega \boldsymbol{J}. \tag{5.2}$$

The electric field can thus be expressed in terms of the DGF and an electric source distribution as follows:

$$\boldsymbol{E}(\boldsymbol{r}) = i\omega \int_{V'} \overline{\boldsymbol{G}}_e(\boldsymbol{r}, \boldsymbol{r}') \cdot \boldsymbol{J}(\boldsymbol{r}')\, dV', \tag{5.3}$$

where V' denotes the volume occupied by the source. Substituting Eq. (5.3) into Eq. (5.2) leads to

$$\boldsymbol{\nabla}\times\left[\overline{\boldsymbol{\alpha}}\cdot\boldsymbol{\nabla}\times\overline{\boldsymbol{G}}_e\right]-2\omega\xi_c\boldsymbol{\nabla}\times\overline{\boldsymbol{G}}_e-\omega^2\overline{\boldsymbol{\epsilon}}\cdot\overline{\boldsymbol{G}}_e=\overline{\boldsymbol{I}}\delta(\boldsymbol{r}-\boldsymbol{r}'),\tag{5.4}$$

where $\overline{\boldsymbol{I}}$ and $\delta(\boldsymbol{r}-\boldsymbol{r}')$ denote the identity dyadic and Dirac delta function, respectively.

According to the well-known Ohm-Rayleigh method, the source term in Eq. (5.4) can be expanded in terms of the solenoidal and irrotational cylindrical vector wave functions in cylindrical coordinates. Thus, it is obtained

$$\begin{aligned}\overline{\boldsymbol{I}}\delta(\boldsymbol{r}-\boldsymbol{r}') &= \int_0^\infty d\lambda\int_{-\infty}^\infty dh\sum_{n=-\infty}^{\infty}\Big[\boldsymbol{M}_n(h,\lambda)\boldsymbol{A}_n(h,\lambda)\\ &\quad+\boldsymbol{N}_n(h,\lambda)\boldsymbol{B}_n(h,\lambda)+\boldsymbol{L}_n(h,\lambda)\boldsymbol{C}_n(h,\lambda)\Big]\end{aligned}\tag{5.5}$$

where the vector wave functions $\boldsymbol{M}$, $\boldsymbol{N}$ and $\boldsymbol{L}$ in cylindrical coordinate system are defined as

$$\boldsymbol{M}_n(h,\lambda) = \boldsymbol{\nabla}\times\left[\Psi_n(h,\lambda)\hat{\boldsymbol{z}}\right],\tag{5.6a}$$

$$\boldsymbol{N}_n(h,\lambda) = \frac{1}{k_\lambda}\boldsymbol{\nabla}\times\boldsymbol{M}_n(h,\lambda),\tag{5.6b}$$

$$\boldsymbol{L}_n(h,\lambda) = \boldsymbol{\nabla}\left[\Psi_n(h,\lambda)\right],\tag{5.6c}$$

with $k_\lambda=\sqrt{\lambda^2+h^2}$, and the generating function given by $\Psi_n(h,\lambda)=J_n(\lambda\rho)e^{i(n\phi+hz)}$. The coefficients $\boldsymbol{A}_n(h,\lambda)$, $\boldsymbol{B}_n(h,\lambda)$, and $\boldsymbol{C}_n(h,\lambda)$ in Eq. (5.5) are to be determined from the orthogonality relations among the cylindrical vector wave functions. Therefore, scalar-dot multiplying both sides of Eq. (5.5) with $\boldsymbol{M}_{-n'}(-h',-\lambda')$, $\boldsymbol{N}_{-n'}(-h',-\lambda')$ and $\boldsymbol{L}_{-n'}(-h',-\lambda')$ each at a time and integrating them over the entire source volume, one can obtain from the orthogonality that

$$\begin{aligned}\boldsymbol{A}_n(h,\lambda) &= \frac{1}{4\pi^2\lambda}\boldsymbol{M'}_{-n}(-h,-\lambda) &(5.7\text{a})\\ \boldsymbol{B}_n(h,\lambda) &= \frac{1}{4\pi^2\lambda}\boldsymbol{N'}_{-n}(-h,-\lambda) &(5.7\text{b})\\ \boldsymbol{C}_n(h,\lambda) &= \frac{\lambda}{4\pi^2(\lambda^2+h^2)}\boldsymbol{L'}_{-n}(-h,-\lambda). &(5.7\text{c})\end{aligned}$$

The unbounded dyadic Green's function can thus be expanded as follows:

$$\begin{aligned}\overline{\boldsymbol{G}}_0(\boldsymbol{r},\boldsymbol{r'}) &= \int_0^\infty d\lambda\int_{-\infty}^{\infty}dh\sum_{n=-\infty}^{\infty}\Big[\boldsymbol{M}_n(h,\lambda)\,\boldsymbol{a}_n(h,\lambda)\\ &\quad+\boldsymbol{N}_n(h,\lambda)\,\boldsymbol{b}_n(h,\lambda)+\boldsymbol{L}_n(h,\lambda)\,\boldsymbol{c}_n(h,\lambda)\Big], \qquad (5.8)\end{aligned}$$

where the vector expansion coefficients $\boldsymbol{a}_n(h,\lambda)$, $\boldsymbol{b}_n(h,\lambda)$ and $\boldsymbol{c}_n(h,\lambda)$ are unknown vector coefficients to be determined from the orthogonality and permittivity and permeability tensors' properties. To obtain these unknown vectors, Eq. (5.8) and Eq. (5.5) are substituted into Eq. (5.4), noting the instinct properties of the vector wave functions of

$$\begin{aligned}\boldsymbol{\nabla}\times\boldsymbol{N}_n(h,\lambda) &= k_\lambda\boldsymbol{M}_n(h,\lambda) &(5.9\text{a})\\ \boldsymbol{\nabla}\times\boldsymbol{M}_n(h,\lambda) &= k_\lambda\boldsymbol{N}_n(h,\lambda) &(5.9\text{b})\\ \boldsymbol{\nabla}\times\boldsymbol{L}_n(h,\lambda) &= 0. &(5.9\text{c})\end{aligned}$$

One can thus obtain

$$\begin{aligned}&\int_0^\infty d\lambda\int_{-\infty}^{\infty}dh\sum_{n=-\infty}^{\infty}\Big[\boldsymbol{M}_n(h,\lambda)\boldsymbol{A}_n(h,\lambda)+\boldsymbol{N}_n(h,\lambda)\boldsymbol{B}_n(h,\lambda)+\boldsymbol{L}_n(h,\lambda)\boldsymbol{C}_n(h,\lambda)\Big]\\ &=\int_0^\infty d\lambda\int_{-\infty}^{\infty}dh\sum_{n=-\infty}^{\infty}\Big\{\boldsymbol{\nabla}\times\Big[\overline{\boldsymbol{\alpha}}\cdot k_\lambda\Big(\boldsymbol{N}_n(h,\lambda)\boldsymbol{a}_n(h,\lambda)+\boldsymbol{M}_n(h,\lambda)\boldsymbol{b}_n(h,\lambda)\Big)\Big]-\\ &\quad 2k_\lambda\omega\xi_c\Big[\boldsymbol{N}_n(h,\lambda)\boldsymbol{a}_n(h,\lambda)+\boldsymbol{M}_n(h,\lambda)\boldsymbol{b}_n(h,\lambda)\Big]-\\ &\quad \omega^2\overline{\boldsymbol{\epsilon}}\cdot\Big[\boldsymbol{M}_n(h,\lambda)\boldsymbol{a}_n(h,\lambda)+\boldsymbol{N}_n(h,\lambda)\boldsymbol{b}_n(h,\lambda)+\boldsymbol{L}_n(h,\lambda)\boldsymbol{c}_n(h,\lambda)\Big]\Big\}. \qquad (5.10)\end{aligned}$$

By substituting Eq. (5.8) into Eq. (5.4), taking respectively the anterior scalar product of Eq. (5.10) with the vector wave equations, and performing the integration over the entire source volume, one can formulate the equations satisfied by the unknown vectors and the known scalar and vector parameters in a matrix form given by

$$[\Phi][X] = [\Theta] \tag{5.11}$$

where

$$[\Phi] = \begin{bmatrix} h^2\alpha_t + \lambda^2\alpha_z - \omega^2\epsilon & -\left(\frac{\omega^2 hg}{k_\lambda} + k_\lambda h\sigma + 2\omega\xi_c k_\lambda\right) & i\omega^2 g \\ -\left(\frac{\omega^2 hg}{k_\lambda} + k_\lambda h\sigma + 2\omega\xi_c k_\lambda\right) & k_\lambda^2\alpha_t - \omega^2\frac{h^2\epsilon+\lambda^2\epsilon_z}{k_\lambda^2} & -\omega^2\frac{ih}{k_\lambda}(\epsilon_z - \epsilon) \\ -i\omega^2\frac{\lambda^2}{k_\lambda^2}g & \omega^2\frac{ih\lambda^2}{k_\lambda^3}(\epsilon_z - \epsilon) & -\omega^2\frac{h^2\epsilon_z+\lambda^2\epsilon}{k_\lambda^2} \end{bmatrix}$$

and $[X]$ and $[\Theta]$ are known and parameter column vectors given by

$$[X] = \Big[\boldsymbol{a}_n(h,\lambda), \boldsymbol{b}_n(h,\lambda), \boldsymbol{c}_n(h,\lambda)\Big]^T, \text{ and } [\Theta] = \Big[\boldsymbol{A}_n(h,\lambda), \boldsymbol{B}_n(h,\lambda), \boldsymbol{C}_n(h,\lambda)\Big]^T.$$

After solving Eq. (5.11), the solutions to $\boldsymbol{a}_n(h,\lambda)$, $\boldsymbol{b}_n(h,\lambda)$ and $\boldsymbol{c}_n(h,\lambda)$ are shown as follows

$$\begin{aligned} \boldsymbol{a}_n(h,\lambda) &= \frac{1}{\Gamma}[\alpha_1\boldsymbol{A}_n(h,\lambda) + \beta_1\boldsymbol{B}_n(h,\lambda) + \gamma_1\boldsymbol{C}_n(h,\lambda)] \\ \boldsymbol{b}_n(h,\lambda) &= \frac{1}{\Gamma}[\alpha_2\boldsymbol{A}_n(h,\lambda) + \beta_2\boldsymbol{B}_n(h,\lambda) + \gamma_2\boldsymbol{C}_n(h,\lambda)] \\ \boldsymbol{c}_n(h,\lambda) &= \frac{1}{\Gamma}[\alpha_3\boldsymbol{A}_n(h,\lambda) + \beta_3\boldsymbol{B}_n(h,\lambda) + \gamma_3\boldsymbol{C}_n(h,\lambda)] \end{aligned}$$

where

$$\Gamma = \epsilon_z\alpha_t(k_\lambda^2 - k_1^2)(k_\lambda^2 - k_2^2)/\alpha_z \tag{5.13}$$

and

$$k_{1,2}^2 = \frac{1}{2\epsilon_z\alpha_t/\alpha_z}\Big[-p_\lambda \pm \sqrt{p_\lambda^2 + 4\epsilon_z\alpha_t/\alpha_z q_\lambda}\Big] \tag{5.14}$$

with p_λ and q_λ given respectively below:

$$\begin{aligned} p_\lambda &= [(\alpha_t/\alpha_z)^2 - (\sigma/\alpha_z)^2]h^2\epsilon - 4h\epsilon\xi_c\omega\sigma/\alpha_z^2 - \\ &\quad [4\epsilon(\xi_c/\alpha_z)^2 + \epsilon\epsilon_z/\alpha_z]\omega^2 + (g^2-\epsilon^2)\omega^2\alpha_t/\alpha_z^2 - h^2\epsilon_z\alpha_t/\alpha_z \end{aligned} \tag{5.15a}$$

$$\begin{aligned} q_\lambda &= -[(\alpha_t/\alpha_z)^2 - (\sigma/\alpha_z)^2]h^4\epsilon_z + 4h^2(2h\xi_c + g\omega)\epsilon_z\omega\sigma/\alpha_z^2 + \\ &\quad \frac{\epsilon_z}{\alpha_z^2}[4h^2\xi_c^2 + 4gh\xi_c\omega + (g^2-\epsilon^2)\omega^2 + 2\alpha_t h^2\epsilon\epsilon_z]\omega^2. \end{aligned} \tag{5.15b}$$

It should be noted that the coupling coefficients β_1, γ_1, α_2, γ_2, α_3 and β_3 were assumed to be zero in [171]. Here it is proved that those coupling coefficients must be considered in the formulation since they are not always zero, and the coupling coefficients $\alpha_{1,2,3}$, $\beta_{1,2,3}$ and $\gamma_{1,2,3}$ are given in detail below

$$\alpha_1 = \frac{\alpha_t}{\alpha_z^2}(h^2\epsilon_z + \lambda^2\epsilon) - \frac{1}{\alpha_z^2}\omega^2\epsilon\epsilon_z, \tag{5.16a}$$

$$\alpha_2 = \beta_1 = \frac{1}{k_\lambda\alpha_z^2}\left[ih\alpha_a(h^2\epsilon_z + \lambda^2\epsilon) + 2\xi_c(h^2\epsilon_z + \epsilon\lambda^2)\omega + hg\epsilon_z\omega^2\right], \tag{5.16b}$$

$$\gamma_1 = -\frac{k_\lambda^2}{\lambda^2}\alpha_3 = \frac{i}{\alpha_z^2}\left[gk_\lambda^2\alpha_t + ih^2\alpha_a(\epsilon-\epsilon_z) + 2h\xi_c(\epsilon-\epsilon_z)\omega - g\epsilon_z\omega^2\right], \tag{5.16c}$$

$$\begin{aligned} \gamma_2 &= -\frac{k_\lambda^2}{\lambda^2}\beta_3 \\ &= \frac{i}{k_\lambda}\Big[h(h^2\frac{\alpha_t}{\alpha_z} + \lambda^2)(\epsilon-\epsilon_z)/\alpha_z + ighk_\lambda^2\alpha_a/\alpha_z^2 \\ &\quad +2g\xi_c k_\lambda^2\omega/\alpha_z^2 - h(\epsilon^2 - \epsilon\epsilon_z - g^2)\omega^2/\alpha_z^2\Big], \end{aligned} \tag{5.16d}$$

$$\beta_2 = \frac{1}{k_\lambda^2}\Big[(h^2\frac{\alpha_t}{\alpha_z} - \lambda^2)(h^2\epsilon_z + \lambda^2\epsilon)/\alpha_z - (h^2\epsilon\epsilon_z + \lambda^2(\epsilon^2 - g^2))\omega^2/\alpha_z^2\Big], \tag{5.16e}$$

$$\begin{aligned} \gamma_3 &= \frac{1}{\omega^2}\Big\{-k_\lambda^2\Big(h^2\frac{\alpha_t^2+\alpha_a^2}{\alpha_z^2} + \lambda^2\frac{\alpha_t}{\alpha_z}\Big) + 4ihk_\lambda^2\alpha_a\xi_c\omega/\alpha_z^2 \\ &\quad +\Big[k_\lambda^2\epsilon\alpha_t + \frac{h^2\alpha_t + \lambda^2\alpha_z}{k_\lambda^2}(h^2\epsilon + \lambda^2\epsilon_z) + 2ih^2g\alpha_a + 4k_\lambda^2\xi_c^2\Big]\omega^2/\alpha_z^2 \\ &\quad +4gh\xi_c\omega^3/\alpha_z^2 + \frac{1}{k_\lambda^2}\left[h^2(g^2-\epsilon^2) - \lambda^2\epsilon\epsilon_z\right]\omega^4/\alpha_z^2\Big\}. \end{aligned} \tag{5.16f}$$

Note that there are some special relations between vectors $\boldsymbol{L}$ and $\boldsymbol{N}$ as shown below:

$$\begin{aligned}
\boldsymbol{L}_n(h,\lambda) &= \boldsymbol{L}_{nt}(h,\lambda)+\boldsymbol{L}_{nz}(h,\lambda) && (5.17\text{a})\\
\boldsymbol{L}'_{-n}(-h,-\lambda) &= \boldsymbol{L}'_{-nt}(-h,-\lambda)+\boldsymbol{L}'_{-nz}(-h,-\lambda) && (5.17\text{b})\\
\boldsymbol{N}_n(h,\lambda) &= \boldsymbol{N}_{nt}(h,\lambda)+\boldsymbol{N}_{nz}(h,\lambda) && (5.17\text{c})\\
\boldsymbol{N}'_{-n}(-h,-\lambda) &= \boldsymbol{N}'_{-nt}(-h,-\lambda)+\boldsymbol{N}'_{-nz}(-h,-\lambda) && (5.17\text{d})\\
\boldsymbol{L}_{nt}(h,\lambda) &= \frac{-ik_\lambda}{h}\boldsymbol{N}_{nt}(h,\lambda) && (5.17\text{e})\\
\boldsymbol{L}'_{-nt}(-h,-\lambda) &= \frac{ik_\lambda}{h}\boldsymbol{N}'_{-nt}(-h,-\lambda) && (5.17\text{f})\\
\boldsymbol{L}_{nz}(h,\lambda) &= \frac{ihk_\lambda}{\lambda^2}\boldsymbol{N}_{nz}(h,\lambda) && (5.17\text{g})\\
\boldsymbol{L}'_{-nz}(-h,-\lambda) &= \frac{-ihk_\lambda}{\lambda^2}\boldsymbol{N}'_{-nz}(-h,-\lambda) && (5.17\text{h})
\end{aligned}$$

where the subscripts t and z denote respectively the transverse component and the longitude component and they apply similarly for the primed functions. Thus Eq. (5.8) is rewritten as follows:

$$\begin{aligned}
\overline{\boldsymbol{G}}_0(\boldsymbol{r},\boldsymbol{r}') &= \int_{-\infty}^{\infty}dh\int_0^{\infty}d\lambda\sum_{n=-\infty}^{\infty}\frac{1}{4\pi^2\lambda\Gamma}\Big\{\tau_1\boldsymbol{M}_n(h,\lambda)\boldsymbol{M}'_{-n}(-h,-\lambda)\\
&\quad+\tau_2\Big[\boldsymbol{M}_n(h,\lambda)\boldsymbol{N}'_{-nt}(-h,-\lambda)+\boldsymbol{N}_{nt}(h,\lambda)\boldsymbol{M}'_{-n}(-h,-\lambda)\Big]\\
&\quad+\tau_3\Big[\boldsymbol{M}_n(h,\lambda)\boldsymbol{N}'_{-nz}(-h,-\lambda)+\boldsymbol{N}_{nz}(h,\lambda)\boldsymbol{M}'_{-n}(-h,-\lambda)\Big]\\
&\quad+\tau_4\Big[\boldsymbol{N}_{nt}(h,\lambda)\boldsymbol{N}'_{-nz}(-h,-\lambda)+\boldsymbol{N}_{nz}(h,\lambda)\boldsymbol{N}'_{-nt}(-h,-\lambda)\Big]\\
&\quad+\tau_5\boldsymbol{N}_{nt}(h,\lambda)\boldsymbol{N}'_{-nt}(-h,-\lambda)+\tau_6\boldsymbol{N}_{nz}(h,\lambda)\boldsymbol{N}'_{-nz}(-h,-\lambda)\Big\}, \quad (5.18)
\end{aligned}$$

where the intermediates τ_1 to τ_6 are defined as

$$\begin{aligned}
\tau_1 &= \alpha_1 && (5.19\text{a})\\
\tau_2 &= \beta_1+\frac{i\lambda^2}{k_\lambda h}\gamma_1 && (5.19\text{b})
\end{aligned}$$

$$\begin{aligned}
\tau_3 &= \beta_1 - \frac{ih}{k_\lambda}\gamma_1 && (5.19c)\\
\tau_4 &= \beta_2 - \frac{ih}{k_\lambda}\gamma_2 - \frac{ik_\lambda}{h}\beta_3 - \gamma_3 && (5.19d)\\
\tau_5 &= \beta_2 + \frac{i\lambda^2}{k_\lambda h}\gamma_2 - \frac{ik_\lambda}{h}\beta_3 + \frac{\lambda^2}{h^2}\gamma_3 && (5.19e)\\
\tau_6 &= \beta_2 - \frac{ih}{k_\lambda}\gamma_2 + \frac{ihk_\lambda}{\lambda^2}\beta_3 + \frac{h^2}{\lambda^2}\gamma_3. && (5.19f)
\end{aligned}$$

By applying the idea of Tai [165] to obtain an exact expression of the irrotational term, it can be formlated from Eq. (5.5):

$$\widehat{\boldsymbol{z}}\widehat{\boldsymbol{z}}\delta(\boldsymbol{r}-\boldsymbol{r}') = \int_0^\infty d\lambda \int_{-\infty}^\infty dh \sum_{n=-\infty}^{\infty} \frac{1}{4\pi^2\lambda}\frac{k_\lambda^2}{\lambda^2}\boldsymbol{N}_{nz}(h,\lambda)\boldsymbol{N}'_{-nz}(-h,-\lambda). \quad (5.20)$$

Apparently, the irrotational term of the unbounded DGF is contained in the dyadic hybrid mode of $\boldsymbol{N}_{nz}(h,\lambda)\boldsymbol{N}'_{-nz}(-h,-\lambda)$.

After careful algebraic manipulations, Eq. (5.18) can be rewritten in the following form

$$\begin{aligned}
\overline{\boldsymbol{G}}_0(\boldsymbol{r},\boldsymbol{r}') = &-\frac{\alpha_z}{\omega^2\epsilon_z\alpha_t}\widehat{\boldsymbol{z}}\widehat{\boldsymbol{z}}\delta(\boldsymbol{r}-\boldsymbol{r}') + \int_{-\infty}^\infty dh \int_0^\infty d\lambda \times\\
&\sum_{n=-\infty}^{\infty} \frac{1}{4\pi^2\lambda\Gamma}\Big\{\tau_1 \boldsymbol{M}_n(h,\lambda)\boldsymbol{M}'_{-n}(-h,-\lambda)\\
&+\tau_2\Big[\boldsymbol{M}_n(h,\lambda)\boldsymbol{N}'_{-nt}(-h,-\lambda) + \boldsymbol{N}_{nt}(h,\lambda)\boldsymbol{M}'_{-n}(-h,-\lambda)\Big]\\
&+\tau_3\Big[\boldsymbol{M}_n(h,\lambda)\boldsymbol{N}'_{-nz}(-h,-\lambda) + \boldsymbol{N}_{nz}(h,\lambda)\boldsymbol{M}'_{-n}(-h,-\lambda)\Big]\\
&+\tau_4\Big[\boldsymbol{N}_{nt}(h,\lambda)\boldsymbol{N}'_{-nz}(-h,-\lambda) + \boldsymbol{N}_{nz}(h,\lambda)\boldsymbol{N}'_{-nt}(-h,-\lambda)\Big]\\
&+\tau_5\boldsymbol{N}_{nt}(h,\lambda)\boldsymbol{N}'_{-nt}(-h,-\lambda) + \tau_7\boldsymbol{N}_{nz}(h,\lambda)\boldsymbol{N}'_{-nz}(-h,-\lambda)\Big\}, \quad (5.21)
\end{aligned}$$

where

$$\tau_7 = \beta_2 + \frac{1}{\omega^2\lambda^2}k_\lambda^2)(k_\lambda^2 - k_1^2)(k_\lambda^2 - k_2^2 + \frac{h}{\lambda^2}(ik_\lambda\beta_3 + h\gamma_3) - \frac{ih}{k_\lambda}\gamma_2. \quad (5.22)$$

The first term of Eq. (5.21) is due to the contribution from the non-solenoidal vector wave functions. The second integration term can be evaluated by making use of the residue theorem either in the λ-domain or h-domain. This irrotational part of DGFs in a gyrotropic chiral medium (the material discussed in Chapter 4) is obtained for the first time when the eigenfunction expansion technique is applied. This irrotational part in specific cases agrees with the previous solutions of a chiroplasma medium by letting $\alpha_z = \alpha_t = 1/\mu$ or an isotropic medium by letting $\epsilon_z = \epsilon$ further if we first set $g = w = 0$.

Evaluation in λ-domain

If the residue theorem is applied in the radial plane, the final expression of the unbounded DGFs can be obtained after mathematical manipulations for $\rho \gtrless \rho'$

$$
\overline{\boldsymbol{G}}_0(\boldsymbol{r},\boldsymbol{r'}) = -\frac{\alpha_z}{\omega^2\epsilon_z\alpha_t}\hat{\boldsymbol{z}}\hat{\boldsymbol{z}}\delta(\boldsymbol{r}-\boldsymbol{r'}) + \frac{i}{4\pi}\int_{-\infty}^{\infty} dh \sum_{n=-\infty}^{\infty} \frac{\alpha_z}{\epsilon_z\alpha_t(k_1^2-k_2^2)} \sum_{j=1}^{2}\frac{(-1)^{j+1}}{\lambda_j^2}\times
$$

$$
\begin{cases}
\boldsymbol{M}^{(1)}_{n,h}(\lambda_j)\boldsymbol{P'}_{-n,-h}(-\lambda_j) + \boldsymbol{Q}^{(1)}_{n,h}(\lambda_j)\boldsymbol{M'}_{-n,-h}(-\lambda_j) \\
\qquad + \boldsymbol{U}^{(1)}_{n,h}(\lambda_j)\boldsymbol{N'}_{-nt,-h}(-\lambda_j) + \boldsymbol{V}^{(1)}_{n,h}(\lambda_j)\boldsymbol{N'}_{-nz,-h}(-\lambda_j), \quad \rho > \rho'; \\
\boldsymbol{M}_{n,h}(-\lambda_j)\boldsymbol{P'}^{(1)}_{-n,-h}(\lambda_j) + \boldsymbol{Q}_{n,h}(-\lambda_j)\boldsymbol{M'}^{(1)}_{-n,-h}(\lambda_j) \\
\qquad + \boldsymbol{U}_{n,h}(-\lambda_j)\boldsymbol{N'}^{(1)}_{-nt,-h}(\lambda_j) + \boldsymbol{V}_{n,h}(-\lambda_j)\boldsymbol{N'}^{(1)}_{-nz,-h}(\lambda_j), \quad \rho < \rho'.
\end{cases}
$$

The vector functions, $\boldsymbol{P}'_{-n,-h}(-\lambda_j)$, $\boldsymbol{Q}_{n,h}(\lambda_j)$, $\boldsymbol{U}_{n,h}(\lambda_j)$ and $\boldsymbol{V}_{n,h}(\lambda_j)$ in Eq. (5.23), are given respectively by

$$\begin{aligned}
\boldsymbol{P}'_{-n,-h}(-\lambda_j) &= \tau_1\boldsymbol{M}'_{-n,-h}(-\lambda_j) + \tau_2\boldsymbol{N}'_{-nt,-h}(-\lambda_j) + \tau_3\boldsymbol{N}'_{-nz,-h}(-\lambda_j)\\
\boldsymbol{Q}_{n,h}(\lambda_j) &= \tau_2\boldsymbol{N}_{nt,h}(\lambda_j) + \tau_3\boldsymbol{N}_{nz,h}(\lambda_j)\\
\boldsymbol{U}_{n,h}(\lambda_j) &= \tau_5\boldsymbol{N}_{nt,h}(\lambda_j) + \tau_4\boldsymbol{N}_{nz,h}(\lambda_j)\\
\boldsymbol{V}_{n,h}(\lambda_j) &= \tau_4\boldsymbol{N}_{nt,h}(\lambda_j) + \tau_7\boldsymbol{N}_{nz,h}(\lambda_j).
\end{aligned} \tag{5.23}$$

Evaluation in h-domain

The contour integration for $z \gtrless z'$ in planar geometry yields four sets of solutions corresponding to four different waves of wave numbers h_i (i=1, 2, 3, and 4), which can be found by rewriting $\Gamma = 0$ in Eq. (5.13) in the h-domain and solving the fourth-order polynomial equation in Mathematica 5.2 package.

For $z > z'$, the DGF is given by

$$\begin{aligned}
\overline{\boldsymbol{G}}_0(\boldsymbol{r},\boldsymbol{r}') &= -\frac{\alpha_z}{\omega^2\epsilon_z\alpha_t}\hat{\boldsymbol{z}}\hat{\boldsymbol{z}}\delta(\boldsymbol{r}-\boldsymbol{r}') + \frac{i}{2\pi}\int_0^\infty d\lambda \sum_{n=-\infty}^{\infty}\frac{\alpha_z}{\epsilon_z\alpha_t\lambda(h_1-h_2)} \times\\
&\quad \sum_{j=1}^{2}\frac{(-1)^{j+1}}{(h_j-h_3)(h_j-h_4)}\Big\{\boldsymbol{M}_{n,\lambda}(h_j)\boldsymbol{P}'_{-n,-\lambda}(-h_j) + \boldsymbol{Q}_{n,\lambda}(h_j)\boldsymbol{M}'_{-n,-\lambda}(-h_j)\\
&\quad +\boldsymbol{U}_{n,\lambda}(h_j)\boldsymbol{N}'_{-nt,-\lambda}(-h_j) + \boldsymbol{V}_{n,\lambda}(h_j)\boldsymbol{N}'_{-nz,-\lambda}(-h_j)\Big\}.
\end{aligned} \tag{5.24}$$

For $z < z'$, the DGF is the same as that for $z > z'$, except for the following replacement to be made

$$\frac{1}{\lambda(h_1-h_2)}\sum_{j=1}^{2}\frac{(-1)^{j+1}}{(h_j-h_3)(h_j-h_4)} \Longrightarrow \frac{1}{\lambda(h_3-h_4)}\sum_{j=3}^{4}\frac{(-1)^{j+1}}{(h_1-h_j)(h_2-h_j)}.$$

The vector wave functions, $\boldsymbol{P}_{n,\lambda}(h_j)$, $\boldsymbol{Q}_{n,\lambda}(h_j)$, $\boldsymbol{U}_{n,\lambda}(h_j)$ and $\boldsymbol{V}_{n,\lambda}(h_j)$ in Eq. (5.24), are given respectively by

$$\begin{aligned}
\boldsymbol{P'}_{-n,-\lambda}(-h_j) &= \tau_1\boldsymbol{M'}_{-n,-\lambda}(-h_j)+\tau_2\boldsymbol{N'}_{-nt,-\lambda}(-h_j)+\tau_3\boldsymbol{N'}_{-nz,-\lambda}(-h_j),\\
\boldsymbol{Q}_{n,\lambda}(h_j) &= \tau_2\boldsymbol{N}_{nt,\lambda}(h_j)+\tau_3\boldsymbol{N}_{nz,\lambda}(h_j),\\
\boldsymbol{U}_{n,\lambda}(h_j) &= \tau_5\boldsymbol{N}_{nt,\lambda}(h_j)+\tau_4\boldsymbol{N}_{nz,\lambda}(h_j),\\
\boldsymbol{V}_{n,\lambda}(h_j) &= \tau_4\boldsymbol{N}_{nt,\lambda}(h_j)+\tau_7\boldsymbol{N}_{nz,\lambda}(h_j).
\end{aligned} \tag{5.25}$$

Now, a complete representation of the DGFs for an unbounded gyrotropic chiral medium has been constructed. It can be seen that an irrotational term has been extracted and these general DGFs are reducible to those of anisotropic, gyroelectric, chiroferrite, and isotropic media. In the presence of interfaces in layered strucutres, the multiple scatterings and transmissions must be taken into account. Hence, scattering DGFs are modeled to consider thess aspects. The cylindrically multilayered and planarly multilayered cases will be discussed subsequently.

5.1.3 Scattering DGFs in cylindrical layered structures

In this part, theoretical analysis is extended to derive scattering DGFs for the f-th region assuming that the current source is located in the s-th layer. As such, the scattering DGFs have a form similar with the unbounded DGF as given in Eq. (5.23). The expression for the scattering DGFs for each region of the layered gyrotropic chiral media can be constructed as

$$\overline{\boldsymbol{G}}_s^{(fs)} = \overline{\boldsymbol{G}}_1 + \overline{\boldsymbol{G}}_2 \tag{5.26}$$

where the dyadics $\overline{\boldsymbol{G}}_j$ $(j = 1,\ 2)$ are given below by Eq. (5.27)

$$\begin{aligned}
\overline{\boldsymbol{G}}_j = \frac{i}{4\pi} \int_0^\infty dh \sum_{n=0}^{\infty} \frac{\alpha_{zs}(2-\delta_n^0)(-1)^{j+1}}{\epsilon_{zs}\alpha_{ts}(k_{1s}^2 - k_{2s}^2)\lambda_{js}^2} \times& \\
\Big\{(1-\delta_f^N)\boldsymbol{M}^{(1)}_{n,h}(\lambda_j^f)\Big[(1-\delta_s^1)A_{Mj}^{fs}\boldsymbol{P'}_{-n,-h}(-\lambda_j^s) + (1-\delta_s^N)B_{Mj}^{fs}\boldsymbol{P'}^{(1)}_{-n,-h}(\lambda_j^s)\Big]& \\
+(1-\delta_f^N)\boldsymbol{Q}^{(1)}_{n,h}(\lambda_j^f)\Big[(1-\delta_s^1)A_{Qj}^{fs}\boldsymbol{M'}_{-n,-h}(-\lambda_j^s) + (1-\delta_s^N)B_{Qj}^{fs}\boldsymbol{M'}^{(1)}_{-n,-h}(\lambda_j^s)\Big]& \\
+(1-\delta_f^N)\boldsymbol{U}^{(1)}_{n,h}(\lambda_j^f)\Big[(1-\delta_s^1)A_{Uj}^{fs}\boldsymbol{N'}_{-nt,-h}(-\lambda_j^s) + (1-\delta_s^N)B_{Uj}^{fs}\boldsymbol{N'}^{(1)}_{-nt,-h}(\lambda_j^s)\Big]& \\
+(1-\delta_f^N)\boldsymbol{V}^{(1)}_{n,h}(\lambda_j^f)\Big[(1-\delta_s^1)A_{Vj}^{fs}\boldsymbol{N'}_{-nz,-h}(-\lambda_j^s) + (1-\delta_s^N)B_{Vj}^{fs}\boldsymbol{N'}^{(1)}_{-nz,-h}(\lambda_j^s)\Big]& \\
+(1-\delta_f^1)\boldsymbol{M}_{n,h}(-\lambda_j^f)\Big[(1-\delta_s^1)C_{Mj}^{fs}\boldsymbol{P'}_{-n,-h}(-\lambda_j^s) + (1-\delta_s^N)D_{Mj}^{fs}\boldsymbol{P'}^{(1)}_{-n,-h}(\lambda_j^s)\Big]& \\
+(1-\delta_f^1)\boldsymbol{Q}_{n,h}(-\lambda_j^f)\Big[(1-\delta_s^1)C_{Qj}^{fs}\boldsymbol{M'}_{-n,-h}(-\lambda_j^s) + (1-\delta_s^N)D_{Qj}^{fs}\boldsymbol{M'}^{(1)}_{-n,-h}(\lambda_j^s)\Big]& \\
+(1-\delta_f^1)\boldsymbol{U}_{n,h}(-\lambda_j^f)\Big[(1-\delta_s^1)C_{Uj}^{fs}\boldsymbol{N'}_{-nt,-h}(-\lambda_j^s) + (1-\delta_s^N)D_{Uj}^{fs}\boldsymbol{N'}^{(1)}_{-nt,-h}(\lambda_j^s)\Big]& \\
+(1-\delta_f^1)\boldsymbol{V}_{n,h}(-\lambda_j^f)\Big[(1-\delta_s^1)C_{Vj}^{fs}\boldsymbol{N'}_{-nz,-h}(-\lambda_j^s) + (1-\delta_s^N)D_{Vj}^{fs}\boldsymbol{N'}^{(1)}_{-nz,-h}(\lambda_j^s)\Big]\Big\}&
\end{aligned} \tag{5.27}$$

where multiple transmissions and reflections have been taken into account, $\lambda_{jf} = \sqrt{k_{jf}^2 - h^2}$ and the subscript f implies the f-th region. The $ABCD$ coefficients are scattering DGF coefficients to be determined from the boundary conditions. By considering the multiple transmissions and reflections, the scattering DGFs are thus constructed physically by inspecting Eq. (5.27) and taking into account all the possible physical modes in the presence of the multiple interfaces as shown in the Fig. 5.1.

For instance, if the source is located in the first/last region (*i.e.*, $1 - \delta_s^1 = 0/1 - \delta_s^N = 0$), the wavelets in the scattering DGFs are only excited by inward-coming/outward-going wavelets with excitation functions $[\boldsymbol{P}'^{(1)}_{-n,-h}(\lambda_{js})$, $\boldsymbol{M}'^{(1)}_{-n,-h}(\lambda_{js})$,

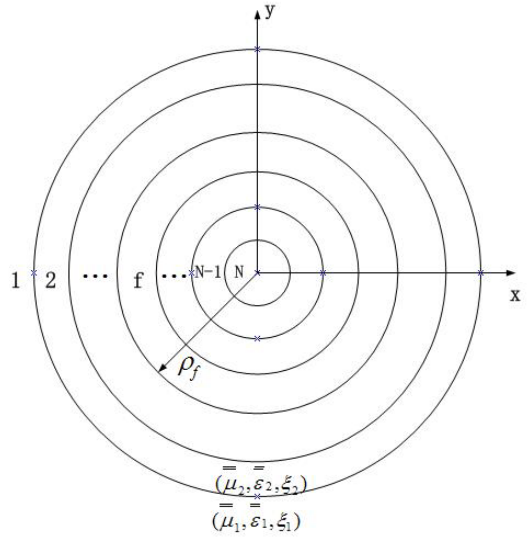

Figure 5.1: Geometry of cylindrical layered gyrotropic chiral media.

$\boldsymbol{N}'^{(1)}_{-nt,-h}(\lambda_{js})$, $\boldsymbol{N}'^{(1)}_{-nz,-h}(\lambda_{js})]$ / $[\boldsymbol{P}'_{-n,-h}(-\lambda_{js})$, $\boldsymbol{M}'_{-n,-h}(-\lambda_{js})$, $\boldsymbol{N}'_{-nt,-h}(-\lambda_{js})$, $\boldsymbol{N}'_{-nz,-h}(-\lambda_{js})]$. When the source point is located in any other layer, the excitation functions consist of both outward-going and inward-coming wavemodes. If the observation point is in the first/last region (*i.e.*, $1 - \delta_f^1 = 0/1 - \delta_f^N = 0$), the field expansions consist of only outward-going/inward-coming wavemodes.

Based on the principle of scattering superposition, we have

$$\overline{\boldsymbol{G}}_e^{(fs)}(\boldsymbol{r}, \boldsymbol{r}') = \overline{\boldsymbol{G}}_0(\boldsymbol{r}, \boldsymbol{r}')\delta_f^s + \overline{\boldsymbol{G}}_s^{(fs)}(\boldsymbol{r}, \boldsymbol{r}'), \tag{5.28}$$

where $\overline{\boldsymbol{G}}_e$ and $\overline{\boldsymbol{G}}_0$ denote the total and unbounded electric DGFs respectively and superscripts f and s respectively denote the field point located in the f-th region and the source located in the s-th region. $\overline{\boldsymbol{G}}_0$ has been derived in Section 5.1.2.

The boundary conditions that must be satisfied by the dyadic Greens' functions at the interface of regions f and $f+1$ at $\rho = \rho_f$ $(f = 1, 2, \ldots, N-1)$ are shown as follows:

$$\widehat{\boldsymbol{\rho}} \times \overline{\boldsymbol{G}}_e^{(fs)}(\boldsymbol{r}, \boldsymbol{r'}) = \widehat{\boldsymbol{\rho}} \times \overline{\boldsymbol{G}}_e^{[(f+1)s]}(\boldsymbol{r}, \boldsymbol{r'}), \tag{5.29a}$$

$$\begin{aligned} & \widehat{\boldsymbol{\rho}} \times \Big[\overline{\boldsymbol{\alpha}}_f \cdot \boldsymbol{\nabla} \times \overline{\boldsymbol{G}}_e^{(fs)}(\boldsymbol{r}, \boldsymbol{r'}) - \omega\xi_{cf}\overline{\boldsymbol{G}}_e^{(fs)}(\boldsymbol{r}, \boldsymbol{r'})\Big] \\ = \;\; & \widehat{\boldsymbol{\rho}} \times \Big[\overline{\boldsymbol{\alpha}}_{f+1} \cdot \boldsymbol{\nabla} \times \overline{\boldsymbol{G}}_e^{[(f+1)s]}(\boldsymbol{r}, \boldsymbol{r'}) - \omega\xi_{c(f+1)}\overline{\boldsymbol{G}}_e^{[(f+1)s]}(\boldsymbol{r}, \boldsymbol{r'})\Big]. \end{aligned} \tag{5.29b}$$

Recursive matrix for scattering coefficients

Based on the multilayer algorithm developed in Section 2.2, a recursive matrix is formulated so as to determine those unknown scattering coefficients. By using the boundary conditions, a set of linear equations satisfied by scattering coefficients can be obtained and then represented by a series of compact matrices as follows:

$$\Big[F_{lj(f+1)}\Big] \cdot \Big\{\Big[\Upsilon_{lj(f+1)s}\Big] + \delta_{f+1}^{s}\Big[U_{(f+1)}\Big]\Big\} = \Big[F_{ljf}\Big] \cdot \Big\{\Big[\Upsilon_{ljfs}\Big] + \delta_{f}^{s}\Big[D_f\Big]\Big\}. \tag{5.30}$$

The intermediate matrices in Eq. (5.30) are defined as

$$[F_{Mjf}] = \begin{bmatrix} \partial\hbar_j & W_{M1} \\ \\ \partial\jmath_j & W_{M2} \end{bmatrix}^T \tag{5.31a}$$

$$[F_{Ljf}] = \begin{bmatrix} (\frac{\tau_{pjf}nh}{\rho_f} + \tau_{qjf}\lambda_{jf}^2)\frac{\hbar_j}{k_{\lambda jf}} & W_{L1} \\ (\frac{\tau_{pjf}nh}{\rho_f} + \tau_{qjf}\lambda_{jf}^2)\frac{\jmath_j}{k_{\lambda jf}} & W_{L2} \end{bmatrix}^T \tag{5.31b}$$

where

$$W_{M1} = \left(\frac{\alpha_{tf}nh}{\rho_f} + \alpha_{zf}\lambda_{jf}^2\right)\hbar_j - \left(\omega\xi_{cf} + h\sigma_f\right)\partial\hbar_j \tag{5.31c}$$

$$W_{M2} = \left(\frac{\alpha_{tf}nh}{\rho_f} + \alpha_{zf}\lambda_{jf}^2\right)\jmath_j - \left(\omega\xi_{cf} + h\sigma_f\right)\partial\jmath_j \tag{5.31d}$$

$$\begin{aligned}
W_{L1} &= \Delta_{\substack{p\\q}jf}\alpha_{tf}\partial\hbar_j + \left(\frac{h\lambda_{jf}^2}{k_{\lambda jf}^2} - \frac{n}{\rho_f}\right)\Delta_{\substack{p\\q}jf}\sigma_f\hbar_j - \\
&\quad \omega\xi_{cf}\left(\frac{hn\tau_{pjf}}{k_{\lambda jf}\rho_f} + \frac{\lambda_{jf}^2\tau_{qjf}}{k_{\lambda jf}}\right)\hbar_j \qquad (5.31e)\\
W_{L2} &= \Delta_{\substack{p\\q}jf}\alpha_{tf}\partial\jmath_j + \left(\frac{h\lambda_{jf}^2}{k_{\lambda jf}^2} - \frac{n}{\rho_f}\right)\Delta_{\substack{p\\q}jf}\sigma_f\jmath_j - \\
&\quad \omega\xi_{cf}\left(\frac{hn\tau_{pjf}}{k_{\lambda jf}\rho_f} + \frac{\lambda_{jf}^2\tau_{qjf}}{k_{\lambda jf}}\right)\jmath_j. \qquad (5.31f)
\end{aligned}$$

As in the matrices $[F_{Ljf}]$, the subscript L denotes Q, U, or V, which comes in pair with $\Delta_{\substack{2\\3}jf}$, $\Delta_{\substack{4\\5}jf}$ or $\Delta_{\substack{4\\7}jf}$, respectively, with the definition of

$$\Delta_{\substack{p\\q}jf} = \frac{h^2(\tau_{pjf} - \tau_{qjf}) + k_{\lambda jf}^2\tau_{qjf}}{k_{\lambda jf}}. \qquad (5.31g)$$

For simplicity, the followings are defined

$$\begin{aligned}
\hbar_j &= H_n^{(1)}(\lambda_{jf}\rho_f), \qquad (5.32a)\\
\partial\hbar_j &= \frac{d\left[H_n^{(1)}(\lambda_{jf}\rho)\right]}{d\rho}\bigg|_{\rho=\rho_f}, \qquad (5.32b)\\
\jmath_j &= J_n(\lambda_{jf}\rho_f), \qquad (5.32c)\\
\partial\jmath_j &= \frac{d\left[J_n(\lambda_{jf}\rho)\right]}{d\rho}\bigg|_{\rho=\rho_f}. \qquad (5.32d)
\end{aligned}$$

The terms τ_{2jf}, τ_{3jf}, τ_{4jf}, τ_{5jf}, and τ_{7jf} are the weighting factors associated with the scattering coefficients A_{lj}^{fs} and B_{lj}^{fs} where $l = M,\ Q,\ U$, or V. They have the same forms as those in Eqs. (5.19) and (5.22) with the only change that each term relating to wave numbers (*e.g.*, λ) will have a subscript of jf (*e.g.*, λ_{jf}) and each term relating to material parameters (*e.g.*, ϵ_z) will have a subscript of f (*e.g.*, ϵ_{zf}) where $j = 1,\ 2$ and f represents the f-th region. The following matrices are also used in the formulation:

$$[\Upsilon_{lj,fs}] = \begin{bmatrix} A_{lj}^{fs} & B_{lj}^{fs} \\ C_{lj}^{fs} & D_{lj}^{fs} \end{bmatrix}, \qquad (5.33a)$$

$$[U_f] = \begin{bmatrix} 1 & 0 \\ 0 & 0 \end{bmatrix}, \tag{5.33b}$$

$$[D_f] = \begin{bmatrix} 0 & 0 \\ 0 & 1 \end{bmatrix}. \tag{5.33c}$$

By defining the following transmission T-matrix

$$[T_{ljf}] = \left[F_{lj,(f+1)f}\right]^{-1} \cdot [F_{lj,ff}] \tag{5.34}$$

where $\left[F_{lj,(f+1)f}\right]^{-1}$ is the inverse matrix of $\left[F_{lj,(f+1)f}\right]$, the linear equation can be expressed by

$$\left[\Upsilon_{lj,(f+1)s}\right] = [T_{ljf}] \cdot \left\{[\Upsilon_{lj,fs}] + \delta_f^s [D_f]\right\} - \delta_{f+1}^s \left[U_{(f+1)}\right]. \tag{5.35}$$

To shorten the expression, a matrix is defined

$$\begin{aligned} \left[T_{lj}^K\right]_{2\times 2} &= [T_{lj,N-1}]\,[T_{lj,N-2}]\cdots[T_{lj,K+1}]\,[T_{lj,K}] \\ &= \begin{bmatrix} T_{lj,11}^K & T_{lj,12}^K \\ T_{lj,21}^K & T_{lj,22}^K \end{bmatrix}. \end{aligned} \tag{5.36}$$

It should be noted that the coefficient matrices of the first and the last regions have the following specific forms

$$[\Upsilon_{lj,1s}] = \begin{bmatrix} A_{lj}^{1s} & B_{lj}^{1s} \\ 0 & 0 \end{bmatrix} \tag{5.37a}$$

$$[\Upsilon_{lj,Ns}] = \begin{bmatrix} 0 & 0 \\ C_{lj}^{Ns} & D_{lj}^{Ns} \end{bmatrix}. \tag{5.37b}$$

Then one may utilize the previously obtained recursive formula to derive all the coefficients of A_{lj}^{fs}, B_{lj}^{fs}, C_{lj}^{fs} and D_{lj}^{fs}.

To gain insight into the specific mathematical expressions of the physical quantities such as the transmission and reflections coefficient matrices, the following three cases are considered subsequently to demonstrate how these coefficients are determined by using the recursive algorithm when the source point is located in the first, the intermediate, and the last regions.

Source in an intermediate layer

$$\begin{aligned}[\Upsilon_{lj,1s}] &= \begin{bmatrix} A_{lj}^{1s} & B_{lj}^{1s} \\ 0 & 0 \end{bmatrix} & \text{(5.38a)}\\ [\Upsilon_{lj,ms}] &= \begin{bmatrix} A_{lj}^{ms} & B_{lj}^{ms} \\ C_{lj}^{ms} & D_{lj}^{ms} \end{bmatrix} & \text{(5.38b)}\\ [\Upsilon_{lj,Ns}] &= \begin{bmatrix} 0 & 0 \\ C_{lj}^{Ns} & D_{lj}^{Ns} \end{bmatrix}. & \text{(5.38c)}\end{aligned}$$

From Eq. (5.36), the recurrence equation becomes

$$\begin{aligned}[\Upsilon_{lj,fs}] &= [T_{lj,f-1}]\cdots[T_{lj,s}]\Big\{[T_{lj,s-1}]\cdots[T_{lj,1}]\,[\Upsilon_{lj,1s}] \\ &\quad +u(f-s-1)\,[D_s]-u(f-s)\,[U_s]\Big\}, \qquad (5.39)\end{aligned}$$

where $u(x-x_0)$ denotes the unit step function. When $f=N$, the coefficients for the first region are given by:

$$A_{lj}^{1s}=\frac{T_{lj,11}^{(s)}}{T_{lj,11}^{(1)}}, \quad B_{lj}^{1s}=-\frac{T_{lj,12}^{(s)}}{T_{lj,11}^{(1)}}. \qquad (5.40)$$

For the last region, the coefficients are given by

$$C_{lj}^{Ns}=T_{lj,21}^{(1)}A_{lj}^{1s}-T_{lj,21}^{(s)}, \quad D_{lj}^{Ns}=T_{lj,21}^{(1)}B_{lj}^{1s}+T_{lj,22}^{(s)}. \qquad (5.41)$$

Substituting Eqs. (5.40) and (5.41) into Eq. (5.39), the remaining coefficients can be obtained for the dyadic Green's functions. If the source is located in the first or last region (*i.e.*, $s = 1$ or N), the formulation of coefficients can be tremendously simplified.

Source in the first region

When the current source is located in the first region (*i.e.*, $s = 1$), the terms containing $(1 - \delta_s^1)$ in Eq. (5.27) vanish. The coefficient matrices in Eqs. (5.33) and (5.37) will be further reduced to:

$$[\Upsilon_{lj,11}] = \begin{bmatrix} 0 & B_{lj}^{11} \\ 0 & 0 \end{bmatrix}, \tag{5.42a}$$

$$[\Upsilon_{lj,m1}] = \begin{bmatrix} 0 & B_{lj}^{m1} \\ 0 & D_{lj}^{m1} \end{bmatrix}, \tag{5.42b}$$

$$[\Upsilon_{lj,N1}] = \begin{bmatrix} 0 & 0 \\ 0 & D_{lj}^{N1} \end{bmatrix}, \tag{5.42c}$$

where $m = 2, 3, \cdots, N-1$. It can be seen that only four coefficients for the first region and the last region, but 8 coefficients for each of the remaining regions or layers, need to be solved for. By following Eq. (5.35), the recurrence relation for coefficients in the f-th layer becomes

$$[\Upsilon_{lj,f1}] = [T_{lj,f-1}] \cdots [T_{lj,1}] \left\{ [\Upsilon_{lj,11}] + [D_1] \right\}. \tag{5.43}$$

When $f = N$ in Eq. (5.43), a matrix equation satisfied by the coefficient matrices in Eq. (5.42) can be obtained. The coefficients for the first region where the source is located ($i.e.$, $s = 1$) is given by:

$$B_{lj}^{11} = -\frac{T_{lj,12}^{(1)}}{T_{lj,11}^{(1)}}. \tag{5.44}$$

The coefficients for the last region can be derived in terms of the coefficients for the first region given by:

$$D_{lj}^{N1} = T_{lj,21}^{(1)} B_{lj}^{11} + T_{lj,22}^{(1)}. \tag{5.45}$$

The coefficients for the intermediate layers can be then obtained by substituting the coefficients in Eqs. (5.44) and (5.45) to Eq. (5.43). Thus, all the coefficients can be obtained by these procedures.

Source in the last region

When the current source is located in the first region ($i.e.$, $s = N$), the coefficients are:

$$\left[\Upsilon_{lj,1N}\right] = \begin{bmatrix} A_{lj}^{1N} & 0 \\ 0 & 0 \end{bmatrix}, \tag{5.46a}$$

$$\left[\Upsilon_{lj,mN}\right] = \begin{bmatrix} A_{lj}^{mN} & 0 \\ C_{lj}^{mN} & 0 \end{bmatrix}, \tag{5.46b}$$

$$\left[\Upsilon_{lj,NN}\right] = \begin{bmatrix} 0 & 0 \\ C_{lj}^{NN} & 0 \end{bmatrix}. \tag{5.46c}$$

Similarly, from the recurrence equation in Eq. (5.35), we have

$$\left[\Upsilon_{lj,fN}\right] = \left[T_{lj,f-1}\right] \cdots \left[T_{lj,1}\right] \left[\Upsilon_{lj,1N}\right] - u(f-N) \left[U_N\right]. \tag{5.47}$$

By letting $s = N$, the coefficient for the first region is

$$A_{lj}^{1N} = \frac{1}{T_{lj,11}^{(1)}}. \tag{5.48}$$

And for the last region, it is found that

$$C_{lj}^{NN} = T_{lj,21}^{(1)} A_{lj}^{1N}. \tag{5.49}$$

Similarly, the remaining coefficients can be obtained by substituting Eq. (5.48) and Eq. (5.49) into Eq. (5.47).

So far, for gyrotropic chiral media in cylindrical layered structures, I have obtained a complete set of solutions to the DGFs in terms of the cylindrical vector wave functions and their scattering coefficients in terms of compact matrices. Reduction can be made to the dyadic Green's functions in less complex media, *e.g.*, anisotropic medium where $\xi_c = 0$, bi-isotropic media where $g = w = 0$, gyroelectric media where $w = 0$ and $\mu = \mu_z$, chiroferrite media where $p = 0$ and $\epsilon = \epsilon_z$, or isotropic media where $\xi_c = g = w = 0$, $\epsilon_z = \epsilon$ and $\mu = \mu_z$.

5.1.4 Scattering DGFs in planar layered structures

The same principle in Eq. (5.28) is used here to get the total DGFs, which consist of the unbounded DGF $\overline{\boldsymbol{G}}_0$ as shown in Section 5.1.2 and the scattering DGFs as given by

$$\overline{\boldsymbol{G}}_s^{(fs)}(\boldsymbol{r}, \boldsymbol{r}') = \sum_{j=1}^{4} \overline{\boldsymbol{G}}_j. \tag{5.50}$$

Two terms are grouped as follows:

$$\begin{aligned}
\overline{\boldsymbol{G}}_1+\overline{\boldsymbol{G}}_2 &= \frac{i}{2\pi}\int_0^\infty d\lambda\sum_{n=-\infty}^{\infty}\frac{\alpha_{zs}}{\epsilon_{zs}\alpha_{ts}\lambda(h_{1s}-h_{2s})}\times\sum_{j=1}^{2}\frac{(-1)^{j+1}}{(h_{js}-h_{3s})(h_{js}-h_{4s})}\times\\
&\Big\{(1-\delta_f^N)\boldsymbol{M}_{n,\lambda}(h_j^f)\Big[(1-\delta_s^1)A_{Mj}^{fs}\boldsymbol{P'}_{-n,-\lambda}(-h_j^s)+(1-\delta_s^N)B_{Mj}^{fs}\boldsymbol{P'}_{-n,-\lambda}(-h_{j+2}^s)\Big]\\
&+(1-\delta_f^N)\boldsymbol{Q}_{n,\lambda}(h_j^f)\Big[(1-\delta_s^1)A_{Qj}^{fs}\boldsymbol{M'}_{-n,-\lambda}(-h_j^s)+(1-\delta_s^N)B_{Qj}^{fs}\boldsymbol{M'}_{-n,-\lambda}(-h_{j+2}^s)\Big]\\
&+(1-\delta_f^N)\boldsymbol{U}_{n,\lambda}(h_j^f)\Big[(1-\delta_s^1)A_{Uj}^{fs}\boldsymbol{N'}_{-nt,-\lambda}(-h_j^s)+(1-\delta_s^N)B_{Uj}^{fs}\boldsymbol{N'}_{-nt,-\lambda}(-h_{j+2}^s)\Big]\\
&+(1-\delta_f^N)\boldsymbol{V}_{n,\lambda}(h_j^f)\Big[(1-\delta_s^1)A_{Vj}^{fs}\boldsymbol{N'}_{-nz,-\lambda}(-h_j^s)+(1-\delta_s^N)B_{Vj}^{fs}\boldsymbol{N'}_{-nz,-\lambda}(-h_{j+2}^s)\Big]\Big\},
\end{aligned} \tag{5.51}$$

and

$$\begin{aligned}
\overline{\boldsymbol{G}}_3+\overline{\boldsymbol{G}}_4 &= \frac{i}{2\pi}\int_0^\infty d\lambda\sum_{n=-\infty}^{\infty}\frac{\alpha_{zs}}{\epsilon_{zs}\alpha_{ts}\lambda(h_{3s}-h_{4s})}\times\sum_{j=3}^{4}\frac{(-1)^{j+1}}{(h_{1s}-h_{js})(h_{2s}-h_{js})}\times\\
&\Big\{(1-\delta_f^N)\boldsymbol{M}_{n,\lambda}(h_j^f)\Big[(1-\delta_s^1)A_{Mj}^{fs}\boldsymbol{P'}_{-n,-\lambda}(-h_{j-2}^s)+(1-\delta_s^N)B_{Mj}^{fs}\boldsymbol{P'}_{-n,-\lambda}(-h_j^s)\Big]\\
&+(1-\delta_f^N)\boldsymbol{Q}_{n,\lambda}(h_j^f)\Big[(1-\delta_s^1)A_{Qj}^{fs}\boldsymbol{M'}_{-n,-\lambda}(-h_{j-2}^s)+(1-\delta_s^N)B_{Qj}^{fs}\boldsymbol{M'}_{-n,-\lambda}(-h_j^s)\Big]\\
&+(1-\delta_f^N)\boldsymbol{U}_{n,\lambda}(h_j^f)\Big[(1-\delta_s^1)A_{Uj}^{fs}\boldsymbol{N'}_{-nt,-\lambda}(-h_{j-2}^s)+(1-\delta_s^N)B_{Uj}^{fs}\boldsymbol{N'}_{-nt,-\lambda}(-h_j^s)\Big]\\
&+(1-\delta_f^N)\boldsymbol{V}_{n,\lambda}(h_j^f)\Big[(1-\delta_s^1)A_{Vj}^{fs}\boldsymbol{N'}_{-nz,-\lambda}(-h_{j-2}^s)+(1-\delta_s^N)B_{Vj}^{fs}\boldsymbol{N'}_{-nz,-\lambda}(-h_j^s)\Big]\Big\}.
\end{aligned} \tag{5.52}$$

The combination of the two terms for the above two equations is due to the fact that each term has a static contribution to the dyadic Green's function because of the integration associated with the pole point $\lambda = 0$. What should be noted is that the multiple reflection and transmission effects have been included in the formulation of the scattering DGFs in the stratified structure shown in Fig. 5.2. The Sommerfeld radiation condition has been taken into account in the construction of DGFs. The contributions from various wave modes to the DGFs have been considered as well.

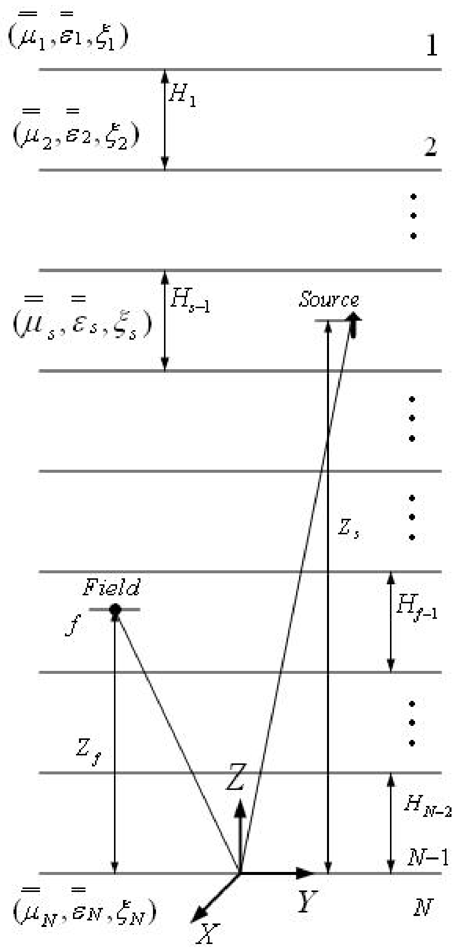

Figure 5.2: Geometry of planarly layered gyrotropic chiral media.

Recursive matrix for scattering coefficients

The boundary conditions that must be satisfied by the dyadic Greens' functions at the interface between regions f and $f+1$ where $z = z_j = \sum_{l=f}^{N-2} H_l$ are shown as follows:

$$\begin{aligned}
&\hat{\boldsymbol{z}} \times \overline{\boldsymbol{G}}_e^{(fs)}(\boldsymbol{r}, \boldsymbol{r'}) = \hat{\boldsymbol{z}} \times \overline{\boldsymbol{G}}_e^{[(f+1)s]}(\boldsymbol{r}, \boldsymbol{r'}), \\
&\hat{\boldsymbol{z}} \times \left[\overline{\boldsymbol{\alpha}}_f \cdot \boldsymbol{\nabla} \times \overline{\boldsymbol{G}}_e^{(fs)}(\boldsymbol{r}, \boldsymbol{r'}) - \omega \xi_{cf} \overline{\boldsymbol{G}}_e^{(fs)}(\boldsymbol{r}, \boldsymbol{r'})\right] \\
&= \hat{\boldsymbol{z}} \times \left[\overline{\boldsymbol{\alpha}}_{f+1} \cdot \boldsymbol{\nabla} \times \overline{\boldsymbol{G}}_e^{[(f+1)s]}(\boldsymbol{r}, \boldsymbol{r'}) - \omega \xi_{c(f+1)} \overline{\boldsymbol{G}}_e^{[(f+1)s]}(\boldsymbol{r}, \boldsymbol{r'})\right].
\end{aligned} \tag{5.53}$$

Note that

$$\begin{aligned}\overline{\boldsymbol{\alpha}}\cdot\boldsymbol{N}_{n,\lambda}(h) &= -\frac{h}{k_\lambda}\sigma\boldsymbol{M}_{n,\lambda}(h)+\alpha_t\boldsymbol{N}_{nt,\lambda}(h)+\alpha_z\boldsymbol{N}_{nz,\lambda}(h), \qquad (5.54a)\\ \overline{\boldsymbol{\alpha}}\cdot\boldsymbol{M}_{n,\lambda}(h) &= \alpha_t\boldsymbol{M}_{n,\lambda}(h)-\frac{k_\lambda}{h}\sigma\boldsymbol{N}_{nt,\lambda}(h)+\frac{h}{k_\lambda}\sigma\boldsymbol{N}_{nz,\lambda}(h) \qquad (5.54b)\end{aligned}$$

which will be used in the implementation of Eq. (5.53).

To simplify the derivation of the general solution of the coefficients, the boundary conditions in Eq. (5.53) can be expressed by a series of compact matrices

$$\left[F_{lj'(f+1)}\right]\cdot\left\{\left[\Upsilon_{lj'(f+1)s}\right]+\delta^s_{f+1}\left[U_{(f+1)}\right]\right\}=\left[F_{lj'f}\right]\cdot\left\{\left[\Upsilon_{lj'fs}\right]+\delta^s_f\left[D_f\right]\right\} \qquad (5.55)$$

where $j'=1,2$ and l denotes M,Q,U and V, respectively. These matrices are given by

$$[F_{M1f}]=\begin{bmatrix}\frac{e^{ih_{1f}z_f}}{(h_{1s}-h_{2s})(h_{1s}-h_{4s})} & \frac{e^{ih_{3f}z_f}}{(h_{3s}-h_{4s})(h_{2s}-h_{3s})}\\ \frac{[h_{1f}\alpha_{tf}-(\omega\xi_{cf}+ih_{1f}\alpha_{af})]e^{ih_{1f}z_f}}{(h_{1s}-h_{2s})(h_{1s}-h_{4s})} & \frac{[h_{3f}\alpha_{tf}-(\omega\xi_{cf}+ih_{3f}\alpha_{af})]e^{ih_{3f}z_f}}{(h_{3s}-h_{4s})(h_{2s}-h_{3s})}\end{bmatrix}, \qquad (5.56)$$

$$[F_{Q1f}]=\begin{bmatrix}\frac{h_{1f}\tau_{21f}e^{ih_{1f}z_f}}{k_{\lambda1f}(h_{1s}-h_{2s})(h_{1s}-h_{4s})} & \frac{\left[(\tau_{21f}-\tau_{31f})(\alpha_{tf}-\alpha_{af})h^2_{1f}+\tau_{31f}(\alpha_{tf}-\alpha_{af})k^2_{\lambda1f}-\tau_{21f}\omega\xi_{cf}h_{1f}\right]e^{ih_{1f}z_f}}{k_{\lambda1f}(h_{1s}-h_{2s})(h_{1s}-h_{4s})}\\ \frac{h_{3f}\tau_{23f}e^{ih_{3f}z_f}}{k_{\lambda3f}(h_{3s}-h_{4s})(h_{2s}-h_{3s})} & \frac{\left[(\tau_{23f}-\tau_{33f})(\alpha_{tf}-\alpha_{af})h^2_{3f}+\tau_{33f}(\alpha_{tf}-\alpha_{af})k^2_{\lambda3f}-\tau_{23f}\omega\xi_{cf}h_{3f}\right]e^{ih_{3f}z_f}}{k_{\lambda3f}(h_{3s}-h_{4s})(h_{2s}-h_{3s})}\end{bmatrix}^T \qquad (5.57)$$

$$[F_{U1f}]=\begin{bmatrix}\frac{h_{1f}\tau_{51f}e^{ih_{1f}z_f}}{k_{\lambda1f}(h_{1s}-h_{2s})(h_{1s}-h_{4s})} & \frac{\left[(\tau_{51f}-\tau_{41f})(\alpha_{tf}-\alpha_{af})h^2_{1f}+\tau_{41f}(\alpha_{tf}-\alpha_{af})k^2_{\lambda1f}-\tau_{51f}\omega\xi_{cf}h_{1f}\right]e^{ih_{1f}z_f}}{k_{\lambda1f}(h_{1s}-h_{2s})(h_{1s}-h_{4s})}\\ \frac{h_{3f}\tau_{53f}e^{ih_{3f}z_f}}{k_{\lambda3f}(h_{3s}-h_{4s})(h_{2s}-h_{3s})} & \frac{\left[(\tau_{53f}-\tau_{43f})(\alpha_{tf}-\alpha_{af})h^2_{3f}+\tau_{43f}(\alpha_{tf}-\alpha_{af})k^2_{\lambda3f}-\tau_{53f}\omega\xi_{cf}h_{3f}\right]e^{ih_{3f}z_f}}{k_{\lambda3f}(h_{3s}-h_{4s})(h_{2s}-h_{3s})}\end{bmatrix}^T \qquad (5.58)$$

$$[F_{V1f}] = \begin{bmatrix} \dfrac{h_{1f}\tau_{41f}e^{ih_{1f}z_f}}{k_{\lambda 1f}(h_{1s}-h_{2s})(h_{1s}-h_{4s})} & \dfrac{\left[(\tau_{41f}-\tau_{71f})(\alpha_{tf}-\alpha_{af})h_{1f}^2+\tau_{71f}(\alpha_{tf}-\alpha_{af})k_{\lambda 1f}^2-\tau_{41f}\omega\xi_{cf}h_{1f}\right]e^{ih_{1f}z_f}}{k_{\lambda 1f}(h_{1s}-h_{2s})(h_{1s}-h_{4s})} \\ \dfrac{h_{3f}\tau_{43f}e^{ih_{3f}z_f}}{k_{\lambda 3f}(h_{3s}-h_{4s})(h_{2s}-h_{3s})} & \dfrac{\left[(\tau_{43f}-\tau_{73f})(\alpha_{tf}-\alpha_{af})h_{3f}^2+\tau_{73f}(\alpha_{tf}-\alpha_{af})k_{\lambda 3f}^2-\tau_{43f}\omega\xi_{cf}h_{3f}\right]e^{ih_{3f}z_f}}{k_{\lambda 3f}(h_{3s}-h_{4s})(h_{2s}-h_{3s})} \end{bmatrix}^T, \tag{5.59}$$

where the superscript T denotes the transpose of the matrices.

The matrices $[F_{lj'f}]$ remain the same form for $j' = 2$ except that the subscript 1 is changed to 2 and the subscript 3 is changed to 4. Furthermore, the denominator which contains the term $(h_{1s}-h_{4s})$ is changed to $(h_{2s}-h_{3s})$ and vice versa. The terms τ_{2jf}, τ_{3jf}, τ_{4jf}, τ_{5jf}, and τ_{7jf} are the weighting factors associated with the scattering coefficients A_{lj}^{fs} and B_{lj}^{fs}. They have the same forms as those in Eq. (5.19) and Eq. (5.22). The only change is that each term relating to wavenumbers (e.g., h) will have a subscript of jf (e.g., h_{jf}) and each term relating to material parameters (e.g., ξ_c) will have a subscript of f (e.g., ξ_{cf}) where j'=1, 2 and f represents the fth layer.

The following matrices are also used in the formulation:

$$[\Upsilon_{lj'fs}] = \begin{bmatrix} A_{lj'}^{fs} & B_{lj'}^{fs} \\ A_{l,j'+2}^{fs} & B_{l,j'+2}^{fs} \end{bmatrix}, \tag{5.60a}$$

$$[U_f] = \begin{bmatrix} 1 & 0 \\ 0 & 0 \end{bmatrix}, \tag{5.60b}$$

$$[D_f] = \begin{bmatrix} 0 & 0 \\ 0 & 1 \end{bmatrix}. \tag{5.60c}$$

By defining the following transmission T-matrix:

$$[T_{lj'f}] = \left[F_{lj'(f+1)f}\right]^{-1} \cdot [F_{lj'ff}], \tag{5.61}$$

where $\left[F_{lj'(f+1)f}\right]^{-1}$ is the inverse matrix of $\left[F_{lj'(f+1)f}\right]$, the linear equations become the following form:

$$\left[\Upsilon_{lj'(f+1)s}\right] = [T_{lj'f}] \cdot \left\{[\Upsilon_{lj'fs}] + \delta_f^s [D_f]\right\} - \delta_{f+1}^s \left[U_{(f+1)}\right]. \tag{5.62}$$

Similarly, the matrix is formulated to simplify the derivation:

$$\begin{aligned} \left[T_{lj'}^K\right]_{2\times 2} &= [T_{lj',N-1}]\,[T_{lj',N-2}] \cdots [T_{lj',K+1}]\,[T_{lj',K}] \\ &= \begin{bmatrix} T_{lj',11}^K & T_{lj',12}^K \\ T_{lj',21}^K & T_{lj',22}^K \end{bmatrix}. \end{aligned} \tag{5.63}$$

Note that the coefficients matrices of the first and the last layers have the following relations:

$$[\Upsilon_{lj'1s}] = \begin{bmatrix} A_{lj'}^{1s} & B_{lj'}^{1s} \\ 0 & 0 \end{bmatrix}; \quad [\Upsilon_{lj'Ns}] = \begin{bmatrix} 0 & 0 \\ A_{l,j'+2}^{Ns} & B_{l,j'+2}^{Ns} \end{bmatrix}. \tag{5.64}$$

In analogy to the cylindrical layered case, three kinds of source locations are studied for the planarly layered case.

Source in an intermediate layer

When the current source is located in an intermediate layer, (i.e. $s \neq 1, N$), only the terms containing $(1 - \delta_f^1)$ for the first layer and $(1 - \delta_f^N)$ for the last layer vanish in (5.51) and (5.52). The coefficient matrices in Eqs. (5.60) and (5.64) will be further simplified:

$$
\begin{aligned}
[\Upsilon_{lj',1s}] &= \begin{bmatrix} A^{1s}_{lj'} & B^{1s}_{lj'} \\ 0 & 0 \end{bmatrix}, \\
[\Upsilon_{lj',ms}] &= \begin{bmatrix} A^{ms}_{lj'} & B^{ms}_{lj'} \\ A^{ms}_{l,j'+2} & B^{ms}_{l,j'+2} \end{bmatrix}, \\
[\Upsilon_{lj',Ns}] &= \begin{bmatrix} 0 & 0 \\ A^{Ns}_{l,j'+2} & B^{Ns}_{l,j'+2} \end{bmatrix}.
\end{aligned}
\tag{5.65}
$$

From Eq. (5.62), the recurrence equation becomes:

$$
\begin{aligned}
[\Upsilon_{lj',fs}] &= [T_{lj',f-1}] \cdots [T_{lj',s}] \cdot \{[T_{lj',s-1}] \cdots [T_{lj',1}] \, [\Upsilon_{lj',1s}] + \\
&\quad u(f-s-1) \, [D_s] - u(f-s) \, [U_s]\} \,,
\end{aligned}
\tag{5.66}
$$

where $u(x - x_0)$ is the unit step function. For $f = N$, the coefficients for the first layer are given by:

$$
\begin{aligned}
A^{1s}_{lj'} &= \frac{T^{(s)}_{lj',11}}{T^{(1)}_{lj',11}}, \\
B^{1s}_{lj'} &= -\frac{T^{(s)}_{lj',12}}{T^{(1)}_{lj',11}}.
\end{aligned}
\tag{5.67}
$$

For the last layer,

$$
\begin{aligned}
A^{Ns}_{l,j'+2} &= T^{(1)}_{lj',21} A^{1s}_{lj'} - T^{(s)}_{lj',21}, \\
B^{Ns}_{l,j'+2} &= T^{(1)}_{lj',21} B^{1s}_{lj'} + T^{(s)}_{lj',22}.
\end{aligned}
\tag{5.68}
$$

Substituting Eq. (5.67) into (5.66), the remaining coefficients can be obtained for the dyadic Green's functions.

Source in the first layer

When the current source is located in the first layer (i.e., $s = 1$), the terms containing $(1 - \delta^1_s)$ in Eqs. (5.51) and (5.52) vanishes. The coefficient matrices in Eqs. (5.60) and (5.64) will be further reduced to:

$$\begin{aligned}
[\Upsilon_{lj',11}] &= \begin{bmatrix} 0 & B_{lj'}^{11} \\ 0 & 0 \end{bmatrix}, \\
[\Upsilon_{lj',m1}] &= \begin{bmatrix} 0 & B_{lj'}^{m1} \\ 0 & B_{l,j'+2}^{m1} \end{bmatrix}, \qquad (5.69) \\
[\Upsilon_{lj',N1}] &= \begin{bmatrix} 0 & 0 \\ 0 & B_{l,j'+2}^{N1} \end{bmatrix},
\end{aligned}$$

where $m = 2, 3, \cdots, N-1$. It can be seen that only four coefficients for the first layer and the last layer, but 8 coefficients for each of the remaining layers, need to be solved for. By following (5.62), the recurrence relation in the f^{th} layer becomes:

$$[\Upsilon_{lj',f1}] = [T_{lj',f-1}] \cdots [T_{lj',1}] \left\{ [\Upsilon_{lj',11}] + [D_1] \right\}. \qquad (5.70)$$

With $f = N$ in (5.43), a matrix equation satisfied by the coefficient matrices in (5.42) can be obtained. The coefficient for the first layer where the source is located (i.e. $s = 1$) is given by:

$$B_{lj'}^{11} = -\frac{T_{lj',12}^{(1)}}{T_{lj',11}^{(1)}}. \qquad (5.71)$$

The coefficient for the last layer can be derived in terms of the coefficients for the first layer given by:

$$B_{l,j'+2}^{N1} = T_{lj',21}^{(1)} B_{lj'}^{11} + T_{lj',22}^{(1)}. \qquad (5.72)$$

The coefficients for the intermediate layers can be then obtained by substituting the coefficients for the first layer in Eq. (5.71) into (5.70). Thus, all the coefficients can be obtained by these procedures.

Source in the last layer

When the current source is located in the first layer (i.e., $s = N$), the coefficients are:

$$[\Upsilon_{lj',1N}] = \begin{bmatrix} A_{lj'}^{1N} & 0 \\ 0 & 0 \end{bmatrix}, \tag{5.73a}$$

$$[\Upsilon_{lj',mN}] = \begin{bmatrix} A_{lj'}^{mN} & 0 \\ A_{l,j'+2}^{mN} & 0 \end{bmatrix}, \tag{5.73b}$$

$$[\Upsilon_{lj',NN}] = \begin{bmatrix} 0 & 0 \\ A_{l,j'+2}^{NN} & 0 \end{bmatrix}. \tag{5.73c}$$

Similarly, from Eq. (5.62), one has

$$[\Upsilon_{lj',fN}] = [T_{lj',f-1}] \cdots [T_{lj',1}]\,[\Upsilon_{lj',1N}] - u(f-N)\,[U_N]\,. \tag{5.74}$$

By letting $f = N$, the coefficient for the first region is

$$A_{lj'}^{1N} = \frac{1}{T_{lj',11}^{(1)}}. \tag{5.75}$$

And for the last layer, it is found that

$$A_{l,j'+2}^{NN} = T_{lj',21}^{(1)} A_{lj'}^{1N}\,. \tag{5.76}$$

Similarly, the remaining coefficients can be obtained by inserting Eq. (5.76) into (5.74).

When the source distribution is given, the electric field, either in cylindrical or planar layered structure, can be computed by Eq. (5.3), in which the local parameters of the source, the stratified layers and the gyrotropic chiral materials in each layer have been taken into account systematically.

5.2 Effective medium theory for general composites

Complementary to the dyadic Green's function method, effective medium theory is another way to describe the functional material especially in periodic lattices in a macroscopic view. DGF method is based on rewriting Maxwell equation by orthogonal eigenfunctional basis in a summation or integral form. Effective medium theory, discussed in my dissertation, depends on discretization of Maxwell equation in terms of multi-scale. This improved homogenization process is based on decomposition of the fields into an averaged non-oscillating part and a corrected term with micro-oscillation, which is based on the asymptotic multi-scale unfolding method. It approximates the fields and effective parameters in finite lattices of periodic chiral or even bianisotropic inclusions with higher accuracy and less requirements of computation time and memory.

A central problem in the theory of composites is to study how physical properties of composites such as permittivity and permeability depend on the properties of their constituents. In general, these properties depend strongly on the microstructure. To predict the effective EM properties of structured artificial materials especially when the wavelength is larger than the periodicity, basic mixing rules have been derived for cylindrical or spherical inclusions [91, 173] based on the evaluation of the field perturbation in the presence of a single inclusion. Further extensions to the case of more complex mixtures (e.g., chiral material, elliptical inclusions, multiphase mixtures) have been successively proposed [138,139,174], and some numerical techniques have been used such as boundary integral equation method, method of moments and finite element method [175–177]. Note that, most of the methods aforementioned, which describe the dielectric responses of each particle and mutual interaction among inclusions, are applicable only for simple shapes with very weak interaction or simple isotropic or anisotropic material constitutions.

To overcome this problem, an improved homogenization based on multiscale expansion [178] is developed to compute the effective constitutive parameters for the most general bianisotropic composites [179], which take into account the mutual interaction of complex-shaped inclusions and the volume fraction effects in a macroscopic view. More importantly, this novel method can be also used to approximate the fields in finite lattices of periodic bianisotropic materials. The fields are computed only in the unit cell and then generalized over the whole volume. Therefore, given a large finite lattice of bianisotropic composites, the time of computation and the memory requirement can be greatly reduced without the loss of accuracy. The proposed advanced homogenization method can study not only the bianisotropic inclusions but also the shape effects of the inclusions, while [180] can only treat lossy isotropic inclusions with regular shapes and it is incapable to analyze complex media or complex shaped inclusions. Hence, this result is a remarkable step further in the development of homogenization method for composite metamaterials.

5.2.1 Formulation

Let us consider a periodic structure of identical bianisotropic inclusions immersed in a matrix. The constitutive relations of the bianisotropic media are given

$$\boldsymbol{D} = \overline{\boldsymbol{\epsilon}} \cdot \boldsymbol{E} + \sqrt{\epsilon_0 \mu_0}\,\overline{\boldsymbol{\xi}} \cdot \boldsymbol{H} \tag{5.77a}$$

$$\boldsymbol{B} = \sqrt{\epsilon_0 \mu_0}\,\overline{\boldsymbol{\zeta}} \cdot \boldsymbol{E} + \overline{\boldsymbol{\mu}} \cdot \boldsymbol{H} \tag{5.77b}$$

where $\overline{\boldsymbol{\xi}}$ and $\overline{\boldsymbol{\zeta}}$ represent two cross-polarization dyadics. The reference unit cell is characterized by Y^α with the periodicity α and scaled unit cell αY, which is the unit volume of the cubes in three-dimensional (3-D) spaces. The configuration is shown in Fig. 5.3. The Maxwell's equations are established in each unit cell

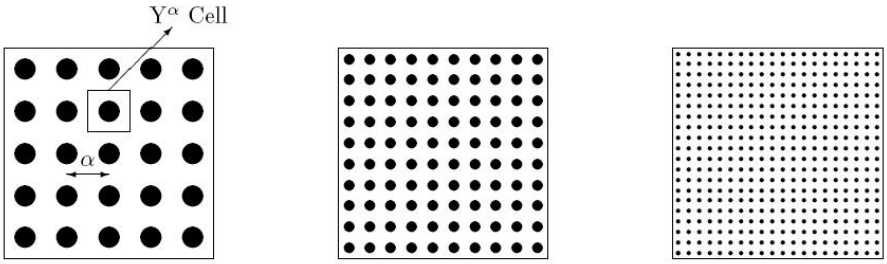

Figure 5.3: Periodic composite materials when periodicity is decreasing

$$\boldsymbol{\nabla} \times \boldsymbol{E}^\alpha(x) = -\frac{\partial \boldsymbol{B}^\alpha(x)}{\partial t} \tag{5.78a}$$

$$\boldsymbol{\nabla} \times \boldsymbol{H}^\alpha(x) = \frac{\partial \boldsymbol{D}^\alpha(x)}{\partial t} + \boldsymbol{J}^\alpha(x). \tag{5.78b}$$

The variable x denotes the smooth variation of the field from cell to cell. Spatial functions of $\overline{\boldsymbol{\epsilon}}$, $\overline{\boldsymbol{\mu}}$, $\overline{\boldsymbol{\xi}}$ and $\overline{\boldsymbol{\zeta}}$ oscillate drastically in the considered structure due to the heterogeneities. These oscillations are difficult to treat numerically. Therefore, homogenization theory can be used to give the macroscopic global properties of the current composite by taking into account the properties of the microscopic structure. Hence, another variable $y = x/\alpha$ is introduced to describe the fast variation within the cell.

Eq. (5.78) can be further rewritten in a matrix form

$$i\omega A^{\alpha}(y)u^{\alpha}(\omega, x) = Mu^{\alpha}(\omega, x) - J^{\alpha}(\omega, x) \tag{5.79}$$

where A^{α} is a 6×6 matrix constituted by the four material dyadics in the unit cell and M represents the rotational operator. When the period of the lattice is quite small compared to the wavelength, the total EM fields can thus be expanded by a function of an average part with a series of corrector terms

$$u^{\alpha}(\omega, x) = u(\omega, x) + \nabla_y \Phi(\omega, x, y) + \alpha \Psi(\omega, x, y) + ... \tag{5.80}$$

where only the first two terms (i.e., macroscopic EM field $u(\omega, x)$ of the cell and the first microscopic corrector $\nabla_y \Phi(\omega, x, y)$ are required for computation. Strong convergence can be obtained without subsequent high-order corrector potentials [181, 182]. Thus, taking the limit of α tending to zero in Eq. (5.79) (see Fig. 5.3) leads to:

$$i\omega A(y)[u(\omega, x) + \nabla_y \Phi(\omega, x, y)] = M_x u(\omega, x) + M_y \Phi(\omega, x, y) - J(\omega, x). \tag{5.81}$$

Scalar-dotting a testing periodic function ϕ in its gradient form, one can arrive at the following equation after the integration over the whole volume is performed:

$$\begin{aligned} &\int_Y i\omega A(y)[u(\omega, x) + \nabla_y \Phi(\omega, x, y)] \cdot \nabla_y \phi(y) dy \\ &\qquad = \int_Y [M_x u(\omega, x) + M_y \Phi(\omega, x, y) - J(\omega, x)] \cdot \nabla_y \phi(y) dy. \end{aligned} \tag{5.82}$$

Due to the convergence theorem of the periodic function, it can be obtained for the right-hand-side term of Eq. (5.82) as follows:

$$\begin{aligned}&\int_Y [M_x u(\omega, x) + M_y \Phi(\omega, x, y) - J(\omega, x)] \cdot \nabla_y \phi(y) dy \\ &\qquad = - \int_Y \phi(y) \nabla [M_x u(\omega, x) + M_y \Phi(\omega, x, y) - J(\omega, x)] dy. \qquad (5.83)\end{aligned}$$

Note that $M_x u(\omega, x) - J(\omega, x)$ is independent on the microscopic variable y and $\nabla_y \cdot M_y = 0$ since M is rotational operator. Therefore, the right-hand side of Eq. (5.83) is zero, and the integral of the limit in Eq. (5.83) becomes

$$\int_Y i\omega A(y)[u(\omega, x) + \nabla_y \Phi(\omega, x, y)] \cdot \nabla_y \phi(y) dy = 0 \qquad (5.84)$$

where the terms of Φ and $\nabla_y \Phi$ are represented as

$$\begin{aligned}\Phi(\omega, x, y) &= u(\omega, x)\psi(\omega, y) = \sum_{j=1}^{6} u_j(\omega, x)\psi_j(\omega, y) \qquad (5.85a) \\ \nabla_y \Phi(\omega, x, y) &= \sum_{j=1}^{6} u_j(\omega, x) \nabla_y \psi_j(\omega, y). \qquad (5.85b)\end{aligned}$$

Thus $u + \nabla_y \Phi$ is given by

$$u(\omega, x) + \nabla_y \Phi(\omega, x, y) = \sum_{j=1}^{6} u_j(\omega, x)[e_j + \nabla_y \psi_j(\omega, y)], \qquad (5.86)$$

where $e_j \in \Re^6$ is the unit basis vector. Inserting Eq. (5.86) into (5.84), one will obtain that ψ_j (j=1,...,6) is the solution of the following equation

$$\int_Y A(y)[e_j + \nabla_y \psi_j(\omega, y)] \cdot \nabla_y \phi(y) dy = 0. \qquad (5.87)$$

Replacing $u + \nabla_y \Phi$ in Eq. (5.79) by (5.85a) and integrating over the unit cell, one has

$$i\omega \int_Y A(y)[u(\omega, x) + u(\omega, x)\nabla_y \psi(\omega, y)] dy = |Y|(Mu(\omega, x) - J(\omega, x)), \qquad (5.88)$$

where $|Y|$ is the normalized volume of the unit cell ($|Y| = 1$). Thus, Eq. (5.88) can be expressed as

$$i\omega A_{eff} u(\omega, x) = M u(\omega, x) - J(\omega, x) \tag{5.89}$$

where the macroscopic effective parameters in the dyadic form can be expressed as

$$A_{j,eff} = \int_Y A(y)[e_j + \nabla_y \psi_j(\omega, y)]dy. \tag{5.90}$$

$A_{j,eff}$ denotes the jth column of the 6×6 effective constitutive matrix $A(y)$, which is comprised of effective permittivity, permeability, and two cross-polarization dyadics. It can be used in all frequency bands only if the periodicity is much smaller than the incidence wavelength.

5.2.2 Numerical validation and results

The major advantage of this approach is that it gives the possibility to accurately evaluate the EM field inside finite lattices when the period of the lattice is small compared with that of the wavelength. This field is the sum of the average field and corrector field as shown in Eq. (5.86). To validate this approach, the electric field in a finite periodic composite material with chiral properties is compared to that obtained by the method proposed in [134] combined with the FEM. In that method, a decomposition scheme is used to transform the chiral medium to their isotropic equivalences characterized by four equivalent permittivity/permeability parameters of $\epsilon_{\pm}$ and $\mu_{\pm}$. This method is significantly important to calculate the electric field because it can remove the term of $\boldsymbol{\nabla} \times \boldsymbol{E}$ from the Helmholtz equations for chiral media, which greatly simplified the numerical computation.

Effective constitutive parameters

Let us first consider infinite lattices of identical chiral cylinder inclusions of various cross sections (see Fig. 5.4) with relative permittivity and permeability $\epsilon_r = \mu_r = 10$ and relative chirality $\kappa = 1$. The host medium is free space. The effects of the edges and discontinuities of the chiral inclusions are studied, which cannot be taken into account in the classical theory of homogenization (e.g. Maxwell-Garnett formulas). Homogenized effective parameters are plotted against the volume fraction. It is found that, for a lattice of square chiral cylinders, the present method produces almost the same effective parameters as Maxwell-Garnett formulas which is normally best suitable for smooth canonical shapes (i.e. ellipsoids). This phenomenon can be explained that for this shape, the interaction of the corners between adjacent inclusions becomes strong and thus enhances the depolarization of the material, which results in the decrease of the effective parameters compared to other shapes [177].

Fig. 5.5 presents the comparison of inclusions with different rounded corners and contours. One can see that at the same fraction index, the inclusion with rounded concave contours gives the biggest effective permittivity. For volume fraction bigger than 0.15, the difference between the curve of inclusion 4 and the other three curves of inclusions 1-3 becomes visibly larger and larger, which indicates the depolarization produced by the corners of inclusion 4 is much more decreased and higher mutual coupling causes a bigger increase in the polarizability density than the other three inclusions. For each inclusion type, the effective parameters reach the upper limits

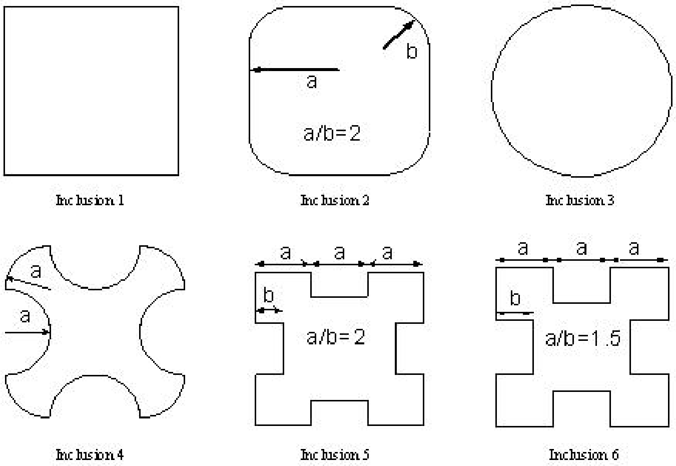

Figure 5.4: Geometry of complex-shaped 2D inclusions

with the maximum available volume fraction. A tradeoff can be observed between the effective parameters and volume fraction. For instance, when it is required to achieve a higher effective parameter, we need to embed more chiral inclusions per unit volume, but we may need to change the shape of the inclusions. If the parameter requirement is not very high, inclusion 4 will be a good choice to save material consumptions.

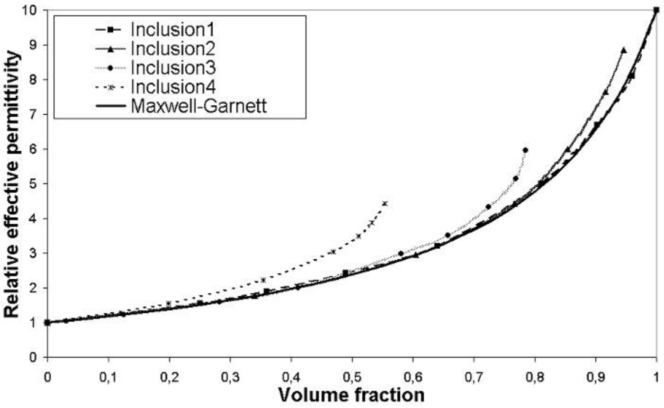

(a)

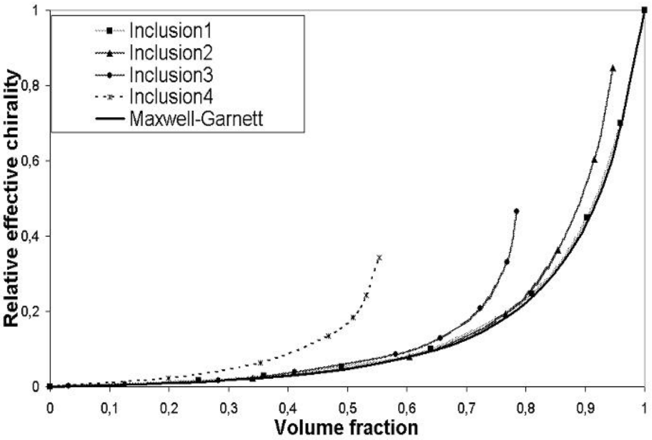

(b)

Figure 5.5: Effective parameters of square lattices of inclusions 1, 2, 3 and 4 ($\epsilon_r = \mu_r = 10$ and $\kappa = 1$) suspended in free space: (a) effective relative permittivity; and (b) effective relative chirality.

Fig. 5.6 presents the responses of chiral inclusions with different concavities. At a fixed fraction, the effective parameters of the inclusion with the biggest concavity are the largest. By comparing with Fig. 5.5, one can observe that the limit values for concave chiral inclusions with corners are higher than the rounded concave ones. For instance, at volume fraction $f = 0.778$, one reads $\epsilon_{eff} = 5.717$ and $\kappa_{eff} = 0.416$ for inclusion 3 from Fig. 5.5, while $\epsilon_{eff} = 6.84$ and $\kappa_{eff} = 0.625$ for inclusion 5 from Fig. 5.6. It can also be found in Fig. 5.6 that effective parameters will increase with the etching ratio b/a (for Inclusion Types 1, 5 & 6, the etching ratio is 0, 0.5, and 0.667, respectively).

The proposed method is utilized to compute effective parameters of 3D spherical/cubic chiral inclusions, which are compared with the results from the Maxwell-Garnett (M-G) formulas. Fig. 5.7 is plotted over the volume fraction from 0 to 0.52, where f_{max} is reached for the lattice of chiral spheres in our model. It can be seen that at low volume fraction, the results of our method are similar to those calculated by M-G formulas. For $f > 0.4$, the differences become more and more significant. The effect of the material depolarization due to the corners is again visible.

Last but not least, the general bianisotropic inclusions embedded in a bianisotropic environment is considered. As a simplified example, the spherical inclusions are considered and it is assumed that $\overline{\boldsymbol{\xi}} = \overline{\boldsymbol{\zeta}} = \overline{\boldsymbol{K}}$. ($\overline{\boldsymbol{\epsilon}}$, $\overline{\boldsymbol{\mu}}$, $\overline{\boldsymbol{K}}_h$) and ($\overline{\boldsymbol{\epsilon}}$, $\overline{\boldsymbol{\mu}}$, $\overline{\boldsymbol{K}}_i$) are respectively the relative parameters for the host (h) media and the cubical inclusions (i)

$$\overline{\boldsymbol{\epsilon}} = \overline{\boldsymbol{\mu}} = \begin{bmatrix} 10 & 0 & 0 \\ 0 & 10 & 0 \\ 0 & 0 & 5 \end{bmatrix} \tag{5.91a}$$

$$\overline{\boldsymbol{K}}_h = \begin{bmatrix} -1 & 0.4 & 0 \\ 0.4 & -0.6 & 0 \\ 0 & 0 & -1.5 \end{bmatrix} \tag{5.91b}$$

$$\overline{\boldsymbol{K}}_i = \begin{bmatrix} 1 & 0.4 & 0 \\ 0.4 & 0.6 & 0 \\ 0 & 0 & 1.5 \end{bmatrix}. \tag{5.91c}$$

The macroscopic effective parameters ($\overline{\boldsymbol{\epsilon}}_{eff}$, $\overline{\boldsymbol{\mu}}_{eff}$, $\overline{\boldsymbol{K}}_{eff}$) at volume fraction $f_{max} = 0.525$ are found to be

$$\overline{\boldsymbol{\epsilon}}_{eff} = \overline{\boldsymbol{\mu}}_{eff} = \begin{bmatrix} 9.96 & 0 & 0 \\ 0 & 9.98 & 0 \\ 0 & 0 & 4.86 \end{bmatrix} \tag{5.92a}$$

$$\overline{\boldsymbol{K}}_{eff} = \begin{bmatrix} 0.0223 & 0.399 & 0 \\ 0.399 & 0.0139 & 0 \\ 0 & 0 & 0.0092 \end{bmatrix}. \tag{5.92b}$$

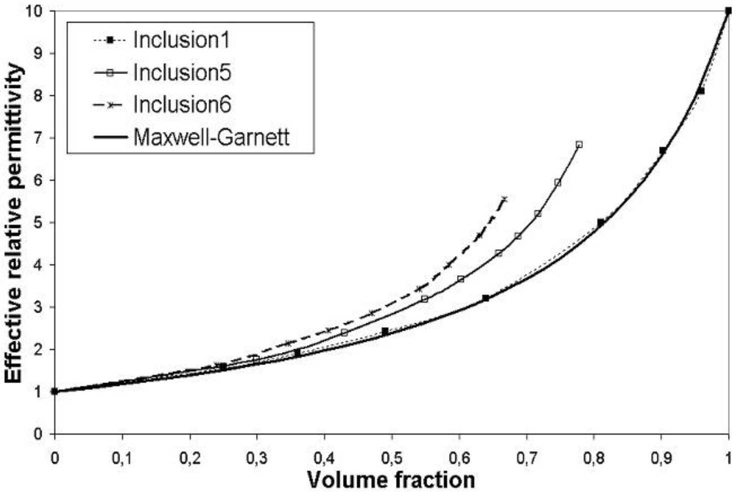

(a) effective relative permittivity

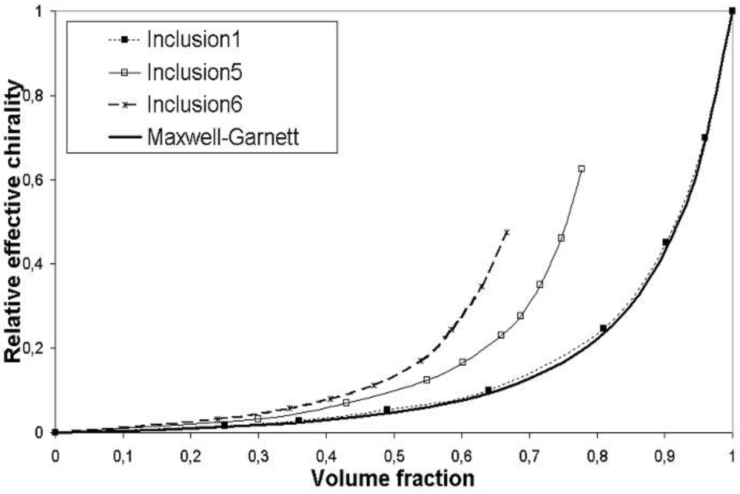

(b) effective relative chirality

Figure 5.6: Effective parameters of square lattices of inclusions 1, 5 and 6 ($\epsilon_r = \mu_r = 10$ and $\kappa = 1$) suspended in free space.

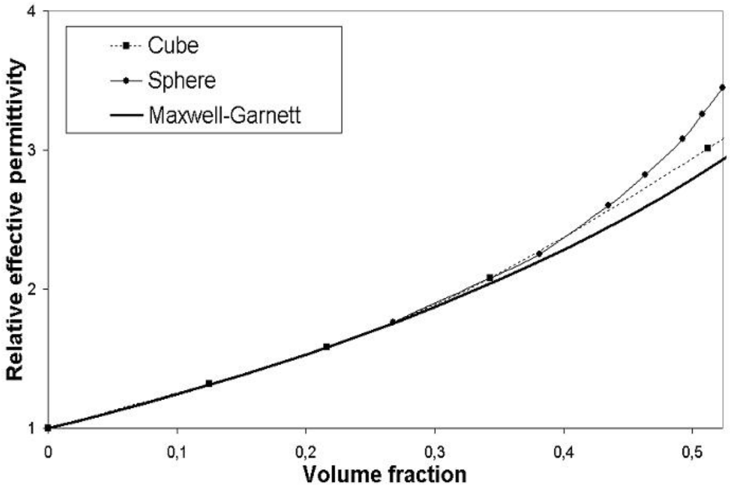

(a) effective relative permittivity

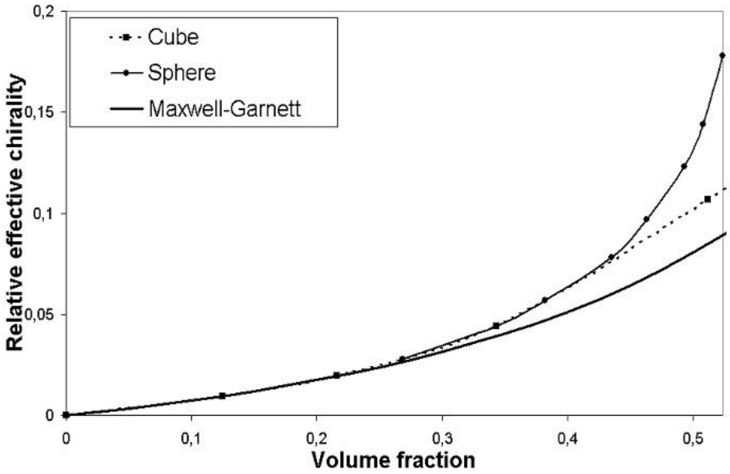

(b) effective relative chirality

Figure 5.7: Effective parameters of square lattices of spherical and cubical inclusions ($\epsilon_r = \mu_r = 10$ and $\kappa = 1$) suspended in free space.

Local fields

As the second round of validations of the approach and the numerical codes proposed in this paper, we compare the total electric fields obtained by our method with the results of the classical FEM. Let us consider a finite lattice of 27 cells made of chiral material with the parameters ($\epsilon_r = \mu_r = 10$ and $\kappa = 2$) with a vacuum cube located at the center of each cell (Fig. 5.8). The lattice is truncated by metallic walls, except on the front $x - y$ surface where a plane wave with $|E_y|/|E_x| = 2$ is imposed. The electric field is calculated in the central $y - z$ plane inside the lattice at 10 MHz. The sizes of each vacuum cube and basic cell are 0.125 and 1 cm^3, respectively.

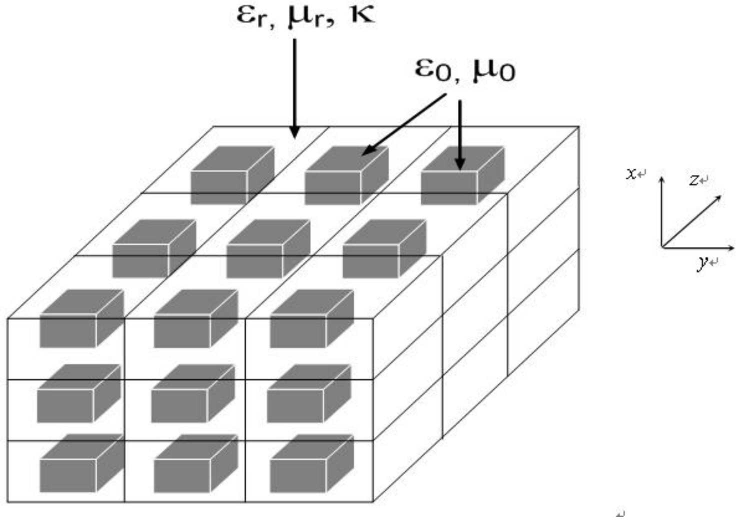

Figure 5.8: Finite periodic lattice containing 27 cubical inclusions.

The total electric field can be expressed as

$$\boldsymbol{E}_T = \boldsymbol{E}_{av} + \boldsymbol{E}_{cor} \tag{5.93}$$

where $\boldsymbol{E}_{av}$ can be obtained by assuming the whole structure is occupied by a homogenized medium with the previously computed effective constitutive parameters, and $\boldsymbol{E}_{cor} = \nabla_y \Phi$ can be solved in the unit cell of the lattice.

Fig. 5.9 represents the amplitude of the x-component of the electric field along the z-axis. In this figure, we plot the averaged E_{av} and corrected E_{cor} and then by adding up those two portions in vector form, we obtain the total field.

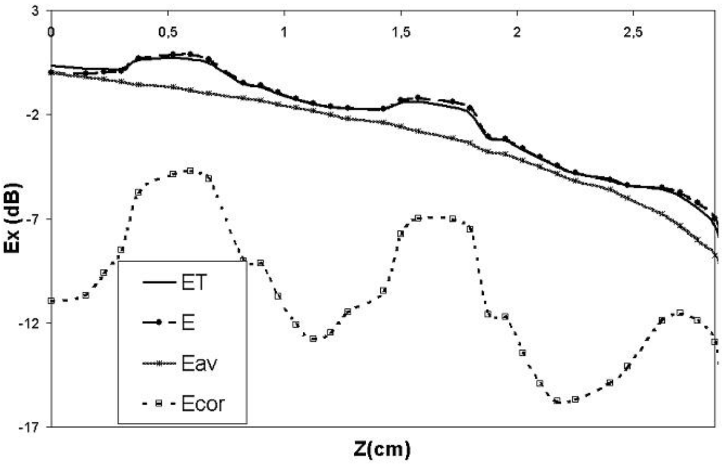

Figure 5.9: Magnitude of the x-component of the electric field as a function of position along z-axis at $x = y = L/2$.

For comparative purposes, the electric field is also calculated by the classical FEM applied to the whole structure, and it is found that the good agreement of the results between the present method and the classical FEM is achieved. The stability and validity of this improved homogenization method have been confirmed. From Fig. 5.9, it can be seen that the averaged field decreases smoothly along the z-direction, while the corrected field varies drastically due to the microscopic heterogeneities, which illustrates the efficiency of the current method compared with the standard homogenization technique (where the field within the microstructure is simply assimilated to averaged field). Therefore, the proposed method provides an effective way to describe the microscopic and macroscopic performances of the composite metamaterials separately and explicitly. It is also shown that only the first-order corrector is required to be taken into account so as to achieve enough good accuracy.

5.3 Summary

In summary, this chapter is devoted to the macroscopic characterization of the inhomogeneous composites from layered structures to periodic constitutions. Since the negative-index materials and metamaterials are normally constituted with heterogeneous elements, the results obtained in this chapter thus cater to the increasing need in the macroscopic study of structured composites. The proposed DGF and homogenization methods are well generalized and can be applied in a variety of sub-cases. Although the DGFs are only developed for gyrotropic chiral materials, the current results are still very useful, because gyrotropic chiral media are already very general and the geometries in two layered structures are both arbitrary. Once the source distribution or illumination is given, the electromagnetic fields are determined based on the proposed eigenfunction expansion and recursive algorithm. Furthermore, periodic lattices, which are commonly used structures in photonics and NIMs, are considered. However, DGFs can not be applied directly due to the 2-dimensional heterogeneity in periodic lattice structures. Therefore, an improved homogenization is developed first to obtain the desired effective parameters. The advantages of the improvements made in the proposed homogenization approach can be concluded: (1) one micro-scale to approximate strong oscillations and the other macro-scale to depict averaged fields; (2) strong interaction of complex-shaped inclusions and edge effects on depolarization are taken into account; and (3) good connection with DGF method. For those periodic structures, the effective parameters computed by the improved homogenization process can thus be utilized by DGFs. Due to the complementarity of DGFs and improved homogenization, combining these two methods will provide more applicabilities and efficiency to the study of macroscopic characterization of inhomogeneous composites.

Chapter 6

Conclusion

In this thesis, electromagnetics in engineered composites have been investigated with special interest in macroscopic properties. There are two interwinded lines: material complexity and NIM realization. The composite materials under investigation in this thesis are quite general, from isotropic to bianisotropic and from single-layered to multilayered. Effective parameters such as permittivity, permeability and chirality were used to study phenomena such as propagation, scattering, and resonance from what was termed NIM. While many valuable insights into the fundamental phenomena and potential applications were yielded along this line, it did not show how to physically realize negative-index materials with such properties. This is where the second line came to join. Along this line, various composite materials from simple to complex, were discussed to find out how to physically realize NIMs by manipulating material's geometry and inherent functionality as well as by using exact electromagnetic solutions. Considering the heterogeneity in practical engineered

NIM composites, two complementary tools have been proposed to characterize the macroscopic responses of structured gyrotropic chiral and bianisotropic composites. Both the heterogeneity and the geometry are considered at very generalized levels. Not only theoretical derivations but also numerical solutions for a wide range of new applications have been studied along the two lines, aiming at developing a more conceptual understanding of electromagnetics in composites.

Future work includes further studies of advanced electromagnetics in infrared region as well as in nanoscale. Future experimental work includes solid-state negative-index materials and its application in small-sized wireless communication components, which could provide a variety of exciting applications. The compactness of such solid-state devices made of composites is a key factor since most of the present metamaterials are bulky. Other work includes further investigation of periodic nature of structured composites in super-lattices and the role of inductive electromagnetic phenomena on the effective parameters. Is the periodicity an essential issue? Can isotropic NIMs be designed by randomly distributed unit elements in a similar way that chiral materials were realized? How can the material study be connected to the size reduction for RF components? In author's opinion, the study on electromagnetics in composites must be conceptually deep in theory with significant impacts in applications.

Bibliography

[1] J. B. Pendry, A. J. Holden, D. J. Robbins, and W. J. Stewart, "Magnetism from conductors and enhanced nonlinear phenomena," *IEEE Trans. Microwave Theory Tech.*, vol. 47, no. 11, pp. 2075–2084, Nov. 1999.

[2] J. Pendry and S. A. Ramakrishna, "Focusing light using negative refraction," *J. Phys.: Condens. Matt.*, vol. 15, no. 37, pp. 6345–6364, Sept. 2004.

[3] V. G. Veselago, "The electrodynamics of substances with simultaneously negative values of ε and μ," *Soviet Physics Uspekhi*, vol. 10, no. 4, pp. 509–514, 1968.

[4] H. Lamb, "On group-velocity," *Proc. London Math. Soc.*, vol. 1, pp. 473–479, 1904.

[5] A. Schuster, *An Introduction to the Theory of Optics*, Edward Arnold, London, 1904.

[6] H. C. Pocklington, "Growth of a wave-group when the group velocity is negative," *Nature*, vol. 71, pp. 607–608, 1905.

[7] G. D. Malyuzhinets, “A note on the radiation principle,” *Sov. Phys. Technical Physics*, vol. 21, pp. 940–942, 1951.

[8] D. V. Sivukhin, “The energy of electromagnetic waves in dispersive media,” *Opt. Spektrosk.*, vol. 3, pp. 308–312, 1957.

[9] R. A. Silin, “Possibility of creating plane-parallel lenses,” *Opt. Spektrosk.*, vol. 44, pp. 189–191, 1978.

[10] J. B. Pendry, A. J. Holden, W. J. Stewart, and I. Youngs, “Extremely low frequency plasmons in metallic mesostructures,” *Phys. Rev. Lett.*, vol. 76, pp. 4773–4776, 1996.

[11] J. B. Pendry, A. J. Holden, D. J. Robbins, and W. J. Stewart, “Low frequency plasmons in thin wire structures,” *J. Phys.: Cond. Matt.*, vol. 10, pp. 4785–4788, 1998.

[12] D. R. Smith, W. J. Padilla, D. C. Vier, S. C. Nemat-Nasser, and S. Schultz, “Composite medium with simultaneously negative permeability and permeability,” *Phys. Rev. Lett.*, vol. 84, pp. 4184–4187, 2000.

[13] D. R. Smith and N. Kroll, “Negative refractive index in left-handed materials,” *Phys. Rev. Lett.*, vol. 85, pp. 2933–2936, 2000.

[14] R. A. Shelby, D. R. Smith, and S. Schultz, “Experimental verification of a negative index of refraction,” *Science*, vol. 292, no. 5514, pp. 77–79, 2001.

[15] R. A. Shelby, D. R. Smith, S. C. Nemat-Nasser, and S. Schultz, "Microwave transimission through a two-dimensional, isotropic, left-handed metamaterial," *Appl. Phys. Lett.*, vol. 78, pp. 489–491, 2001.

[16] J. B. Pendry, "Negative refraction makes a perfect lens," *Phys. Rev. Lett.*, vol. 85, pp. 3966–3969, 2000.

[17] A. A. Houck, J. B. Brock, and I. L. Chuang, "Experimental observations of a left-handed material that obeys Snell's law," *Phys. Rev. Lett.*, vol. 90, pp. 137401, 2003.

[18] G. V. Eleftheriades and K. G. Balmain (Eds.), *Negative-Refraction Metamaterials: Fundamental Principles and Applications*, John Wiley & Sons, IEEE Press, New York, 2005.

[19] R. W. Ziolkowski and N. Engheta (Eds.), *Electromagnetic Metamaterials: Physics and Engineering Applications*, John Wiley & Sons, IEEE Press, New York, 2006.

[20] J. Brown, "Artificial dielectrics," *Progress in Dielectrics*, vol. 2, pp. 195–225, 1960.

[21] R. W. Ziolkowski and A. Kipple, "Causality and double-negative metamaterials," *Phys. Rev. E*, vol. 68, pp. 026615, 2003.

[22] R. Marqués, F. Medina, and R. Rafii-El-Idrissi, "Role of bianisotropy in negative permeability and left-handed metamaterials," *Phys. Rev. B*, vol. 65, pp. 144440, 2002.

[23] R. Marqués, J. D. Baena, M. Beruete, F. Falcone, T. Lopetegi, M. Sorolla, F. Martin, and J. Gracia, "Ab initio analysis of frequency selective surfaces based on conventional and complementary split ring resonators," *J. Opt. A: Pure Appl. Opt.*, vol. 7, no. 2, pp. 38–43, Feb. 2005.

[24] Y. J. Hsu, Y. C. Huang, J. S. Lih, and J. L. Chern, "Electromagnetic resonance in deformed split ring resonators of left-handed meta-materials," *J. Appl. Phys.*, vol. 96, pp. 1979–1982, 2004.

[25] C. R. Simovski and S. He, "Frequency range and explicit expressions for negative permittivity and permeability for an isotropic medium formed by a lattice of perfectly conducting ω particles based on the quasi-static lorentz theory," *Phys. Lett. A*, vol. 311, pp. 254–263, 2003.

[26] H. Chen, L. Ran, J. Huangfu, X. Zhang, K. Chen, T. M. Grzegorczyk, and J. A. Kong, "Left-handed materials composed of only S-shaped resonators," *Phys. Rev. B*, vol. 70, pp. 057605, 2004.

[27] H. Chen, L. Ran, J. Huangfu, X. Zhang, K. Chen, T. M. Grzegorczyk, and J. A. Kong, "Negative refraction of a combined double S-shaped metamaterial," *Appl. Phys. Lett.*, vol. 86, pp. 151909, 2005.

[28] P. Markoš and C. M. Soukoulis, "Numerical studies of left-handed materials and arrays of split ring resonators," *Phys. Rev. E*, vol. 65, pp. 036622, 2002.

[29] N. Katsarakis, T. Koschny, M. Kafesaki, E. N. Economou, E. Ozbay, and C. M. Soukoulis, "Left- and right-handed transmission peaks near the magnetic

resonance frequency in composite metamaterials," *Phys. Rev. B*, vol. 70, pp. 201101, 2004.

[30] J. F. Woodley, M. S. Wheeler, and M. Mojahedi, "Left-handed and right-handed metamaterials composed of split ring resonators and strip wires," *Phys. Rev. E*, vol. 71, pp. 066605, 2005.

[31] A. Sihvola, "Metamaterials and depolarization factors," *Prog. In Electromagn. Res.*, vol. 51, pp. 1–26, 2006.

[32] X. D. Chen, B. I. Wu, J. A. Kong, and T. M. Grzegorczyk, "Retrieval of the effective constitutive parameters of bianisotropic metamaterials," *Phys. Rev. E*, vol. 71, pp. 046610, 2005.

[33] J. B. Pendry and D. R. Smith, "Reversing light with negative refraction," *Physics Today*, vol. 57, no. 6, pp. 37, June 2004.

[34] S. O'Brien and J. B. Pendry, "Magnetic activity at infrared frequencies in structured metallic photonic crystals," *J. Phys.: Cond. Matt.*, vol. 14, pp. 6383–6394, 2002.

[35] S. A. Ramakrishna, "Physics of negative refractive index materials," *Rep. Prog. Phys.*, vol. 68, pp. 449–521, 2005.

[36] S. O'Brien, D. McPeake, S. A. Ramakrishna, and J. B. Pendry, "Near-infrared photonic band gaps and nonlinear effects in negative magnetic metamaterials," *Phys. Rev. B*, vol. 69, pp. 241101, 2004.

[37] V. M. Shalaev, W. Cai, U. K. Chettiar, H. K. Yuan, A. K. Sarychev, V. P. Drachev, and A. V. Kildishev, "Negative index of refraction in optical metamaterials," *Opt. Lett.*, vol. 30, no. 24, pp. 3356–3358, Dec. 2005.

[38] A. Grbic and G. V. Eleftheriades, "Sub-wavelength focusing using a negative-refractive-index transmission-line lens," *IEEE Antennas Wirel. Propagat. Lett.*, vol. 2, pp. 186–189, 2003.

[39] G. V. Eleftheriades, A. K. Iyer, and P. C. Kremer, "Planar negative refractive index media using periodically L-C loaded transmission lines," *IEEE Trans. Microwave Theory Tech.*, vol. 50, no. 12, pp. 2702–2712, Dec. 2002.

[40] A. Grbic and G. V. Eleftheriades, "Negative refraction, growing evanescent waves and sub-diffraction imaging in loaded-transmission-line metamaterials," *IEEE Trans. Microwave Theory Tech.*, vol. 51, no. 12, pp. 2297–2305, Dec. 2003.

[41] A. K. Iyer, P. C. Kremer, and G. V. Eleftheriades, "Experimental and theoretical verification of focusing in a large, periodically loaded transmission line negative refractive index metamaterial," *Optics Express*, vol. 11, no. 4, pp. 155–157, 2003.

[42] A. Grbic and G. V. Eleftheriades, "Growing evanescent waves in negative-refractive-index transmission-line media," *Appl. Phys. Lett.*, vol. 82, no. 12, pp. 1815–1817, Mar. 2003.

[43] O. F. Siddiqui, S. J. Erickson, G. V. Eleftheriades, and M. Mojahedi, "Time-domain measurement of negative group delay in negative-refractive-index transmission-line metamaterials," *IEEE Trans. Microwave Theory Tech.*, vol. 52, no. 5, pp. 1449–1454, May 2004.

[44] A. Lai, C. Caloz, and T. Itoh, "Composite right/left-handed transmission line metamaterials," *IEEE Microwave Magazine*, vol. 5, no. 3, pp. 34–50, Sept. 2004.

[45] A. Sanada, C. Caloz, and T. Itoh, "Characteristics of the composite right/left-handed transmission lines," *IEEE Microw. Wirel. Compon. Lett.*, vol. 14, no. 2, pp. 68–70, Feb. 2004.

[46] C. Caloz, A. Sanada, and T. Itoh, "A novel composite right-/left-handed coupled-line directional coupler with arbitrary coupling level and broad bandwidth," *IEEE Trans. Microwave Theory Tech.*, vol. 52, no. 3, pp. 980–992, Mar. 2004.

[47] C. Caloz and T. Itoh, *Electromangetic Metamaterials*, John Wiley & Sons, New York, 2006.

[48] A. Priou and T. Itoh (Eds.), *Electromagnetic Applications of Photonic Band Gap Materials and Structures*, EMW Publishing, Cambridge, Massachusetts, 2003.

[49] T. Decoopman, G. Tayeb, S. Enoch, D. Maystre, and B. Gralak, "Photonic crystal lens: from negative refraction and negative index to negative permittivity and permeability," *Phys. Rev. Lett.*, vol. 97, pp. 073905, 2006.

[50] S. Zouhdi, A. V. Dorofeenko, A. M. Merzlikin, and A. P. Vinogradov, "Zero width band gap effect in photonic crystals made of metamaterials," *Phys. Rev. B*, vol. 75, pp. 035125, 2007.

[51] E. Yablonovitch, "An idea for thin subwavelength cavity resonators using metamaterials with negative permittivity and permeability," *Phys. Rev. Lett.*, vol. 58, no. 20, pp. 2059–2062, 1987.

[52] P. A. Belov, S. A. Tretyakov, and A. J. Viitanen, "Nonreciprocal microwave bandgap structures," *Phys. Rev. E*, vol. 66, pp. 016608, 2002.

[53] "Mini-special issue on electromagnetic crystal structures, design, synthesis, and applications," *IEEE Trans. Microwave Theory Tech.*, vol. 47, no. 11, 1999.

[54] "Special issue on electromagnetic applications of photonic band gap materials and structures," *Progress In Electromagnetic Research*, vol. 41, 2003.

[55] K. Yasumuto (Ed.), *Electromagnetic Theory and Applications for Photonic Crystals*, CRC Press, Taylor & Francis, 2006.

[56] M. Notomi, "Theory of light propagation in strongly modulated photonic crystals: Refractionlike behavior in the vicinity of the photonic band gap," *Phys. Rev. B*, vol. 62, pp. 10696–10705, 2000.

[57] C. Luo, S. G. Johnson, and J. D. Joannopoulos, “All-angle negative refraction in a three-dimensionally periodic photonic crystal,” *Appl. Phys. Lett.*, vol. 81, no. 13, pp. 2352–2354, Sept. 2002.

[58] X. Y. Ao and S. L. He, “Three-dimensional photonic crystal of negative refraction achieved by interference lithography,” *Opt. Lett.*, vol. 29, no. 21, pp. 2542–2554, Nov. 2002.

[59] Z. C. Ruan and S. L. He, “Coupling between plane waves and bloch waves in photonic crystals with negative refraction,” *Phys. Rev. B*, vol. 71, pp. 045111, 2005.

[60] Z. C. Ruan and S. L. He, “Open cavity formed by a photonic crystal with negative effective index of refraction,” *Opt. Lett.*, vol. 30, no. 17, pp. 2308–2310, 2005.

[61] J. L. He, J. Yi, and S. L. He, “Giant negative Goos-Hanchen shifts for a photonic crystal with a negative effective index,” *Optics Express*, vol. 14, no. 7, pp. 3024–3029, 2006.

[62] S. He, Y. Jin, Z. Ruan, and J. Kuang, “On subwavelength and open resonators involving metamaterials of negative refraction index,” *New Journal of Physics*, vol. 7, pp. 210, 2005.

[63] N. Gracia and M. Nieto-Vesperinas, “Left-handed materials do not make a perfect lens,” *Phys. Rev. Lett.*, vol. 88, pp. 207403, 2002.

[64] N. Fang and X. Zhang, “Imaging properties of a metamaterial superlens,” *Appl. Phys. Lett.*, vol. 82, no. 2, pp. 161–163, 2003.

[65] S. A. Ramakrishna, J. B. Pendry, D. Schurig, D. R. Smith, and S. Schultz, “The asymmetric lossy near-perfect lens,” *Journal of Modern Optics*, vol. 49, no. 10, pp. 1747–1762, 2003.

[66] A. Grbic and G. V. Eleftheriades, “Overcoming the diffraction limit with a planar left-handed transmission-line lens,” *Phys. Rev. Lett.*, vol. 92, pp. 117403, 2004.

[67] N. Fang, H. Lee, C. Sun, and X. Zhang, “Sub-diffraction-limited optical imaging with a silver superlens,” *Science*, vol. 308, no. 5721, pp. 534–537, 2005.

[68] D. R. Smith, “How to build a superlens,” *Science*, vol. 308, no. 5721, pp. 502–503, 2005.

[69] Y. Jin and S. He, “Focusing by a slab of chiral medium,” *Optics Express*, vol. 13, no. 13, pp. 4974–4979, 2005.

[70] S. Tretyakov, A. Sihvola I. Nefedov, S. Maslovski, and C. Simovski, “Waves and energy in chiral nihility,” *J. Electromag. Waves Appli.*, vol. 17, no. 5, pp. 695–706, 2003.

[71] J. A. Kong, “Electromagnetic wave interaction with stratified negative isotropic media,” *Progress in Electromagnetics Research*, vol. 35, pp. 1–52, 2002.

[72] H. Y. Yao, L. W. Li, C. W. Qiu, Q. Wu, and Z. N. Chen, “Properties of electromagnetic waves in a multilayered cylinder filled with double negative and positive materials,” *accepted by Radio Science*, 2006.

[73] C. W. Qiu, H. Y. Yao, S. N. Burokur, S. Zouhdi, and L. W. Li, “Electromagnetic scattering properties in a multilayered metamaterial cylinder,” *accepted by IEICE Trans. Commun*, 2007.

[74] R. Ruppin, “Extinction properties of a sphere with negative permittivity and permeability,” *Solid State Commun.*, vol. 116, no. 8, pp. 411–415, 2000.

[75] L. W. Li, D. You, M. S. Leong, and T. S. Yeo, “Electromagnetic scattering by multilayered chiral-media structures: a scattering-to-radiation transform,” *Progress In Electromagnetics Research*, vol. 26, pp. 249–291, 2000.

[76] J. R. Richmond, “Scattering by a dielectric cylinder of arbitrary cross-section shape,” *IEEE Trans. Antennas Propagat.*, vol. 13, no. 3, pp. 334–341, May 1965.

[77] J. R. Richmond, “TE-wave scattering by a dielectric cylinder of arbitrary cross-section shape,” *IEEE Trans. Antennas Propagat.*, vol. 14, no. 4, pp. 460–464, July 1966.

[78] A. J. Ward and J. B. Pendry, “Refraction and geometry in Maxwell’s equation,” *Journal of Modern Optics*, vol. 43, no. 4, pp. 773–793, 1996.

[79] C. W. Qiu, S. N. Burokur, S. Zouhdi, and L. W. Li, “Study on energy transport in chiral nihility and chirality nihility effects,” *JOSA A*, vol. to be submitted, 2007.

[80] N. Engheta, “An idea for thin subwavelength cavity resonators using metamaterials with negative permittivity and permeability,” *IEEE Antennas Wirel. Propagat. Lett.*, vol. 1, no. 1, pp. 10–13, 2002.

[81] A. Alù and N. Engheta, “Pairing an epsilon-negative slab with a mu-negative slab: Resonance, tunneling and transparency,” *IEEE Trans. Antennas Propagat.*, vol. 51, no. 10, pp. 2558–2571, Oct. 2003.

[82] J. A. Kong, *Electromagnetic Wave Theory*, John Wiley, New York, third edition, 1990.

[83] B. S. Luk’yanchuk and V. Ternovsky, “Light scattering by a thin wire with a surface-plasmon resonance: Bifurcations of the Poynting vector field,” *Phys. Rev. B*, vol. 73, pp. 235432, 2006.

[84] C. H. Tang, “Macroscopic performance analysis of metamaterials synthesized from microscopic 2-D isotropic cross split-ring resonator array,” *J. Appl. Phys.*, vol. 28, no. 5, pp. 628–634, 1957.

[85] C. W. Qiu, H. Y. Yao, S. N. Burokur, S. Zouhdi, and L. W. Li, “Electromagnetic scattering properties in a multilayered metamaterial cylinder,” *IEICE Trans. Commun.*, vol. accepted, 2007.

[86] A. Alu and N. Engheta, "Resonances in sub-wavelength cylindrical structures made of pairs of double-negative (DNG) and double-positive (DPS) or ϵ-negative (ENG) abd μ-negative (MNG) coaxial shells," *Proc. of ICEAA'03, Turin, Italy*, pp. 435–438, Sept. 2003.

[87] P. Alitalo, S. Maslovski, and S. Tretyakov, "Near-field enhancement and imaging in double cylindrical polariton-resonant structures: Enlarging superlens," *Phys. Lett. A*, vol. 357, no. 4-5, pp. 397–400, 2006.

[88] A. Sommerfeld, *Electrodynamics (translated from the German by E. G. Ramberg)*, Academic Press, New York, 1964.

[89] J. V. Bladel, "Electromagnetic fields in the presence of rotating bodies," *Proc. IEEE*, vol. 64, no. 3, pp. 301–318, Mar. 1976.

[90] L. Rayleigh, "On the influence of obstacles arranged in rectangular order on the properties of a medium," *Phil. Mag.*, vol. 34, pp. 481–502, 1892.

[91] J. C. Maxwell, *A Treatise on Electricity and Magnetism*, Dover, New York, 1954.

[92] L. Lewin, "The electrical constants of a material loaded with spherical particles," *Proc. Inst. Elec. Eng.*, vol. 94, pp. 65–68, 1947.

[93] L. Jylhä, I. Kolmakov, S. Maslovski, and S. Tretyakov, "Modeling of isotropic backward-wave materials composed of resonant spheres," *J. Appl. Phys.*, vol. 99, pp. 043102, 2006.

[94] C. L. Holloway, E. F. Kuester, J. Baker-Jarvis, and P. Kabos, "A double negative (DNG) composite medium composed of magnetodielectric spherical particles embedded in a matrix," *IEEE Trans. Antennas Propagat.*, vol. 51, no. 10, pp. 2596–2603, Oct. 2003.

[95] W. C. Chew, *Waves and Fields in Inhomogeneous Media*, Van Nostrand, New York, 1990.

[96] A. L. Aden and M. Kerker, "Scattering of electromagnetic waves from two concentric spheres," *J. Appl. Phys.*, vol. 22, pp. 1242–1246, 1951.

[97] R. J. Tarento, K. H. Bennemann, P. Joyes, and J. Van de Walle, "Mie scattering of magnetic spheres," *Phys. Rev. E*, vol. 69, pp. 026606, 2004.

[98] N. K. Uzunoglu, P. G. Gottis, and J. G. Fikioris, "Excitation of electromagnetic waves in a gyroelectric cylinder," *IEEE Trans. Antennas Propagat.*, vol. 33, no. 1, pp. 90–99, Jan. 1985.

[99] J. B. Titchener and J. R. Willis, "The reflection of electromagnetic waves from stratified anisotropic media," *IEEE Trans. Antennas Propagat.*, vol. 39, no. 1, pp. 35–39, Jan. 1991.

[100] L. W. Li, C. K. Lee, T. S. Yeo, and M. S. Leong, "Radio wave propagation along earth-space paths in the presence of a multi-layered anisotropic forest," *Electromagnetics*, vol. 22, no. 3, pp. 235–260, May 2002.

[101] J. C. Monzon, "Three-dimensional scattering by an infinite homogeneous anisotropic circular cylinder: A spectral approach," *IEEE Trans. Antennas Propagat.*, vol. 35, no. 6, pp. 670–682, June 1987.

[102] M. A. Hasan and P. L. E. Uslenghi, "Electromagnetic scattering from nonlinear anisotropic cylinders. I. fundamental frequency," *IEEE Trans. Antennas Propagat.*, vol. 38, no. 4, pp. 523–533, Apr. 1990.

[103] Y. L. Geng, X. B. Wu, L. W. Li, and B. R. Guan, "Mie scattering by an uniaxial anisotropic sphere," *Phys. Rev. E*, vol. 70, no. 5, pp. 056609, 2004.

[104] R. D. Graglia, P. L. E. Uslenghi, and R. S. Zich, "Moment method with isoparametric elements for three-dimensional anisotropic scatterers," *Proc. IEEE*, vol. 77, pp. 750–760, 1989.

[105] J. I. Dadap, J. Shan, K. B. Eisenthal, and T. F. Heinz, "Second-harmonic Rayleigh scattering from a sphere of centrosymmetric material," *Phys. Rev. Lett.*, vol. 83, pp. 4045–4048, 1999.

[106] V. V. Varadan, A. Lakhtakia, and V. K. Varadan, "Scattering by three-dimensional anisotropic scatterers," *IEEE Trans. Antennas Propagat.*, vol. 37, pp. 800–802, 1989.

[107] C. W. Qiu, L. W. Li, T. S. Yeo, and S. Zouhdi, "Scattering by rotationally symmetric anisotropic spheres: Potential formulation and parametric studies," *Phys. Rev. E*, p. accepted, 2007.

[108] C. W. Qiu, L. W. Li, Q. Wu, and T. S. Yeo, "Field representations in general gyrotropic media in spherical coordinates," *IEEE Antennas Wirel. Propagat. Lett.*, vol. 4, pp. 467–470, Dec. 2005.

[109] R. Ruppin, "Intensity distribution inside scatterers with negative-real permittivity and permeability," *Microwave Opt. Technol. Lett.*, vol. 36, no. 3, pp. 150–154, 2003.

[110] V. Kuzmiak and A. A. Maradudin, "Scattering properties of a cylinder fabricated from a left-handed material," *Phys. Rev. B*, vol. 66, pp. 045116, 2002.

[111] A. Alù and N. Engheta, "Achieving transparency with plasmonic and metamaterial coatings," *Phys. Rev. E*, vol. 72, pp. 016623, 2005.

[112] R. G. Newton, *Scattering Theory of Waves and Particles*, McGrow-Hill, New York, second edition, 2002.

[113] J. C. Monzon, "Three-dimensional field expansion in the most general rotationally symmetric anisotropic material: Application to scattering by a sphere," *IEEE Trans. Antennas Propagat.*, vol. 37, no. 6, pp. 728–735, June 1989.

[114] M. Kerker, *The Scattering of the Light and Other Electromagnetic Radiation*, Academic Press, New York, 1969.

[115] J. E. McDonald, "Large-sphere limit of the radar back-scattering coefficient," *Quart. J. Roy. Meteorol. Soc.*, vol. 88, pp. 183–186, Apr. 1962.

[116] C. F. Bohren and D. R. Huffman, *Absorption and Scattering of Light by Small Particles*, Wiley, New York, 1998.

[117] Z. B. Wang, B. S. Luk'yanchuk, M. H. Hong, Y. Lin, and T. C. Chong, "Energy flow around a small particle investigated by classical Mie theory," *Phys. Rev. B*, vol. 70, pp. 35418, 2004.

[118] W. Weiglhofer and W. Paponsek, "Skalare hertz'sche potentiale für gyrotrope medien," *AEU*, vol. 39, pp. 343–346, Nov-Dec 1985.

[119] W. Weiglhofer, "Field representation in gyrotropic media by one scalar superpotential," *IEEE Trans. Antennas Propagat.*, vol. 35, no. 11, pp. 1301–1302, Nov. 1987.

[120] S. Liu, L. W. Li, M. S. Leong, and T. S. Yeo, "Field representations in general rotationally uniaxial anisotropic media using spherical vector wave functions," *Microwave and Optical Technology Letters*, vol. 25, no. 3, pp. 159–162, May 2000.

[121] S. Liu, L. W. Li, M. S. Leong, and T. S. Yeo, "Theory of gyroelectric waveguides," *Prog. In Electromagn. Res.*, vol. 29, pp. 231–259, 2000.

[122] L. W. Li, N. H. Lim, M. S. Leong, and T. S. Yeo, "Eigenfunctional expansion of dyadic Green's functions in gyrotropic media using cylindrical vector wave functions," *Prog. Electromagn. Res.*, vol. 43, pp. 101–121, 2003.

[123] W. Magnus and F. Oberhettinger, *Formulas and Theorems for the Special Functions of Mathematical Physics*, Chelsea, New York, 1949.

[124] D. F. Arago, “Sur une modification remarquable qu’éprouvent les rayons lumineux dans leur passage á travers certains corps diaphanes, et sur quelques autres nouveaux phénomènes d’optique,” *Mem. Inst.*, vol. 1, pp. 93–134, 1811.

[125] J. B. Biot, “Mémoire sur un nouveau genre d’oscillations que les molécules de la lumière éprouvent, en traversant certains cristaux,” *Mem. Inst.*, vol. 1, pp. 1–372, 1812.

[126] J. B. Biot, “Phénomènes de polarisation successive, observés dans des fluides homogènes,” *Bull. Soc. Philomath.*, pp. 190–192, 1815.

[127] A. Fresnel, “Mémoire sur la double réfraction que les rayons lumineux éprouvent en traversant les aiguilles de cristal de roche suivant des directions parallèles à l’axe,” *Oeuvres*, vol. 1, pp. 731–751, 1822.

[128] T. M. Lowry, *Optical Rotatory Power*, Dover, New York, 1964.

[129] S. Bassiri, C. H. Papas, and N. Engheta, “Electromagnetic wave propagation through a dielectric-chiral interface and through a chiral slab,” *J. Opt. Soc. Am. A*, vol. 5, no. 9, pp. 1450–1459, 1988.

[130] A. Priou (Ed.), *Bianisotropic and Bi-isotropic Media and Applications, PIER* **9**, EMW Publishing, Cambridge, Massachusetts, 1994.

[131] M. P. Silverman and R. B. Sohn, “Effects of circular birefringence on light propagation and reflection,” *Am. J. Phys.*, vol. 54, pp. 69–76, 1986.

[132] T. G. Kharina, S. A. Tretyakov, A. A. Sochava, C. R. Simovski, and S. Bolioli, "Experimental studies of artificial omega med," *Electromagnetics*, vol. 18, no. 4, pp. 423–437, 1998.

[133] A. H. Sihvola, "Temporal dispersion in chiral composite materials: A theoretical study," *J. Electromagn. Waves Appli.*, vol. 6, no. 9, pp. 1177–1196, 1992.

[134] I. V. Lindell, A. H.Sihvola, S. A Tretyakov, and A. J. Viitanen, *Electromagnetic Waves in Chiral and Bi-Isotropic Media*, Artech House, Boston, London, 1994.

[135] A. J. Viitanen and I. V. Lindell, "Chiral slab polarization transformer for aperture antennas," *IEEE Trans. Antennas Propagat.*, vol. 39, pp. 75–82, Jan. 1991.

[136] J. B. Pendry, "A chiral route to negative refraction," *Science*, vol. 306, no. 5700, pp. 1353–1355, 2004.

[137] S. Tretyakov, A. Sihvola, and L. Jylhä, "Backward-wave regime and negative refraction in chiral composites," *Photonics and Nanostructures - Fundamentals and Applications*, vol. 3, pp. 107–115, 2005.

[138] A. H. Sihvola and I. V. Lindell, "Chiral Maxwell-Garnett mixing formula," *Electron. Lett.*, vol. 26, no. 2, pp. 118–119, 1990.

[139] A. H. Sihvola and I. V. Lindell, "Polarisability and mixing formula for chiral ellipsoids," *Electron. Lett.*, vol. 26, no. 14, pp. 1007–1009, 1990.

[140] A. Ishimaru, S. W. Lee, Y. Kuga, and V. Jandhyala, "Generalized constitutive relations for metamaterials based on the quasi-static Lorentz theory," *IEEE Trans. Antennas Propagat.*, vol. 51, no. 10, pp. 2550–2557, Oct. 2003.

[141] S. L. Prosvirnin and S. Zouhdi, "On the effective constitutive parameters of metal-dielectric arrays of complex-shaped particles," *J. Electromagn. Waves Appli.*, vol. 20, no. 5, pp. 583–598, 2006.

[142] D. L. Jaggard, A. R. Mickelson, and C. H. Papas, "On electromagnetic waves in chiral media," *Appl. Phys.*, vol. 18, pp. 211–216, 1979.

[143] M. Born, "On the theory of optical activity. I. General theory of a system of coupled isotropic oscillators. II. Molecules with a binary axis of symmetry," *Proc. Roy. Soc. London. Series A, Math.Phys. Sci.*, vol. 150, no. 86, pp. 84–105, 1935.

[144] E. U. Condon, "Theories of optical rotatory power," *Rev. Mod. Phys.*, vol. 9, pp. 432–457, 1937.

[145] T. Roth and G. L. J. A. Rikken, "Observation of magnetoelectric linear birefringence," *Phys. Rev. Lett.*, vol. 88, no. 6, pp. 063001, 2002.

[146] F. Jonsson and C. Flytzanis, "Polarization state dependence of optical parametric processes in artificially gyrotropic media," *J. Opt. A: Pure Appl. Opt.*, vol. 2, no. 4, pp. 299–142, 2000.

[147] A. Ishimaru, *Electromagnetic Wave Propagation, Radiation, and Scattering*, Prentice Hall, New Jersey, 1991.

[148] C. H. Papas, *Theory of Electromagnetic Wave Propagation*, McGraw-Hill, New York, 1965.

[149] C. W. Qiu, H. Y. Yao, L. W. Li, S. Zouhdi, and M. S. Leong, "On the constitutive relations of G-chiral media and the possibility to realize negative-index media," *Microw. Opt. Tech. Lett.*, vol. 48, no. 12, pp. 2534–2538, 2006.

[150] V. M. Agranovich, Yu. N. Gartstein, and A. A. Zakhidov, "Overcoming the diffraction limit with a planar left-handed transmission-line lens," *Phys. Rev. B*, vol. 73, pp. 045113, 2006.

[151] L. D. Landau and E. M. Lifshitz, *Electrodynamics of Continuous Media*, Pergamon Press, Oxford, second edition, 1984.

[152] A. Lakhtakia, *Beltrami Fields in Chiral Media*, World Scientific, Singapore, 1994.

[153] N. Grigorenko, A. K. Geim, H. F. Gleeson, Y. Zhang, A. A. Firsov, I. Y. Khrushchev, and J. Petrovic, "Nanofabricated media with negative permeability at visible frequencies," *Nature Letters*, vol. 438, pp. 335–338, 2005.

[154] A. Lakhtakia, "An electromagnetic trinity from "negative permittivty" and "negative permeability"," *Intl. J. Infrar. Millim. Waves*, vol. 22, pp. 1734–1741, 2001.

[155] C. Zhang and T. J. Cui, "Negative reflections of electromagnetic waves in chiral media," *arXiv:physics/0610172 (unpublished)*, 2006.

[156] M. P. Silverman, "Reflection and refraction at the surface of a chiral medium: Comparison of gyrotropic constitutive relations invariant or noninvariant under a duality transformation," *J. Opt. Soc. Am. A*, vol. 3, pp. 830–837, 1986.

[157] J. Q. Shen, "Negative refractive index in gyrotropically magnetoelectric media," *Phys. Rev. B*, vol. 73, pp. 045113, 2006.

[158] A. H. Sihvola and I. V. Lindell, "Bi-isotropic constitutive relations," *Microwave Opt. Tech. Lett.*, vol. 11, pp. 295–297, 1991.

[159] C. F. Bohren, "Light scattering by an optically active sphere," *Chem. Phys. Lett.*, vol. 29, pp. 458–462, 1974.

[160] S. Tretyakov, C. R. Simovski, and M. Hudlička, "Bianisotropic route to realization and matching backward-wave slabs," *arXiv:cond-matt/0607120 (unpublished)*, 2006.

[161] Q. Cheng and T. J. Cui, "Negative refractions in uniaxially anisotropic chiral media," *Phys. Rev. B*, vol. 73, pp. 113104, 2006.

[162] C. W. Qiu, L. W. Li, H. Y. Yao, and S. Zouhdi, "Properties of Faraday chiral media: Green dyadics and negative refraction," *Phys. Rev. B*, vol. 74, pp. 115110, 2006.

[163] N. Engheta, D. L. Jaggard, and M. W. Kowarz, "Electromagnetic waves in Faraday chiral media," *IEEE Trans. Antennas Propagat.*, vol. 40, no. 4, pp. 367–374, Apr. 1992.

[164] J. A. Kong, "Image theory for bianisotropic media," *IEEE Trans. Antennas Propagat.*, vol. 19, no. 3, pp. 451–452, May 1971.

[165] C. T. Tai, *Dyadic Green's Functions in Electromagnetic Theory*, IEEE Press, New Jersey, second edition, 1994.

[166] E. Sanchez-Palencia, *Non-homogenous Media and Vibration Theory*, Springer-Verlag, Berlin, 1980.

[167] D. Cheng and W. Ren, "Green dyadics in reciprocal uniaxial bianisotropic media by cylindrical vector wave functions," *IEEE Trans. Microwave Theory Tech.*, vol. 54, no. 3, pp. 2917–2924, Sept. 1994.

[168] L. W. Li, P. S. Kooi, M. S. Leong, and T.S. Yeo, "Electromagnetic dyadic Green's function in spherically multilayered media," *IEEE Trans. Microwave Theory Tech.*, vol. 42, no. 12, pp. 2302–2310, Dec. 1994.

[169] L. W. Li, P. S. Kooi, M. S. Leong, and T. S. Yeo, "A general expression of dyadic Green's function in radially multilayered chiral media," *IEEE Trans. Antennas Propagat.*, vol. 43, no. 3, pp. 232–238, Mar. 1995.

[170] I. V. Lindell and F. Olyslager, "Analytic green dyadic for a class of nonreciprocal anisotropic media," *IEEE Trans. Antennas Propagat.*, vol. 45, no. 10, pp. 1563–1565, Oct. 1997.

[171] D. Cheng, "Eigenfunction expansion of the dyadic Green's function in a gyroelectric chiral medium by cylindrical vector wave functions," *Phys. Rev. E*, vol. 55, pp. 1950–1958, Feb. 1997.

[172] I. V. Lindell and W. S. Weiglhofer, "Green dyadic for a uniaxial bianisotropic medium," *IEEE Trans. Antennas Propagat.*, vol. 42, no. 7, pp. 1013–1016, July 1994.

[173] J. Lam, "Magnetic permeability of a simple cubic lattice of conducting magnetic spheres," *J. Appl. Phys.*, vol. 60, pp. 4230–4235, 1986.

[174] A. H. Sihvola, *Electromagnetic Mixing Formulas and Applications*, Electromagnetic Waves Series 47, IEE Publishing, London, 1999.

[175] B. Sareni, L. Krahenbuhl, A. Beroual, and A. Nicolas, "A boundary integral equation method for the calculation of the effective permittivity of periodic composites," *IEEE Trans. Magn.*, vol. 33, no. 2, pp. 1580–1583, Mar. 1997.

[176] F. Wu and K. W. Whites, "Quasi-static effective permittivity of periodic composites containing complex shaped dielectric particles," *IEEE Trans. Antennas Propagat.*, vol. 49, no. 8, pp. 1174–1182, Aug. 2001.

[177] K. W. Whites and F. Wu, "Effects of particle shape on the effective permittivity of composite materials with measurements for lattices of cubes," *IEEE Trans. Microwave Theory Tech.*, vol. 50, no. 7, pp. 1723–1729, July 2002.

[178] D. Cioranescu and P. Donato, *An Introduction to Homogenization*, Oxford University Press, New York, 1999.

[179] O. Ouchetto, C. W. Qiu, S. Zouhdi, L. W. Li, and A. Razek, "Homogenization of 3d periodic bianisotropic metamaterials," *IEEE Trans. Microwave Theory Tech.*, vol. 54, no. 11, pp. 3893–3898, Nov. 2006.

[180] O. Ouchetto, S. Zouhdi, A. Bossavit, G. Griso, and B. Miara, "Modeling of 3d periodic multiphase composites by homogenization," *IEEE Trans. Microwave Theory Tech.*, vol. 54, no. 6, pp. 2615–2619, June 2006.

[181] D. Cioranescu, A. Damlamian, and G. Griso, "Periodic unfolding and homogenization," *C. R. Acad. Sci. Paris, Ser. I*, vol. 335, pp. 99–104, 2002.

[182] A. Bossavit, G. Griso, and B. Miara, "Modelling of periodic electromagnetic structures: Bianisotropic materials with memory effects," *J. Math. Pures Appl.*, vol. 84, pp. 819–850, 2005.

Publication

---

1. C.-W. Qiu, S.-N. Burokur, S. Zouhdi, and L.-W. Li, “Chiral Nihility Effects on Energy Flow in Chiral Materials”, accepted by JOSA A, 2007
2. C.-W. Qiu, Hai-Ying Yao, L.-W. Li, S. Zouhdi, and T.-S. Yeo, “Eigenfuctional Representation of Dyadic Green’s Functions in Planarly Multilayered General Faraday Chiral Media”, Journal of Physics A: Mathematical and Theoretical, vol. 40, no. 21, pp. 5751-5766, May 2007
3. C.-W. Qiu, L.-W. Li, and T.-S. Yeo, “Vector Eigenfunction Expansion of Green Dyadics for Radially Multilayered Rotationally Uniaxial Anisotropic Media”, submitted to IEEE Trans. Antennas Propagat., 2007
4. C.-W. Qiu, S. Zouhdi, and S. Tretyakov, “Theoretical and Case Studies of Cloakings on Wire Scatterers: Rotation Effects, Resonant Scattering, and Resonance Shifts”, submitted to Physical Review E, 2007
5. C.-W. Qiu, S. Zouhdi, S. Tretyakov, and L.-W. Li, “Nonreciprocal and Gyrotropic Effects of Chiral Nihility to Achieve Negative-Index Materials”, submitted to IEEE Trans. Antennas Propagat., 2007

6. H.-Y. She, C.-W. Qiu, L.-W. Li, and S.-J. Chua, "Multiple Electric and Magnetic Resonances of Plasmonic Nanoparticles in Light Scattering", submitted to Physical Review B, 2007
7. C.-W. Qiu and S. Zouhdi, "Comment on "Negative refractive index in gyrotropically magnetoelectric media"", Physical Review B, 75, 196101 (2007)
8. C.-W. Qiu, H.-Y. Yao, S.-N. Burokur, S. Zouhdi, and L.-W. Li, "Electromagnetic Scattering Properties in a Multilayered Metamaterial Cylinder", IEICE Transactions on Electronics (special section on ISAP'06), vol. E-90-B, no. 9, September 2007
9. C.-W. Qiu, H.-Y. Yao, L.-W. Li, T.-S. Yeo, and S. Zouhdi, "Routes to Left-Handed Media by Magnetoelectric Couplings", Physical Review B, 75, 245214, (2007)
10. C.-W. Qiu, H.-Y. Yao, L.-W. Li, S. Zouhdi, and T.-S. Yeo, "Backward Waves in Magnetoelectrically Chiral Media: Propagation, Impedance and Negative Refraction", Physical Review B, 75, 155120 (2007)
11. H.-Y. Yao, L.-W. Li, C.-W. Qiu, Q. Wu, and Z.-N. Chen, "Scattering Properties of Electromagnetic Waves in a Multilayered Cylinder Filled with Double Negative and Positive Materials", Radio Science, vol. 42, RS2006, doi:10.1029 / 2006RS003509, 2007
12. C.-W. Qiu, L.-W. Li, T.-S. Yeo, and S. Zouhdi, "Scattering by Rotationally Symmetric Anisotropic Spheres: Potential Formulation and Parametric Stud-

ies", Physical Review E, 75, 026609 (2007)

13. C.-W. Qiu, Le-Wei Li, S. Zouhdi, T.-S. Yeo, and Q. Wu, "On the Integral identities Consisting of Two Spherical Bessel Functions", IEEE Transaction of Antennas and Propagation, vol. 55, no. 1, pp. 240-244, Jan 2007
14. O. Ouchetto, C.-W. Qiu, S. Zouhdi, L.-W. Li, and A. Razek, "Homogenization of 3D Periodic Bianisotropic Metamaterials", IEEE Transactions on Microwave Theory and Techniques, vol. 54, no. 11, pp. 3893-3898, Dec 2006
15. C.-W. Qiu, H.-Y. Yao, S. Zouhdi, L.-W. Li, and M.-S. Leong, "On the Constitutive Relations of G-Chiral Media and the Possibility to Realize Negative-Index Media", Microwave and Optical Technology Letters, vol. 48, no. 12, pp. 2534-2538, 2006
16. C.-W. Qiu, L.-W. Li, H.-Y. Yao, and S. Zouhdi, "Properties of Faraday Chiral Media: Green Dyadics and Negative Refraction", Physical Review B, 74, 115110 (2006), (selected for the Oct. 2, 2006 issue of Virtual Journal of Nanoscale Science & Technology published by the American Institute of Physics and the American Physical Society)
17. C.-W. Qiu, L.-W. Li, Q. Wu, and T.-S. Yeo, "Field Representations in General Gyrotropic Media in Spherical Coordinates", IEEE Antennas and Wireless Propagation Letters, vol. 4, pp. 467-470, Dec 2005